

**The response of ASTM F1537 Co-28Cr-6Mo
alloy with different phase constituents
to low-temperature plasma carburising**

by

Xia LUO

A thesis submitted to
The University of Birmingham
for the degree of
DOCTOR OF PHILOSOPHY

School of Metallurgy and Materials
The University of Birmingham
Birmingham B15 2TT
United Kingdom

January, 2014

UNIVERSITY OF
BIRMINGHAM

University of Birmingham Research Archive

e-theses repository

This unpublished thesis/dissertation is copyright of the author and/or third parties. The intellectual property rights of the author or third parties in respect of this work are as defined by The Copyright Designs and Patents Act 1988 or as modified by any successor legislation.

Any use made of information contained in this thesis/dissertation must be in accordance with that legislation and must be properly acknowledged. Further distribution or reproduction in any format is prohibited without the permission of the copyright holder.

SYNOPSIS

Co–Cr alloys are the most widely used metallic biomaterials for metal-on-metal joint prostheses. However, concerns about increased revision rate associated with large head metal-on-metal replacements have been raised recently. Release of such toxic ions as Cr and Co from corrosion–wear induced nano-sized wear debris has been envisaged as the potential cause. This research was aimed at studying the response of medical grade ASTM F1537 Co-28Cr-6Mo alloy with different phase constituents to low-temperature plasma carburising and the tribocorrosion behaviour of the plasma S-phase surface engineered alloy with a view of addressing the tribocorrosion problems of the current metal-on-metal joint prostheses.

To this end, a series of heat treatments were designed to produce samples with an α -FCC dominated (>95%), an ϵ -HCP dominated (>97%) and a dual phased (40% ϵ -HCP) microstructures. An optimised low-temperature plasma carburising (LTPC) treatment (450 °C/10 h in a gas mixture of 98.5 % H₂ and 1.5 % CH₄) was applied to the Co-28Cr-6Mo alloy with different phase constituents. The microstructure of the plasma carburised surface layers were characterised by XRD, GDS, SEM/EDX and TEM, and the properties of the surface carburised layers were evaluated using micro- and nano-indentation, reciprocating wear and electrochemical corrosion tests, and tribocorrosion tests at different electrochemical potentials. Post-test examinations were conducted to study mechanisms involved.

The experimental results have showed that the response of the Co-28Cr-6Mo alloy to the

LTPC treatment is highly dependent on the phase constituent. For example, the same LTPC treatment produced a 7 μm -thick carbon supersaturated S-phase layer on the originally α -FCC dominated (>95%) FCC-PC sample while a 2 μm -thick Co_3C dispersed layer was formed on the originally ϵ -HCP dominated (>97%) sample.

The LTPC treatment can significantly increase the hardness, load bearing capacity and dry wear resistance of all the Co–28Cr-6Mo samples with different phase constituents. The nanohardness is similar (12 GPa) for the S-phase layer formed on the FCC-PC sample and for the Co_3C dispersed layer formed on HCP-PC sample, which is about 3 times that of the as-received material. Whilst the dry wear resistance is higher for the HCP-PC than for the FCC-PC, the latter shows a better corrosion resistance than the former. The FCC-PC sample has a higher load bearing capacity than the HCP-PC and 40HCP-PC samples when loaded under 25 and 50 g mainly; however, when loaded at 100 g or above, the HCP-PC sample outperforms the 40HCP-PC and FCC-PC samples.

The tribocorrosion properties of Co–28Cr-6Mo alloy with different phase constituents have been effectively enhanced by the LTPC treatment in terms of reduced and stable current over the whole sliding period at anodic potentials and reduced total wear volume at all potentials except OCP. The HCP-PC samples show a much lower total wear volume than the FCC-PC samples at all potentials except 400 mV (SCE).

ACKNOWLEDGEMENTS

I would like to express my sincere gratitude to my supervisors: Prof. H. Dong and Dr. X.Y. Li for their patient guidance and assistance throughout this study and for giving me this study opportunity.

I also gratefully acknowledge scholarships provided by the China Scholarship Council and The University of Birmingham.

I would also like to thank Dr. Jian Chen, Dr. Wei Li, Dr. Raja Khan, Dr. Ran Ji, Mr. Dennis Formosa, Mr. Kaijie Lin, Mr. Jun Zhou and Mr. Ran Liu for their help and consultation.

Special thanks go to Dr. Yong Sun from De Montfort University and Dr. Ligang Zhang for their advice and cutting insight.

I would also like to show my appreciation to the School of Metallurgy and Materials at the University of Birmingham for the support.

Finally, I would like to say thank you to my family and friend, especially my mother and Mr. Tunan Guan for their constant love and support.

PUBLICATIONS

- [1] X. Luo, X. Li, Y. Sun and H. Dong, Tribocorrosion behavior of S-phase surface engineered medical grade Co–Cr alloy, *Wear*, 302 (2013) 1615-1623.
- [2] X. Luo and X.Y. Li, Design and characterisation of a new duplex surface system based on S-phase hardening and carbon-based coating for ASTM F1537 Co–Cr–Mo alloy, *Applied Surface Science*, Available online 4 December 2013, ISSN 0169-4332, <http://dx.doi.org/10.1016/j.apsusc.2013.11.141>.
- [3] X. Luo, X. Li, and H. Dong, Response of FCC/HCP phase constituents of ASTM F-1537 Co-Cr alloy to low temperature plasma carburising, 19th Congress of the International Federation for Heat Treatment and Surface Engineering, 2011, Glasgow, UK.
- [4] X. Luo, X. Li, and H. Dong, Microstructure Characterisation of Low Temperature Plasma Carburised ASTM F1537 Co-Cr alloy, 11th International Conference on Materials Chemistry, 2013, Coventry, UK

CONTENT

CHAPTER 1 INTRODUCTION.....	7
1.1 The concerns over metal-on-metal hip joint prostheses	7
1.2 Aims and objectives.....	11
CHAPTER 2 LITERATURE REVIEW	13
2.1 Properties and applications of Co-Cr alloys	13
2.2 Physical metallurgy	14
2.2.1 Phase constituents and stacking fault.....	14
2.2.2 Sigma (σ) phase.....	17
2.2.3 The alloying elements	18
2.2.4 Co_3C	19
2.2.5 Processing methods.....	20
2.3 Corrosion of Co-Cr alloys	21
2.3.1 Introduction	21
2.3.2 Corrosion mechanism of Co-Cr alloys.....	22
2.3.3 Factors associated with corrosion	24
2.4 Wear of Co-Cr alloys.....	25
2.4.1 Introduction	25
2.4.2 Wear mechanisms	26
2.4.3 Factors associated with wear.....	27
2.5 Tribocorrosion of Co-Cr alloy	30
2.5.1 Introduction	30

2.5.2 Synergism effects between corrosion and wear and the involved mechanisms	30
2.5.3 Factors associated with tribocorrosion	33
2.6 Surface engineering of Co-Cr alloys	35
2.6.1 Introduction to surface engineering	35
2.6.2 Surface coating of Co-Cr alloys	36
2.6.3 Surface modification on Co-Cr alloys	41
CHAPTER 3 EXPERIMENTAL	47
3.1 Materials and Sample Preparation	47
3.2 Sample treatment	47
3.2.1 Heat treatment	47
3.2.2 Low temperature plasma carburising	48
3.3 Characterisation and property evaluation	49
3.3.1 Microstructural observation	49
3.3.1.1 Preparation of metallographic samples	49
3.3.1.2 Optical and scanning electron microscope (SEM)	50
3.3.1.3 Transmission electron microscopy (TEM)	50
3.3.2 Phase identification	51
3.3.2.1 X-Ray diffraction (XRD)	51
3.3.2.2 Electron backscatter diffraction (EBSD)	51
3.3.2.3 TEM observation	51
3.3.3 Composition depth profiling	52

3.3.4 Mechanical property measurement	52
3.3.4.1 Microhardness and load bearing capacity measurement	52
3.3.4.2 Nanoindentation test	53
3.3.4.3 Nanoindentation associated with EBSD technique	54
3.3.5 Wear test	55
3.3.6 Corrosion Test	55
3.3.7 Tribocorrosion Test	56
CHAPTER 4 RESULTS	59
4.1 Microstructure of as-received material	60
4.2 Microstructure of heat-treated samples	62
4.2.1 FCC sample	63
4.2.2 HCP sample	64
4.2.3 40HCP sample	66
4.2.4 TEM analysis on the heat-treated samples	67
4.3 Microstructure of plasma carburised samples	69
4.3.1 FCC-PC	70
4.3.2 HCP-PC	71
4.3.3 TEM analysis on the 40HCP-PC sample	72
4.4 Mechanical properties	74
4.4.1 Microhardness	75
4.4.1.1 Heat-treated samples	75
4.4.1.2 Plasma carburised samples	76

4.4.2 Load-bearing capacity of plasma carburised samples.....	77
4.4.3 Nanoindentation analysis	79
4.4.3.1 Surface nanoindentation of bulk samples	80
4.4.3.2 Nanoindentation of FCC and HCP grains	82
4.5 Electrochemical corrosion	84
4.5.1 Corrosion resistance of heat-treated samples	84
4.5.1.1 Anodic polarisation.....	84
4.5.1.2 Post test SEM observations	86
4.5.2 Corrosion behaviour of plasma carburised samples	87
4.5.2.1 Anodic polarisation tests	87
4.5.2.2 Post test SEM observations	88
4.6 Tribological Properties	89
4.6.1 As-received and heat-treated samples	90
4.6.1.1 Coefficient of friction	90
4.6.1.2 Wear volume.....	90
4.6.1.3 Wear track observations	91
4.6.2 Plasma-carburised samples	93
4.6.2.1 Coefficient of friction	93
4.6.2.2 Wear volume.....	94
4.6.2.3 Wear track observation	95
4.6.3 Comparison of wear	96
4.7 Tribocorrosion	96

4.7.1 Potentiodynamic sliding tests without load	97
4.7.1.1 Heat-treated samples.....	97
4.7.1.2 Plasma carburised samples	98
4.7.1.3 Effect plasma carburising	98
4.7.2 Potentiodynamic sliding tests under load.....	99
4.7.2.1 Heat-treated samples.....	99
4.7.2.2 Plasma carburised samples	99
4.7.2.3 Effect of plasma carburising.....	100
4.7.2.4 Comparison between corrosion and tribocorrosion conditions	101
4.7.3 Effect of potential on electrochemical behaviour during potentiostatic sliding wear test	101
4.7.3.1 Heat-treated samples.....	101
4.7.3.2 Plasma carburised samples	103
4.7.4 Effect of potential on wear performance during potentiostatic sliding wear test	105
4.7.4.2 Plasma carburised samples	109
4.7.4.3 Comparison between heat-treated and plasma carburised samples....	111
CHAPTER 5 DISCUSSION	113
5.1 Introduction	113
5.2 Phase Transformation during LTFC Treatment	115
5.2.1 FCC Structured Co-Cr Substrate.....	115
5.2.2 HCP structured Co-Cr substrate.....	116

5.3 Hardening by LTPC Treatment	121
5.3.1 Surface hardening of FCC-PC samples	121
5.3.2 Surface hardening of HCP-PC samples	122
5.4 Tribological Properties	123
5.4.1 Coefficient of friction.....	123
5.4.2 Wear mechanism.....	125
5.5 tribocorrosion properties.....	127
5.5.1 General synergistic effect between wear and corrosion.....	127
5.5.2 Mechanical wear and chemical wear	128
5.5.4 Tribocorrosion mechanism	131
5.5.3 Potential impact and limitation	133
CHAPTER 6 CONCLUSIONS	136
CHAPTER 7 FUTURE WORK.....	140
REFERENCES	141
LIST OF TABLES	
LIST OF FIGURES	
TABLES	
FIGURES	

CHAPTER 1 INTRODUCTION

1.1 The concerns over metal-on-metal hip joint prostheses

The human hip joint is a typical synovial ball-in-socket joint consisting of an acetabular cup articulating with a femoral head and a cartilage cushion located between two counterparts serving as a lubricated layer. The main function of hip joint is to maintain mobility of human body to do such daily activities as walking and running and extensive exercises which involve turning, twisting et al. causing torsional forces on the joint. Besides this, it supports the weight of human body under both dynamic and static conditions.

Osteoarthritis result from these repeated daily normal activities combined with natural aging or injury of hip joint, leading to degeneration and loss of lubricated cartilage cushion. Repetitive usage of joint without protection of cartilage cushion causes pains and swelling of joint, so called osteoarthritis. To eliminate the pain and restore mobility, surgeons attempt to remove the affected bones and use hip joint prostheses as substitutes. According to National Joint Registry (NJR) for England and Wales 7th annual report 2010, osteoarthritis is the cause of 93% of the total patients receiving hip primary implantation surgeries. Other factors such as avascular necrosis, fractured neck of femur, congenital dislocation and inflammatory arthropathy are key reasons for patients to receive hip replacement surgeries as well.

The materials used for hip joint prostheses are required to perform well in the corrosive human body environment. Three aspects have been considered as key demands for selection

of the biomaterials. Firstly, the materials should not induce adverse physiological reactions and at the same time human normal physiological reactions don't affect their properties, as termed biocompatibility. Secondly, adequate mechanical properties (mechanical strength and Young's modulus) play an important part in the performance of this sort of spherical bearing. Last but not the least is surface degradation due to corrosion and corrosion-wear. The body fluid can be regarded as a 0.9% NaCl solution with small amounts of other inorganic salts and protein. It is highly corrosive for some metals and alloys because the large amount of chloride ions can induce localised corrosion. Thus, superior corrosion resistance is desirable for biomaterials. Meanwhile, high corrosion-wear resistance is also essential for the articulating surfaces i.e. bearing surfaces of such joint prostheses as hip and knee joints.

The searching for suitable materials as substitutes of affected bones dates back to 1820s from wooden blocks, porcine tissue, ivory, polymer (polytetrafluorethylene (PTFE) and ultra high molecular weight polyethylene (UHMWPE)) to metals (stainless steel, Co-Cr and Ti alloys). The properties of metal candidates for biomaterials are tabulated in Table 1.1.1 [1].

Various designs of hip joint prostheses and combination of materials have also been investigated to obtain low friction and wear bearings. Smith-Petersen made the first attempt to fabricate a molded cup from a Co-Cr alloy in 1938. In 1956, G. K. McKee and John Watson-Farrar separated the molded cup to two parts including a Co-Cr spherical femoral head with a long stem and a Co-Cr acetabular cup. Orthopaedic surgeon Sir John Charnley developed an acetabulum of polymer (PTFE and UHMWPE) as a replacement for cartilage

cushion to reduce friction, which pattern has been the most popular hip joint prostheses design and widely used today as a metal femoral stem and ball component articulating against a polyethylene acetabular component. The popularity of these metal-on-metal bearings has been reduced. [2]

Study by Goodman et al. [3] suggests that polyethylene wear particles lead to a decrease of net bone formation and an increase of osteoclasts, indicating that these particles provoked osteoclastic bone resorption, and eventually periprosthetic aseptic loosening termed osteolysis. The same phenomenon has been observed by other researchers [4, 5]. Above evidences show that polyethylene particles play the major role in inducement of macrophagic osteolysis in the vicinity of PE cup prostheses, which is the key complication following hip joint arthroplasty and the main reason for revising loosened implants. The same problem happens for metal-on-metal hip joint implants.

Due to the prevention of polyethylene particle-induced osteolysis and reduced wear, the renewed interest in metal-on-metal total hip prostheses for potentially longer life-span prostheses has arisen recently. The modern metal-on-metal articulation shows markedly reduced wear compared to conventional metal-on-polyethylene combination *in vitro* tests [6, 7]. However, patients with metal-on-metal prostheses had dramatically elevated metal ion concentrations compared with patients receiving a different bearing surface combination by numerous studies as summarised in Table 1.1.2 [8, 9].

What is worse, patients using large head metal-on-metal total hip joint prostheses experience greater risk for revision than patients using a different bearing surface combination as shown in Table 1.1.3 from the U.K./Wales registry [10].

The reasons why such a high failure rate of metal-on-metal total hip joint prostheses occurred have been investigated by several researchers [11-13]. Studies show that the common causes contributing to failure are pseudotumor formation, aseptic loosening, metal hypersensitivity reactions, metal sensitivity and neck fracture [11, 14], most of which are associated with wear debris and resultant metal ion release.

Wear is inevitable in the implantation of prostheses from the first step patients took after surgeries. Although metal-on-metal articulations show much less wear volume compared with metal-on-polyethylene articulation, the size of particles generated by metal-on-metal articulation is an order of magnitude smaller [15] than that of PE particles, resulting in large contact surface area between metal particles and human body system and following generation of metallic ions. Owing to metal wear debris, patients suffer from “adverse reactions to metal debris (ARMD)” or “adverse local tissue reaction (ALTR)” which results in implant loosening and necrosis. Natsu et al. [13] studied the histopathology of ARMD by examining periprosthetic soft tissues at revision surgery from failed ones and concluded that ARMD includes a series of inflammatory response consisting of pure metallosis newly termed pseudotumors, aseptic lymphocytic vasculitis associated lesion (ALVAL) first introduced by Willert et al. [16] in 2005 and granulomatous inflammation. The tissue necrosis

attribute to these inflammatory cell response.

Another concern is the elevated level of metal ions such as cobalt and chromium in whole blood, red blood cell, urine and serum in patients after metal-on-metal total hip arthroplasties. Metal ions can cause such adverse physiological reactions as carcinogenicity, metal hypersensitivity and toxicity [14, 17-19]. Thus, it is an emergency task for us to reduce wear and metal ions of metal-on-metal bearings to expand life-span of metal-on-metal hip joint prostheses, which forms the theme of this thesis.

1.2 Aims and objectives

The overall aim of this project was to enhance the wear and tribocorrosion resistance of a medical grade Co-Cr alloy, thus extending the life-span of metal-on-metal hip joint prostheses.

The specific scientific and clinical objectives were:

- To systematically study the response of medical grade ASTM F1537 Co-28Cr-6Mo alloy with different FCC/HCP ratios to low temperature plasma carburising (LTPC) treatment, thus advancing scientific understanding and establishing technical database for optimising the LTPC technology.
- To generate carbon S-phase on ASTM F1537 Co-28Cr-6Mo alloy by applying optimised low temperature plasma carburising treatment to improve the tribocorrosion behaviour of the medical grade Co-Cr alloy in simulated body fluid under tribo-contact conditions.

- To fully characterise the chemical composition, microstructure and phase constituents of the LTPC surface carburised layer.
- To evaluate the mechanical, tribological, corrosion and tribocorrosion properties of the surface carburised layer and to identify the degradation mechanisms of the surface treated layer.

To this end, plasma carburising treatments were carried out using a DC plasma unit with a gas mixture of 98.5 % H_2 and 1.5 % CH_4 at 450 °C. The surface carburised layers were characterised by XRD, GDS, SEM/EDX and TEM. Both surface hardness and depth hardness were tested using a microhardness and a nano-indentation tester. Detailed wear properties in air were analysed using a reciprocating tribometer. The corrosion resistance was determined in terms of corrosion potentials and corrosion currents. The tribocorrosion behaviours of surface layer during unidirectional sliding in Ringer's solution under cyclic potentiodynamic and potentiostatic conditions were investigated using a pin-on-disc tribometer integrated with a potentiostat for electrochemical control. Post-test examination was conducted to study the materials various degradation mechanisms involved; and the results are discussed in terms of the relative contribution of wear and corrosion and their synergy.

CHAPTER 2 LITERATURE REVIEW

2.1 Properties and applications of Co-Cr alloys

Co-Cr alloys can be categorised into wear-resistant materials, corrosion-resistant materials and corrosion-wear resistant biomaterials according to their applications. Corrosion-wear resistant Co-Cr alloys are widely used as metallic biomaterials for metal-on-metal joint prostheses due to their good mechanical properties, acceptable biocompatibility, superior wear behaviour and superior corrosion resistance [17, 20, 21]. The Co-Cr prosthetic alloys are designated as ASTM F75, ASTM F799, ASTM F90, ASTM F562 and ASTM F1537 to describe the compositions of Co-Cr alloys as tabulated in Table 2.1.1.

Co-Cr alloys are also popular in industrial sectors including manufacturing dies, fan blades, filters, nozzles, valve parts et al. owing to their combination of high tensile strength, superior weldability, high corrosion resistance and exceptional wear resistance especially at elevated temperature. Stellite family alloys are desirable candidate for hardfacing deposits to protect materials from wear and corrosion at high temperature.

This study was focused on the study of medical grade Co-Cr alloys as metallic biomaterials for metal-on-metal joint prostheses. Other metallic materials used for manufacturing hip prostheses are austenitic stainless steel and Ti-6Al-4V (ASTM F136) [22]. Stainless steel 316L (ASTM F138) is the type commonly used for bone fixation devices such as screws and prosthesis due to lower cost, good mechanical strength and acceptable corrosion resistance [1].

Ti-6Al-4V possesses high mechanical properties than CPTi, thus are selected to manufacture joint prosthesis components (such as stems connected with bones). Co-Cr alloys are best choices for bearing surface, because of their high hardness and superior corrosion-wear behaviour, although Co-Cr alloys do not show as good corrosion resistance as Ti-6Al-4V [23]. Among these three types of metallic biomaterials, stainless steel exhibits the most susceptibility to pitting corrosion and crevice corrosion, while these two kinds of corrosion are seldom observed for Co-Cr alloy and Ti-6Al-4V [17]. The shortcoming of Co-Cr alloys is the stress shielding of bone resulting from relative high Young's modulus of Co-Cr alloys compared to that of human bones, which may deteriorate the interface between prosthesis and bone and lead to bone loosening.

2.2 Physical metallurgy

2.2.1 Phase constituents and stacking fault

Co-Cr alloys are known to develop two allotropic forms, hexagonal-close-packed (HCP), which is stable at temperature below 970 °C and face-centred-cubic (FCC), stable above 970 °C. The transformation from α (FCC) to ϵ (HCP) phase is very sluggish, due to the limited chemical driving force available at the temperature range, thus the metastable α phase becomes the dominant phase [24].

Although the chemical driving force of the transformation of the metastable α (FCC) phase to ϵ (HCP) phase is not high enough under normal cooling condition, this transformation can be

achieved by plastically straining α (FCC) phase (strain-induced transformation) [25], by quenching from temperatures corresponding to the α (FCC) phase field of stability (athermal martensite transformation) [25] or by isothermal aging at temperatures between 800-850 °C [26].

The FCC to HCP allotropic transformation in Co and Co-based alloys occurs by a martensitic transformation mechanism. The stacking fault energy of FCC Co is low at 10-50 mJm⁻², consequently extensive stacking faults can be seen in the Co-Cr alloy [27]. Olson et al. [28] proposed a nucleation mechanism of the FCC to HCP transformation indicating that an existing defect serves as a nucleation site under the condition that the free energy of this embryo is zero or negative. Such lattice defects serve as the preferential nucleation sites of ϵ (HCP) phase [28, 29] and facilitate the formation of strain induced martensite ϵ phase [27].

In addition, alloying elements markedly affect SFE as shown in Figure 2.2.1 [30]. Alloying elements Fe, Mn, Ni and C increase the SFE and lead to low extent of separation of the partial dislocation (stacking fault), thus stabilising the FCC allotrope. While Mo, Cr and W lower SFE and benefit the separation of the partial dislocation (stacking fault), stabilising the HCP allotrope.

Huang et al. [25, 31] studied the grain size effect on the formation of athermal and strain induced martensite. They found that the amount of athermal martensite follows a sigmoidal trend with grain size $d^{1/2}$ while saturated amount of strain induced martensite decreases with

grain size.

Song et al. [32, 33] investigated the formation of athermal and isothermal martensite in Co-Cr (0.05 wt % C) alloy powders. It is found that 64 vol % athermal martensite can form through rapid cooling from 1150 °C, however only 10-15 vol % athermal martensite can form for forged and cast materials [34, 35]. The powder structure favoured the nucleation of ϵ -embryos due to the large active nucleation sites provided by high density of free surface, numerous grain boundaries and grain growth within powder particles. The morphology of athermal martensite is straight transgranular markings. This athermal martensite nucleated with a (111) habit plane in the FCC grains. The microstructure of HCP evolved from laths to “pearlite” after isothermal development. This isothermal transformation is governed by the Shockley partials and solute clusters. Figure 2.2.2 illustrates the morphologies of different HCP phase [32, 36].

Rajan [37] found that the isothermal transformation in a wrought high carbon Co-Cr alloy took place by a two-stage process concurrently with a discontinuous precipitation of carbides. During stage 1, FCC structure transformed to highly faulted band-like HCP₁ phase. After 20 hours (stage 2), HCP₁ or FCC structure transformed to low faulted HCP₂ lamellae.

Saldivar Garcia et al. [36] studied the isothermal transformation in a wrought low carbon Co-Cr alloy and found that the amount of isothermal martensite followed a sigmoidal trend with aging time and the morphology of isothermal martensite is similar to the HCP₂ reported

by Rajan [37].

2.2.2 Sigma (σ) phase

It can be seen from the Co-Cr binary phase diagram [38] (Figure 2.2.3) that the stable phases at 300°C or below are the ϵ -HCP and σ phase in Co-28%Cr alloy as denoted by the vertical dotted line. The σ phase is an intermetallic topologically close-packed (tcp) phase with a tetragonal crystal structure [39]. The crystal chemistry of σ phase in 20 different binary systems has been reviewed by Joubert [40]. The σ phase can form in A-B binary system in which A has a BCC crystal structure with a large atomic radius and B has a FCC or HCP crystal structure with a relatively small atomic radius. According to this (Figure 2.2.4) [40], Cr_xCo_y , Mo_xCo_y (Cr,Mo) $_x\text{Co}_y$ type σ phases are possible to form in ASTM F1537 Co-Cr alloy. Cr and Mo are the A-type element having a BCC crystal structure with a large atomic radius of 0.130 and 0.139 nm respectively, and Co is the B-type element having a HCP crystal structure with a relatively small atomic radius of 0.125 nm.

The addition of C or N elements and the cooling rate which change the thermodynamics conditions affect the formation of the σ phase in Co-Cr alloys. Kurosu et al. [41] reported that the σ phase precipitated at the grain boundaries and grew along the grain boundaries at the later stage of isothermal aging heat treatment in a Co-29Cr-6Mo alloy without addition of C or N. Mori et al.[42] found that a 800°C/24h aging heat treatment also led to the precipitation of the σ phase in a Co-29Cr-6Mo alloy with N. Ramirez et al. [43] found that the addition of C in a cast ASTM F-75 Co-Cr alloy facilitated the formation of M_{23}C_6 at the expense of the σ

phase according to the reaction of $\sigma + C \rightarrow M_{23}C_6$ during solidification. Chen et al. [44] observed the presence of σ phase in both high carbon and low carbon Co-Cr alloys (Figure 2.2.5).

As an intermetallic phase, the σ phase is brittle and deleterious to the mechanical properties [45]. Chen et al. [44] found that the torn-off σ phase promoted abrasion wear in low carbon Co-Cr alloy and surface fatigue in high carbon Co-Cr alloy during the uni-directional wear tests in Hanks' solution.

2.2.3 The alloying elements

In Co-Cr alloys, the alloying elements significantly influenced the thermodynamic stability of FCC or HCP, the allotropic transformation either from FCC to HCP or from HCP to FCC, mechanical and corrosion properties.

The key addition of a large amount (25-30 wt%) of alloying element Cr is responsible for the superior corrosion resistance of Co-Cr alloy due to the formation of a tens of nanometre thick chromium oxide passive layer on the surface. Chromium also serves as forming elements of MC, M_6C , M_7C_3 and $M_{23}C_6$ carbides and hence produces increased mechanical strength and wear resistance by carbide precipitations. Figure 2.2.6 [46] exhibits the possible carbide forming under different conditions. Chromium, tungsten and molybdenum provide solid-solution strengthening effects.

The content of carbon varies up to 3.0 wt% in cobalt-based alloys. Based on the content of carbon, Co-Cr alloys can be categorised into low carbon (lower than 0.07 wt% carbon) and high carbon alloys (more than 0.2 wt% carbon) [47]. Carbon acts as the major forming elements of carbides and hence enhances the mechanical strength and wear resistance. Besides its contribution to the formation of carbides, carbon is a FCC stabiliser and raises the SFE.

2.2.4 Co₃C

Although the Co₃C phase has not been found in the as-received Co-Cr alloy, it indeed formed during the process of low temperature plasma carburising in this study. Thus the property, application and previous manufacturing methods of the Co₃C phase are reviewed in this section. The Co₃C phase is a metastable transition metal carbide having an excellent combination of high melting temperature, high hardness, good electric and thermal conductivity, magnetic properties, unique catalytic and electrocatalytic properties [48-50] and superior electrochemical hydrogen storage capacity [51]. It has drawn increasing attention in the applications of ultra-high-density magnetic recording media [49], hydrogen storage materials [51] and electrocatalysts in fuel cells [50]. A lot of efforts have been made to manufacture Co₃C phase by mechanical alloying [51], a magnetron co-sputtering of both Co and C [52] and pulsed IR laser irradiation [53] to obtain mainly crystalline nano- and micro-Co₃C particles.

2.2.5 Processing methods

Co-Cr alloys can be manufactured in different ways including casting, forged and powder metallurgy, followed by heat treatments such as solution, aging, hot isostatic pressing (HIP) or sintering to obtain different microstructure and resultant mechanical properties. Table 2.2.1 [1] listed the properties of Co-Cr alloys after different processing history.

The thermomechanically process led to a nearly two times higher yield strength and tensile strength compared to casting treatment for surgical Co-Cr alloys. Investment-casting produced coarse dendrites and large carbides at the grain boundaries, while forging caused fine-grain equiaxial grains as shown in Figure 2.2.7 [54].

Cawley et al. [55] found the different fraction and morphology of carbides were produced by casting (AC), solution annealed heat treatment (HT), hot isostatic pressing (HIP), hot isostatic pressing and solution annealed heat treatment (HIP&HT) and sintering followed by HIP and then HT (ST&HIP&HT). The as-cast samples with highest fraction of carbides showed lowest abrasive wear-rate compared to other thermal processed samples, but no correlation between fraction of carbides and hardness can be observed. Blocky morphology carbides formed at the grain boundaries and within the grains for all samples except ST&HIP&HT one. ST&HIP&HT samples only exhibited fine distribution intergranular carbides. All the carbides were rich in Cr and Mo.

The HIPed Co-Cr alloy possess a fine grain microstructure and enhanced mechanical strength,

ductility and toughness compared to cast alloys[33].

2.3 Corrosion of Co-Cr alloys

2.3.1 Introduction

Basically, corrosion involves a pair of anodic and cathodic reactions. In the anodic reaction, metals are oxidised or dissolved and metal ions are released into a solution.



The electrons migrate through the anode to the cathode. This is determined by the nature of the corrosive medium. The most typical cathodic reactions are as follows:

- Hydrogen ion reduction (acidic environment): $2H^{+} + 2e^{-} \rightarrow H_2$
- Reduction of water (neutral/alkaline environment): $2H_2O + 2e^{-} \rightarrow H_2 + 2OH^{-}$
- Oxygen reduction (acidic environment): $O_2 + 4H^{+} + 4e^{-} \rightarrow 2H_2O$
- Oxygen reduction (neutral/alkaline environment): $O_2 + 2H_2O + 4e^{-} \rightarrow 4OH^{-}$

The type of cathodic reaction is affected by the surrounding environment (e.g. pH, temperature and oxygen content).

For materials used for hip joint prosthesis, corrosion has been regarded as a key issue to address for long-span use. The human body environment is very harsh, which can be regarded as an oxygenated 0.9% NaCl solution with organic species. Corrosion of the implant degrades

the mechanical properties (fatigue life and mechanical strength) of materials, and result in loss of material eventually the loosening of implant. The metal ions released by products of corrosion causes human body adverse reaction such as metal hypersensitivity and toxicity.

Co-Cr alloys show excellent resistance to corrosion mainly due to the addition of a large amount of (25-30 wt %) of alloying element Cr and the formation of several nanometre thick chromium oxide layer on the surface. This passive oxide layer is a kind of kinetic barrier to corrosion, which can stop the migration of ions and electrons as shown in Figure 2.3.1 [1].

The research done by Malayoglu et al. [56] analysed the chemical composition of the passive film forming on the surface of Stellite 6 in air and under a electrochemical condition by means of X-ray photoelectron spectroscopy (XPS). The finding in this work demonstrated that the layer on the as-polished Stellite 6 consisted of Cr and Co oxide/hydroxide, while after anodic polarisation, the outmost layer consisted of $\text{Cr(OH)}_3/\text{Cr}_2\text{O}_3$ and WO_2 and sublayer was composed of $\text{Cr(OH)}_3/\text{Cr}_2\text{O}_3$. The composition of air formed and corroded surface is shown in Figure 2.3.2.

2.3.2 Corrosion mechanism of Co-Cr alloys

Corrosion can be generally classified as two groups: general corrosion and localised corrosion. General corrosion takes place on the whole metal surface resulting in the uniform degradation. While, localized corrosion initiates at specific surface heterogeneities such as inclusion, solute-segregated grain boundaries or mechanical dissolutions at a high local

dissolution rate. Aggressive ions such as chloride ions can significantly accelerate the localized corrosion process. Among various forms of localized corrosion, pitting, crevice corrosion and tribocorrosion are the most common forms in the corrosion of biomedical implant materials. In this thesis, tribocorrosion will be emphasized and discussed in next section.

Karimi et al. [57] studied the long-term corrosion behaviour of Co-Cr alloys by measuring the weight loss and concentration of metallic ions during static immersion test in phosphate buffered solution. The XPS results show that the protective oxide layer mainly consists of Cr, confirmed by lowest concentration of Cr compared to other elements in the alloys. Co is the preferred dissolved elements.

Malayoglu et al. [58] assessed the pitting and crevice corrosion behaviour of cast and HIPed Stellite 6 with very similar chemical composition in 3.5% NaCl at different temperature in terms of breakdown potential and breakdown temperature of passive state. It is found that HIPed Stellite 6 exhibited better localised corrosion resistance even at high temperature up to 90 degree C than the cast Stellite 6 and the carbide/matrix boundaries served as the preferred sites for pitting initiation. The predominant dissolved element was Co. The difference in carbide chemical composition and crystal structure between cast and HIPed materials plays an important role in retaining passivity.

Several researchers [59, 60] investigated the galvanic corrosion mechanism between Co-Cr

and titanium and titanium alloys. The results show that this kind of coupling exhibits good resistance to galvanic corrosion. Furthermore, galvanic corrosion can be eliminated by using self-mate coupling materials.

Liang et al. [61] studied the pitting corrosion of Co-Cr alloys in Tyrode's solution in the presence a gas mixture of O₂, CO₂ and N₂ to simulate the flowing of body fluid. Co-Cr alloys show good corrosion resistance to general corrosion with a corrosion rate of 0.105 µm/year at a flow rate of 38.83 kg/h and low sensitivity to pitting corrosion in both static and gas flowing solution. With the increase of gas flowing rate, the breakdown potential (E_b) of Co-Cr alloys in Tyrode's solution decreases.

2.3.3 Factors associated with corrosion

Metikos-Hukovic et al. [62] studied the dependence of corrosion stability of Co-Cr alloys on the alloying elements in Hank's solution by measuring the polarisation curve and the amount of metallic ions in the static immersion tests in the simulated physiological solution (Hank's solution). It has been found that the corrosion behaviour of Co-Cr is mainly dependent on the presence of Cr and the corrosion resistance of Co-Cr alloys is better than that of pure Cr due to the contribution of Mo to the alloy passivity. The release of metallic ions from Co-Cr-Mo alloy increases with decrease of pH of solution.

Hsu et al. [63] investigated the effect of biological solutions on the corrosion behaviour of Co-Cr-Mo alloys by comparing the electrochemical response of Co-Cr-Mo alloys to urine,

serum and joint fluid. It has been found that Co-Cr-Mo alloys shows much larger passive region in the urine than in the joint fluid and serum during potentiodynamic tests, while the corrosion resistance in the joint fluid and serum is lower than that in the urine.

2.4 Wear of Co-Cr alloys

2.4.1 Introduction

Bhushan [64] defined that wear is the surface damage or removal of material from one or both of two solid surfaces in a sliding, rolling, or impact motion relative to one another. There are six principal wear modes including adhesive, abrasive, fatigue, impact by erosion and percussion, chemical (or corrosive) and electrical-arc-induced wear. Most of wear is controlled by the adhesive-, abrasive-, corrosive-wear mechanisms or the combination of them [64]. In adhesive wear, the sliding surfaces under load adhere together through solid phase welding of asperities. Subsequent detachment from either surface results in loss of material [65]. In abrasive wear, loss of material from the surface is caused by sliding abrasives under load. Both free-flowing particles (third body) and abrasives attached to the counterbody (two body) cause wear [65].

Many studies have been done to study the wear behaviour of Co-Cr alloys for hip joint prosthesis use [55, 66, 67]. The wear behaviour of materials is influenced by the nature of material (stacking fault, hardness, ductility, surface roughness, microstructure and phase constituents) and the testing or working conditions such as load, environment and counterpart

materials. The test methods can be divided into two main categories: (1) *in vitro* studies including conventional wear test techniques (pin-on-disc and reciprocating) and hip simulation wear test; and (2) *in vivo* studies by examination of the explanted prosthesis.

2.4.2 Wear mechanisms

The abrasive mechanism of Cobalt-based alloys has been extensively investigated by several researchers [68-70]. Emphasis has been put on the effect of size, type and distribution of carbide on the wear rate. The researches indicated that small carbides made little contribution to wear resistance because they were directly removed from wear track. Though large carbides were cut by the abrasives, they contributed to wear resistance in the way of much less depth of cut compared to that in the soft FCC matrix.

Frank and co-investigators [71, 72] systematically studied the wear mechanisms of cobalt-based alloys under dry sliding condition and obtained a wear map as shown in Figure 2.4.1 revealing the correlation between wear rate and the sliding test parameters (the loads and the sliding velocity).

The results indicated that the dry sliding of Stellite alloys against WC-Co was controlled by oxidation mechanism at low loads or sliding speed, while adhesion and abrasion mechanisms at high loads or sliding speed. The wear rate was strongly affected by the kinetics of formation of oxide, the nature of oxide and the attachment between oxide and the surface at low loads or sliding speed. At high loads or sliding speed, cracks started to nucleate and

propagate to facilitate the formation of wear debris.

Chen et al. [73] compared the tribological behaviour of Stellite 21 alloy in air and in NaCl solution using a reciprocating tribometer. The results indicated that the wear process was predominated by abrasive and adhesive mechanism with signs of parallel abrasion marks and adhesion craters.

The work by Persson et al. [27] showed that Stellite 21 alloy has excellent resistance to galling (severe adhesion) and stable low friction coefficient at 0.25 using load scanner under a increasing load from 100N to 1300N at room temperature and 250 °C. The excellent wear resistance is attributed to the formation of surface layer through FCC→HCP martensite transformation.

2.4.3 Factors associated with wear

In general, the wear rate agrees with the wear equation Equation 2.4.1 based on the relationship developed by Holm and improved by Archard [65].

$$V = K \frac{F_N}{H} d \quad \text{Equation 2.4.1}$$

where V is the wear volume, F_N is the applied normal load, H is the hardness and d is the sliding distance. Hardness of Co-Cr alloy mainly depends on the precipitation of carbides, solution strengthening effect on matrix and the precipitation of HCP phase from soft FCC matrix.

Cawley et al. [55] compared the wear resistance of Co-Cr-Mo alloys with same chemical composition after different thermal treatments and concluded that the lowest wear rate is corresponding to the highest carbide volume fraction through micro-abrasion test using SiC abrasives. The as-cast microstructure possessed highest carbide fraction and showed best wear resistance compared to HIPed, sintered and solution treated microstructure. It is interesting to find that the wear rate did not correlate with the hardness, which disagreed with the wear equation Equation 2.4.1. The work by Shetty et al. [68, 69] also showed the importance of carbides on the wear resistance.

Chen et al. [44] investigated the effect of second phase (intermetallic σ phase) on the wear behaviour of low and high carbon Co-Cr alloys and found that the torn-off σ phase promoted abrasion wear in low carbon Co-Cr alloy and surface fatigue in high carbon Co-Cr alloy, although the percentage of σ phase was lower than 5%.

The crystallographic nature of two allotropic forms (FCC and HCP) also influences the tribological behaviour of Co-Cr alloys. The HCP structure shows 30% less coefficient of friction and lower wear rate than the FCC structure [64]. The limited number of slip systems of HCP has been considered to result in a better tribological performance. A mode [74] shown in Figure 2.4.2 has been proposed that HCP Co deforms by slippage when pressed against each other, causing many air gaps at each junction. In contrast, the FCC has 12 slip systems without such air gaps, so that the friction and wear is higher than the HCP.

Saldivar-Garcia et al. [66] examined the tribological behavior of a pair of cast and wrought Co-Cr alloys counterparts with different combinations such as FCC-FCC, HCP-FCC, HCP-HCP and HCP-biphase using pin-on-disc technique under a load of 266.8N. The work showed that HCP components exhibited better wear resistance compared to FCC components and the pair both with HCP crystal structure showed the best tribological response in terms of reduced wear volume. Plastic deformation and oxidation were believed to be the dominant mechanisms. FCC structure favoured the plastic deformation due to the relatively large amount of slip systems. In contrast, HCP metals possessed fewer slip systems and poor ductility making plastic deformation hard to take place. No significant correlation between tribological performance and hardness differentials could be found.

High work-hardening rate of Co-Cr alloys is another key factor associated with tribological behaviour [24, 27, 75]. The stacking fault energy of FCC is low at $10\text{-}50\text{ mJm}^{-2}$, which facilitates the FCC \rightarrow HCP martensite transformation during sliding contact. The HCP phase nucleated at lattice defects such as stacking faults and twins. The (0001) basal plane of HCP phase were preferably orientated parallel to the worn surfaces, which can be sheared easily during sliding. However, Saldivar-Garcia [66] examined the wear debris of FCC counterparts by means of XRD analysis. The results showed that no strain-induced HCP formed during pin-on-disc tests, meaning that the wear process was not greatly influenced by stacking fault energy.

2.5 Tribocorrosion of Co-Cr alloys

2.5.1 Introduction

The addition of a large amount (25-30 wt%) of alloying element Cr and the formation of a tens of nanometre thick chromium oxide layer on the surface are responsible for the superior corrosion resistance of Co-Cr alloy [17, 76, 77]. However, tribocorrosion is an inevitable issue for long-term joint prostheses subjected to simultaneously corrosion and wear, which is affected by the synergistic system between corrosion and wear. The passive film on the contact area could be removed by sliding motion between counterparts during tribocorrosion process, which accelerates the corrosion process in corrosive medium [76]. At the same time, such tribological properties as wear resistance and coefficient of friction are deteriorated by the formation of corrosion products [78]. Neville and co-investigators [79, 80] have systematically investigated the tribocorrosion behaviour of Co-Cr alloys by in situ electrochemical measurements and concluded that tribocorrosion plays a very important role in degradation of Co-Cr alloys in biological environment. A variety of contact modes involving tribocorrosion are demonstrated in Figure 2.5.1 [81].

2.5.2 Synergism effects between corrosion and wear and the involved mechanisms

During a tribocorrosion process, the material loss depends on pure mechanical part (wear), pure chemical part (corrosion) and more importantly the interaction between corrosion and wear resulting in wear-induced corrosion and corrosion-induced wear [78, 82-84]. Many

efforts have been made to separate mechanical part from chemical part by several investigators [76, 85, 86]. The total wear loss can be simply given by the sum of mechanical wear (V_{mech}) and chemical wear (V_{chem}) as depicted in Equation 2.5.1.

$$V_T = V_{\text{mech}} + V_{\text{chem}} \quad \text{Equation 2.5.1}$$

The volume loss due to chemical wear can be calculated according to the Faraday's law [81].

$$V_{\text{chem}} = \frac{ItM}{nF\rho} \quad \text{Equation 2.5.2}$$

where I is the current over the sliding period, t is sliding time, M is the atomic mass of the material, n is the valence of dissolution and passivation, F is the Faraday's constant (96458C/mol) and ρ is the density of alloy.

Several attempts have been made to identify the tribocorrosion regime [81, 87, 88]. Diomidis [82] introduced two factors, K_c and K_m , to assess the ratio between contribution of corrosion and wear to material loss and the influence of passive film on the contribution of wear. These two newly introduced factors are very useful determining the tribocorrosion regimes to material degradation.

K_c is the ratio of material loss caused by chemical part and that resulted from mechanical part.

- (i) When $K_c > 1$, corrosion predominates the tribocorrosion process and thus the material loss is mainly governed by reactivity of materials in the electrolyte.

(ii) When $K_c < 1$, wear predominates the tribocorrosion process.

(iii) When $K_c \ll 1$, the material loss due to chemical reaction can be negligible compared to the total material loss.

K_m represents the ratio of material loss resulting from mechanical wear on the bare surface (or surface without passive film protection) and on the repassivated surface within the wear track.

(I) When $K_m > 1$, the repassivated film is not easily removed and can protect material from mechanical wear.

(II) When $K_m < 1$, the material removal by mechanical wear is accelerated by the formation of repassivated film.

Buscher [89] investigated the tribocorrosion behaviour and wear debris of FCC matrix Co-Cr alloy in Ringer's solution. The research revealed that the worn surface consisted of a nanocrystalline layer with base materials, strain-induced martensite HCP phase and fine oxides, due to the steady high strain and resultant constant deformation and recrystallisation within the worn surface. The morphology of wear debris is fine globular and lamellar shaped, corresponding to that of grains in nanocrystalline layer and HCP phase. Owing to the low stacking fault energy, Co-Cr alloys underwent the strain-induced martensite transformation and the strain-induced martensite needles gave sufficient support to the surface nanocrystalline layer. Thus, the crack nucleation and propagation within wear track and consequently formation of wear debris were attributed to the properties of nanocrystalline

layer itself, rather than failure of substrate underneath this layer.

Stack et al. [90] studied the micro-abrasion-corrosion mechanisms of a Co-Cr on UHMWPE couple in Ringer's solution and construct synergism maps using micro-abrasion-corrosion apparatus with SiC particles. The results suggested that the passive film was promoted and corrosion dominated the abrasion at anodic potential at low loads.

2.5.3 Factors associated with tribocorrosion

In a tribocorrosion system, the synergistic effects between wear and corrosion need comprehensive consideration on corrosion and wear and are affected by many factors. On one hand, corrosion is accelerated by wear. The passive film at the contact area is removed or damaged in a single cycle or a certain amounts of cycles by sliding motion, which increases the ratio of active-to-passive area resulting in the cathodic shift of corrosion potential, increased current and a negative shift of OCP. Material loss from corrosion can be derived from two parts including the loss from the dissolution of bare material reacting with electrolyte and the formation of passive films, which may be followed by removal or damaging by sliding motion. On the other hand, wear is either accelerated or slowed by corrosion. The corrosion products broken down by wear can serve as third party abrasion particles resulting in corrosion-induced wear. At the same time, the corrosion products produced on the surface in wear track can modify the surface tribological behaviour such as coefficient of friction and change the wear mechanism. Oxide film can work as protective film to stop the interaction between two counterparts.

In general, the critical factors influencing the tribocorrosion behaviour under electrochemical condition compose of four main aspects including the properties of materials, the mechanical solicitations, the solution properties and the electrochemical state as listed in Figure 2.5.2 [81] in detail.

Mathew et al. [76] compared the tribocorrosion behaviour of biomedical grade Co-Cr alloys using two different tribometer configurations and studied the dependence of tribocorrosion mechanism on load. A linearly reciprocating tribometer (system A) is utilised to assess the *in vitro* tribocorrosion behaviour of flat metal samples against alumina balls, while a configuration with a cylindrical metal pin pressed against an oscillating alumina ball (system B) is employed to simulate *in vivo* condition. The results showed that the dominant tribocorrosion mechanism of Co-Cr alloys shifted from wear-corrosion to mechanical wear as a function of load, i.e. the contact stress. The results suggested that the protein in the bovine calf serum assisted in the formation of protective tribolayer against corrosion.

Tipper et al. [67] analysed the volumetric wear rate and wear debris from Co-Cr with high and low carbon content in newborn bovine calf serum and draw a conclusion that the wear rate produced by hip simulator run on the biaxial rig also related to the content of carbon of Co-Cr alloys, revealing the similar dependence of the results produced by simple wear configurations on carbon content. The high carbon against high carbon pair exhibited lowest wear rate. In addition, it was the first attempt on qualification of wear debris produced from *in vitro* tests with nanometre size.

The work [79, 86] by Neville and co-workers assessed the tribocorrosion behaviour of wrought high carbon and low carbon Co-Cr alloys in three types of solution (0.36 % NaCl solution, Dulbecco's Modified Eagle's medium (DMEM) and 50% calf bovine serum). The results showed that high carbon Co-Cr alloy exhibited the best tribocorrosion performance with only half of the wear loss of low carbon Co-Cr alloy and the lowest coefficient of friction in DMEM and calf bovine serum. The proteins in calf bovine serum benefited reducing friction, but harshed material degradation due to their effect on corrosion and tribocorrosion, which was inconsistent with the finding by Mathew [76]. In DMEM lubricant, a 2-3 nm organometallic layer formed on Co-Cr due to the enhanced interaction between ion release and amino acid, contributing to reduced friction and wear.

In order to isolate the lubricating effect of such organic species as proteins and amino acid, Ringer's solution was select as lubricant in tribocorrosion tests [89].

2.6 Surface engineering of Co-Cr alloys

2.6.1 Introduction to surface engineering

Surface engineering has proved to be a promising method to enhance the properties of the surface and near-surface areas of metallic implant components in a desirable way. It can fall into two broad categories including surface coating and surface modification process. In coating processes a material is deposited onto the surface to produce a thin layer normally with different composition, structure and properties [91]. Normally, there is a distinct

boundary between the substrate and the coating caused by the characteristics differences, resulting in de-bonding of the coating under large tangent force; in addition, when the relatively soft substrate deforms under a high normal force load applied to the coating, the surface system collapse due to so-called ‘thin-ice effect’ (Figure 2.6.1) [92].

A surface modification process alters the surface properties by introducing some elements and changing the surface microstructure but the substrate material is still on the surface. De-bonding and/or ‘thin-ice effect’ will not occur in a modified surface due to non-existence of a boundary between the treated layer and the significantly hardened thick case. Many efforts have been made to improve metal-on-metal articulations by surface engineering means [92-100]. The detailed technologies are listed in Figure 2.6.2 [101].

2.6.2 Surface coating of Co-Cr alloys

The coatings investigated for the Co-Cr alloys for implant prostheses mainly consist of the deposition of metal nitride (TiN, CrN and CrCN), metal oxide (Al_2O_3 , ZrO_2) and diamond like carbon (DLC) coatings.

Efforts have been made by many researchers [93-96, 102] to deposit coatings on Co-Cr alloys for biomedical use through physical vapour deposit process including magnetron sputtering, reactive sputtering and arc evaporative to improve the tribological behaviours, thus to extend the service life of implants.

The work done by Pham et al.[94, 96] showed that a dense TiN film with columnar structure

can be deposited on the Co-Cr substrate by magnetron sputtering method. In the magnetron sputtering process, a Ti target is bombarded with argon flow discharge. Sputtered atoms from target then condense on the surface of a substrate forming a thin layer. The use of magnetron can constrain the electrons and increase the ionizing electron-atom collision rate, thus increasing the sputtering on the target and deposition rates. Pham et al. found that the mechanical properties of Co-Cr alloys including surface hardness, critical load and elastic modulus were significantly enhanced by TiN coating. In addition, the biocompatibility of Co-Cr alloys was improved by the deposition of TiN in terms of cell attachment.

The research by Wisbey et al. [95] exhibited that the application of TiN coating can improve the pitting corrosion resistance of Co-Cr alloys without galvanic corrosion and reduce the harmful metallic ion release.

However, the study by Harman et al. [103] found that the TiN coating on the prosthesis can suffer from delamination during its employment. The in-vivo study by Raimondi et al. [104] showed the failure mode of TiN coated titanium alloy heads after revision from patients and suggested the delamination of TiN coating and consequent accelerated wear of both TiN coating and polyethylene, which were considered to be the primary reason for failure of implants.

Fisher et al. [102] firstly reported the wear behaviour of CrN and CrCN coatings as orthopedic bearing surfaces and found that CrN and CrCN coatings were effective in reducing

wear debris and metal ion release owing to high hardness, good toughness and cohesive strength. However, Österle et al. [105] found the formation of Cr_2O_3 nano-particles wear debris of CrN coating during reciprocating wear tests, which is a issue needing to be addressed since Cr^{6+} decreases cell vitality of macrophages.

Metal oxide coatings such as Al_2O_3 and ZrO_2 coatings have been proved to be beneficial in enhancing the material resistance to corrosion and wear, due to their good biocompatibility [106], electrochemical resistance, improved surface wettability and high hardness [107, 108]. Kumar et al. [109] compared the wear rate of UHMWPE against zirconia ceramic (Y-PSZ), SUS 316L stainless steel and alumina ceramic in three different lubricant mediums including calf bovine serum, saline and distilled water. They found that the tribopair of polyethylene against zirconia ceramic showed the lowest wear factor, which was 10 to 20% less than that of polyethylene against SUS 316L stainless steel, and 40 to 60% less than that of polyethylene against alumina based on the lubricant medium.

Ceramic coating can be generally deposited by electron beam-PVD (EB-PVD) [110, 111], CVD [112], plasma spraying [113] and electrophoretic deposition [114] methods. PVD technology is a line-of-sight process [111] so that only implants with simple surface topographies can be coated by PVD. In the plasma spraying process, the ceramic particles are melted in a high temperature plasma torch and propelled to the substrate. The melt ceramic is rapidly cooling on the surface of substrate and forms thick coatings. But the thickness ($> 30 \mu\text{m}$) of coating produced by plasma spraying method is too thick which limits its application

on Co-Cr alloys for sophisticated ball shape implant [107]. Another problem of plasma spraying technology is the poor bonding strength between substrate and coating due to the flat lamella microstructure with a lot of voids and defects and resultant high thermal insulation and cracks [112]. The deposition rates of CVD are normally low and CVD may cause environmental concerns [112].

More recently, a family of coatings based on carbon has been developed including diamond-like carbon (DLC) and diamond coatings, showing some preliminary potential in biomedical grade [115].

Due to their exceptional friction and wear characteristics, chemical inertness and biocompatibility [116], DLC is a very attractive coating for enhancing prostheses surface properties [117]. DLC is normally produced in the forms of amorphous carbon (a-C) and hydrogenated amorphous carbon (a-C:H).

Oñate et al. [116] compared the effect of DLC, TiN coating and nitrogen ion implantation on reducing the wear of UHMWPE-on-metal articulation by 5 million cycles wear tests using a knee wear apparatus. DLC and TiN coating were deposited on the Co-Cr femoral head. Nitrogen ion implantation was carried out on both polyethylene and Co-Cr alloy to produce a hardened case. The highest UHMWPE wear loss was observed for the PVD TiN coated Co-Cr against UHMWPE articulation, while the best reduction in UHMWPE wear loss was obtained by the nitrogen implanted and DLC coated Co-Cr against UHMWPE tribopairs

showing the lowest polyethylene material transfer. What is more attractive for DLC coating is the excellent biocompatibility verified by both *in vitro* and *in vivo* biocompatibility tests based on FDA regulations and ISO 10993 standards.

The research by Saikoo et al. [118] revealed that DLC did not perform differently from Co-Cr in terms of gravimetric wear of polyethylene as a counterpart of polyethylene assessed using a biaxial rocking motion (BRM) simulator.

The main problem faced by DLC coatings in clinical use is the occurrence of delamination along the coating/substrate interface due to the low-bonding and/or ‘thin-ice effect’ in excessive contact loading, localized blistering and pitting in aqueous corrosive media which are caused by the relative nature of DLC compared to metallic alloy substrate [119].

The recently developed sputtered carbon and carbon with some chromium coatings, known as Graphite-iCTM (GiC coating), exhibit high hardness from 1500 to 4000HV, low coefficient of friction ranging from 0.08 to 0.16 and low wear rate, normally better than those of conventional DLC coatings. GiC coating had a microstructure of amorphous-like graphite with mainly sp^2 (as in graphite) and partly sp^3 (as in diamond) bonding. As well known, bulk graphite is used to be lubricant materials. The low friction and low wear rate of this sputtered carbon coating was contributed to the graphitization process of a diamond structure resulted by high ion bombardment power. In the graphitization process, a graphite tribolayer was formed between the coating and opposing surface. On the other hand, its hardness was up to

4000 HV. The hardness of GiC depends on the ratio of sp^2/sp^3 . The combination of high hardness and low friction result in the excellent tribological performance (very low friction and very low wear rate at very high load) [120].

A closed field unbalanced d.c. magnetron system (Figure 2.6.3) [121] was employed to deposited carbon/chromium co-sputtering coatings so-called GiC. A thin layer of pure chromium coating was deposited first to produce good adhesion between carbon coating and metal substrate, followed by deposition of carbon coating doped with chromium. However, very few studies on this coating for clinical application have been reported.

2.6.3 Surface modification on Co-Cr alloys

Another approach to enhance the surface properties is to produce a strengthened surface layer within the substrate by surface modification. Many efforts have been made on medical Co-Cr alloys by ion implantation and thermochemical methods.

Ion implantations making use of bombarding a substrate with ions are divided into ion-beam surface modification and plasma-enhanced ion implantation for introducing a large amount of elements such as nitrogen and carbon into a substrate surface. Since the mid 1980's, ion implantation with nitrogen has been conducted on the metallic bearing surface made of Co-Cr-Mo to improve wear resistance.

The conventional ion implantation process involves an ion beam which is accelerated to a

certain level of ion energy to implant into the surface of substrate and displace the host surface atoms [122]. The ion energy generally ranges from 20 to 200 keV.

However, the thickness of conventional ion implantation modified layer is normally less than 0.2 μm [97] which is far less than the average annual linear rate of Co-Cr-Mo. It has been confirmed by Bowsher et al. [123] when they investigated the effect of nitrogen ion implantation on the wear behaviour of Co-Cr on Co-Cr hip prostheses using a physiological hip simulator. The results showed that the depth of nitrogen ion implantation was only 0.2 μm and nitrogen ion-implanted Co-Cr tribopair exhibited no improvement on volumetric wear compared to untreated Co-Cr tribopair, indicating no clinical benefit for metal-on-metal hip implants. In addition, its line-of-sight nature makes it difficult to generate a uniform modified layer especially for geometric complicated components. Further, it is impossible to prevent the metal ion release [124].

In the last two decades, a new technique called Plasma Based Ion Implantation (PBII) has been developed, also known as Plasma Source Ion Implantation (PSII) [125] and Plasma Immersion Ion Implantation (PIII) [126], which utilises a plasma discharge consisting of the desired species instead of a mono-energetic ion beam. The workpiece to be ion-implanted is biased with a high negative voltage and immersed in plasma, so as to accelerate ions in the sheath potential fall around the workpiece surface and introduce ions on the workpiece surface. Ions can be implanted three-dimensionally by plasma process. Therefore, it is suitable for components with complicated shapes such as hip implant, circumventing the

line-of-sight disadvantage of conventional ion implantation. This technology demands low activation energy from 0.60 – 0.75 eV [127, 128].

Ikeda et al. [129] assessed the improvement of wear and corrosion properties of a Co-Cr alloy for orthopaedic use by PBII and found that both the wear and corrosion properties were enhanced by PBII method. Other investigators [128, 130] also have made attempts to modify the surface properties of medical Co-Cr alloys by PBII and compared the mechanical, wear and corrosion behaviour change induced by PBII. A PBII treatment at 500 – 600 °C for a process time of 3 h can lead to a combination of increased surface hardness to 20–25 GPa and subsequent wear resistance improvement by nearly one order of magnitude compared to standard state of Co-Cr alloys due to the precipitation of a CrN phase. However, recent study [130] revealed that the PBII at 350 °C, 400 °C and 550°C led to elevated corrosion rates determined from the Tafel slope measured in Ringer's solution (pH 6.2), which were 5, 10 and 56 times respectively of that of untreated Co-Cr alloys even when no CrN precipitates formed at 350 °C. The corrosion rates enlarged with the nitrogen PBII temperature mainly caused by the unpreventable formation of CrN phase above 400°C. The decrease of corrosion resistance is possibly related to no complete formation of a passivation Cr₂O₃ layer due to the strong affinity of chromium for nitrogen, thus lack of mobility of chromium inside the alloy. Further tribocorrosion study [131] on nitrogen PBII treated Co-Cr alloys in simulated body fluid indicated that an PBII treatment above 400 °C resulted in an greater cobalt ion release which is harmful to human body, although reduced wear volume.

Another catalogue of widely-used surface modification technology is thermochemical

treatment by introducing alloying species including carbon, nitrogen, a combination of carbon and nitrogen or boron into a component surface by a mass transfer in forms of gas, liquid, solid or plasma. A modified case can be produced by carburising, nitriding, carbonitriding and boriding to improve the surface properties including hardness, wear resistance, corrosion resistance etc.

Conventional carburising are normally performed at high temperatures around 950 °C with a high carbon potential atmosphere and produces a carbon-modified layer by the absorption of carbon on the surface and followed by diffusion of carbon into the interior of the materials. Such factors as diffusion coefficient [132], treatment temperature, carbon potential and gas environment [133, 134] play an important part in gaseous carburising process.

The first attempt on utilising plasma as the carbon source was made in 1970s [135], followed by development from laboratory to industrial application by other researchers [136, 137], showing a bright future. From a point of both economic and environmental view, plasma carburizing exhibited high efficient combining higher carburising rate, lower treatment temperature (350 °C - 500 °C), less energy demanding, reduced gas supply and more environmental friendly [138] compared to conventional gaseous carburising. It has proved to be effective in improving the hardness of metals by producing a carbon-diffused layer without any dimensional changes due to the low treatment temperature [139].

Research by Zhang and Bell [98] based on plasma modification in 1985 demonstrated that it

was possible to get a improvement of surface hardness and wear resistance without loss of corrosion of an austenitic stainless steel by low-temperature plasma surface alloying process. The novel technique makes it come true to have a desirable stainless steel surface with both high wear resistance and excellent corrosion resistance. During the past two decades, a family of low-temperature plasma surface alloying processes has been developed to generate super stainless steel surfaces for improving wear, corrosion and fatigue properties, but with the deficiency of relatively high the friction coefficient varying from 0.5 to 0.7 depending on the tests conditions.

A metastable and interstitial supersaturated ‘expanded austenite’, so-called ‘S-phase’, can be generated without the formation of chromium carbides or nitrides during low-temperature ($<420\text{ }^{\circ}\text{C}$ for nitriding and $<500\text{ }^{\circ}\text{C}$ for carburising) plasma alloying process [140]. According to the types of interstitials in S-phase, there are two basic types of S-phase consisting of nitrogen S-phase with the introduction of N and carbon S-phase with the introduction of carbon. Sun et al. [140] indicated that the nature of ‘S-phase’ layer itself was a highly distorted and disordered FCC structure with high levels of compressive stress. Although the mechanism and condition for formation of S-phase are still a matter of debate, high content of Cr and an FCC structure are necessary.

More recently, the work done by Dong et al. [99] discovered in 2002 that S-phase can be formed in Co-Cr alloys via low-temperature ($<500\text{ }^{\circ}\text{C}$) plasma carburizing for the first time. The surface hardness was dramatically improved from 400 HV0.05 for the untreated Co-Cr to

above 1200 HV0.05 for the carburised samples due to the formation of carbon S-phase during the low-temperature carburizing without the formation of Cr carbide and loss of corrosion resistance or even improvement of the corrosion resistance [99]. Significant enhancement of wear resistance in air, distilled water and Ringer's solution and good biocompatibility were achieved [141]. Carbon as the strongest FCC stabiliser in Co-Cr alloys is responsible for the generation of S-phase in dual phase (FCC and HCP) Co-Cr alloys [100].

The low temperature plasma carburising technology to produce S-phase in biomedical grade Co-Cr alloy has been applied on hip joints made of cast Co-Cr alloys by an international biomedical device manufacturing company. However, it is found that the same technique conducted on many hip joint prostheses produced S-phase layer with different thickness thus affecting the wear and corrosion performance directly (unpublished work). Habibi [141] treated an HCP dominated Co-Cr alloy and found that low temperature plasma carburising cannot form a single S-phase combined with good wear and corrosion resistance.

It seems that the phase constituents and FCC – HCP ratio of substrate Co-Cr alloys are expected to be responsible for the discrepancy. However, the mechanism involved has not been investigated. Clearly, it is a timely task to study the substrate effect on the formation of S-phase for the aim of producing harder and thicker S-phase cases.

CHAPTER 3 EXPERIMENTAL

3.1 Materials and sample preparation

Medical grade (ASTM F1537) Co-28Cr-6Mo alloy (Carpenter Technology Corporation), with the chemical composition listed in Table 3.1.1, was used as the substrate material in this study.

Samples were cut from 28 mm diameter bars to discs of a thickness of 6 mm.

After heat treatment (details see the next section), one surface of each sample was wet ground with SiC paper down to 1200 grit and then polished with 6 μm , 3 μm diamond paste and 0.25 μm colloidal silica to Ra about 15 nm. The samples were cleaned in ultrasonic device with soapy water and acetone before low temperature plasma carburising treatments.

3.2 Sample treatment

3.2.1 Heat treatment

In order to study the effect of phase composition on the response to low-temperature plasma carburising, a series of heat treatments were adapted to produce samples with different ϵ -HCP to α -FCC ratios. The as-received material was first solution heat treated at 1250 °C for 1.5 hours using the Lenton high temperature furnace followed by air cooling, and then aged at 850 °C for 4 and 15 hours before water quenching [36]. Heating-up rate was 8 °C/min and over temperature was controlled within 5 °C above set temperature according to the working condition of furnace.

3.2.2 Low temperature plasma carburising

Based on some preliminary studies in conjunction with past research [141], low-temperature temperature plasma alloying with carbon or low-temperature temperature plasma carburising treatment (LTPC) conditions were selected. The LTPC was carried out in a Klöckner DC plasma unit at 450 °C for 10 hours with a gas mixture of H₂ (98.5 vol %) and CH₄ (1.5 vol %). This DC plasma furnace consists of a 40 kW DC power supply, a cooling water supply system, a gas mixture supply system, an evacuation pump and a cold wall chamber. The LTPC process includes the following four steps:

- Evacuating: The pressure of chamber was evacuated below 10^{-1} mbar to minimize oxygen and nitrogen content and then the gas mixture for carburising was introduced into the chamber before DC power on. The pressure was set at 4-5 mbar.
- Heating: After power on, plasma formed on the surface of samples. Positive ions was accelerated and bombarding the sample surface to heat up sample to set temperature. The temperature was monitored using a thermal couple.
- Diffusion: C was absorbed onto the sample surface and diffused into the substrate due to chemical potentials difference between sample surface and substrate.
- Cooling: After 10 hours treatment at 450 °C, the samples were cooled down in the chamber with treatment gas mixture until temperature of samples was below 50 °C

For clarity, the samples with and without plasma treatment were coded as shown in Table

3.2.1.

3.3 Characterisation and property evaluation

3.3.1 Microstructural observation

3.3.1.1 Preparation of metallographic samples

The metallographic samples of as-received heat-treated and plasma carburised material were prepared by cutting, mounting, grinding, polishing and etching. All the samples were first cut using a silicon blade in an Accutom-5 wafering cutting machine. The plasma carburised samples were cut normal to the surface.

Then, these samples were mounted in conductive bakelite using a Struers hot mounting device, ground down to 1200 grit using a Struers automatic polishing wheel and then polished with 6 μm diamond paste on a satin woven acetate cloth, followed by polishing with 1 μm diamond paste on a woollen cloth and finally polishing with 0.25 μm colloidal silica paste on a porous neoprene cloth. A flat and mirror-like finish was achieved for both optical and electronic microscopic observation by this procedure.

Finally, the polished samples were electro-etched in a 15% HNO_3 solution using a source of direct electric current. The sample served as the cathode and a graphite rod was used as anode. After 10 seconds, the samples were taken out and rinsed with water.

Note: The plan-view microstructure of plasma carburised samples was examined in the as-carburised condition.

3.3.1.2 Optical and scanning electron microscopy (SEM)

The microstructure of all etched samples and the plan-view microstructure of as-carburised samples were inspected by a Carl Zeiss Axioskop 2 MAT optical microscope, a Philips XL-30 LaB₆ filament scanning electron microscope (SEM) and a JEOL 7000 field emission gun SEM with Oxford Instruments INCA Energy-dispersive X-ray spectroscopy (EDX) detector and Electron backscatter diffraction (EBSD) accessories. The EDX facility was used to measure the chemical composition of some microstructure features. The EBSD accessory was utilised to determine the phase constituents.

3.3.1.3 Transmission electron microscopy (TEM)

The microstructures of as-received, heat-treated and plasma carburised samples were characterised using a JEOL JEM-2100 LaB₆ TEM with an operating voltage of 200 kV. The plan-view TEM samples of as-received and heat-treated samples were prepared by a normal method consisting of grinding to about 50 μm in thickness and then ion milling to less than 100 nm in thickness using a Gatan Precision Ion Polishing System (PIPS). The cross-sectional TEM samples of plasma carburised samples were prepared by the following steps shown in Figure 3.3.1 [142]. (1) Two stacks were cut and glued together using G-1 epoxy on a hot plate with the plasma carburised surfaces facing each other. The cross-sectional area of this glued stack was 3 x 3 mm². (2) The glued stack was sectioned to a less than 1 mm-thick piece followed by grinding and polishing to about 50 μm . (3) The very thin glued piece was separated into two pieces. (4) This piece was finally thinned using a Quanta 3D FEG focus ion beam (FIB) miller to less than 100 nm as shown in Figure 3.3.2.

3.3.2 Phase identification

3.3.2.1 X-Ray diffraction (XRD)

The phase constituents of all samples were investigated using a Philips X'Pert X-Ray diffractometer with a Cu-K α radiation ($\lambda=1.540598$ Å). A monochromatic X-ray beam impinged the sample surface with an incident angle 2θ from 20° to 100° at a step of 0.02° with a measure time of 1 s per step. The data were collected and analysed by High score X'pert software to identify the phases.

3.3.2.2 Electron backscatter diffraction (EBSD)

The phase constituents of heat-treated and plasma carburised samples were also examined by EBSD using an Oxford Instruments camera and associated INCA software attached to JEOL 7000 SEM by indexing the Kikuchi patterns. The samples were tilt to 70° and facing the phosphor screen. The EBSD measurements were carried out at a low magnification of 1000 times in order to get information from a sufficient number of grains and performed under an operating voltage of 20 kV in order to generate enough signals. EBSD maps were obtained from each samples using a step size of approximately $0.47\text{ }\mu\text{m}$. Any microstructures with a thickness less than $0.47\text{ }\mu\text{m}$ cannot be detected.

3.3.2.3 TEM observation

The microstructure, phase constituents and the orientation relationship between phases in

as-received, 40HCP and 40HCP-PC samples were studied using a JEOL 2100 LaB₆ Emission TEM by indexing the electron beam diffraction patterns.

3.3.3 Composition depth profiling

A LECO GDS-750 QDP glow discharge spectrometer (GDS) was used to probe the chemical composition changes as a function of depth. The atoms in sample surface are ejected and excited by an argon plasma. The excited atoms finally return to their fundamental energy level and emit a characteristic X photon which is measured with spectrometers. The concentrations of elements in a certain depth can be determined from the intensity of the characteristic photons. The machine was calibrated for Co-Cr-Mo alloy to determine the chemical composition

3.3.4 Mechanical property measurement.

3.3.4.1 Microhardness and load bearing capacity measurement

Microhardness and depth hardness profiling

The microhardness of the as-received and heat-treated samples and the hardness depth profiles of the plasma carburised samples were measured using a Mitutoyo hardness machine under a load of 25 g for a measure time of 10 s with a Vicker pyramid indenter.

Load bearing capacity

The load-bearing capacity of the plasma carburised samples was also evaluated using the

Mitutoyo hardness machine applying a load ranging from 10 g to 1000 g for a measure time of 10 s. A Vicker pyramid indenter was employed to obtain the hardness value. Post-indentation observation using SEM was carried on the indents of all plasma carburised samples to investigate the crack shape and location.

3.3.4.2 Nanoindentation test

Nanoindentation tests with a diamond Berkovich indenter were carried out on the FCC, HCP, FCC-PC and HCP-PC sample surfaces for the measurement of mechanical properties without effect of substrate.

During a nanoindentation test, load and displacement were recorded when the indenter was pressed into the sample surface at peak load of 100 mN for a duration of 10 s using a computer controlled Nano Test 600 machine. At least 10 points were selected to test on each sample to ensure the reliable determination of hardness and reduced modulus values of samples. The typical load-displacement curve (P-h curve) is shown in Figure 3.3.3 and schematic representation of cross-sectional view of an indent showing the parameters used for calculating hardness (H) and reduced elastic modulus (E_r) is depicted in Figure 3.3.4 [143]. Hardness (H) and reduced elastic modulus (E_r) were calculated based on the P-h curves following the Oliver – Pharr method [143]. The equations were as follows:

$$H = \frac{P_{\max}}{A} \quad \text{Equation 3.3.1}$$

$$S = \frac{dP}{dh} \quad \text{Equation 3.3.2}$$

$$E_r = \frac{\sqrt{\pi}}{2} \frac{S}{\sqrt{A}} \quad \text{Equation 3.3.3}$$

where P_{\max} is the peak load, A is the contact area, P is the load, h is the displacement and S is the measured stiffness based on the partial fitting of the 20% unloading curve.

The contact area can be determined by an area function $F(h_c)$.

$$A = F(h_c) \quad \text{Equation 3.3.4}$$

$$h_c = h - h_s \quad \text{Equation 3.3.5}$$

$$h_s = \epsilon \frac{P_{\max}}{S} \quad \text{Equation 3.3.6}$$

where h_c is the calculated plastic depth, h_s is the displacement of the surface at the perimeter of the contact, h_{\max} is the displacement at peak load and ϵ is the geometric constant of indenter.

3.3.4.3 Nanoindentation associated with EBSD technique

Nanoindentation tests were carried out on the 40HCP sample coupled with post-indentation EBSD examination to investigate the relationship between mechanical properties and different grain orientations. 100 tests were carried out in a arrangement of 10 x 10 in a square area using a computer controlled Nano Test 600 machine. The testing peak load was 100 mN and the duration time was 10 s.

For plasma carburised sample (40HCP-PC), cross-sectional nano-hardness was measured after selecting an EBSD-examined area. After nanoindentation, the indented area was re-studied by EBSD. The nano-hardness depth profiles of both original FCC and HCP Co phases area were obtained.

3.3.5 Wear test

A reciprocating tribometer was used to evaluate the sliding wear resistance of all samples. Schematic diagram of the reciprocating tribometer is shown in Figure 3.3.5. The tester employs an 12.5 mm diameter WC/Co ball articulating against the specimen surface under a load of 30 N at a stroke length of 4 mm at a frequency of 0.92 Hz and the total sliding distance was 172.224 m. The ball contains 8 % cobalt and 94% tungsten carbide. The hardness of counterpart ball is 1500 HV and Young's modulus is 629 GPa. The Hertzian contact stress is around 1117 GPa. Each test were repeated at least three times. The wear volume was obtained by integrating the cross-sectional area of the wear track determined by a profilometer, and then multiplying the length of track. The wear factor was calculated by dividing the wear volume by the sliding length and load. An Ambios XP-200 Stylus Profilers was also used to record the change in surface morphology to profile sliding wear track and surface roughness. The wear tracks were inspected using SEM and EDX for determining the chemical composition of wear debris and wear tracks.

3.3.6 Corrosion Test

Potentialodynamic polarisation tests were carried out to assess the corrosion properties of both untreated and treated samples in full strength Ringer's solution (NaCl 6 g, KCl 0.075 g, CaCl₂ 0.1 g, NaHCO₃ 0.1 g per litre of water) which was made by dissolving eight 1/4 strength Ringer's solution tablets bought from LAB M company in distilled water (approximately pH 7.8). A flat cell was used with a working electrode area of 1 cm². A Ag/AgCl electrode was

served as reference electrode, a platinum wire was used as the auxiliary electrode, and the sample was mounted as a working electrode. Cyclic potentiodynamic measurements were conducted to obtain the polarization curve using an ACM GILL AC potentiostat. The scan rate is 1 mV/s and testing time for OCP is 10 minutes. The sample surfaces before and after corrosion tests were examined using SEM.

3.3.7 Tribocorrosion Test

Before tribocorrosion tests, samples were washed in soap water, rinse well, then cleaned in acetone and dried in air. Schematic diagram of the tribo-electrochemical cell is depicted in Figure 3.3.6 [84]. Before assembling into the tribo-electrochemical cell, samples were masked using lacquer to create a test area of $1.3 \times 1.3 \text{ cm}^2$ exposed to the electrolyte. 1M Ringer's solution was used as the electrolyte. A Saturated Calomel Electrode (SCE) served as the reference electrode, a platinum wire was used as the auxiliary electrode, and the sample was mounted as a working electrode. An alumina ball of 8 mm in diameter was used as the slider. The hardness and the young's modulus of the ball is 1700 HV and 371 GPa, respectively.

The tribocorrosion test system was composed of a pin-on-disc tribometer and an electrochemical potentiostat. During the tests, the samples fixed in the tribo-electrochemical cell were rotating against the stationary alumina ball, under testing load and speed conditions. Friction coefficient was recorded under various testing conditions. At the same time, electrochemical measurements were performed using an ACM GILL AC potentiostat.

Cyclic potentiodynamic measurements were conducted to obtain the polarization curve during sliding at a contact load of 20 N and a rotation speed of 60 rotations per minutes (rpm) after 600 s OCP stabilization. The hertzian stress is around 1166 GPa. These tests conditions were selected for comparison purpose since Sun et al. [84] investigated the tribocorrosion behaviour of S-phase surface engineered AISI 316 stainless steel under the same conditions. “Sliding under load” was used in this study to represent the conditions when the rotating sample under load. Cyclic potentiodynamic measurements of rotating samples at a speed of 60 rpm were also performed without load on samples after 600 s OCP stabilisation to indicate the contribution from unworn area outside the wear track to material tribocorrosion behavior during unidirectional sliding. “Rotation without load” was used to represent the conditions where the sample rotates without load as a benchmark to “sliding” to show corrosion effect.

After cyclic polarisation measurement, four potentials were selected and applied on each sample constantly and each potentiostatic test conducted on the sample for 4800 s including 600 s before sliding, 3600 s during unidirectional sliding and 600 s after sliding. Each test was repeated once. The scan rate is 1 mV/s.

After each test, a profilometer was employed to measure cross-sectional profile of wear track. Each wear track was repeatedly measured for at least 3 times at 3 different positions to get wear area. The wear volume was calculated by multiplying average wear area by circumferential length of the wear track. The wear tracks and counterpart balls were studied using a Brunel SP80 optical microscope and a Philips XL-30 LaB6 filament SEM with EDX

accessory.

CHAPTER 4 RESULTS

As described in the experimental part, a series of heat treatments were designed for the heat treatment of the as-received ASTM F1537 Co-28Cr-6Mo alloy (AR) to obtain materials with different percentages of ϵ -HCP Co phase in the microstructure. The samples coded FCC and HCP in this study represent the materials with nearly fully ($>95\%$) α -FCC phase and nearly fully ($>95\%$) ϵ -HCP Co phase, respectively since it is difficult to get 100% α -FCC or 100% ϵ -HCP structures after many heat treatment attempts. The AR sample was used as the benchmark for the heat-treated samples. Then, the heat-treated materials with different percentages of ϵ -HCP Co phase were plasma carburised in conventional direct current furnace using the same optimal treatment conditions (time, temperature, gas mixture and pressure).

A series of microstructure characterisation and property evaluation were carried out on all samples in order to systematically study the response of the Co-28Cr-6Mo alloy with different FCC/HCP phase constituents to low temperature plasma carburising (LTPC) treatment in terms of microstructure, mechanical properties (micro-hardness and nano-hardness), dry wear, corrosion and tribocorrosion behaviour.

In this chapter, the experimental results are presented in order of microstructure (including as-received (AR), heat-treated and plasma carburised), mechanical properties (including micro-hardness and nano-hardness), corrosion (corrosion resistance of all samples), tribology (wear resistance of all samples) and tribocorrosion (including potentiodynamic sliding tests without load, potentiodynamic sliding tests under load, effect of potential on electrochemical

behaviour during potentiostatic sliding wear test and effect of potential on wear performance during potentiostatic sliding wear test).

4.1 Microstructure of as-received material

In order to systematically investigate the microstructure of the as-received Co-Cr samples, these samples were observed by optical microscopy, SEM and TEM. EDX analysis was carried out on the AR sample to investigate the chemical composition of localised areas or phase. Both XRD and TEM analyses were performed to identify the phase constituents of the AR sample.

The microstructure of the as-received materials, as shown in Figure 4.1.1, consists of equiaxed matrix grains approximately 8 μm in diameter and particles mainly along grain boundaries. The size of these particles varied from 0.5 to 4 μm as detailed in SEM micrographs (Figures 4.1.2-4.1.3). The composition revealed by the EDX on spot 1 is close to that of the alloy although it showed a lower content of Mo and a higher content of C than in the alloy. Most probably, the large instrument error of EDX for the measurement of such light element of carbon may have, to some extent, led to the relatively low value of Mo measured. The EDX analysis on the large particles denoted as spot 2 in Figure 4.1.3 showed a high content of carbon, chromium and molybdenum. While spot 3, on the small particle, showed a high content of carbon and molybdenum. The content of cobalt in these particles (spots 2 and 3) are relatively lower than that in the matrix (spot 1). This may indicate that the large particles are chromium carbides and the small ones are molybdenum carbides.

The XRD chart of the as-received material is shown in Figure 4.1.4. It can be seen that the as-received material possesses two phases of α -FCC and ϵ -HCP with the former dominating as evidenced by the high intensities of $\alpha(111)$ and $\alpha(200)$ peaks. The d-spacing of $(111)_\alpha$ and $(200)_\alpha$ peak was 0.206 nm and 0.179 nm respectively, from which the lattice parameter of the α -FCC Co was calculated to be $a=0.358$ nm. The lattice parameter of the α -FCC phase in this Co-28Cr-6Mo alloy is larger than that of pure Co α -FCC phase ($a=0.354$ nm), which is mainly due to the substitution of larger atoms of Cr and Mo to Co atoms. No clear peaks of carbides could be identified from the XRD chart with certain confidence mainly due to the broadening and overlapping of the peaks of the α -FCC and ϵ -HCP Co phases in conjunction with a high background. Therefore, TEM was used to further characterise the microstructure.

Figure 4.1.5 shows the plan view TEM microstructures of the AR sample and corresponding selected area diffraction (SAD) patterns of carbide and α -FCC matrix. Figure 4.1.5a shows an equiaxed large carbide denoted as B in the α -FCC matrix, which contains annealing twins (denoted as C). The diffraction pattern from the carbide (Figure 4.1.5b) can be indexed to $[\bar{1}12]$ zone for $M_{23}C_6$ ($M=Cr_{0.77}Co_{0.15}Mo_{0.08}$) ($a=1.084$ nm).

Figure 4.1.6 shows typical defects such as annealing and micro twins (Figure 4.1.6 a) and stacking faults (Figure 4.1.6 b) in the AR sample, mainly due to the low stacking fault energy of Co-Cr alloy which facilitates the formation of stacking faults. Thin plates of ϵ -HCP phase were observed within α -FCC grains, as can be seen in Figure 4.1.7. A relationship between α -FCC and ϵ -HCP Co phases was found as (Figure 4.1.7 b): $[\bar{1}\bar{1}1]_\alpha // [001]_\epsilon$ and $(112)_\alpha //$

(010)_ε. This indicates that the α-FCC and ε-HCP Co phases follow the Shoji–Nishiyama (S–N) orientation relationship which was also observed by Li [144].

4.2 Microstructure of heat-treated samples

In order to obtain samples with different FCC/HCP phase constituents, As discussed in Chapter 3, a series of heat treatments were designed (see Table 3.2.1) and applied to the AR samples by referring the study done by Saldívar García et al. [36] to obtain samples with nearly fully α-FCC (sample FCC), nearly fully ε-HCP (sample HCP) and mixed α-FCC/ε-HCP (sample 40HCP).

The heat treated samples were XRD scanned and the intensity of peak $[10\bar{1}1]_{\text{HCP}}$ and $[200]_{\text{FCC}}$ were used to calculate their HCP percentages using Equation 4.2.1 developed by Gilland and Sage [36].

$$f^{\text{HCP}}(\text{wt \%}) = \frac{I_{10\bar{1}1}^{\text{HCP}}}{I_{10\bar{1}1}^{\text{HCP}} + 1.5 I_{200}^{\text{FCC}}} \quad \text{Equation 4.2.1}$$

A summary of calculated weight percentage of the HCP phase in three treatment conditions is shown in Figure 4.2.1. It can be seen that the constituent of HCP structure can match with the treatment designed although a small quantity of ε-HCP and α-FCC phase remained in the FCC and HCP samples. It is difficult, if not impossible, to get a full FCC or HCP structure under the laboratory conditions obtainable. The HCP percentage of each sample was also confirmed by EBSD analysis as summarised in Table 4.2.1. (Details will be reported in

Sections 4.2.1-4.2.3) Comparing Figure 4.2.1 with Table 4.2.1 revealed some small deviation in HCP phase concentration. This is mainly caused by the different methods employed they have their own limitations. For example, some limitations in determining the phase constituents by EBSD need to be considered such as unsolved areas, grain boundaries and defects of the microstructure and residual stress etc.

All the heat-treated samples were also characterised by optical microscopy, SEM, TEM and EDX and the detailed results are reported in the following sub-sections according to the three groups of samples with different phase constituents.

4.2.1 FCC sample

Figure 4.2.2 shows the XRD pattern of the FCC sample with more than 95% α -FCC phase. As indexed, the XRD pattern is dominated by strong α -FCC phase peaks with only one weak ϵ -HCP peak $\epsilon(10\bar{1}1)$. The d-spacing of $\alpha(111)$ peak was 0.207 nm, from which the lattice parameter of α -FCC Co was calculated to be $a=0.359$ nm, which is marginally larger than or similar to that (0.358 nm) for the α -FCC Co in the as-received materials.

The microstructure of the FCC sample (Figure 4.2.3) is composed of equiaxed grains in the size from 8 to 100 μm in diameter. The carbides observed for the AR sample shown in Figure 4.1.2 were mostly dissolved during the 1200°C/1.5 h solution treatment as only very small particles (Figure 4.2.3a). Detailed high resolution SEM observation shows a high density of twins (Figure 4.2.3b denoted as T) and small carbides in the size of 1 μm (Figure 4.2.3b

denoted as P).

EBSD technique was also used to further confirm the phase constituent obtained by XRD and to study the distribution of phases and their orientation (Figure 4.2.4). It was found that the area fraction of ϵ -HCP phase is only 0.1% in solution treated conditions (Table 4.2.1). This discrepancy could be caused by the fact that some micro-twins planes may have contributed to the intensity of the $\epsilon(10\bar{1}1)$ peak in the XRD chart shown in Figure 4.2.2. This is supported by the high density of micro twins detected by EBSD (Fig. 4.2.4c). Grain orientation map shown in Figure 4.2.4 (c) indicates that the grains are randomly orientated with no preferred orientation, which is in line with most solution treated microstructure.

4.2.2 HCP sample

Figure 4.2.5 is the XRD pattern taken from the HCP sample, which was treated by aging at 850°C for 15 h (Table 3.2.1). Indexing of the peaks identified high intensity of ϵ -HCP peaks $\epsilon(10\bar{1}0)$, $\epsilon(0002)$ and $\epsilon(10\bar{1}1)$ peaks at 2θ 41.2°, 44.3° and 47.0°. Only one low intensity independent $\alpha(200)$ peak at 2θ 51.0° for α -FCC phase was indexed. The weight percentage of ϵ -HCP phase was calculated to be 97.01% based on the Equation 4.2.1, which indicates that the 850°C/15h aging treatment after solution treatment resulted in a nearly full HCP structure. A large amount of low intensity peaks can be seen in Figure 4.2.5 from the XRD pattern of HCP sample, which could be tentatively indexed to Co_2Mo_3 σ phase as denoted by the vertical lines. Further EDX and TEM investigation was carried out to identify carbides and σ phase.

The microstructure of etched HCP sample is shown in Figure 4.2.6, revealing some different microstructural features compared to the FCC sample (Figure 4.2.3) with equiaxed grains. High magnification SEM image of the HCP sample (Figure 4.2.6b) shows irregular shaped discontinuous particles and plates with various thicknesses embedded in the equiaxed matrix grains. Based on the XRD results, the matrix grains contributed to the dominant ϵ -HCP Co phase and the plates and irregular shaped particles within grains and along grain boundaries could be σ phase or carbides.

Figure 4.2.7 shows the EBSD phase map and crystal orientation map of the HCP sample, which confirmed that the HCP sample is dominated by ϵ -HCP phase with a small amount of residual α -FCC phase. The area percentage of the ϵ -HCP phase is measured to be 94.40% as summarised in Table 4.2.1, which is consistent with the results calculated by XRD analysis. The thin-plate carbides cannot be detected by EBSD phase mapping (Figure 4.2.7b), mainly because they are too thin (less than 0.5 μm) to be resolved due to the resolution limitation of the detector. Figure 4.2.7c shows the crystal orientation map of the ϵ -HCP phase, which indicates randomly orientated ϵ -HCP grains. Compared with the solution-treated FCC sample shown in Figure 4.2.4c, the HCP grains size is smaller and the grain boundaries are more irregular, which implies that the phase transformation from α -FCC to ϵ -HCP phases are via the nucleation and growth within original the α -FCC grains.

Figure 4.2.8 is the back-scattered electron (BSE) microscope image of the unetched HCP sample showing the matrix ϵ -HCP grains with varying contrast. No difference in chemical

composition can be found among slightly differently contrasted matrix grains according to repeated EDX point chemical composition analysis on each grain. The difference in contrast among grains is most probably caused by the different crystal orientations [145]. Figure 4.2.9 shows a high magnification BSE image with corresponding EDX line scan and point analysis on the plates and irregular shaped particles. It can be seen that the dark and white contrasted thin and irregular shaped particles were distributed within the grains and along grain boundaries. The EDX line scan analysis across the dark contrasted thin plate and irregular features in Figure 4.2.9 revealed a high content of Cr, Mo and C and low content of Co. These dark contrasted precipitates within grains could possibly be $M_{23}C_6$, which will be further discussed in TEM section.

Figure 4.2.10 shows the BSE image of the unetched HCP sample and corresponding EDX point analysis. It can be seen that the white contrasted island-like particles are rich in Mo and Cr and lean in Co than that in the matrix (point 3). However, the carbon content is equivalent to the matrix. From above EDX results, it may imply that this white contrasted particles could possibly be a $Co_2(Cr, Mo)_3$ structured σ phase. The EDX analysis on the dark contrasted irregular shape microstructure along grain boundaries revealed high Mo, Cr and C content and low in Co content, which is possibly $M_{23}C_6$ carbides. Again, TEM work was carried out to confirm this (see Section 4.2.4).

4.2.3 40HCP sample

Figure 4.2.11 shows the XRD pattern taken from 40HCP sample with, as expected, a high

intensity of both ϵ -HCP and α -FCC peaks. Based on Equation 4.2.1, the weight percentage of the ϵ -HCP phase in the sample was calculated to be 39.01% as shown in Figure 4.2.1. This sample was solution treated and short time (4 h) aged and water quenched, which resulted in 40% HCP phase. This indicates an uncompleted FCC to HCP phase transformation as designed for mixed ϵ -HCP and α -FCC phases.

Optical and SEM microstructures shown in Figures 4.2.12 and 4.2.13 revealed a mixed structure of ϵ -HCP and α -FCC phases. It assembles the FCC structure (less feature grains) and the HCP structure (ϵ -HCP grains with σ phase and carbide precipitates) as described in Sections 4.2.1 and 4.2.2.

Figure 4.2.14 shows the EBSD phase maps and crystal orientation map of the HCP sample. The area percentage of the HCP sample is measured to be 49.70% as summarised in Table 4.2.1, which is 10% more than the results calculated by XRD analysis (Figure 4.2.1). As discussed in Section 4.2.1 and the beginning of this chapter, the limitation of EBSD for defected crystals is responsible for the difference. It can be seen from Figures 4.2.14 (c) and (d) that no preferred orientation of FCC and HCP grains were observed; however, some HCP thin plates were formed along the twinning boundaries.

4.2.4 TEM analysis on the heat-treated samples

SEM and EDX analysis (Figure 4.2.8 – 4.2.10) revealed three types of precipitates in the HCP matrix:

1. Long thin plates, rich in C and Cr
2. Small particles, rich in C and Cr
3. Irregular shaped particles rich in Mo

In addition, some particles along grain boundaries were formed in the HCP and 40HCP samples. In order to identify these particles precipitated in the ϵ -HCP dominated samples, TEM was carried out on the 40HCP sample.

Figures 4.2.15a and b show the TEM longitudinal and transverse view of the thin plate precipitates observed by SEM. It can be seen that the thin plates have a shape of thin rectangle block. Indexing of the SAD patterns from these blocks revealed a Cr_{23}C_6 -like carbide: M_{23}C_6 , $\text{M} = \text{Cr}, \text{Mo}$. Figure 4.2.16 shows $[2\bar{1}10]$ ϵ -HCP matrix pattern superimposed with twin set of $[110]$ M_{23}C_6 patterns in an orientation of $[2\bar{1}10]_{\text{HCP}} // [110]_{\text{M}_{23}\text{C}_6}$, $(0002)_{\text{HCP}} // (1\bar{1}1)_{\text{M}_{23}\text{C}_6}$. Calculated crystal constant from the SAD pattern is $a = 1.084 \text{ nm}$.

Figures 4.2.17a and 4.2.18a are TEM microstructures of irregular precipitates presented within HCP grains and along grain boundaries, respectively. It was found from the corresponding SAD patterns (Figures 4.2.17 b and 4.2.18 b) that these precipitates are M_{23}C_6 , $\text{M} = \text{Cr}, \text{Mo}$.

The existence of the $\sigma\text{-Co}_2(\text{Mo},\text{Cr})_3$ phase was confirmed for these white contrasted particles shown in the BSE image (Figures 4.2.10). As shown in Figure 4.2.19, TEM microstructure and corresponding SAD pattern revealed particle $\text{Co}_2(\text{Cr},\text{Mo})_3$ σ phase in the ϵ -HCP matrix

and SAD pattern of 40HCP sample [123].

Figure 4.2.20 shows the microstructure of ϵ -HCP plates embedded in the FCC matrix and corresponding diffraction patterns. Indexing of the diffraction patterns revealed that the ϵ -HCP phase maintained a preferred orientation with the FCC phase, $[2\bar{1}\bar{1}0]_{\epsilon} // [110]_{\alpha}$, $(0001)_{\epsilon} // (1\bar{1}1)_{\alpha}$.

4.3 Microstructure of plasma carburised samples

The above FCC, HCP and 40HCP samples were all surface plasma carburised at 450°C for 10 h. The AR sample was not plasma carburised due to many large intergranular carbides which caused the problem on investigating the effect of HCP and FCC Co on the plasma carburised layer. In order to investigate the layer structure and phase constituents of the plasma carburised samples, XRD analysis was carried out on all plasma carburised samples. The cross-section and plan view microstructures of these samples were examined by both optical microscopy and SEM in low and high magnifications. GDS was performed to investigate the element depth concentrations to reveal the diffusion depth of carbon in different substrates. Finally, TEM analysis was carried out on HCP-PC and 40HCP-PC samples. The surface layer phase transformation during the low temperature plasma carburising treatment has been studied.

4.3.1 FCC-PC

The XRD patterns of the FCC and FCC-PC samples are shown in Figure 4.3.1. It can be seen that the FCC-PC sample showed a set of XRD peaks similar to that for the FCC sample but shifted to lower angles. This is the characteristic of carbon S-phase [146] and the peaks can be indexed to FCC structured S-phase planes as shown in Figure 4.3.1. The d-spacing of S(111) and S(200) was 0.218 nm and 0.190 nm respectively, which are significantly larger than that of $\alpha(111)$ (0.207 nm) and $\alpha(200)$ (0.180 nm) of the FCC sample indicating the supersaturation of carbon in the S-phase layer. The HCP peak shown in the FCC sample was not detected in the surface layer after plasma carburising treatment. This may indicate a HCP to FCC phase transformation during the plasma carburising.

Figure 4.3.2 shows the OM and SEM surface morphology of the FCC-PC sample. Because of the plastic deformation during the plasma carburising, surface features can be clearly seen in terms of equiaxed grains with many twins. Compared with the surface morphology of FCC sample (Figure 4.2.3), no change in grain size can be observed but strong surface relief and more crystal defects, such as twins and slip lines are evidential (Figure 4.3.2 b). OM and SEM observations on the cross-sectional section of the FCC-PC sample revealed a featureless 7 μm - thick surface layer (Figure 4.3.3). A white line between the surface layer and the substrate was observed in the optical micrograph (Fig. 4.3.3a) but no such boundary can be observed in the SEM micrograph (Fig. 4.3.3b). This is the characteristic of the carbon S-phase, indicating that no precipitation or compound was formed during the plasma carburising treatment.

GDS composition depth profiles of the FCC-PC sample are shown in Figure 4.3.4, demonstrating that carbon was diffused into the surface of the FCC sample during the plasma carburising process and it peaked at the outmost surface (about 15 wt%). As the distance from the surface increased, the carbon concentration decreased to a substrate value at a depth of 7 μm , which is in good agreement with the optical and SEM observations (Figure 4.3.3) of the carburised case. The content of chromium and molybdenum was high at the surface and decreased with the depth, while the content of cobalt was low at the outmost surface and then increased with the depth, indicating that the outmost surface layer was rich in chromium, molybdenum and lean in cobalt.

4.3.2 HCP-PC

The XRD patterns of the HCP and HCP-PC samples are shown in Figure 4.3.5. Compared with the XRD patterns of the HCP sample, the XRD pattern of the HCP-PC sample changed in two aspects. Firstly, original ϵ -HCP peaks and α -FCC peaks are still presented but shifted to lower angles, indicating expanded ϵ and α phases (S-phase) due to carbon alloying during the plasma carburising treatment. Secondly, a new peak at $2\theta\ 38^\circ$ and some other weak peaks were detected which cannot be confidently indexed to any known phases due to the broadening and overlap possible between $2\theta\ 40^\circ\sim 50^\circ$. Further TEM analyses were carried out and the results will be delivered in Section 4.3.3.

An OM image taken from the surface of the HCP-PC sample (Figure 4.3.6) shows similar features as for the untreated HCP sample (Figure 4.2.6). However, the high magnification

SEM image shown in Figure 4.3.7 revealed a different feature (Figure 4.2.6): fine particles distributed evenly over the whole surface. A cross-sectional optical micrograph showed a very thin layer on the top of the HCP-PC sample (Figure 4.3.8). Further high resolution SEM observation (Figure 4.3.9) revealed a 2 μm -thick surface layer consisting of fine needles grown from surface towards the cone and oriented differently within different matrix HCP grains.

The GDS composition depth profiles of the HCP-PC sample are shown in Figure 4.3.10. It indicates that carbon was diffused into the ϵ -HCP sample during the plasma carburising treatment. However, the carbon diffusion depth was only about 2-3 μm , which was much shallower than that of carbon diffusion layer formed on FCC-PC sample. The carbon content at the outmost surface for the HCP-PC sample was about 10 wt%, which was also much lower than that for the FCC-PC sample.

4.3.3 TEM analysis on the 40HCP-PC sample

As the 40HCP sample consists of about 40% ϵ -HCP and 60% α -FCC phase, its response to surface plasma carburising would be determined by both α -FCC and ϵ -HCP phases. As can be seen in Figure 4.3.11, XRD patterns of the 40HCP-PC sample could be indexed to S-phase and expanded ϵ_c -HCP phase with a peak at 2θ 38° difficult to index. Figures 4.3.12 and 4.3.13 show the surface morphology and surface layer structure for the 40HCP-PC sample, respectively. It can be seen that the observed surface features and layer structure from the FCC-PC and the HCP-PC samples are presented in the original α -FCC and ϵ -HCP grains. A

major difference in surface layer thickness can be clearly seen in Figure 4.3.13 with only 2 μm layer formed in an original ϵ -HCP grains but 7 μm formed in an original α -FCC grain. Again, the GDS composition depth profiles of the 40HCP-PC sample, shown in Figure 4.3.14, is an average value of FCC-PC and HCP-PC samples with a carbon diffusion depth of 5 μm .

TEM study on plasma carburised surface layer was carried out on the 40HCP-PC sample, which made it possible to characterise the surface layers formed during plasma carburising on both ϵ -HCP and α -FCC structured matrix in one sample.

Figure 4.3.15a is a stitched TEM microstructure showing a surface layer structure formed on an original α -FCC grain. As can be seen from the microstructure, there is no clear interface can be identified. The dotted line drawn on the figure for the interface between the carburised layer and the substrate was based on the thickness measured from SEM observation. SAD patterns taken from the surface layer, from top to interface, even further towards the substrate, revealed same FCC structure zone patterns of $B = [110]$. However, the d-spacing calculated based on the SAD patterns from the carburised layer is changed with the distance from the outmost surface. The closer to the surface, the bigger the d-spacing, which is consistent with the carbon depth distribution. Compared with the SAD patterns shown in Figure 4.3.15c, the pattern from the top area A (Figure 4.3.15a) is characterised by faint spots and distortions, while the pattern shown in Figure 4.3.15c taken from the area B close to the interface shows sharp spots and identical pattern.

Figure 4.3.16a shows the TEM microstructure of the carburised surface layer formed in ϵ -HCP structured grain. The SAD patterns from this layer have been systematically analysed and a Co_3C (PDF code: 00-026-0450) phase was identified (Figures 4.3.16b and c) for the fine needles formed on the original HCP grains after plasma carburising treatment. The Co_3C needles grew in the HCP matrix with a preferred relationship of $[01\bar{1}0]_{\text{HCP}} // [210]_{\text{Co}_3\text{C}}, (0002)_{\text{HCP}} // (\bar{1}\bar{1}22)_{\text{Co}_3\text{C}}$. The elongation of the diffraction spots and the strikes in Figure 4.3.16b was perpendicular to the needles, indicating fine needle shape effect of the Co_3C microstructure. The M_{23}C_6 particles observed in the HCP sample (Figures 4.2.15-4.2.18) were also found in the surface layer of HCP-PC sample as evidenced in Figures 4.3.17 and Figure 4.3.18, indicating no phase transformation for those carbides during plasma carburising.

Above observed surface layer structures within α -FCC and ϵ -HCP grains are representative of FCC and HCP samples, respectively, as SEM observation revealed in section 4.2.1 to 4.2.3 showed analogy surface layer structures of the later to the former.

4.4 Mechanical properties

As described in Chapter 3, Surface hardness was assessed on all samples using a microhardness tester to show the effect of heat treatment and low-temperature plasma carburising (LTPC) treatments on the hardness of ASTM F1537 Co-28Cr-6Mo alloy. Nanoindentation was conducted on sample surfaces to investigate the mechanical response of FCC/HCP phase constituents to the LTPC treatments. Cross-section microhardness was measured on all plasma carburised samples to study the change of hardness with depth.

Cross-section nano-hardness was also assessed on the 40HCP-PC sample to obtain a phase related depth nanohardness profiles. Microhardness under different loads was evaluated on all plasma carburised samples to investigate the load-bearing capacity.

4.4.1 Microhardness

The microhardness of heat-treated and plasma carburised samples was measured under a low load of 25g. The microhardness of heat-treated samples was used to investigate the effect of ϵ -HCP phase content on sample hardness, which acted as bench marks for the surface hardness after plasma carburising. The cross-section hardness profiles of plasma carburised samples were also measured to investigate the effect of concentration of carbon on hardness in micro scale with association of the corresponding GDS results. The load-bearing capacity of plasma carburised samples was assessed by means of microhardness at different loads.

4.4.1.1 Heat-treated samples

The microhardness of as-received (AR) and heat-treated samples is presented in Figure 4.4.1. Compared with the hardness of the AR sample (509HV), the hardness of the solution heat-treated FCC sample is similar (486HV). However, after aging at 850°C for 4 and 15 h the hardness of the corresponding 40HCP and HCP samples increased to 548HV and 604HV, respectively. The change in hardness after different heat treatments can be attributed to the microstructure evolution. As reported in the last section, the FCC sample is nearly fully α -FCC structured and hence has showed the lowest hardness whilst the HCP sample is nearly

fully ϵ -HCP structured and thus has exhibited the highest hardness. The 40HCP sample with a mixture of ϵ -HCP and α -FCC structure showed a hardness value in between the hardness for FCC and HCP. This implies that the hardness of the heat treated samples increased with the percentage of ϵ -HCP phase in their microstructures.

4.4.1.2 Plasma carburised samples

Surface hardness

The surface hardness of low-temperature plasma carburised samples is plotted in Figure 4.4.2. Compared with the corresponding heat-treated samples, the surface hardness of all the plasma carburised samples significantly increased. For example, after the plasma carburising treatment, the surface hardness of an originally α -FCC phase dominated FCC sample increased from 486 (Sample FCC) to 1270HV (Sample FCC-PC). The surface hardness of the partially (40HCP) and nearly fully ϵ -HCP structured HCP samples increased from 548HV and 604HV to 1162HV and 1156HV, respectively following the plasma carburising treatment. This clearly indicates that the hardness increase of Co-28Cr-6Mo alloy after the same low-temperature plasma carburising treatment depends on the original microstructure i.e. the FCC/HCP phase ratios. As evidenced in Figure 4.4.2, the hardening effect is more significant for the originally α -FCC dominated FCC sample than for the originally ϵ -HCP structured HCP and 40HCP samples. Judging by the average hardness, the hardening effect conferred by the LT-PC is generally decreased with increasing the percentage of ϵ -HCP phase although the difference in hardness for HCP and 40HCP is within the experimental error. The potential mechanisms involved will be discussed in the discussion chapter.

Depth hardness profiles

Figure 4.4.3 shows the cross-section hardness depth profiles of plasma carburised samples. It can be seen from Figure 4.4.3 that the hardness of S-phase layer formed on FCC-PC sample is about 1270 HV at the surface, which decreased gradually to the hardness of the substrate (FCC sample) about 480 HV at a depth of 9 μm . This is in line with the carbon concentration depth profile shown in Fig. 4.4.4 (a). The surface hardness of HCP-PC sample is approximately 1160 HV, which decreased sharply with increasing depth. This is in a good agreement with the trend of the carbon content depth profile (Fig. 4.4.4c). The hardness depth profile of 40HCP-PC sample is in between the hardness depth profiles for the carburised HCP-PC and FCC-PC samples. This profile is consistent with the carbon concentration depth profile of 40HCP-PC (Fig. 4.4.4b).

4.4.2 Load-bearing capacity of plasma carburised samples

The load-bearing capacity (LBC) of the plasma treated samples was assessed by measuring the hardness under a range of loads and the hardness-load profiles thus obtained for the carburised samples are profiled in Figure 4.4.5. It can be seen from Figure 4.4.5 that the measured hardness of FCC-PC decreased gradually with load when the applied load is less than 50 g and then quickly dropped from 1125 HV to 769 HV when the load increased from 50 g to 100 g. While for HCP-PC sample, the surface hardness was maintained above 1000 HV until a 200 g load was applied, when the hardness was reduced to 770 HV. Then the hardness was only moderately decreased to HV 620 when the load was further increased from

200 g to 1000 g. The hardness of the 40HCP-PC sample continually decreased with the applied load in the range of 25-200 g and this change was slowed down when the applied load above 200 g.

Post indentation SEM observation showed that when the load was below 100 g, no cracks could be observed for the FCC-PC sample; however, some circumferential cracks were found within the indents when the applied load reached 100 g (Figure 4.4.6a). For the HCP-PC sample, no cracks can be seen until 300 g as evidenced by the SEM picture shown in Figure 4.4.6b. Post indentation SEM observations also revealed that for the 40HCP-PC sample, no crack can be detected until 300 g, Figure 4.4.6 (c) and (d).

Clearly, it can be seen from Figures 4.4.5 and 4.4.6 that when load under 25 and 50 g, the FCC sample has better load bearing capacity than the HCP-PC and 40HCP-PC samples. However, when loaded at 100 g or above, the order is changed and the HCP-PC sample outperformed the 40HCP-PC and FCC-PC samples. This can be attributed to the following two main factors.

The one factor is the effect of the surface and substrate hardness. When the applied load is low (for example 50 g), the penetration depth of the indenter is very small. Hence, the measured hardness or LBC mainly is determined by the hardness of the surface hardened layer. As shown in Figure 4.4.3, the FCC-PC sample possesses the highest hardness within the first 6 μm and therefore it has the highest LBC. However, when tested under a load of 100

g, the depth of the indentation in all plasma carburised samples was around 2 μm . Hence, the depth of stress field was estimated to reach approximately 20 μm using the well-known '10 times rule'. Clearly, the measure hardness is a composite hardness of the surface hardened layer and the substrate. Accordingly, the effect of substrate hardness should have played a significant role as evidenced by the opposite order in the load bearing capacity. This is evidenced in Figure 4.4.2, where the HCP sample exhibited the highest substrate hardness.

The other factor is the different behaviour of crack initiation and propagation for the S-phase dominated FCC sample and for the Co_3C dominated HCP sample. The cracks in FCC-PC sample (Figure 4.4.6a) developed parallel to the edge of indent while those in HCP-PC and 40HCP-PC sample (Figures 4.4.6b and d) distributed along the boundaries of different carbide grains and the edge of indent. This is largely because the surface of FCC-PC sample was dominated by a FCC structured solid solution S-phase that was prone to slip under contact stress and therefore parallel cracks were produced in the indent. On the other hand, the surface layer of HCP-PC sample was composed of brittle and thin-plate-shaped orthorhombic structure Co_3C carbides with limited slip systems; therefore crack initiated along such defects as carbide boundaries and the edge of indent due to bending.

4.4.3 Nanoindentation analysis

Nanoindentation tests were conducted on some samples to reveal the relationship between the nanohardness/reduced modulus and the microstructure and phases (α -FCC, ε -HCP, S-phase and Co_3C). The 40HCP sample contains a mixture of both α -FCC and ε -HCP Co phases and

was used for nanoindentation tests. The EBSD was used to identify the α -FCC and ϵ -HCP grains with nano-indents. Nanoindentation mapping on the cross-section of the surface layer formed on 40HCP-PC was also established by EBSD before and post nanoindentation in the same area. The results of above investigations are reported in the following parts.

4.4.3.1 Surface nanoindentation of bulk samples

Figure 4.4.7 depicts the nanoindentation results of hardness (H) and reduced modulus (E_r) for heat-treated FCC (α -FCC phase dominating) and HCP (ϵ -HCP phase dominating) samples and subsequently plasma carburised FCC-PC (S-phase dominating) and HCP-PC (Co_3C dominating) samples.

It can be seen that the nanohardness of the FCC sample is 4.9 GPa and after the plasma carburising treatment, the surface nanohardness of the FCC-PC sample increased to 12.4 GPa. The HCP sample possesses a hardness of 6.7 GPa, which is increased to 12.0 GPa after the plasma carburising treatment. This observation is consistent with the surface hardness results measured by a microhardness tester shown in Figure 4.4.2. The above surface nanohardness results confirm that the LTPC treatment can effectively harden both α -FCC and ϵ -HCP structured Co-Cr alloy surfaces. The nanohardness of the HCP sample is higher than that of the FCC sample, confirming that the hardness of Co-Cr alloys should increase with the fraction of the ϵ -HCP Co phase in the microstructure.

The FCC-PC and HCP-PC samples showed very similar nanohardness, indicating that the

Co₃C layer formed on the HCP structured Co-Cr alloy by plasma carburising is as hard as the S-phase case produced on the FCC structured Co-Cr alloy. This observation is not consistent with the surface hardness measured by a microhardness tester (see Figure 4.4.2), which showed a higher surface hardness for the S-phase case than for the Co₃C layer. The inconsistency was mainly caused by the effect of the thickness of the surface hardened case. As reported in Section 4.1, the thickness of the surface hardened layer formed on the FCC-PC and HCP-PC is about 7 and 2 μm , respectively. It is known that the depth of indent produced by a microhardness tester is much deeper than that produced by a nanohardness tester. Therefore, the stress field produced by the microhardness tester will well exceed the 2 μm -thin Co₃C layer and hence a low composite hardness value is expected. On the other hand, the penetration depth of the nano indenter is very shallow and accordingly the hardness measured by nanoindentation can reveal the real hardness of the superficial surface area of the LTPC treated Co-Cr alloy.

The Young's modulus (E) of the FCC and FCC-PC samples is very similar (around 240 GPa) and difference is not significant when taking account of the experimental error. The HCP sample exhibited a reduced modulus of 225 GPa, which was increased to 261 GPa after the plasma carburising treatment. The significant increase in E for the plasma treated HCP-PC samples is mainly due to the phase transformation from ϵ -HCP Co phase to Co₃C phase during the LTPC treatment.

The hardness-to-Young's modulus ratio (H/E), which is a measure of the elastic deformation

capacity, of the FCC, FCC-PC, HCP and HCP-PC samples is shown in Figure 4.4.7b. It can be seen that the H/E of the FCC sample (0.021) is lower than that (0.030) of the HCP sample; however, after plasma carburising, the H/E of the FCC-PC (0.050) is higher than (0.046) of the HCP-PC sample. The above results clearly demonstrate that the LTPC treatment has resulted in an increase in H/E_r for both originally α -FCC dominating and ϵ -HCP dominating Co-Cr samples with the former being more significant than the latter. Hence, the elastic deformation capacity is expected to be improved by the LTPC treatment for both the α -FCC and ϵ -HCP structured Co-Cr samples.

4.4.3.2 Nanoindentation of FCC and HCP grains

Figure 4.4.8 shows the nanoindentation mapping of the 40HCP sample super-imposed by EBSD image to investigate the hardness dependence on the phase constituent (α -FCC Co, ϵ -HCP Co phases) and their grain orientations.

Figure 4.4.8a exhibits the phase distribution of selected testing area revealed by EBSD with yellow for α -FCC Co, blue for ϵ -HCP Co and black for unsolved points due to a low amount of back-scattered electron signals. The nanoindents caused the depressions of sample surface and the resultant low volume of back-scattered electron signals. As a result, the nanoindented areas appear black, which can be used to identify the location of nanoindents. It can be seen from Figure 4.4.8a that the 10 x 10 triangular-shaped black nanoindents are distributed on both the α -FCC and the ϵ -HCP grains. Figure 4.4.8b shows the orientation of α -FCC grains coloured based on the orientation key inserted in the bottom right corner. Five α -FCC grains

with different orientations were picked to measure their nanohardness and reduced modulus and the results are plotted in Figure 4.4.8c. The nanohardness of these five α -FCC grains varied from 4.1 to 5.6 GPa. Grain 1 exhibited the lowest average nanohardness and largest error bar. The nanohardness of grain 2 is slightly higher than that of grain 1 and the variation of nanohardness is also very large. The average nanohardness of grains 3 and 4 is similar and their error bar is much smaller than that of grains 1 and 2. Grain 5 possessed the highest average nanohardness and a small error bar. The E of these five grains is around 240 GPa but grains 1 and 2 exhibited a large variation in E.

Figures 4.4.8e and f show the ϵ -HCP Co phase normal direction grain map and the corresponding crystal mimic and reverse pole figures for grains 1-4. The nanoindentation results including nanohardness and reduced modulus are summarised in Figure 4.4.8e. For the ϵ -HCP grains, grain 3 and grain 4 possessed the same nanohardness of 7.4 GPa, which is higher than that of grain 1 (5.7 GPa) and grain 2 (6.1 GPa). Grain 3 and grain 4 showed a smaller error bar compared with grains 1 and 2. Grain 1 exhibited the largest error bar in nanohardness. The average E of all ϵ -HCP grains is around 230 GPa. A very large variation of E ranging from 208 to 260 GPa can be observed for grain 1, while grains 3 and 4 showed a very small error bar.

4.4.3.3 Cross-section nanoindentation on the LTPC treated surface layer

Figures 4.4.9 and 10 show the cross-sectional hardness distribution with depth and phase type. The indents presented are close to each other and therefore the neighbouring indents, which

could influence the value of the other indents. Two typical columns consisting of 7 nanoindents were selected from fifteen columns to represent the depth distribution of nanohardness for originally FCC structured Co-Cr as marked in blue and originally HCP structured Co-Cr as marked in red. The nanohardness depth profiles were shown in Figure 4.4.10. It can be seen that the nanohardness of the originally FCC structured area has a high hardness of about 11.2 GPa at the near surface area, which is gradually decreased with the depth to reach the substrate hardness at a depth of about 8 μ m. The original HCP area showed a similar nanoindentation value as for the original FCC area but it dropped steeply within the first 5 μ m before it reached the substrate hardness.

4.5 Electrochemical corrosion

As described in Chapter 3, in order to investigate their corrosion behaviour in Ringer's solution, anodic polarisation tests were carried out on heat-treated and plasma carburised Co-28Cr-6Mo alloy samples. The anodic polarisation curves were plotted and the corrosion potential for each sample was estimated. Post-test observations by SEM were carried out on all samples to study the corrosion mechanisms involved. The electrochemical corrosion test results are reported in this section.

4.5.1 Corrosion resistance of heat-treated samples

4.5.1.1 Anodic polarisation

The potentiodynamic polarisation curves of the heat-treated samples are compared with the

as-received (AR) sample in Figure 4.5.1. It can be seen that the anodic polarisation curves of all the heat-treated samples are different from that of the AR sample. The corrosion potential (Table 4.5.1) of the AR sample is -138.3 mV (Ag/AgCl). The FCC sample showed a negative shift in corrosion potential to -177.4 mV (Ag/AgCl) compared to the AR sample. The corrosion potential of 40HCP and HCP samples also changed to a more negative value of -224.1 and -228.9 mV (Ag/AgCl), respectively.

The anodic zone of anodic polarisation curves for the heat-treated samples can be generally divided into three zones including passive and transpassive zones, indicating good passivation behaviour of the heat-treated samples. While for the AR sample, small vibrations in current density as marked by black circle in Figure 4.5.1 can be observed at the very beginning of anodic potential most probably due to the electrochemical noise. The corrosion potential of the AR is superior to the heat-treated sample.

Within the group of the heat-treated samples, the 40HCP and HCP samples possessed almost the same anodic current and corrosion potentials. The nearly full α -FCC Co-Cr alloy (i.e. FCC sample) showed a nobler corrosion potential by about 50 mV more positive than partial (i.e. the 40HCP sample) and nearly full (i.e. the HCP sample) ϵ -HCP Co-Cr alloys. This indicates that the corrosion potential of the heat-treated Co-Cr alloys decreased by the formation of ϵ -HCP Co phase.

4.5.1.2 Post test SEM observations

Figure 4.5.2 illustrates the SEM microstructure of the AR, FCC, HCP and 40HCP samples before and after the anodic polarisation tests. Figures 4.5.2a, c, e and g show typical as-polished morphologies before the anodic polarisation tests. After the anodic polarisation tests, the SEM micrograph of the AR sample (Figure 4.5.2b) showed clear intergranular corrosion around grain boundaries, especially around the boundaries of intergranular carbides due to the depletion of chromium in these areas.

The SEM observations on the anodic polarisation tested FCC sample (Figure 4.5.2d) revealed less severe intergranular corrosion than the AR sample. This could be attributed to the much less carbides due to a 1200 °C/1.5 h solution treatment and dissolution of carbides. For the FCC sample, grain boundaries can be seen after anodic polarisation test, which implies that the potentiodynamic polarisation tests led to mild intergranular corrosion along the grain boundaries of equiaxed grains of the FCC sample.

Figure 4.5.2f shows the surface morphologies of HCP sample after potentiodynamic polarisation tests. Only very fine carbides precipitated during aging treatment can be observed. No pits or other localised dissolution area can be found. The 40HCP sample after potentiodynamic polarisation tests (Figure 4.5.2h) showed similar feature to the HCP sample in the HCP structured area and a mild general corrosion in the FCC structured area. No intergranular corrosion or localised dissolution can be found. The post-test observations on the AR and heat-treated samples are consistent with the potentiodynamic polarisation curves

in Figure 4.5.1 with the AR sample showing severe localised corrosion.

4.5.2 Corrosion behaviour of plasma carburised samples

4.5.2.1 Anodic polarisation tests

The anodic polarisation curves of the plasma carburised samples together with the AR for comparison are plotted in Figure 4.5.3 and the corrosion potentials of the plasma carburised samples are listed in Table 4.5.2.

As shown in Figure 4.5.3 that after the plasma carburising treatment, the corrosion behaviour of Co-Cr alloy changed. It can be found by comparing Table 4.5.2 with Table 4.5.1 that the corrosion potential of the FCC-PC sample is -102.4 mV (Ag/AgCl), which is 75.0 mV (Ag/AgCl) nobler than that of the FCC sample. The corrosion potential of the 40HCP-PC and HCP samples increased from -224.1 and -228.9 to -185.3 and -181.4 mV (Ag/AgCl), respectively. Clearly, the low-temperature plasma carburising treatment has led an increase of corrosion potential for all the heat-treated samples. The increase of the corrosion potential for originally α -FCC structured Co-Cr alloy (i.e. FCC) is more significant than that for partially (40HCP) and fully (HCP) ϵ -HCP structured Co-Cr alloy.

When compared to the AR sample, only the FCC-PC sample showed a nobler corrosion potential than the AR sample. In the group of plasma carburised samples, the FCC-PC sample exhibited the most positive corrosion potential at -102.4 mV (Ag/AgCl) and slightly lower anodic current compared to other two plasma treated samples. The 40HCP-PC and HCP-PC

samples possessed similar or almost the same anodic corrosion behaviour. This indicates that the S-phase layer produced on α -FCC dominating Co-Cr structure (i.e. FCC sample) possessed better corrosion resistance than Co_3C layer formed on partially and near fully ϵ -HCP structured 40HCP and HCP samples in terms of corrosion potential and anodic current. The anodic zone of anodic polarisation curves for plasma carburised samples can be generally divided into passive and transpassive zones, revealing a good passivation ability.

The anodic polarisation curves of materials before and after plasma carburising treatments are plotted together in Figure 4.5.4 for the comparison of anodic current. All the plasma carburised samples showed a slightly lower anodic current than that for the heat-treated samples. Clearly, the plasma carburising treatment has enhanced the corrosion resistance of Co-Cr alloy with different fractions of ϵ -HCP phase in terms of increased corrosion potential and reduced anodic current.

4.5.2.2 Post test SEM observations

Figure 4.5.5 illustrates the SEM microstructure of as-carburised FCC-PC samples before and after potentiodynamic polarisation tests. It can be seen that before corrosion test, the surface relief of the FCC-PC sample can be clearly seen due to plastic deformation. After the corrosion tests, the surface relief of the FCC-PC sample is less profound than that of as-carburised one, mainly because the sample surface was covered by a polarisation film and/or the general corrosion during the corrosion tests. No pits or intergranular corrosion can be found after the corrosion test, indicating that the change of surface morphologies would be

mainly due to the general corrosion.

The SEM micrographs of the HCP-PC samples before and after corrosion tests are demonstrated in Figure 4.5.6. Before the potentiodynamic polarisation tests, carbides can be observed on the surface. While after the potentiodynamic polarisation tests, the surface of the sample was covered by dark corrosion products as shown in Figure 4.5.6b and no other corrosion features can be found.

However, the 40HCP-PC samples (Figure 4.5.7) showed some mild intergranular corrosion near carbides as marked by the white circles after potentiodynamic polarisation tests.

4.6 Tribological Properties

In order to assess the wear behaviour of as-received, heat-treated and plasma carburised samples, reciprocating wear tests were performed on all samples against a WC/Co ball under a load of 30 N for 6.5 h at a frequency of 0.92 Hz in the air and at room temperature around 20 °C with a stroke length of 4mm. A relatively high load of 30 N was used to accelerate the wear process and produce measurable wear tracks for all samples, especially the surface modified samples in order to complete the wear tests within a reasonable time period. Post test SEM observations were carried on all samples and counterpart balls to reveal the related mechanisms and necessary EDX analysis was used to study the chemical composition at different locations. The friction and wear results are reported in this section.

4.6.1 As-received and heat-treated samples

4.6.1.1 Coefficient of friction

Figure 4.6.1 depicts the average coefficient of friction (CoF) of the AR and heat-treated samples during half an hour reciprocating wear tests. The AR sample showed the lowest friction coefficient of 0.217. All the heat-treated samples possessed a similar friction coefficient ranging from 0.364 to 0.375. The solution treated FCC sample showed marginally higher CoF as compared with the solution and aging treated HCP and 40HCP samples.

4.6.1.2 Wear volume

The 2D cross-section profiles of wear tracks on the AR and heat-treated samples are demonstrated in Figure 4.6.2, from which the wear volume was calculated. It can be seen from Figure 4.6.2 that the wear track formed on the ϵ -HCP phase predominating HCP sample is much broader and wider than those formed on partially or nearly full α -FCC predominating 40HCP and FCC samples, respectively.

The wear volume of the AR and heat-treated samples are depicted in Figure 4.6.3. The AR sample exhibited the highest wear resistance compared to the all heat-treated samples as evidenced by the lowest wear volume, which might be related to its low coefficient of friction. The α -FCC dominated FCC sample and mixture phased 40HCP sample exhibited a similar wear volume of about $1.000 \times 10^{-10} \text{ m}^3$.

The nearly full ϵ -HCP structured HCP sample experienced unexpected severe wear approximately 1.7 times of that of the FCC and 40HCP samples, although the HCP sample possessed the highest hardness (Fig. 4.4.1). Hence, detailed investigation was carried out by SEM and EDX to study the mechanism involved in this unexpected high wear volume for the HCP sample.

4.6.1.3 Wear track observations

The wear tracks formed in the AR and the heat-treated samples by reciprocating wear tests were examined by SEM and EDX.

Figure 4.6.4a exhibits the wear track morphologies of the AR sample after reciprocating dry wear test. It can be seen that the wear track was unevenly covered by dark flakes or powders especially along the wear tracks areas. EDX on the dark area (spot 1 in Figure 4.6.4b) revealed a high content of oxygen as shown in Figure 4.6.4c. This indicates that oxidation wear may have played a part in the dry wear process. The morphology of the oxidation layer was wrinkle-shaped due to the repeated reciprocating rubbing against the counterpart ball.

A lot of craves and tail-like fine grooves near the craves parallel to the sliding direction can be found as indicated by the white arrows in Figure 4.6.4b. They were mainly caused by the break-down and spallation of large intergranular carbides from the sample surface. The very hard and large carbide debris then served as third-body abrasive particles and resulted in the tail-like grooves. The dry wear mechanism of the AR sample was dominated by oxidation and

abrasive wear. The large intergranular carbides would confer both beneficial and deteriorating effect on the wear resistance. The hard carbides enhanced the wear resistance of the AR sample when they stayed in the sample surface. However, the carbides could also accelerate the wear when the hard carbides were pulled off the sample surface and acted as hard abrasives.

Figure 4.6.5a shows the wear track morphology and wear debris of the FCC sample after reciprocating dry wear test. It can be seen that the wear track was covered by more black flakes than that of the AR sample. EDX analysis on the black area (spot 3) and other area (spot 4) in Figure 4.6.5b revealed also a high content of oxygen in the black area (Fig. 4.6.5d). Only very fine parallel grooves can be found without spallation and tale-like grooves compared to the AR sample, which was mainly due to the significant reduction in carbides by solution heat treatment. The wear debris (Figure 4.6.5c) on the counterpart ball showed a fine powder compact form with some irregular shaped wear particles. No sharp and hard abrasion particles were formed during the dry reciprocating wear tests of the FCC sample. The wear of the FCC sample is dominated by mild oxidation wear and polishing by the hard counterpart ball.

The wear track morphology of the HCP sample is depicted in Figure 4.6.6 showing features different from the AR and FCC samples. A large amount of broad and deep groove can be seen in the wear track with a little coverage of flakes (as marked by the white circles) that were identified to be oxides by EDX. Detailed SEM observation in Figure 4.6.6b showed the

presence of large wear craters as marked by white arrows, which were most likely induced by the micro-adhesive interaction between the ball and the sample surface. The material transferred from the craters to the counterpart ball roughened the counterpart surface and in turn resulted in the deep and broad grooves. Many very fine parallel grooves and thin-plate-shaped wear particles also can be seen in Figure 4.6.6b as marked by the black circles. The size of the thin-plate-shaped wear particles is consistent with the width of very fine grooves. Hence, it is reasonable to assume that the fine grooves were mainly caused the third-body abrasive effect of such thin-plate carbides in the HCP sample. The wear debris on the counterpart ball after against the HCP sample consisted of a large amount of very fine irregular shaped wear debris as shown in Figure 4.6.6c. The wear of the HCP sample was dominated by server abrasion and adhesion together with mild oxidation.

The wear track morphology of 40HCP is shown in Figure 4.6.7. It can be seen that the wear track is characterized by some black flakes and very fine grooves. However, no wear craters and resultant broad grooves can be seen for the 40HCP sample presumably due to the reduction of ϵ -HCP phase and thin-plate-shaped carbide phases as compared to the HCP sample.

4.6.2 Plasma-carburised samples

4.6.2.1 Coefficient of friction

The plasma carburised samples exhibited a higher friction coefficient than their substrate

materials and 40HCP-PC showed the highest friction coefficient of 0.526 among all the plasma treated samples. The formation of S-phase layer on α -FCC Co-Cr substrate (i.e. FCC sample) by LTPC treatment resulted in a rise of coefficient of friction from 0.375 to 0.481. The precipitation of Co_3C layer on ϵ -HCP Co-Cr substrate (i.e. HCP sample) by the LTPC treatment also caused an increase of coefficient of friction from 0.364 to 0.481.

4.6.2.2 Wear volume

The 2D cross-section profiles of the wear tracks formed on the plasma carburised samples are shown in Figure 4.6.9, from which the wear volume was quantified. The cross-sectional wear track profiles of all the carburised samples (Figure 4.6.9) revealed that the carburised layers were removed from the wear track as the maximum depth of wear track of each sample exceeded its surface layer thickness. The underneath substrate could have made some contribution to the wear volume measured.

The wear volume of the plasma carburised samples is depicted in Figure 4.6.10. Compared to the as-received AR sample ($0.641 \times 10^{-10} \text{ m}^3$), all plasma carburised sample showed a much lower wear volume ($0.039\text{-}0.109 \times 10^{-10} \text{ m}^3$). This should be attributed to the significantly increased hardness by the low temperature plasma carburising treatment used. It can be seen from Figure 4.6.10 that the HCP-PC sample exhibited the lowest wear volume compared among all the plasma carburised samples, while the FCC-PC sample showed the highest wear volume of $0.109 \times 10^{-10} \text{ m}^3$.

It seems that the wear decreased with the ϵ -HCP percentage in the substrate. This could be attributed to the load bearing capacity (LBC) and contribution of their substrate to wear resistance. The FCC-PC sample exhibited the lowest LBC than the 40HCP-PC and HCP-PC under loads higher than 100g (Figure 4.4.5) because the α -FCC structured substrate is softer than the ϵ -HCP structured substrate.

4.6.2.3 Wear track observation

Figure 4.6.11 shows the wear track morphology of the FCC-PC sample, which is very smooth, superficial and narrow (Figure 4.6.11a). Detailed SEM observation exhibited some dark layers in the wear track (Figure 4.6.11b). EDX analysis showed a high fraction of oxygen in the dark area (spot 5), revealing very mild oxidation wear. The detailed SEM observation (Figure 4.6.11b) showed a very smooth surface with only fine parallel grooves caused by the polishing against the counterpart WC/Co ball. The counterpart WC/Co ball was also worn by sliding against the FCC-PC sample. This is evidenced by the bright white small round-shaped wear debris in the wear track as marked by white circles in Figure 4.6.11b which contained W as revealed by EDX analysis. This implies that the wear resistance of the FCC-PC sample could be comparable to that of the counterpart WC/Co ball.

Figure 4.6.12 shows the wear track morphology of the HCP-PC sample. The wear track exhibited a higher coverage of black flakes than that of the FCC-PC samples. The black area (spot 7) was identified as oxide by EDX. Detailed SEM observation as marked by white arrows in Figure 4.6.12b showed very fine and tail-like parallel grooves starting from certain

points in the wear track, which was induced by the pulling-off of very thin Co_3C plates and the resultant third-body abrasive wear. The HCP-PC sample was dominated by mild oxidation and abrasive wear.

For the 40HCP-PC sample (Figure 4.6.13), the wear track showed combination features of that of the FCC-PC and the HCP-PC samples with mild oxide layers, fine grooves in the Co_3C phased area and relatively smooth polished surface in the S-phase area.

4.6.3 Comparison of wear

The wear volume of AR, heat-treated and plasma carburised samples are plotted in Figure 4.6.14 for comparison. It can be seen that for FCC and 40HCP materials, the wear volume decreased nearly by one order of magnitude by plasma carburising. For the HCP material, the wear volume reduced by approximately 1.65 orders of magnitude. The low temperature plasma carburising treatment has led to a significant improvement of wear resistance for all materials with different FCC/HCP ratios. This could be attributed to the formation of S-phase and Co_3C surface layers, and thus dramatic enhancement of surface hardness by plasma carburising.

4.7 Tribocorrosion

As discussed in Chapter 2, the articulating surfaces (or bearing surface) of artificial joint prostheses work under combined attack of wear and corrosion or tribocorrosion. Hence, based

on the previous results, the AR, FCC, HCP, FCC-PC and HCP-PC samples were selected for detailed tribocorrosion tests in simulated body fluid – Ringer’s solution. Firstly, potentiodynamic tests were performed under two different conditions: (1) sample rotating without load to establish the anodic polarisation curves under *corrosion only condition* and (2) sample rotating against an alumina ball under 20 N to establish the anodic polarisation curves under *tribocorrosion condition*. “Sliding” was used in this study to represent the conditions when the rotating sample under load. “Rotation” was used to represent the conditions where the samples rotate without load as a benchmark to “sliding” to show corrosion effect.

The change of coefficient of friction was also recorded during potentiodynamic sliding tests. Based on the anodic polarisation curves under tribocorrosion condition, one cathodic potential, OCP and three anodic potentials were selected to investigate the tribocorrosion behaviour of all samples under different polarisation conditions in terms of OCP, current, coefficient of friction, wear volume and mechanism. The outcomes of these tests are reported in this section.

4.7.1 Potentiodynamic sliding tests without load

4.7.1.1 Heat-treated samples

Figure 4.7.1 showed the potentiodynamic polarisation curves of the AR and heat-treated samples tested under rotation only condition. It can be seen that compared to the AR sample (-212.50 mV (SCE)), the corrosion potential of the FCC and HCP sample shifted cathodically

to -250.50 and -310.19 mV (SCE), respectively. The AR sample showed large vibration in current density during the early stage of anodic zone as marked by black circle due to electrochemical noise. No such vibration in current can be found for the FCC and HCP samples. The FCC sample outperformed the HCP sample in terms of corrosion potential.

4.7.1.2 Plasma carburised samples

Figure 4.7.2 shows the potentiodynamic polarisation curves of the AR and the plasma carburised FCC-PC and HCP-PC samples tested under rotation only condition. After plasma carburising treatments, the FCC-PC and HCP-PC samples showed more positive corrosion potentials at -108.91 and -134.06 mV (SCE) respectively compared to the AR sample (-212.50 mV (SCE)). The FCC-PC and the HCP-PC samples exhibited very similar anodic polarisation behaviour.

4.7.1.3 Effect of plasma carburising

The potentiodynamic polarisation curves of samples before and after plasma carburising treatment are plotted in Figure 4.7.3. It can be seen that the samples after plasma carburising treatment showed better corrosion behaviour than the samples before plasma carburising treatment in terms of nobler corrosion potential and lower anodic current. Clearly, the corrosion properties of both the FCC and HCP samples were improved by the low temperature plasma carburising treatment.

4.7.2 Potentiodynamic sliding tests under load

4.7.2.1 Heat-treated samples

Figure 4.7.4 depicts the anodic polarisation curves of the AR, FCC and HCP samples under tribocorrosion condition (i.e. potentiodynamic sliding tests under load). These three types of samples showed almost the same anodic polarisation curves under sliding condition. The corrosion potential of these three heat-treated samples positioned approximately at -520.00 mV (SCE).

Figure 4.7.5 presents the coefficient of friction curves measured during potentiodynamic tests under sliding for the AR and heat-treated samples. They showed similar coefficient of friction ranging from 0.30 to 0.40. This may related to the lubrication capability of corrosion products.

4.7.2.2 Plasma carburised samples

Figure 4.7.6 illustrated the anodic polarisation curves of the AR and plasma carburised samples under tribocorrosion condition. It can be observed that after plasma carburising, the corrosion potentials of the FCC-PC and HCP-PC samples shifted anodically to -433.71 and -385.62 mV(SCE) respectively compared to the AR sample. The plasma carburised samples also showed a reduction in current density by near half an order of magnitude compared to the AR sample.

Figure 4.7.7 presents the coefficient of friction curves measured during potentiodynamic tests under sliding (tribocorrosion) for the AR and plasma carburised samples. The FCC-PC sample exhibited the highest coefficient of friction (ranging from 0.39 to 0.46) during the potentiodynamic polarisation test. The coefficient of friction of the plasma carburised HCP-PC sample ranged from 0.28 to 0.43.

4.7.2.3 Effect of plasma carburising

The anodic polarisation curves were plotted in Figure 4.7.8 for comparing the tribocorrosion behaviour of samples before and after plasma carburising treatment. The plasma carburised samples showed more positive corrosion potentials and lower anodic current than the heat-treated samples. Obviously, the tribocorrosion properties of the heat treated FCC and HCP Co-Cr samples were effectively improved by the low temperature plasma carburising treatment in terms of increased and corrosion potential and reduced anodic current.

Figure 4.7.9 presents the coefficient of friction curves measured during potentiodynamic tests under sliding (tribocorrosion) for samples before and after plasma carburising treatment. It can be seen that the FCC-PC sample showed higher coefficient of friction than the FCC sample. When the testing time was less than 1600 s, the HCP samples possessed higher coefficient of friction. When the testing time exceeded 1600 s, the coefficient of friction of the HCP-PC sample dramatically increased and was higher than that of the HCP sample.

4.7.2.4 Comparison between corrosion and tribocorrosion conditions

Figure 4.7.10 showed the samples under rotating without load (corrosion) and rotating under load (tribocorrosion) conditions. Under sliding (tribocorrosion) condition, all samples exhibited different potentiodynamic behaviour in terms of corrosion potential and anodic current compared to those found rotation without load (corrosion). It was observed that the corrosion potential cathodically shifted for all samples due to sliding motion. An increase of nearly two orders of magnitude in anodic current is observed for all samples due to sliding. Such a negative shift of the corrosion potential and an increase of anodic current are mainly attributed to the removal or damage of passive films by sliding motion and activation of materials inside the wear track in a passive system.

4.7.3 Effect of potential on electrochemical behaviour during potentiostatic sliding wear test

After potentiodynamic sliding wear tests, one cathodic potential (-800 mV (SCE)), open circuit potential and three anodic potentials (-250, 0 and 400 mV (SCE)) were selected to be applied on samples during potentiostatic sliding wear test.

4.7.3.1 Heat-treated samples

During the sliding in the cathodic region (-800 mV (SCE)), the currents of the AR and heat-treated samples are negative, revealing that no electrochemical corrosion occurred at a cathodic potential of -800 mV (SCE) and the material loss is totally attributed to mechanical wear, which is important for separating mechanical wear from chemical wear.

Under open circuit condition, OCP were continuously recorded by the potentiostat and the results of the AR and heat-treated samples were plotted in Figure 4.7.11. It can be seen that before loading, the open circuit potentials for the AR sample increased up to -152 mV due to the formation of a passive film on the surface exposed to electrolyte. At the commencement of loading, open circuit potentials for the AR sample decreased sharply to a more negative potential. This is mainly due to initial oxide layer break down by sliding motion, leading to the exposure of fresh material or activation of materials inside wear track.

The heat-treated samples responded the same to loading. During the one-hour sliding (sample rotating under load) period, the OCP of the AR sample kept constantly around -510 mV (SCE). The FCC sample exhibited similar OCP as the AR sample, but slightly larger vibration than the AR sample. However, the HCP sample showed increasing OCP with sliding time and 25 mV more positive OCP than the AR and FCC samples.

The OCP value should depend on the ratio of active-to-passive area. The longer sliding goes, the more area is active, the more negative OCP is. However, for the AR and heat-treated samples, no significant drop of open circuit potential can be observed with increasing sliding time and the expansion of wear track area, indicating a stable ratio of active-to-passive area for these three types of samples and a good repassibility of materials inside the wear track during each sliding cycle. After sliding, the OCP of the AR and heat-treated increased dramatically to a lower potential than those before sliding.

The current of the AR and heat-treated samples during potentiostatic sliding tests are plotted in Figure 4.7.12. Four main observations can be made from Figure 4.7.12. Firstly, at all anodic potentials (-250, 0 and 400 mV (SCE)), the current of the AR and heat-treated samples increased greatly in the presence of sliding revealing the effect of wear on corrosion behaviour and corrosion accelerated by wear.

Secondly, the effect of heat treatment on the corrosion current is potential dependent. At -250 mV (SCE), the FCC sample showed higher current than the AR sample and the HCP sample showed similar current but larger fluctuation than the AR sample during sliding. At 0 mV (SCE), the trend changed to opposite. At 400 mV (SCE), both the FCC and HCP samples exhibited higher current but smaller fluctuations than the AR sample.

Thirdly, the average currents during sliding period increased as a function of applied potential for all sample as shown in Table 4.7.1. The last observation is the dramatic fluctuations of current of the AR and heat-treated samples, which are related to the breakdown and repassivation of passive film after a certain number of cycles of sliding.

4.7.3.2 Plasma carburised samples

It can be seen from Table 4.7.1 that the average currents of all plasma carburised samples are negative at cathodic potential (-800 mV (SCE)), indicating no occurrence of electrochemical corrosion.

The OCP curves of the AR and plasma carburised samples are shown in Figure 4.7.13. Under open circuit condition, the plasma carburised samples possessed constantly higher OCP than the AR samples. This indicated that the low temperature plasma carburising treatment improved the corrosion behaviour of Co-Cr alloy in terms of nobler OCP. The OCP of the HCP-PC sample is higher than that of the FCC-PC sample. No significant drop of OCP with sliding time can be observed for the AR and HCP-PC sample, revealing good repassibility of materials inside the wear track during each sliding cycle. For the FCC-PC sample, the OCP slight decreased with sliding time and enlargement of wear track.

As shown in Figure 4.7.14, at anodic potentials, the current of all the plasma carburised samples also increased greatly in the presence of sliding. At all anodic potentials, the currents of the plasma carburised samples are constantly lower and more stable than that of the AR sample during sliding period. In the group of the plasma carburised samples, the current of the FCC-PC sample is higher at -250 mV (SCE) and lower at 400 mV (SCE) compared to that of the HCP-PC sample over the sliding duration, and both the FCC-PC and HCP-PC samples showed similar current at 0mV (SCE) as shown in Figure 4.7.14. This indicates that S-phase formed on FCC-PC sample exhibits worse corrosion resistance at -250 mV (SCE), comparable corrosion resistance at 0 mV (SCE) and better corrosion resistance at 400 mV (SCE) than Co_3C surface layer formed on the HCP-PC sample. The average currents during sliding period increased with applied potential for the plasma carburised samples as listed in Table 4.7.1.

4.7.3.3 Comparison between heat-treated and plasma carburised samples

The OCP of samples before and after plasma carburising treatments during sliding tests are compared in Figure 4.7.15. It can be seen that the FCC-PC sample exhibited constantly 65 mV more positive OCP than the FCC sample, and the HCP-PC sample showed nearly 100 mV more positive OCP than uncarburised HCP sample. Clearly, the tribocorrosion behaviour of Co-Cr alloy was improved in terms of more positive OCP.

The corrosion current of the samples before and after plasma carburising treatments is shown in Figures 4.7.16 and 17. The current of carburised FCC-PC and HCP-PC samples is more stable and lower over the whole sliding period at anodic potentials compared to uncarburised FCC and HCP samples. This indicates that the tribocorrosion behaviour of Co–Cr samples with either nearly full FCC structure or HCP structure has been improved in terms of lower anodic current by the low temperature plasma carburising treatment under sliding (tribocorrosion) condition. This could be attributed partially to the improved corrosion resistance as evidenced in Figure 4.7.3 and partially to the strong mechanical support to surface oxide film from underneath hard S-phase layer for the FCC-PC sample and Co_3C layer for the HCP-PC sample.

4.7.4 Effect of potential on wear performance during potentiostatic sliding wear test

The typical cross-section profiles of wear tracks of all samples produced at -800, OCP, -250, 0 and 400mV (SCE) are shown in Figures 4.7.18-4.7.20, from which the total wear volume (V_T) was calculated. The total wear volume resulting from both corrosion and wear is plotted

in Figure 4.7.21 and listed in Table 4.7.1. The average current and the average coefficient of friction (COF) obtained in sliding wear tests under different potentials are also summarised in Table 4.7.1. The contribution of corrosion and wear to total volume will be discussed in the next chapter.

4.7.4.1 Heat-treated samples

It can be seen from Figure 4.7.21 that the material loss of the AR and heat-treated sample increased with increasing applied potential. Compared to the AR sample, the FCC sample showed slightly higher or equal material loss at potentials lower than 0 mV (SCE), but lower material loss when potential reached 0 mV (SCE). On the contrary, the HCP sample exhibited lower material loss when potential was lower than 0 mV (SCE), but greater material loss at 0 and 400 mV (SCE). This will be discussion in the next chapter from the mechanical wear and chemical wear points of view.

Figure 4.7.22 depicts the coefficient of friction of the AR and heat-treated samples as a function of applied potential. No significant effects of applied potentials on coefficient of friction are observed for these three samples. The AR and heat-treated samples all experienced the highest coefficient of friction under open circuit condition. This may be related to the lubrication ability of corrosion products forming on the surface.

In order to study the mechanisms involved, the morphology of wear tracks formed in all samples during sliding at cathodic, OC and anodic potentials was examined by SEM. The

counterpart balls were also observed using optical microscopy. The typical SEM and optical micrographs are shown in Figures 4.7.23, 24 and 25 for the AR, FCC and HCP samples, respectively.

For the AR sample, the observations have revealed that the wear track morphology produced at cathodic potential (-800 mV (SCE)) and at OCP is similar. As shown in Figure 4.7.23a, uneven deep and broad abrasion grooves are found in wear tracks produced at OCP, which is in agreement with the very rough cross-section profiles of the wear track as shown in Figure 4.7.18a. This is mainly because no oxide film or film without enough thickness was formed on the contact area between the alumina ball and the AR sample surface. At cathodic potential no oxide film would form due to the negative current; at OCP where the total current from the total sample surface is zero, the current from the rest of surface not subjected to sliding is negative, thus current derived from wear track is positive and a new passive film begins to form in the wear track. Without thick enough protective surface oxide film, direct metal-to-alumina contact and adhesive wear may have occurred since it is known that α -FCC Co is the dominating phase of the AR sample and FCC structured Co-Cr material is prone to adhere to alumina sliders. The transferred materials on the balls as shown in Figure 4.7.23c were work-hardened by the repeat sliding motion, which caused the deep and rough grooves observed in Figure 4.7.23a and 4.7.18a and severe material loss.

Parallel fine grooves can be found in wear tracks produced at anodic potentials and the typical morphology of wear track can be seen from Figure 4.7.23b that they are much smoother than

those produced at cathodic and OCP potentials. This is mainly because at anodic potentials, oxide films are thick enough to work as protective films at the real contact area to prevent the direct contact between Co-Cr and alumina, thus resulting in much reduced adhesion and material transfer. This is supported by the fact that less Co-Cr material was transferred onto the alumina counterpart ball when sliding at anodic potentials (Figure 4.7.23d) than sliding at cathodic or OCP (Figure 4.7.23c).

The FCC samples exhibited similar wear track and counterpart ball morphology as the AR samples at all potentials. The typical wear track and ball morphologies at OCP and 0 mV (SCE) are shown in Figure 4.7.24. It indicated that the FCC samples suffered from the same wear mechanisms as the AR samples because the dominating phase of the FCC sample is also α -FCC Co phase.

For HCP samples, deep abrasion grooves are also found in wear tracks produced at cathodic potential and OCP as shown in Figure 4.7.25a, which is in line with the rough profiles of the wear tracks in Figure 4.7.20a. The typical observations on counterpart balls tested at cathodic potential and OCP in Figure 4.7.25c suggested that adhesive wear occurred when no stable and thick oxide films formed, although ϵ -HCP Co and carbide phase are harder than α -FCC Co phase. The transferred hard ϵ -HCP Co material on the balls resulted in the deep and rough grooves found in Figure 4.7.20a and 4.7.25a. At anodic potentials, the oxide films acted as protective films between the sample surface (ϵ -HCP Co and carbide phase) and alumina balls, resulting in much smoother wear track as shown in Figure 4.7.20b and 4.7.25b.

4.7.4.2 Plasma carburised samples

It can be seen from Figure 4.7.21 that the material loss of plasma carburised samples also increased as a function of applied potential. Compared to the AR samples, the carburised FCC-PC and HCP-PC samples experienced much lower material loss at all potentials except at OCP which is much more positive than that of the AR sample.

In the group of plasma carburised samples, the HCP-PC samples outperformed the FCC-PC samples and showed much lower total wear volume at all potentials except 400 mV (SCE). This will be discussed in the discussion chapter based on the anodic current, the contribution of chemical wear to total wear volume and the lubrication ability of corrosion products.

The coefficient of friction of the AR and plasma carburised samples is plotted in Figure 4.7.26. No special trends can be observed for the plasma carburised samples. The coefficient of friction of the FCC-PC samples changed from 0.33 to 0.39. The coefficient of friction of the HCP-PC samples varied from 0.25 to 0.37 and the HCP-PC sample had a relative low coefficient of friction at -250mV (SCE) and 0mV (SCE). Compared to the AR sample, the FCC-PC sample possessed a similar or higher coefficient of friction at all potentials. However, the HCP-PC sample showed a lower coefficient of friction than the AR sample at all potentials except 400 mV (SCE). It is also interesting to find that the HCP-PC sample had a lower coefficient of friction than the AR and FCC-PC samples at -250 mV (SCE) and 0 mV (SCE). The small total wear volume of HCP-PC sample at -250 mV (SCE) and 0 mV (SCE)

as shown in Figure 4.7.21 may be related to the low coefficient of friction.

The SEM images of typical wear track morphologies and optical micrographs of typical ball morphologies of the plasma carburised samples are shown in the Figures 4.7.27-28.

For the FCC-PC samples, the wear tracks produced at cathodic and open circuit potentials are also very rough with deep marks (Figure 4.7.19a and Figure 4.7.27a). This is in line with the observed transferred Co-Cr on the alumina ball shown in Figure 4.7.27c. This implies that although the FCC structured Co-Cr materials can be effectively hardened by carburising, adhesive wear still occurred when sliding at cathodic potential and OCP without the formation of thick and stable oxide films.

On the other hand, after sliding against an alumina ball at anodic potentials the wear surface is relatively smooth with some fine abrasion marks (Figure 4.7.27b). This is supported by the fact that the very limited transferred Co-Cr could be found on the alumina ball slider (Figure 4.7.27d) after sliding against FCC-PC surfaces at anodic potentials. This demonstrates that when sliding at anodic potentials, relatively thick and stable surface oxide films can be formed due to passivation. When supported by the underneath strong S-phase layer, this oxide film could withstand the mechanical loading and tribological action; in addition, potential damage of surface oxide films could be healed by repassivation at anodic potentials.

For the HCP-PC sample, the wear tracks tested at cathodic potential, OCP and -250mV (SCE)

are very similar. Figure 4.7.28 shows the typical morphology of wear tracks produced at these three potentials with uneven, deep and broad resulting from the material transferred onto the balls as evidenced from the observations of counterpart balls in Figure 4.7.28c. The wear tracks produced at 0 mV (SCE) and 400 mV (SCE) are smoother compared to those produced at lower potentials mainly due to the formation of oxide passive films.

4.7.4.3 Comparison between heat-treated and plasma carburised samples

It can be seen from Figure 4.7.21 that at cathodic potential, the total wear volume was reduced by 64% due to the formation of S-phase on FCC structured Co-Cr substrate and 57% due to the formation of Co_3C on HCP structured Co-Cr substrate. At -250mV (SCE), 0mV (SCE) and 400mV (SCE), the total volume was reduced by 62%, 59% and 58% respectively for FCC structure Co-Cr substrate. For HCP structure Co-Cr substrate, the total volume was reduced by 88%, 72% and 62% respectively at -250mV (SCE), 0mV (SCE) and 400mV (SCE). The total wear volume of Co-Cr samples was reduced by low temperature plasma carburising treatments at all potentials except OCP.

Figure 4.7.29 depicts the coefficient of friction of samples before and after plasma carburising treatment as a function of applied potential. It can be seen that the FCC-PC sample showed a relative high coefficient of friction at the anodic potentials compared to the uncarburised FCC sample, while the HCP-PC sample revealed a relative low coefficient of friction at -250mV (SCE) and 0mV (SCE) and a high coefficient of friction at 400mV (SCE) compared to the uncarburised HCP sample. This may be related to the lubrication ability of corrosion products

forming on the surface.

CHAPTER 5 DISCUSSION

5.1 Introduction

As reviewed in Chapter 2 (Section 2.6.3), Habibi has explored low temperature plasma carburising (LTPC) of medical grade Co-Cr alloy dominated by α -FCC and reported some preliminary mechanical, wear and corrosion properties of the treated material. His work also revealed that S-phase could not be successfully produced in ϵ -HCP phase dominated Co-Cr alloys but the mechanism was not clear.

As has been discussed in Section 2.2.1 that the transformation from high-temperature α -FCC phase to low-temperature ϵ -HCP phase is so sluggish that all commercially available medical-grade Co-Cr alloys contain, more or less residual α -FCC phase depending on their thermo-mechanical processing history. Some initial application of the LTPC to medical grade Co-Cr alloys has also revealed varying degrees of success to form desirable S-phase layers on the LTPC treated materials. Therefore, it is hypothesized based on the above observations that the response of medical grade Co-Cr alloys could be related to their phase constituents in terms of the ratio of α -FCC to ϵ -HCP phases. However, no other work has been conducted to investigate the response of Co-Cr alloys with different amounts of ϵ -HCP phase (which always presents in all biomedical grade Co-Cr alloys to LTPC) and the mechanisms involved, which formed the theme of this study.

In addition, no investigation has been carried out to systematically study the tribocorrosion

behaviour of both originally FCC and HCP structured Co-Cr alloys after plasma carburising, which is the most important properties determining the life-span of metallic hip joint prosthesis under biophysical *in-vivo* conditions. In the present thesis, optimized plasma carburising treatment has been applied on a medical grade Co-Cr alloy with different FCC/HCP ratios produced by designing a series of heat treatments and their tribocorrosion behavior has been investigated.

As demonstrated in the last chapter, the low-temperature plasma carburising has facilitated the formation of tribologically useful surface S-phase and Co_3C layers on the Co-28Cr-6Mo alloy with varying amount of ϵ -HCP phase. The S-phase layer formed on the α -FCC structured substrate and the Co_3C layer formed on the ϵ -HCP structured substrate have increased hardness, wear, corrosion and tribocorrosion properties as compared to the respective uncarburised substrate.

Most of the results have been interpreted and discussed in the last chapter and in this chapter, advance scientific understanding of some selected scientifically interesting phenomenon and/or technologically important results are discussed in detail. To this end, Chapter 5 begins with the phase transformation during the LTPC treatment of Co-28Cr-6Mo alloy, followed by the dry tribological behaviour of the treated samples and ends with their tribocorrosion properties.

5.2 Phase transformation during LTPC treatment

It has been found in the study that during low temperature plasma carburising treatment of the Co-28Cr-6Mo alloy S-phase can be formed only on the original α -FCC phase whilst a Co_3C layer forms on the ϵ -HCP phase. This is, to some extent, similar to the phenomenon observed in low-temperature plasma nitrided duplex stainless steel [147]. This is mainly related to the diffusion coefficient of alloying elements, the amount of Cr, solid solubility of C in Cobalt, thermodynamic and kinetic factors and the crystal structure of substrate and surface layer. The role of all these factors will be discussed in this section in particular the formation of Co_3C layer during the LTPC of ϵ -HCP dominated Co-28Cr-6Mo alloy samples.

5.2.1 FCC Structured Co-Cr Substrate

The experimental results reported in Chapter 4 have clearly shown that a carbon supersaturated metastable S-phase layer can be formed on the FCC structured Co-Cr alloy during the low temperature plasma carburising treatment, which is supported by the work by Li, Chen and Luo [100, 101]

The phase transformation from the FCC structured Co-Cr alloy to the carbon supersaturated S-phase during low temperature plasma carburising can be explained by the theory of paraequilibrium diffusion reactions. The term paraequilibrium generally stands for a metastable equilibrium occurring under conditions where the interstitial solutes are effectively mobile to redistribute while the substitutional solutes are less mobile to be stay in place [146].

In this study, the diffusion coefficient of Cr is $9.5 \times 10^{-22} \text{ m}^2/\text{s}$ (1273-1643K) while the diffusion coefficient of C is $2.25 \times 10^{-14} \text{ m}^2/\text{s}$ (723-1073K) [101]. The dramatic difference in diffusion coefficient between substitutional Cr and interstitial C solutes enables the interstitial C atoms to diffuse over a relatively large distance in the FCC structured Co-Cr alloy whereas the substitutional Cr atoms cannot at a relatively low temperature of 450°C for a short treatment time of 10 h (see Section 3.2.2). Hence, from the thermodynamic point of view, C can establish an equilibrium state while Cr cannot, thus a metastable equilibrium being established.

As discussed in Chapter 2, the solid solubility of carbon in FCC structured Co-Cr alloy is only <1 wt%; however, the highest carbon content in the S-phase surface layer is ~15 wt% (Figure 4.3.4). This can be attributed to the high affinity of Cr to C. Although during low temperature plasma carburising at 450 °C, Cr atom cannot diffuse a long enough distance necessary for the formation of carbides, C atoms can be attracted by the substitutional Cr atoms to the interstitial positions near the substitutional Cr atoms. The formation of this atom pairs or clusters can be described by the term ‘dipion’ [148] , which facilitates the establishment of a high content of carbon in the S-phase surface layer.

5.2.2 HCP structured Co-Cr substrate

The experimental results have shown that a Co_3C dispersed layer formed on the surface of ϵ -HCP structured Co-Cr alloy during the low temperature plasma carburising treatment. The orientation of surface Co_3C plates depends on the grain orientation of the substrate ϵ -HCP

grains as shown in Figure 4.3.9 mainly due to the preferred orientation relationship between them (see Section 4.3). The detailed TEM observation has further revealed that the dispersed Co_3C is thin needle shaped with a thickness of only about 50 nm (Fig. 4.3.16a).

Clearly, the microstructure of the surface layer formed on the ϵ -HCP structured Co-Cr alloy differs greatly from the S-phase formed on the α -FCC structured Co-Cr alloy. An important difference between the diffusion of C into FCC Co and HCP Co is that the solubility of C in FCC Co is less than 1 wt% while the solubility of C in HCP Co is much smaller (nearly zero) according to the phase diagram (Figure 5.2.1) [149].

Thus the introduced C atoms in HCP structured Co-Cr alloy by low-temperature plasma carburising cannot form solid solution but mainly form carbides. In ASTM F1537 Co-28Cr-6Mo alloy, the Cr, Mo and Co elements are all carbide formers. The Cr-C, Mo-C and Co-C binary phase diagrams are characterised by many types of carbides; however, only Co_3C has been identified by TEM (Figure 4.3.16) to be the dominant phase within the plasma carburised surface of originally ϵ -HCP structured Co-Cr alloy.

It is known that Co_3C is a high-pressure phase and hence it is metastable carbide. Therefore, the formation of Co_3C during low-temperature plasma carburising will be discussed in terms of interface chemical reaction and diffusion (which is common in some solid-state diffusion cases [150]) and special microstructure in conjunction with plasma-assisted reaction.

According to the interface chemical reaction and diffusion theory [148], for the formation of Co_3C , the diffusion specie C would react chemically with the ϵ -HCP structured Co phase to form a new kind of carbide first, and then a chemical reaction would take place mainly at the interface between the newly formed carbide and the HCP structured Co substrate. The chemical reaction is carried on by the diffusion of C through the new carbide. The first-forming carbide can be predicted by selecting the phase with the highest positive free energy change (driving force) of formation of individual carbide [145, 151].

The thermodynamics data for possible carbide (Cr_{23}C_6 , Cr_7C_3 , Cr_3C_2 , Mo_2C and Co_2C) formations is well reviewed in literature (Figure 5.2.2) [152] except the data for Co_3C formation. Due to the lack of reliable thermodynamics data for the formation of this metastable Co_3C phase, the free energy change for the formation of Co_3C has been estimated by comparing the formation of Co_2C and Co_3C according to work done by Iskhakov [153].

For chromium carbides, several possible reactions may take place to form carbides during the low temperature plasma carburising treatments of HCP structured Co-Cr alloy:



The free energy change of forming the above carbides can be calculated from the following equations:

$$\Delta G_{Cr_{23}C_6} (J mol^{-1}) = -53666.7 - 12.77T (K) \quad \text{Equation 5.2.4}$$

$$\Delta G_{Cr_7C_3} (J mol^{-1}) = -51803.3 - 11.9T (K) \quad \text{Equation 5.2.5}$$

$$\Delta G_{Cr_3C_2} (J mol^{-1}) = -46430 - 9.7T (K) \quad \text{Equation 5.2.6}$$

For Molybdenum carbides, possible reaction is as follows:



The equation for calculating the free energy change of forming Mo_2C is shown below:

$$\Delta G_{Mo_2C} (J mol^{-1}) = -47900 - 8.8T (K) \quad \text{Equation 5.2.8}$$

For cobalt carbides, two possible reactions may occur in the plasma carburising treatments:



The corresponding equation for calculating free energy change for the formation of Co_2C is as follows:

$$\Delta G_{Co_2C} (J mol^{-1}) = 16527 - 8.7T (K) \quad \text{Equation 5.2.11}$$

The free energy change ($J mol^{-1}$) for all possible carbide formations at 450 °C (723 K) is listed in the following table based on the above equations (4.5.4, 4.5.5, 4.5.6, 4.5.8, 4.5.11).

$\Delta G_{Cr_{23}C_6}$	$-62899.4 J mol^{-1}$
$\Delta G_{Cr_7C_3}$	$-60407.0 J mol^{-1}$
$\Delta G_{Cr_3C_2}$	$-53443.1 J mol^{-1}$
ΔG_{Mo_2C}	$-54262.4 J mol^{-1}$
ΔG_{Co_2C}	$10236.9 J mol^{-1}$

Clearly, the Reaction 4.5.9 exhibited the positive free energy change (driving force) for carbide formation. Thus, Co_2C would be the most likely first-forming phase at interface compared to Cr_{23}C_6 , Cr_7C_3 , Cr_3C_2 and Mo_2C .

The free energy change for forming Co_2C and Co_3C can be estimated based on a metastable Co-C phase diagram on the (G, X) coordinates in Figure 5.2.3 [153]. The blue line AB means the free energy change for Co_3C formation, while the red line CD means the free energy change for Co_2C formation. The AB line is longer than CD line, which reveals that the free energy change for Co_3C formation would be higher than that for Co_2C formation. This is supported by the free energy change data for the formation of Co_2C and Co_3C at 298K: 13933 Jmol^{-1} for Co_2C and 37656 Jmol^{-1} for Co_3C [154]. Clearly, among all these potential carbides, Co_3C has the highest positive free energy change and thus the Co_3C phase is the first-forming carbide during interface chemical reaction.

As reported by Iskhakov et al.,[153] nanostructured metastable phase Co_3C can be formed by pulsed plasma vaporisation mainly due to the plasma-assisted deposition and the nanostructure. Similarly, the DC plasma used in this study can activate and provide high enough energy for carbon diffuse and react with Co to form Co_3C carbide. In addition, the formation of Co_3C carbides would be also facilitated by its extremely thin needle-like structure (Fig. 4.3.16a). Hence, the specific area (S) of the Co_3C is very large. According to the discussion in [153], the surface energy density (γ) of Co_3C in the plasma treated layer obtained by the LTPC would be so high that the contribution of the surface energy $S \times \gamma$ to the

thermodynamic Gibbs potential ΔG was comparable to the formation enthalpy of the metastable carbide $\Delta G \sim S \gamma \geq \Delta H^{\text{carbide_Co(C)}}$.

Another factor should be pointed out here is the preferred orientation relationship between the ϵ -HCP Co phase and the Co_3C phase. As found in previous microstructure characterisation result part, the ϵ -HCP and Co_3C phases maintained a preferred orientation relationship of $[01\bar{1}0]_{\text{HCP}} // [210]_{\text{Co}_3\text{C}}, (0002)_{\text{HCP}} // (\bar{1}22)_{\text{Co}_3\text{C}}$ which would facilitate the nucleation of Co_3C .

5.3 Hardening by LTPC Treatment

As have reported in Section 4.4 of Chapter 4, the surface hardness of both FCC and HCP structured Co-28Cr-6Mo alloy can be significantly improved by the low temperature plasma carburising treatment used in the research. However, the hardening mechanisms involved would be different in view of the nature of the surface layers formed during the low temperature plasma carburising treatment.

5.3.1 Surface hardening of FCC-PC samples

It is known from Section 4.3 that after the low-temperature plasma carburising, a carbon supersaturated S-phase layer without any precipitates was formed the originally α -FCC dominated FCC-PC. The surface hardness significantly increased from 486 to 1270 HV0.025 (Fig. 4.4.2). Therefore, the surface hardening of the FCC-PC sample after the low-temperature plasma carburising should be attributed to the formation of the carbon

supersaturated S-phase solid solution.

The hardening response of the FCC structured Co-28Cr-6Mo alloy (i.e. the sample FCC) to low temperature plasma carburising is similar to that of austenitic stainless steel to plasma carburising. This hardening effect can be attributed to the solid solution hardening effect by the extremely large amount of carbon or supersaturation of carbon (up to 15 wt%) in the FCC cobalt lattice (Figure 4.3.4).

Solid solution strengthening is an effective way to improve the strength of all metals by introducing either substitutional or interstitial elements into the crystal lattice and forming substitutional or interstitial solid solution. The introduced atoms induce the stress fields near substitutional or interstitial atom sites, which interact with those of the dislocations, reduce the mobility of dislocations and thus enhance the strength of metals. For the hardening of the FCC-PC sample, the previous XRD results for plasma carburised FCC structured Co-Cr alloy showed both a downshift in diffraction angle and broadening for the (111) and (200) peaks, which revealed an expansion of the crystal lattice and compressive residual stress. The supersaturated carbon induced lattice defects result in extensive interaction with both edge and screw dislocations and strengthening of surface layer [146].

5.3.2 Surface hardening of HCP-PC samples

As reported in Section 4.3.2, following the low-temperature plasma carburising treatment, a very thin surface layer was formed on the originally ϵ -HCP grains (Figs. 4.3.9 and 4.3.16).

The surface layer consists of very fine Co_3C needles precipitated in the HCP grains with a preferred orientation relationship. As shown in Figure 4.4.2, the surface hardness significantly increased from 604 to 1156 HV0.025.

Therefore, it is reasonable to deduct that for the HCP structured Co-28Cr-6Mo alloy, the surface is hardened by the precipitation of Co_3C layer in the HCP grains i.e. precipitation hardening. This is because the precipitation of very thin plate shaped Co_3C in the HCP matrix will cause strong lattice distortion and stress field in view of their coherent interface between the Co_3C and the HCP matrix. In addition, Co_3C itself is hard and difficult to be cut through by dislocation. Therefore, homogeneous distribution of very thin plate shaped Co_3C in the surface layer will effectively retard or stop the movement of dislocations, thus forming strong precipitation hardening.

5.4 Tribological properties

5.4.1 Coefficient of friction

Friction is the resistance of the relative motion of two contact solid bodies, which leads to the deformation, wear and eventual change of the contact surfaces with energy dissipation.

It can be found from Figure 4.6.1 that the friction coefficient of the as-received AR sample (0.217) is lower than that (0.364-0.375) for all three heat-treated samples (FCC, 40HCP and HCP). This cannot simply explained by the hardness difference between these samples since

the hardness of the AR sample is higher than the FCC but lower than both the HCP and 40HCP samples.

It can be seen from the wear surfaces of these tests samples that the wear track formed on the AR sample is smoother and shallower than that formed in the three heat treated samples (Fig.4.6.2). In addition, the wear track formed in the AR sample is covered a black layer of oxides (Fig. 4.6.4). It is known that the friction of a surface mainly depends on its surface roughness, chemical nature and the counterface. In this study, the counterface used is the same for all the tests. Therefore, the low coefficient of friction of the AR sample could be partially attributed to the smooth wear surface and the ceramic nature of the black oxide tribofilms formed during the dry sliding tests.

For the plasma treated samples, it is clear by comparing Figure 4.6.9 with Figure 4.6.2 that the wear tracks produced on the plasma treated samples are at least as smooth as or even smoother than that formed on the heat treated samples. Hence, the significantly increased coefficient of the heat-treated samples after the low-temperature plasma carburising (Figure 4.6.8) cannot be attributed to the difference in wear surface roughness.

The high CoF for the FCC-PC sample could be attributed to the fact that the supersaturation of carbon in S-phase solid solution can reduce the oxidation processes during dry wear tests as comparing the wear track images of the FCC and FCC-PC samples in Figure 4.6.5a and 4.6.11a, respectively. For the HCP and HCP-PC samples, the former produced much more

wear than the latter (Fig.4.6.14). The large amount of round wear debris could act as small rollers between the articulating surfaces. Hence, low friction is expected due to the change from sliding to localised rolling. However, the HCP-PC produced much less wear debris for localised rolling.

5.4.2 Wear mechanism

As summarised in Figure 4.6.14, the optimal low-temperature plasma carburising treatment can dramatically increase the wear resistance of Co-28Cr-6Mo alloy with different microstructures and phases.

As shown in Figures 4.6.5 to 4.6.7, although black oxide wear debris was observed in the wear tracks of the heat treated FCC, HCP and 40HCP samples, abrasive wear occurred to these samples as evidenced by the parallel abrasion grooves. As discussed in Section 2.4, the abrasive wear (V) of a surface mainly depends on its hardness (H):

$$V = K \frac{F_N}{H} d \quad \text{Equation 2.4.1}$$

Therefore, the significantly improved wear resistance of the plasma carburised samples should be attributed to the greatly increased surface hardness. When the surface hardness is increased, the penetration depth of the asperities from the counterface will be reduced and hence the abrasive wear is reduced. This is evidenced by the very fine grooves and the mild abrasion wear found in the wear surface of the plasma hardened samples (Figures

4.6.11a-4.6.13a).

In addition, the significantly hardened surface can effectively support the oxide film formed during dry sliding wear. This is supported by the black wear debris observed on the wear surface of the plasma hardened samples (Figs 4.6.11b-4.6.13b). Therefore, the wear mechanism changed from severe abrasive and adhesive wear for the heat treated sample to mild oxidation and micro-abrasion wear.

It is noted that both the microhardness and the ratio of H/Er of the S-phase layer formed on the FCC-PC sample are higher than that of the Co_3C precipitated layer formed on the HCP-PC sample. Therefore, better wear resistance would be expected for the former than for the latter. However, the wear volume of the HCP-PC samples is only 40% of that of the FCC-PC sample (Fig. 4.6.14).

This seemingly abnormal result could be explained by taking account of the substrate hardness and the load bearing capacity of these two samples. It is known from Figure 4.6.9 that after the 30 N reciprocating wear tests, the plasma modified surface layer formed on both the FCC-PC and HCP-PC samples were worn through to their substrate. In this case, the contribution of their substrate should be taken into account.

It is worthwhile mentioning that although the surface hardness of S-phase layer formed on the FCC-PC sample is higher than that of Co_3C precipitated layer formed on the HCP-PC sample,

the latter possesses a higher load bearing capacity under loads higher than 100g than the former mainly due to the difference of their substrate hardness. Thus under a relatively high load, the stronger mechanical support from the substrate to surface has contributed to the lower wear volume of the HCP-PC sample as compared to that of the FCC-PC sample.

5.5 tribocorrosion properties

5.5.1 General synergistic effect between wear and corrosion

The tribocorrosion behaviour of a carburised layer on the surface of Co–28Cr-6Mo material has been studied systematically under both potentiodynamic and potentiostatic conditions in the tribocorrosion process. The material loss depends on pure mechanical part (wear), pure chemical part (corrosion) and more importantly the interaction between corrosion and wear resulting in wear-induced corrosion and corrosion-induced wear.

On one hand, corrosion is accelerated by wear. The passive film at the contact area is removed or damaged in a single cycle or a certain amounts of cycles by sliding motion, which increases the ratio of active-to-passive area resulting in the cathodic shift of corrosion potential, increased current and a negative shift of OCP. Material loss from corrosion can be derived from two parts including the loss from the dissolution of bare material reacting with electrolyte and the formation of passive films which may be followed by removal or damaging by sliding motion.

On the other hand, wear is either accelerated or slowed by corrosion. The corrosion products broken down by wear can serve as third body abrasion particles resulting in corrosion-induced wear. At the same time, the corrosion products produced on the surface in wear track can modify the surface tribological behaviour such as coefficient of friction and change the wear mechanism. Oxide film can work as protective film to stop the interaction between two counterparts.

5.5.2 Mechanical wear and chemical wear

It is important to derive tribocorrosion components including the contribution of chemical and mechanical parts to total material loss. Efforts have been made by several investigators [76, 82, 84] to separate wear caused by mechanical part and chemical part. The total wear loss (V_T) can be simply given by the sum of mechanical wear (V_{mech}) and chemical wear (V_{chem}), where V_{mech} includes material loss due to pure mechanical wear without the effect of corrosion and corrosion-induced wear, and V_{chem} includes material loss due to pure corrosion without mechanical wear and wear-induced corrosion.

$$V_T = V_{\text{mech}} + V_{\text{chem}} \quad \text{Equation 2.5.1}$$

The volume loss due to chemical wear can be calculated according to the Faraday's law

$$V_{\text{chem}} = ItM/(nF\rho) \quad \text{Equation 2.5.2}$$

where I is the current over the sliding period, t is sliding time, M is the atomic mass of the material, n is the valence of dissolution and passivation, F is the Faraday's constant (96,458C/mol) and ρ is the density of alloy. For Co–Cr alloys the valence is corresponding to

2 for the dissolution of Co and Cr in the active region and the valence is corresponding to 3 for the passivation of Co and Cr in the passive region. Under the dynamic condition in tribocorrosion test, the exact valence value is unknown. A valence value (n) of 2.5 is selected to represent the periodic activation and repassivation state. The results of V_{chem} and V_{mech} are listed in Table 4.7.1 and depicted in Figure 5.5.1-5.5.3.

AR sample

For the AR samples, it can be seen from Figure 5.5.1 that the V_{mech} and V_{chem} increase with increasing the applied potential and V_{mech} is the predominating part, indicating that wear is slightly accelerated by corrosion. However, the increase of V_{chem} is much slower than that of V_{mech} , indicating that the formation of oxide films cannot protect the material from wear sufficiently.

FCC and FCC-PC samples

Figure 5.5.2 shows that the V_{mech} , V_{chem} and the ratio of V_{chem} -to- V_{mech} increase with increasing the applied potential and V_{mech} is the predominating part for both FCC and FCC-PC samples. This indicates that wear is slightly accelerated by corrosion. However, the increase of V_{mech} is much slower than that of V_{chem} of both FCC and FCC-PC samples, indicating that the formation of oxide films protects material from wear to some extent. At 400mV (SCE), V_{chem} raises up to the value of V_{mech} for the FCC and FCC-PC samples.

It has been shown that the compared with the FCC sample, the FCC-PC sample exhibits the lower value not only in total wear volume but also in individual V_{chem} part and V_{mech} part at all potentials except OCP which is much more positive (-433.71 mV(SCE)) than that (-523.66 mV(SCE)) of the FCC sample. It is responsible for the improved hardness, good corrosion resistance as shown in potentiodynamic tests due to the formation of superhard S-phase layer by low temperature plasma carburising and good repassivation rate. The improved hardness reduces the real contact area. At the same time, hard material can give passive film a strong support, so that passive films will be broken down easily and prevent the interaction between the ball and the sample surface. For example, the pure mechanical wear at -800 mV for the FCC sample is three-times of that for FCC-PC sample as shown in Table 4.7.1.

HCP and HCP-PC samples

As has been reported in Figure 5.5.3, the V_{mech} and V_{chem} of both HCP and HCP-PC increase with applied potential. The ratio of V_{chem} -to- V_{mech} of the HCP sample increased with increasing applied potential except at 400 mV (SCE). The V_{mech} of both HCP and HCP-PC samples is the predominating part as for both the FCC and FCC-PC samples, revealing that corrosion accelerates wear process. For the HCP sample, the V_{mech} increase much slower than that of V_{chem} , indicating that the formation of oxide films protects material from wear. At 400mV (SCE), V_{chem} increases to the value of V_{mech} for the HCP sample.

Clearly, the HCP-PC sample exhibits a lower value not only in total volume but also in individual V_{chem} part and V_{mech} part at all anodic potentials than the HCP sample. This could

be attributed to the improved hardness and good corrosion resistance measured by potentiodynamic tests due to the formation of hard and corrosion resistant Co_3C dominated layer by low temperature plasma carburising. The surface hard Co_3C layer can provide the thin passive films formed under anodic potentials a strong mechanical support, thus inhibiting the broke-down of passive films. This can effectively prevent both the mechanical and chemical interaction between the counterpart ball and the sample surface in Ringer's solution.

The pure mechanical wear at -800 mV from wear track for the HCP sample is similar to that for the HCP-PC sample as shown in Table 4.7.1. The pure mechanical wear at OCP from wear track for the HCP sample is even lower than that for the HCP-PC samples although the HCP-PC samples possess a much higher hardness than the HCP samples. This is mainly because of the difference in wettability and resultant lubrication conditions between HCP Co and Co_3C phase when no thick enough passive films can form at OCP.

5.5.4 Tribocorrosion mechanism

AR samples

The observations on the wear tracks of the AR samples (Fig. 4.7.23) tested under OCP and 400 mV(SCE) showed two typical tribocorrosion mechanisms of the AR samples. At cathodic and OC potentials, the material was transferred to the ball and the process is dominated by severe adhesive wear. At anodic potentials, the adhesive wear is reduced due to the formation of thin passive film between the contact surfaces. Wide and parallel grooves can be seen in the wear track with less material transfer from the sample surface to the counterpart ball,

which suggests the abrasive wear mechanism. This is in good agreement with the calculated V_{mech} results as shown in Figure 5.5.1

FCC and FCC-PC samples

At cathodic and OC potentials, no or less effect of chemical part on mechanical part should be made by the tribocorrosion process. The effect of the formation of S-phase on total wear loss is more significant at anodic potentials. At cathodic and OC potentials, FCC and FCC-PC samples exhibited different tribocorrosion mechanisms.

When the FCC samples are tested at anodic potentials, although surface oxide films will form due to passivation, without mechanical support from the substrate, such oxide film could be easily damaged and partially removed. Therefore, fine oxide fragments could serve as abrasives to cause abrasive wear and locally transferred and work-hardened materials could also contribute to the abrasive wear.

For plasma carburised FCC-PC samples, the hard S-phase layer can effectively support surface oxide films formed during sliding at anodic potentials. Hence, the tribopair will change from metal-to-ceramic to ceramic-to-ceramic and micro-polishing mechanism predominates. However, the reason why the FCC and FCC-PC samples showed similar tribocorrosion resistance at OCP is not very clear and further study may be needed.

HCP and HCP-PC samples

At cathodic and OC potentials, the materials of both HCP and HCP-PC samples significantly were transferred to the counterpart ball without the protection of passive films. The much harder HCP-PC samples even show higher material volume loss which may be due to the poorer wettability or worse lubrication conditions than the softer HCP samples. At anodic potentials, thick enough passive film can modify the surface friction condition and also change the contact mode. In this case, the very hard Co_3C layer can give the surface passive films much stronger mechanical support than HCP Co phase, thus lead to the much reduced total material loss.

Comparison between FCC-PC and HCP-PC samples

The total wear volume, V_{mech} and V_{chem} of the HCP-PC samples are constantly lower than those of the FCC-PC samples under all potentials except the total wear volume and V_{chem} under 400 mV(SCE). This implies that the chemical wear part of the HCP-PC sample is accelerated under 400 mV(SCE) which should be responsible for the higher material loss than the FCC-PC sample.

5.5.5 Potential impact and limitation

Based on the wear volume of all samples under different potentials, wear factors can be calculated by dividing wear volume by time and load. The results of wear factors are listed in Table 5.5.1. This parameter can be used as an indication for estimated service life of as-received, heat-treated samples, S-phase engineered (FCC-PC sample) and Co_3C layer

enhanced (HCP-PC sample) ASTM 1537 Co-28Cr-6Mo alloy under different potentials in Ringer's solution. Due to the magnetic properties of Co_3C phase, the plasma carburised HCP-PC sample cannot be used for implant material. However, the tribocorrosion characterisation reveals that it is suitable for tribocorrosion working conditions.

Clearly, this investigation has revealed, for the first time, that except for under OCP conditions, the S-phase engineered Co–Cr surface possesses a significantly improved corrosion wear resistance than the uncarburised FCC structured Co–Cr alloy. According to the research by Velten et al., the range of body potential ranges from 363 to 463mV vs. SCE, therefore it is estimated according the current research results shown in above Table 5.5.1 that the life of S-phase engineered Co–Cr surface could be at least twice that of the uncarburised Co–Cr surface.

However, the electrolyte used in this study is Ringer's solution, which can only simulate the inorganic salts part of body fluids without considering the complicated effect of such organic species as proteins and amino acid. Some researchers [79] have conducted tribocorrosion investigations using bovine calf serum containing proteins and found that proteins can assist in the formation of protective tribolayer against corrosion. In addition, the unidirectional sliding mode used in this study is much simpler than the contact mode in actual triaxial hip or knee joint movement. Therefore, in further study, it is desirable to conduct in situ tribocorrosion tests in more relevant biological environments (such as Dulbecco's Modified Eagle's Medium) using hip or knee simulators if possible.

The tribopair used in this investigation is metal-to-ceramic rather than the popular tribopair used in metal-to-metal hip joints. This is mainly to make sure that only the disc sample is subjected to electrochemical actions without the influence of the counterpart ball, which is a simplified in vitro study method widely used for tribocorrosion electrochemical measurement. Metal-on-metal contact can result in more severe adhesive wear than metal-on-ceramic pair, and what is more abrasive wear of Co–Cr bearing surface by bone cement and loose carbides have also been observed. The S-phase engineered superhard Co–Cr–Mo surfaces (more than 1200HV0.025 at the surface) could effectively reduce adhesive wear for metal-to-metal hip joints and abrasive wear of Co–Cr bearing surfaces of metal-to-polymer hip or knee joints with bone cement fixation.

CHAPTER 6 CONCLUSIONS

A systematic investigation has been conducted to study the response of a medical grade ASTM F1537 Co-28Cr-6Mo alloy with different phase constituents to low-temperature plasma carburizing. Based on the results and discussion presented in the last two chapters, the following conclusions can be drawn:

Part I - Microstructure of as-received and heat treated material

1. The microstructure of the as-received Co-28Cr-6Mo alloy consists of fine (approximately 8 μm) α -FCC and ϵ -HCP grains together with carbides (0.5-4.0 μm) mostly distributed along the grain boundaries.
2. After solution treatment at 1250 °C for 1.5 h followed by air cooling, the microstructure of the Co-28Cr-6Mo alloy is dominated by the α -FCC phase (>95%).
3. Further aging treatment of the solution treated material at 850 °C for 15 followed by water quenching can produce a ϵ -HCP phase dominated (>97%) microstructure (coded as 'HCP'); when the aging time is reduced to 4 h, a mixed microstructure with about 40% ϵ -HCP phase and 60% α -FCC phase can be produced.

Part II - Microstructure of the plasma carburised samples

4. A 7 μm -thick carbon supersaturated S-phase layer without precipitates can be generated

on the nearly fully FCC structured Co-28Cr-6Mo alloy (coded as 'HCP-PC') by low-temperature plasma carburising treatment at 450°C for 10 h with a gas mixture of 98.5 vol% H₂ and 1.5 vol% CH₄.

5. A 2 µm-thick surface layer with Co₃C dispersed in the HCP structured matrix can be generated on the nearly fully HCP structured Co-28Cr-6Mo alloy (coded as 'HCP-PC') by the low-temperature plasma carburising treatment. The Co₃C phase shows a fine needle structure and grows from surface towards the core.
6. A S-phase layer and a Co₃C dispersed layer can be generated by the low-temperature plasma carburising treatment on the originally FCC and HCP structured grains respectively of the 40% HCP structured Co-28Cr-6Mo alloy (coded as '40HCP-PC').

Part III - Mechanical properties of the plasma carburised samples

7. The surface hardness of Co-28Cr-6Mo alloy with different FCC/HCP ratios has been improved by the low-temperature plasma carburising treatment. The surface hardness of the FCC-PC (S-phase dominating) sample is 1270 HV_{0.025}; the surface hardness of the HCP-PC (Co₃C dominating) and 40HCP-PC samples is 1156 and 1162 HV_{0.025}, respectively.
8. The FCC-PC and HCP-PC samples show very similar nanohardness measured by a nanohardness tester, indicating that the Co₃C dominated layer formed on the HCP

structured Co-28Cr-6Mo alloy by the low-temperature plasma carburising is as hard as the S-phase case produced on the FCC structured Co-28Cr-6Mo alloy.

9. The FCC-PC sample has a higher load bearing capacity than the HCP-PC and 40HCP-PC samples when loaded under a relatively low load of 25 and 50 g mainly due to its relatively thick hardened case. However, when loaded at 100 g or above, the order is changed and the HCP-PC sample outperforms the 40HCP-PC and FCC-PC samples mainly due to their hard substrate.
10. The the low-temperature plasma carburising treatment has resulted in an increase in hardness to reduced modulus ratio for both originally α -FCC dominating and ϵ -HCP dominating Co-Cr samples with the former being more significant than the latter.

Part IV - Corrosion and wear properties of the plasma carburised samples

11. After the low-temperature plasma carburising, the corrosion potential tested in Ringer's solution is -102.3, -185.3 and -181.4 mV(SCE) respectively of the originally α -FCC structured (FCC-PC), partially ϵ -HCP structured (40HCP-PC) and fully (HCP-PC) ϵ -HCP structured samples.
12. Among all the three plasma treated samples, the FCC-PC shows the best corrosion behaviour in Ringer's solution in terms of the highest corrosion potential and the lowest corrosion current density mainly due to the formation of the S-phase layer.

13. The low-temperature plasma carburising treatment can significantly improve the wear resistance of the Co-28Cr-6Mo alloy with different FCC/HCP ratios mainly due to increased hardness. The HCP-PC sample has exhibited the lowest wear volume among all the plasma carburised samples.

Part V -Tribocorrosion properties of the plasma carburised Co-28Cr-6Mo alloy

14. The low-temperature plasma carburising treatment has resulted in an anodic shift in corrosion potential and a decrease in anodic current under potnetiodynamic for Co-28Cr-6Mo alloy with different FCC/HCP ratios. The HCP-PC sample shows more positive corrosion potential than the FCC-PC sample under tribocorrosion condition.
15. The current of the plasma carburised FCC-PC and HCP-PC samples is more stable and lower over the whole sliding period at anodic potentials compared to uncarburised FCC and HCP samples. The corrosion resistance of Co-28Cr-6Mo alloy under tribocorrosion condition has been improved by the low-temperature plasma carburising treatment.
16. The low-temperature plasma carburising treatment has led to a reduction in total wear volume at all potentials except OCP. The HCP-PC samples show a much lower total wear volume than the FCC-PC samples at all potentials except 400 mV (SCE).

CHAPTER 7 FUTURE WORK

This work has shown the different responses of Co-28Cr-6Mo alloy with different FCC/HCP ratios to low-temperature plasma carburising treatment. The results have demonstrated that the carburised FCC structured Co-28Cr-6Mo alloy could be a desirable material for hip joint prostheses due to its unique combination of improved hardness, corrosion, wear and tribocorrosion resistance. However, the tests were only carried out under laboratory conditions. To fully address the problems associated with metal-on-metal hip joint prostheses and advance our scientific understanding, some future work is briefly outlined below.

1. The laboratory tribocorrosion results have shown that the S-phase modified Co-28Cr-6Mo alloy exhibited the lowest wear volume under 400 mV(SCE) which is the human body potential. Simulation tests of plasma carburised hip joint prostheses should be conducted to demonstrate the technological potential of the new technology.
2. The study on the relationship between the carburising time and layer thickness of Co₃C dispersed layer on HCP structured Co-28Cr-6Mo alloy is suggested to establish the kinetics; STEM study of the Co₃C dispersed layer to advance scientific understanding and the formation mechanisms involved.

REFERENCES

- [1]. B.D. Ratner, A.S. Hoffman, F.J. Schoen, and J.E. Lemons, *Biomaterials Science: An Introduction to Materials in Medicine*. 2004: Elsevier Science.
- [2]. A.J. Smith, P. Dieppe, K. Vernon, M. Porter, and A.W. Blom, *Failure rates of stemmed metal-on-metal hip replacements: analysis of data from the National Joint Registry of England and Wales*. The Lancet. **379**(9822): p. 1199-1204.
- [3]. S. Goodman, P. Aspenberg, Y. Song, G. Knoblich, P. Huie, D. Regula, and L. Lidgren, *Tissue ingrowth and differentiation in the bone-harvest chamber in the presence of cobalt-chromium-alloy and high-density-polyethylene particles*. Journal of Bone and Joint Surgery - Series A, 1995. **77**(7): p. 1025-1035.
- [4]. Y. Abu-Amer, I. Darwech, and J.C. Clohisy, *Aseptic loosening of total joint replacements: mechanisms underlying osteolysis and potential therapies*. Arthritis Research & Therapy, 2007. **9**.
- [5]. K.J. Kim, Y. Kobayashi, and T. Itoh, *Osteolysis model with continuous infusion of polyethylene particles*. Clinical Orthopaedics and Related Research, 1998(352): p. 46-52.
- [6]. M. Schmidt, H. Weber, and R. Schon, *Cobalt chromium molybdenum metal combination for modular hip prostheses*. Clinical Orthopaedics and Related Research, 1996(329): p. S35-S47.
- [7]. I.C. Clarke, V. Good, P. Williams, D. Schroeder, L. Anissian, A. Stark, H. Oonishi, J. Schuldies, and G. Gustafson, *Ultra-low wear rates for rigid-on-rigid bearings in total hip replacements*. Proceedings of the Institution of Mechanical Engineers, Part H: Journal of Engineering in Medicine, 2000. **214**(4): p. 331-347.
- [8]. S.J. MacDonald, R.W. McCalden, D.G. Chess, R.B. Bourne, C.H. Rorabeck, A. Cleland, and F. Leung, *Metal-on-metal versus polyethylene in hip arthroplasty: A randomized clinical trial*. Clinical Orthopaedics and Related Research, 2003(406): p. 282-296.
- [9]. W. Brodner, P. Bitzan, V. Meisinger, A. Kaider, F. Gottsauner-Wolf, and R. Kotz, *Serum cobalt levels after metal-on-metal total hip arthroplasty*. Journal of Bone and Joint Surgery-American Volume, 2003. **85A**(11): p. 2168-2173.
- [10]. N.J. Registry, *National Joint Registry (NJR) for England and Wales 7th annual report 2010*, National Joint Registry: UK.

- [11]. D. Fabi, B. Levine, W. Paprosky, C. Della Valle, S. Sporer, G. Klein, H. Levine, and M. Hartzband, *Metal-on-Metal Total Hip Arthroplasty: Causes and High Incidence of Early Failure*. Orthopedics, 2012. **35**(7): p. e1009-16.
- [12]. A.K. Matthies, J.A. Skinner, H. Osmani, J. Henckel, and A.J. Hart, *Pseudotumors Are Common in Well-positioned Low-wearing Metal-on-Metal Hips*. Clinical Orthopaedics and Related Research, 2012. **470**(7): p. 1895-1906.
- [13]. S. Natu, R.P. Sidaginamale, J. Gandhi, D.J. Langton, and A.V.F. Nargol, *Adverse reactions to metal debris: histopathological features of periprosthetic soft tissue reactions seen in association with failed metal on metal hip arthroplasties*. Journal of Clinical Pathology, 2012. **65**(5): p. 409-418.
- [14]. J.A. Browne, C.D. Bechtold, D.J. Berry, A.D. Hanssen, and D.G. Lewallen, *Failed Metal-on-Metal Hip Arthroplasties: A Spectrum of Clinical Presentations and Operative Findings*. Clinical Orthopaedics and Related Research, 2010. **468**(9): p. 2313-2320.
- [15]. P.F. Doorn, P.A. Campbell, J. Worrall, P.D. Benya, H.A. McKellop, and H.C. Amstutz, *Metal wear particle characterization from metal on metal total hip replacements: Transmission electron microscopy study of periprosthetic tissues and isolated particles*. Journal of Biomedical Materials Research, 1998. **42**(1): p. 103-111.
- [16]. H.G. Willert, G.H. Buchhorn, A. Fayyazi, R. Flury, M. Windler, G. Koster, and C.H. Lohmann, *Metal-on-metal bearings and hypersensitivity in patients with artificial hip joints - A clinical and histomorphological study*. Journal of Bone and Joint Surgery-American Volume, 2005. **87A**(1): p. 28-36.
- [17]. S. Virtanen, I. Milosev, E. Gomez-Barrena, R. Trebse, J. Salo, and Y.T. Kontinen, *Special modes of corrosion under physiological and simulated physiological conditions*. Acta Biomaterialia, 2008. **4**(3): p. 468-476.
- [18]. A. Sargeant and T. Goswami, *Hip implants - Paper VI - Ion concentrations*. Materials & Design, 2007. **28**(1): p. 155-171.
- [19]. K. Merritt and S.A. Brown, *Release of hexavalent chromium from corrosion of stainless-steel and cobalt-chromium alloys*. Journal of Biomedical Materials Research, 1995. **29**(5): p. 627-633.
- [20]. S. Kurosu, H. Matsumoto, and A. Chiba, *Grain refinement of biomedical Co-27Cr-5Mo-0.16N alloy by reverse transformation*. Materials Letters, 2010. **64**(1): p. 49-52.
- [21]. J. Lutz, C. Diaz, J.A. Garcia, C. Blawert, and S. Maendl, *Corrosion behaviour of medical CoCr alloy after nitrogen plasma immersion ion implantation*. Surface &

Coatings Technology, 2011. **205**(8-9): p. 3043-3049.

- [22]. P.J. Andersen, *I.102 - Metals for Use in Medicine*, in *Comprehensive Biomaterials*, D. Editor-in-Chief: Paul, Editor. 2011, Elsevier: Oxford. p. 5-20.
- [23]. P.H. Long, *Medical Devices in Orthopedic Applications*. Toxicologic Pathology, 2008. **36**(1): p. 85-91.
- [24]. S. Atamert and H. Bhadeshia, *Comparison of the microstructures and abrasive wear properties of stellite hardfacing alloys deposited by arc-welding and laser cladding*. Metallurgical Transactions a-Physical Metallurgy and Materials Science, 1989. **20**(6): p. 1037-1054.
- [25]. P. Huang and H.F. Lopez, *Effects of grain size on development of athermal and strain induced epsilon martensite in Co-Cr-Mo implant alloy*. Materials Science and Technology, 1999. **15**(2): p. 157-164.
- [26]. A.J. Saldívar and H.F. López, *Role of aging on the martensitic transformation in a cast cobalt alloy*. Scripta Materialia, 2001. **45**(4): p. 427-433.
- [27]. D.H.E. Persson, S. Jacobson, and S. Hogmark, *Effect of temperature on friction and galling of laser processed Norem 02 and Stellite 21*. Wear, 2003. **255**(1-6): p. 498-503.
- [28]. G.B. Olson and M. Cohen, *General mechanism of martensitic nucleation. I. General concepts and FCC-HCP transformation*. Metallurgical Transactions a-Physical Metallurgy and Materials Science, 1976. **7**(12): p. 1897-1904.
- [29]. H. Kashani, M.S. Laridjani, A. Amadeh, M. Khodagholi, and S. Ahmadzadeh, *The influence of volumetric dilution on the strain induced $\gamma \rightarrow \epsilon$ martensitic transformation in GTAW processed Co-Cr-Mo alloy*. Materials Science and Engineering: A, 2008. **478**(1-2): p. 38-42.
- [30]. C.T. Sims, N.S. Stoloff, and W.C. Hagel, *Superalloys II*. 1987: Wiley.
- [31]. P. Huang and H.F. Lopez, *Athermal epsilon-martensite in a Co-Cr-Mo alloy: grain size effects*. Materials Letters, 1999. **39**(4): p. 249-253.
- [32]. C. Song, H. Park, H. Seong, and H.F. Lopez, *Development of athermal and isothermal epsilon-martensite in atomized Co-Cr-Mo-C implant alloy powders*. Metallurgical and Materials Transactions a-Physical Metallurgy and Materials Science, 2006. **37A**(11): p. 3197-3204.
- [33]. C.B. Song, H.B. Park, H.G. Seong, and H.F. Lopez, *Development of athermal epsilon-martensite in atomized Co-Cr-Mo-C implant alloy powders*. Acta

Biomaterialia, 2006. **2**(6): p. 685-691.

- [34]. A. de J. Saldívar García, A. Maní Medrano, and A. Salinas Rodríguez, *Effect of solution treatments on the FCC/HCP isothermal martensitic transformation in Co-27Cr-5Mo-0.05C aged at 800°C*. Scripta Materialia, 1999. **40**(6): p. 717-722.
- [35]. H.F. Lopez and A.J. Saldivar-Garcia, *Martensitic transformation in a cast Co-Cr-Mo-C alloy*. Metallurgical and Materials Transactions a-Physical Metallurgy and Materials Science, 2008. **39A**(1): p. 8-18.
- [36]. A. Garcia, A.M. Medrano, and A.S. Rodriguez, *Formation of Hcp martensite during the isothermal aging of an Fcc Co-27Cr-5Mo-0.05C orthopedic implant alloy*. Metallurgical and Materials Transactions a-Physical Metallurgy and Materials Science, 1999. **30**(5): p. 1177-1184.
- [37]. K. Rajan, *Phase-transformation in a wrought Co-Cr-Mo-C alloy*. Metallurgical Transactions a-Physical Metallurgy and Materials Science, 1982. **13**(7): p. 1161-1166.
- [38]. *Metals Handbook*. 8th ed. Vol. Vol 8. 1973, Ohio: American Society for Metals.
- [39]. J.C. Crivello, M. Palumbo, T. Abe, and J.M. Joubert, *Ab initio ternary -phase diagram: The Cr–Mo–Re system*. Calphad, 2010. **34**(4): p. 487-494.
- [40]. J.M. Joubert, *Crystal chemistry and Calphad modeling of the σ phase*. Progress in Materials Science, 2008. **53**(3): p. 528-583.
- [41]. S. Kurosu, H. Matsumoto, and A. Chiba, *Isothermal Phase Transformation in Biomedical Co-29Cr-6Mo Alloy without Addition of Carbon or Nitrogen*. Metallurgical and Materials Transactions A, 2010. **41**(10): p. 2613-2625.
- [42]. M. Mori, K. Yamanaka, and A. Chiba, *Phase decomposition in biomedical Co–29Cr–6Mo–0.2N alloy during isothermal heat treatment at 1073 K*. Journal of Alloys and Compounds, (0).
- [43]. L.E. Ramírez, M. Castro, M. Méndez, J. Lacaze, M. Herrera, and G. Lesoult, *Precipitation path of secondary phases during solidification of the Co–25.5%Cr–5.5%Mo–0.26%C alloy*. Scripta Materialia, 2002. **47**(12): p. 811-816.
- [44]. Y. Chen, Y. Li, S. Kurosu, K. Yamanaka, N. Tang, Y. Koizumi, and A. Chiba, *Effects of Sigma Phase and Carbide on the Wear Behavior of CoCrMo Alloys in Hanks' Solution*. Wear, (0).
- [45]. K. Yamanaka, M. Mori, K. Kuramoto, and A. Chiba, *Development of new Co–Cr–W-based biomedical alloys: Effects of microalloying and thermomechanical processing on microstructures and mechanical properties*. Materials & Design, 2014.

55(0): p. 987-998.

- [46]. C.R. Brooks, *Heat Treatment, Structure, and Properties of Nonferrous Alloys*. 1982: American Society for Metals.
- [47]. S.B. Goodman, E. Gómez Barrena, M. Takagi, and Y.T. Kontinen, *Biocompatibility of total joint replacements: A review*. Journal of Biomedical Materials Research Part A, 2009. **90A**(2): p. 603-618.
- [48]. L.E. Toth, *Transition metal carbides and nitrides*. 1971: Academic Press.
- [49]. T. Hayashi, S. Hirono, M. Tomita, and S. Umemura, *Magnetic thin films of cobalt nanocrystals encapsulated in graphite-like carbon*. Nature, 1996. **381**(6585): p. 772-774.
- [50]. R. Bashyam and P. Zelenay, *A class of non-precious metal composite catalysts for fuel cells*. Nature, 2006. **443**(7107): p. 63-66.
- [51]. P. Gao, Y. Wang, S. Yang, Y. Chen, Z. Xue, L. Wang, G. Li, and Y. Sun, *Mechanical alloying preparation of fullerene-like Co₃C nanoparticles with high hydrogen storage ability*. International Journal of Hydrogen Energy, 2012. **37**(22): p. 17126-17130.
- [52]. T.J. Konno and R. Sinclair, *Crystallization of co-sputtered amorphous cobalt carbon alloys: morphology and kinetics of spherulitic growth*. Materials Science and Engineering: A, 1994. **179 – 180, Part 1**(0): p. 297-302.
- [53]. J. Pola, M. Urbanová, D. Pokorná, J. Šubrt, S. Bakardjieva, P. Bezdička, and Z. Bastl, *IR laser-induced formation of amorphous Co–C films with crystalline Co, Co₂C and Co₃C nanograins in a graphitic shell*. Journal of Photochemistry and Photobiology A: Chemistry, 2010. **210**(2–3): p. 153-161.
- [54]. J.R. Davis and A.I.H. Committee, *Nickel, Cobalt, and Their Alloys*. 2000: Asm International.
- [55]. J. Cawley, J.E.P. Metcalf, A.H. Jones, T.J. Band, and D.S. Skupien, *A tribological study of cobalt chromium molybdenum alloys used in metal-on-metal resurfacing hip arthroplasty*. Wear, 2003. **255**(7–12): p. 999-1006.
- [56]. U. Malayoglu, A. Neville, and G. Beamson, *Characterisation of the passive film on HIPed Stellite 6 alloy using X-ray photoelectron spectroscopy*. Materials Science and Engineering a-Structural Materials Properties Microstructure and Processing, 2005. **393**(1-2): p. 91-101.
- [57]. S. Karimi, T. Nickchi, and A.M. Alfantazi, *Long-term corrosion investigation of AISI*

- 316L, Co–28Cr–6Mo, and Ti–6Al–4V alloys in simulated body solutions. Applied Surface Science*, 2012. **258**(16): p. 6087-6096.
- [58]. U. Malayoglu, A. Neville, and H. Lovelock, *Assessing the kinetics and mechanisms of corrosion of cast and HIPed Stellite 6 in aqueous saline environments*. *Corrosion Science*, 2005. **47**(8): p. 1911-1931.
- [59]. R. Venugopalan and L.C. Lucas, *Evaluation of restorative and implant alloys galvanically coupled to titanium*. *Dental Materials*, 1998. **14**(3): p. 165-172.
- [60]. N.M. Taher and A.S. Al Jabab, *Galvanic corrosion behavior of implant suprastructure dental alloys*. *Dental Materials*, 2003. **19**(1): p. 54-59.
- [61]. C. Liang, R. Zheng, N. Huang, and B. Wu, *Electrochemical behaviour of Ti–Ni SMA and Co–Cr alloys in dynamic Tyrode's simulated body fluid*. *Journal of Materials Science: Materials in Medicine*, 2010. **21**(5): p. 1421-1426.
- [62]. M. Metikoš-Huković, Z. Pilić, R. Babić, and D. Omanović, *Influence of alloying elements on the corrosion stability of CoCrMo implant alloy in Hank's solution*. *Acta Biomaterialia*, 2006. **2**(6): p. 693-700.
- [63]. R.W.-W. Hsu, C.-C. Yang, C.-A. Huang, and Y.-S. Chen, *Electrochemical corrosion studies on Co–Cr–Mo implant alloy in biological solutions*. *Materials Chemistry and Physics*, 2005. **93**(2–3): p. 531-538.
- [64]. B. Bhushan, *Principles and Applications of Tribology*. 1999: John Wiley & Sons.
- [65]. R. Chattopadhyay, *Surface Wear: Analysis, Treatment, and Prevention*. 2001: Asm International.
- [66]. A.J. Saldivar-Garcia and H.F. Lopez, *Microstructural effects on the wear resistance of wrought and as-cast Co-Cr-Mo-C implant alloys*. *Journal of Biomedical Materials Research Part A*, 2005. **74A**(2): p. 269-274.
- [67]. J.L. Tipper, P.J. Firkins, E. Ingham, J. Fisher, M.H. Stone, and R. Farrar, *Quantitative analysis of the wear and wear debris from low and high carbon content cobalt chrome alloys used in metal on metal total hip replacements*. *Journal of Materials Science: Materials in Medicine*, 1999. **10**(6): p. 353-362.
- [68]. H.R. Shetty, T.H. Kosel, and N.F. Fiore, *A study of abrasive wear mechanisms in cobalt-base alloys*. *Wear*, 1983. **84**(3): p. 327-343.
- [69]. H.R. Shetty, T.H. Kosel, and N.F. Fiore, *A study of abrasive wear mechanisms using diamond and alumina scratch tests*. *Wear*, 1982. **80**(3): p. 347-376.

- [70]. V.M. Desai, C.M. Rao, T.H. Kosel, and N.F. Fiore, *Effect of carbide size on the abrasion of cobalt-base powder metallurgy alloys*. Wear, 1984. **94**(1): p. 89-101.
- [71]. A. FRENK and J.-D. WAGNIÈRE, *LASER CLADDING WITH COBALT-BASED HARDFACING ALLOYS*. J. Phys. IV France, 1991. **01**(C7): p. C7-65-C7-68.
- [72]. A. Frenk and W. Kurz, *MICROSTRUCTURAL EFFECTS ON THE SLIDING WEAR-RESISTANCE OF A COBALT-BASED ALLOY*. Wear, 1994. **174**(1-2): p. 81-91.
- [73]. J. Chen, X.Y. Li, T. Bell, and H. Dong, *Improving the wear properties of Stellite 21 alloy by plasma surface alloying with carbon and nitrogen*. Wear, 2008. **264**(3-4): p. 157-165.
- [74]. E. Rabinowicz, *Friction and Wear of Materials*. 1995: Wiley.
- [75]. H. Kashani, A. Amadeh, and A. Ohadizadeh, *Effect of temperature on the strain induced $\gamma \rightarrow \epsilon$ phase transformation in Stellite 21 during wear test*. Materials Science and Engineering: A, 2006. **435–436**(0): p. 474-477.
- [76]. M.T. Mathew, M.J. Runa, M. Laurent, J.J. Jacobs, L.A. Rocha, and M.A. Wimmer, *Tribocorrosion behavior of CoCrMo alloy for hip prosthesis as a function of loads: a comparison between two testing systems*. Wear, 2011. **271**(9-10): p. 1210-1219.
- [77]. I. Milosev and H.H. Strehblow, *The composition of the surface passive film formed on CoCrMo alloy in simulated physiological solution*. Electrochimica Acta, 2003. **48**(19): p. 2767-2774.
- [78]. Y. Sun and E. Haruman, *Effect of electrochemical potential on tribocorrosion behavior of low temperature plasma carburized 316L stainless steel in 1 M H₂SO₄ solution*. Surface & Coatings Technology, 2011. **205**(17-18): p. 4280-4290.
- [79]. Y. Yan, A. Neville, and D. Dowson, *Tribo-corrosion properties of cobalt-based medical implant alloys in simulated biological environments*. Wear, 2007. **263**: p. 1105-1111.
- [80]. Y. Yan, A. Neville, D. Dowson, S. Williams, and J. Fisher, *Electrochemical instrumentation of a hip simulator: a new tool for assessing the role of corrosion in metal-on-metal hip joints*. Proceedings of the Institution of Mechanical Engineers Part H-Journal of Engineering in Medicine, 2010. **224**(H11): p. 1267-1273.
- [81]. D. Landolt, S. Mischler, and M. Stemp, *Electrochemical methods in tribocorrosion: a critical appraisal*. Electrochimica Acta, 2001. **46**(24-25): p. 3913-3929.
- [82]. N. Diomidis, J.P. Celis, P. Ponthiaux, and F. Wenger, *Tribocorrosion of stainless steel*

in sulfuric acid: Identification of corrosion-wear components and effect of contact area. Wear, 2010. **269**(1-2): p. 93-103.

- [83]. P. Henry, J. Takadoum, and P. Bercot, *Tribocorrosion of 316L stainless steel and TA6V4 alloy in H₂SO₄ media.* Corrosion Science, 2009. **51**(6): p. 1308-1314.
- [84]. Y. Sun and E. Haruman, *Tribocorrosion behaviour of low temperature plasma carburised 316L stainless steel in 0.5 M NaCl solution.* Corrosion Science, 2011. **53**(12): p. 4131-4140.
- [85]. J. Jiang, M.M. Stack, and A. Neville, *Modelling the tribo-corrosion interaction in aqueous sliding conditions.* Tribology International, 2002. **35**(10): p. 669-679.
- [86]. Y. Yan, A. Neville, D. Dowson, and S. Williams, *Tribocorrosion in implants - assessing high carbon and low carbon Co-Cr-Mo alloys by in situ electrochemical measurements.* Tribology International, 2006. **39**(12): p. 1509-1517.
- [87]. J. Jiang and M.M. Stack, *Modelling sliding wear: From dry to wet environments.* Wear, 2006. **261**(9): p. 954-965.
- [88]. D. Landolt, S. Mischler, M. Stemp, and S. Barril, *Third body effects and material fluxes in tribocorrosion systems involving a sliding contact.* Wear, 2004. **256**(5): p. 517-524.
- [89]. R. Buscher and A. Fischer, *Metallurgical aspects of sliding wear of fcc materials for medical applications.* Materialwissenschaft Und Werkstofftechnik, 2003. **34**(10-11): p. 966-975.
- [90]. M.M. Stack, J. Rodling, M.T. Mathew, H. Jawan, W. Huang, G. Park, and C. Hodge, *Micro-abrasion-corrosion of a Co-Cr/UHMWPE couple in Ringer's solution: An approach to construction of mechanism and synergism maps for application to bio-implants.* Wear, 2010. **269**(5-6): p. 376-382.
- [91]. D.H. Mattox, *Handbook of Physical Vapor Deposition (PVD) Processing: Film Formation, Adhesion, Surface Preparation and Contamination Control.* 1998: Noyes Publications.
- [92]. P.A. Dearnley, *A review of metallic, ceramic and surface-treated metals used for bearing surfaces in human joint replacements.* Proceedings of the Institution of Mechanical Engineers Part H-Journal of Engineering in Medicine, 1999. **213**(H2): p. 107-135.
- [93]. V.-H. Pham, S.-W. Yook, Y. Li, G. Jeon, J.-J. Lee, H.-E. Kim, and Y.-H. Koh, *Improving hardness of biomedical Co-Cr by deposition of dense and uniform TiN films using negative substrate bias during reactive sputtering.* Materials Letters, 2011.

65(11): p. 1707-1709.

- [94]. V.-H. Pham, S.-H. Jun, H.-E. Kim, and Y.-H. Koh, *Deposition of titanium nitride (TiN) on Co–Cr and their potential application as vascular stent*. Applied Surface Science, 2012. **258**(7): p. 2864-2868.
- [95]. A. Wisbey, P.J. Gregson, and M. Tuke, *Application of PVD TiN coating to Co-Cr-Mo based surgical implants*. Biomaterials, 1987. **8**(6): p. 477-480.
- [96]. V.-H. Pham, S.-W. Yook, E.-J. Lee, Y. Li, G. Jeon, J.-J. Lee, H.-E. Kim, and Y.-H. Koh, *Deposition of TiN films on Co–Cr for improving mechanical properties and biocompatibility using reactive DC sputtering*. Journal of Materials Science: Materials in Medicine, 2011. **22**(10): p. 2231-2237.
- [97]. B.R. Lanning and R. Wei, *High intensity plasma ion nitriding of orthopedic materials: Part II. Microstructural analysis*. Surface and Coatings Technology, 2004. **186**(1–2): p. 314-319.
- [98]. Z.L. Zhang and T. Bell, *STRUCTURE AND CORROSION RESISTANCE OF PLASMA NITRIDED STAINLESS STEEL*. Surface Engineering, 1985. **1**(2): p. 131-136.
- [99]. H. Dong, C.X. Li, and T. Bell, *Plasma surface treatment of Co-Cr*, 2003: UK.
- [100]. X.Y. Li, N. Habibi, T. Bell, and H. Dong, *Microstructural characterisation of a plasma carburised low carbon Co-Cr alloy*. Surface Engineering, 2007. **23**(1): p. 45-51.
- [101]. J. Chen, *Plasma surface alloying of CoCr alloys to combat wear* in Department of Metallurgy and Materials 2008, University of Birmingham: Birmingham.
- [102]. J. Fisher, X.Q. Hu, T.D. Stewart, S. Williams, J.L. Tipper, E. Ingham, M.H. Stone, C. Davies, P. Hatto, J. Bolton, M. Riley, C. Hardaker, G.H. Isaac, and G. Berry, *Wear of surface engineered metal-on-metal hip prostheses*. Journal of Materials Science: Materials in Medicine, 2004. **15**(3): p. 225-235.
- [103]. M.K. Harman, S.A. Banks, and W.A. Hodge, *Wear analysis of a retrieved hip implant with titanium nitride coating*. Journal of Arthroplasty, 1997. **12**(8): p. 938-945.
- [104]. M. Teresa Raimondi and R. Pietrabissa, *The in-vivo wear performance of prosthetic femoral heads with titanium nitride coating*. Biomaterials, 2000. **21**(9): p. 907-913.
- [105]. W. Österle, D. Klaffke, M. Griepentrog, U. Gross, I. Kranz, and C. Knabe, *Potential of wear resistant coatings on Ti–6Al–4V for artificial hip joint bearing surfaces*. Wear, 2008. **264**(7–8): p. 505-517.

- [106]. P. Christel, A. Meunier, M. Heller, J.P. Torre, and C.N. Peille, *Mechanical properties and short-term in vivo evaluation of yttrium-oxide-partially-stabilized zirconia*. Journal of Biomedical Materials Research, 1989. **23**(1): p. 45-61.
- [107]. S.K. Yen, M.J. Guo, and H.Z. Zan, *Characterization of electrolytic ZrO₂ coating on Co–Cr–Mo implant alloys of hip prosthesis*. Biomaterials, 2001. **22**(2): p. 125-133.
- [108]. S.K. Yen and S.W. Hsu, *Electrolytic Al₂O₃ coating on co-cr-mo implant alloys of hip prosthesis*. J Biomed Mater Res, 2001. **54**(3): p. 412-8.
- [109]. P. Kumar, M. Oka, K. Ikeuchi, K. Shimizu, T. Yamamuro, H. Okumura, and Y. Kotoura, *Low wear rate of UHMWPE against zirconia ceramic (Y-PSZ) in comparison to alumina ceramic and SUS 316L alloy*. Journal of Biomedical Materials Research, 1991. **25**(7): p. 813-828.
- [110]. D.S. Almeida, C.R.M. Silva, M.C.A. Nono, and C.A.A. Cairo, *EB–PVD TBCs of zirconia co-doped with yttria and niobia, a microstructural investigation*. Surface and Coatings Technology, 2006. **200**(8): p. 2827-2833.
- [111]. U. Schulz and M. Schmücker, *Microstructure of ZrO₂ thermal barrier coatings applied by EB-PVD*. Materials Science and Engineering: A, 2000. **276**(1–2): p. 1-8.
- [112]. T. Goto, *Thermal barrier coatings deposited by laser CVD*. Surface and Coatings Technology, 2005. **198**(1–3): p. 367-371.
- [113]. V.J.P. Lim, K.A. Khor, L. Fu, and P. Cheang, *Hydroxyapatite–zirconia composite coatings via the plasma spraying process*. Journal of Materials Processing Technology, 1999. **89–90**(0): p. 491-496.
- [114]. Z. Xu, G. Rajaram, J. Sankar, and D. Pai, *Electrophoretic deposition of YSZ electrolyte coatings for solid oxide fuel cells*. Surface and Coatings Technology, 2006. **201**(7): p. 4484-4488.
- [115]. A. Grill, *Diamond-like carbon coatings as biocompatible materials--an overview*. Diamond and Related Materials, 2003. **12**(2): p. 166-170.
- [116]. J.I. Oñate, M. Comin, I. Bracerás, A. García, J.L. Viviente, M. Brizuela, N. Garagorri, J.L. Peris, and J.I. Alava, *Wear reduction effect on ultra-high-molecular-weight polyethylene by application of hard coatings and ion implantation on cobalt chromium alloy, as measured in a knee wear simulation machine*. Surface and Coatings Technology, 2001. **142–144**(0): p. 1056-1062.
- [117]. V.M. Tiainen, *Amorphous carbon as a bio-mechanical coating - mechanical properties and biological applications*. Diamond and Related Materials, 2001. **10**(2): p. 153-160.

- [118]. V. Saikko, T. Ahlroos, O. Calonijs, and J. Keranen, *Wear simulation of total hip prostheses with polyethylene against CoCr, alumina and diamond-like carbon*. Biomaterials, 2001. **22**(12): p. 1507-14.
- [119]. P.A. Dearnley and A. Neville, *Coatings tribology drivers for high density plasma technologies* Surface Engineering, 2010. **26**(1-2): p. 80-96.
- [120]. S. Yang, D. Camino, A.H.S. Jones, and D.G. Teer, *Deposition and tribological behaviour of sputtered carbon hard coatings*. Surface and Coatings Technology, 2000. **124**(2-3): p. 110-116.
- [121]. S.K. Field, M. Jarratt, and D.G. Teer, *Tribological properties of graphite-like and diamond-like carbon coatings*. Tribology International, 2004. **37**(11-12): p. 949-956.
- [122]. W.A. Grant and J.S. Colligon, *Ion beam techniques for material modification*. Vacuum, 1982. **32**(10-11): p. 675-683.
- [123]. J.G. Bowsher, A. Hussain, P. Williams, J. Nevelos, and J.C. Shelton, *Effect of ion implantation on the tribology of metal-on-metal hip prostheses*. The Journal of Arthroplasty, 2004. **19**(8, Supplement): p. 107-111.
- [124]. O. Öztürk, U. Türkan, and A.E. Eroğlu, *Metal ion release from nitrogen ion implanted CoCrMo orthopedic implant material*. Surface and Coatings Technology, 2006. **200**(20-21): p. 5687-5697.
- [125]. J.R. Conrad, *Sheath thickness and potential profiles of ion - matrix sheaths for cylindrical and spherical electrodes*. Journal of Applied Physics, 1987. **62**(3): p. 777-779.
- [126]. J. Tendys, I.J. Donnelly, M.J. Kenny, and J.T.A. Pollock, *Plasma immersion ion implantation using plasmas generated by radio frequency techniques*. Applied Physics Letters, 1988. **53**(22): p. 2143-2145.
- [127]. J. Lutz, W. Jürgen Gerlach, and M. Stephan, *Pill nitriding of fcc-alloys containing Ni and Cr*. Physica Status Solidi (A) Applications and Materials Science, 2008. **205**(4): p. 980-984.
- [128]. I.M. Eichertopf, A. Lehmann, J. Lutz, J.W. Gerlach, and S. Mändl, *Mechanical surface properties of CoCr alloys after nitrogen PIII*. Plasma Processes and Polymers, 2007. **4**(SUPPL.1): p. S44-S48.
- [129]. D. Ikeda, M. Ogawa, Y. Hara, Y. Nishimura, O. Odusanya, K. Azuma, S. Matsuda, M. Yatsuzuka, and A. Murakami, *Effect of nitrogen plasma-based ion implantation on joint prosthetic material*. Surface and Coatings Technology, 2002. **156**(1-3): p. 301-305.

- [130]. J. Lutz, C. Díaz, J.A. García, C. Blawert, and S. Mändl, *Corrosion behaviour of medical CoCr alloy after nitrogen plasma immersion ion implantation*. Surface and Coatings Technology, 2011. **205**(8–9): p. 3043-3049.
- [131]. J. Lutz and S. Mändl, *Reduced tribocorrosion of CoCr alloys in simulated body fluid after nitrogen insertion*. Surface and Coatings Technology, 2010. **204**(18–19): p. 3043-3046.
- [132]. G.G. Tibbetts, *Diffusivity of carbon in iron and steels at high temperatures*. Journal of Applied Physics, 1980. **51**(9): p. 4813-4816.
- [133]. W. Gräfen and B. Edenhofer, *New developments in thermo-chemical diffusion processes*. Surface and Coatings Technology, 2005. **200**(5–6): p. 1830-1836.
- [134]. O. Karabelchtchikova, S.M. Hsiang, and J.R.D. Sisson, *Multi-objective optimisation of gas carburising process in batch furnaces with endothermic carburising atmosphere*. Surface Engineering, 2009. **25**(1): p. 43-49.
- [135]. B. Edenhofer, *Carbonitriding in the Plasma of Glow Discharge*. CARBONITRIEREN IN PLASMA DER GLIMMENTLADUNG., 1973. **28**(3): p. 165-172.
- [136]. H. Gutschmann and W. Grafen, *Erfahrungen mit einer plasmaaufkohlungsanlage in der getriebefertigung*. HTM - Haertereitechnische Mitteilungen, 1996. **51**(2): p. 119-123.
- [137]. W. Gräfen, *Plasma-carburising furnaces in European industry*. Heat Treatment of Metals, 1996. **23**(4): p. 87-90.
- [138]. T. Bell, Y. Sun, and A. Suhadi, *Environmental and technical aspects of plasma nitrocarburising*. Vacuum, 2000. **59**(1): p. 14-23.
- [139]. B. Edenhofer, W. Gräfen, and J. Müller-Ziller, *Plasma-carburising — a surface heat treatment process for the new century*. Surface and Coatings Technology, 2001. **142–144**(0): p. 225-234.
- [140]. Y. Sun, X.Y. Li, and T. Bell, *X-ray diffraction characterisation of low temperature plasma nitrided austenitic stainless steels*. Journal of Materials Science, 1999. **34**(19): p. 4793-4802.
- [141]. N. Habibi, *Low-temperature plasma surface engineering of medical grade Co-Cr alloys*, 2008, The University of Birmingham: Birmingham, UK.
- [142]. X.Y. Li, Y. Sun, A. Bloyce, and T. Bell. *XTEM characterisation of low temperature plasma nitrided AISI 316 austenitic stainless steel*. in CONFERENCE SERIES- INSTITUTE OF PHYSICS. 1997.

- [143]. W.C. Oliver and G.M. Pharr, *An improved technique for determining hardness and elastic modulus using load and displacement sensing indentation experiments*. Journal of Materials Research, 1992. **7**(6): p. 1564-1583.
- [144]. Y. Li, Y. Yamashita, N. Tang, B. Liu, S. Kurosu, H. Matsumoto, Y. Koizumi, and A. Chiba, *Influence of carbon and nitrogen addition on microstructure and hot deformation behavior of biomedical Co–Cr–Mo alloy*. Materials Chemistry and Physics, 2012. **135**(2–3): p. 849-854.
- [145]. B.-J. Lee, *Prediction of Ti/Al₂O₃ interface reaction products by diffusion simulation*. Acta Materialia, 1997. **45**(10): p. 3993-3999.
- [146]. H. Dong, *S-phase surface engineering of Fe-Cr, Co-Cr and Ni-Cr alloys*. International Materials Reviews, 2010. **55**(2): p. 65-98.
- [147]. C.E. Pinedo, L.B. Varela, and A.P. Tschietschin, *Low-temperature plasma nitriding of AISI F51 duplex stainless steel*. Surface and Coatings Technology, 2013. **232**(0): p. 839-843.
- [148]. *Diffusion in Solids—Recent Developments*. 1975, New York: Associated Press.
- [149]. V.K. Portnoi and A.V. Leonov, *Mechanochemical synthesis of Co-C materials*. Inorganic Materials, 2012. **48**(6): p. 593-600.
- [150]. Z. Cui, F. Gao, and J. Qu, *Interface-reaction controlled diffusion in binary solids with applications to lithiation of silicon in lithium-ion batteries*. Journal of the Mechanics and Physics of Solids, 2013. **61**(2): p. 293-310.
- [151]. J. Wang, L.G. Zhang, H.S. Liu, L.B. Liu, and Z.P. Jin, *Interfacial reaction between Sn–Ag alloys and Ni substrate*. Journal of Alloys and Compounds, 2008. **455**(1–2): p. 159-163.
- [152]. R.G. Colters, *Thermodynamics of binary metallic carbides: A review*. Materials Science and Engineering, 1985. **76**(0): p. 1-50.
- [153]. R.S. Iskhakov, S.V. Stolyar, L.A. Chekanova, E.M. Artem'ev, and V.S. Zhigalov, *High-pressure phases in nanocrystalline Co(C) films obtained by pulsed plasma vaporization*. Journal of Experimental and Theoretical Physics Letters, 2000. **72**(6): p. 316-319.
- [154]. S. Shatynski, *The thermochemistry of transition metal carbides*. Oxidation of Metals, 1979. **13**(2): p. 105-118.

LIST OF TABLES

Table 1.1.1	Typical mechanical properties of implant metals. [1]
Table 1.1.2	Metal ion concentrations of patients. [8, 9]
Table 1.1.3	Revision rates by prosthesis type at one, three and five years for primary hip replacement procedures, undertaken between 1st April 2003 and 31st December 2009, which were linked to a HES/PEDW episode. [10]
Table 2.1.1	Chemical composition of biomedical grade Co-Cr alloys.
Table 2.2.1	Mechanical properties of cobalt-based biomedical grade alloys. [1]
Table 3.1.1	Chemical compositions of as-received materials.
Table 3.2.1	Sample code and corresponding treatment conditions.
Table 4.2.1	Area fractions of ϵ -HCP of different heat-treated samples based on EBSD analysis.
Table 4.5.1	Corrosion potentials of heat-treated samples based on anodic polarisation curves.
Table 4.5.2	Corrosion potentials of all plasma carburised sample surface based on anodic polarisation curves.
Table 4.7.1	Summary of tribocorrosion results.
Table 5.5.1	Total wear factor of all samples.

LIST OF FIGURES

- Figure 2.2.1 Effect of alloying additions on the HCP to FCC transformation in cobalt as a function of solubility in FCC cobalt, showing relating solubility with the effect of an element on the transformation temperature. [30]
- Figure 2.2.2 SEM micrographs showing the morphology of (a) athermal martensite (striations) in a powder structure Co-Cr alloy [32] and (b) isothermal martensite (discontinuous lamellae) in a wrought low carbon Co-Cr alloy [36].
- Figure 2.2.3 The Co-Cr phase diagram with the vertical dotted line corresponding to the 28 % Cr-containing Co-based alloy which is the composition of Cr in ASTM F1537 Co-Cr-Mo alloy. [38]
- Figure 2.2.4 Periodic table showing the element pairs for the formation of σ phase. The crystal structure and atomic radius of pure Cr, Co and Mo and the possible element pairs of σ phase are highlighted. [40]
- Figure 2.2.5 Compositional images showing the σ phases denoted by white arrows, respectively, for (a) low carbon and (b) high carbon alloys. [44]
- Figure 2.2.6 Effect of adding elements of varying electronegativity on type of carbides formed in Co-based alloys, carbon assumed 0.1-0.6 %. [46]
- Figure 2.2.7 Effect of processing on the microstructure of Co-Cr-Mo surgical implant alloys. (a) Investment-cast alloy. (b) Forged alloy. [54]
- Figure 2.3.1 Schematic of the interface of a passivated metal surface in a biological solution. [1]
- Figure 2.3.2 Key components of (a) the air-formed passive film and (b) corroded surface. [56]
- Figure 2.4.1 Dry sliding wear map for Stellite 6 against a WC-Co 90/10 disc. [72]
- Figure 2.4.2 Schematic of plastic flow for hexagonal metals. Because of the limited number of slip planes, the two metals do not conform after slippage which reduces the degree of metal-metal contact. [74]
- Figure 2.5.1 Different contact modes involving tribocorrosion. [81]
- Figure 2.5.2 Schematic of four types of factors affecting the tribocorrosion system

under electrochemical condition. [81]

- Figure 2.6.1 Schematic depiction of coating collapse caused by excessive point contact loading – the ‘thin-ice effect. [92]
- Figure 2.6.2 Classification of surface engineering technologies. [101]
- Figure 2.6.3 The closed field unbalanced magnetron sputter ion plating system (plan view). [121]
- Figure 3.3.1 Schematic of the steps of a cross-sectional TEM sample preparation. [142]
- Figure 3.3.2 Secondary electron image of cross-sectional TEM sample thinned using a Quanta 3D FEG FIB miller
- Figure 3.3.3 typical load-displacement curve measured using nanoindentation device. [143]
- Figure 3.3.4 Schematic representation of cross-sectional view of an indent showing the parameters used for calculating hardness (H) and reduced elastic modulus (E_r). [143]
- Figure 3.3.5 Schematic diagram of the reciprocating tribometer.
- Figure 3.3.6 Schematic diagram of the tribo-electrochemical cell. [84]
- Figure 4.1.1 Optical micrographs showing the microstructure of the AR sample.
- Figure 4.1.2 SEM observation showing the microstructure of the AR sample.
- Figure 4.1.3 Secondary electron micrographs showing the microstructure of the AR sample and EDX analysis of the AR sample.
- Figure 4.1.4 XRD spectra for AR sample.
- Figure 4.1.5 (a) TEM microstructure of the AR sample and corresponding SAD patterns of (b) $M_{23}C_6$ carbide ($B=[\bar{1}12]$) from B area and (c) α -FCC phase ($B=[1\bar{1}0]$) from C area
- Figure 4.1.6 TEM microstructure of defects observed in the AR sample: a) Micro twins and b) stacking faults $\vec{g} = [220]$.
- Figure 4.1.7 (a) TEM micrograph and (b) corresponding SAD pattern from α -FCC and ϵ -HCP phases in the AR sample.
- Figure 4.2.1 Amount of HCP phase after designed heat treatments based on XRD.

- Figure 4.2.2 XRD spectra for the FCC sample
- Figure 4.2.3 (a) Optical and (b) SEM microstructure of the FCC sample.
- Figure 4.2.4 (a) SEM of as-polished (b) phase map showing the phase distribution with yellow for α -FCC, blue for ϵ -HCP and red for $M_{23}C_6$ ($M=Cr_{0.77}Co_{0.15}Mo_{0.08}$) and (c) crystal orientation map of the FCC sample,
- Figure 4.2.5 XRD spectra for the HCP sample.
- Figure 4.2.6 Optical and SEM micrograph showing the microstructure of HCP sample.
- Figure 4.2.7 (a) SEM, (b) phase map (yellow for α -FCC, blue for ϵ -HCP, red for $M_{23}C_6$ ($M=Cr_{0.77}Co_{0.15}Mo_{0.08}$)) and light green for sigma phase (c) crystal orientation map of ϵ -HCP coloured according to the crystal direction parallel to the normal direction of HCP sample.
- Figure 4.2.8 Back-scattered electron microscope image showing the microstructure of the HCP sample.
- Figure 4.2.9 EDX line scan across the dark contrasted thin plate and irregular shape microstructures
- Figure 4.2.10 EDX analysis on white and dark contrasted particles.
- Figure 4.2.11 XRD spectra for 40HCP sample.
- Figure 4.2.12 Optical micrograph showing the microstructure of 40HCP sample.
- Figure 4.2.13 SEM micrograph showing the microstructure of 40HCP sample.
- Figure 4.2.14 (a) secondary electron micrograph of as-polished 40HCP sample.
- Figure 4.2.14 (b) phase map showing the phase distribution with yellow for α -FCC, blue for ϵ -HCP, red for $M_{23}C_6$ ($M=Cr_{0.77}Co_{0.15}Mo_{0.08}$) and light green for sigma phase.
- Figure 4.2.14 (c) crystal orientation map of α -FCC coloured according to the crystal direction parallel to the normal direction of 40HCP sample.
- Figure 4.2.14 (d) crystal orientation map of ϵ -HCP coloured according to the crystal direction parallel to the normal direction of 40HCP sample.

- Figure 4.2.15 Bright field TEM microstructure of thin rectangle blocks from 40HCP sample (a) longitudinal view and (b) transverse view.
- Figure 4.2.16 (a) SAD pattern taken from the precipitates shown in Figure 4.2.15. (b) Indexing of the patterns: $[2\bar{1}10]_{\text{HCP}} // [110]_{\text{M}_{23}\text{C}_6}$
- Figure 4.2.17 (a) Bright field TEM microstructure and b) corresponding SAD pattern showing ϵ -HCP matrix and irregular shaped M_{23}C_6 particle in 40HCP sample.
- Figure 4.2.18 (a) Bright field TEM microstructure and b) corresponding SAD pattern, showing irregular shaped M_{23}C_6 particles along FCC matrix grains in 40HCP sample.
- Figure 4.2.19 (a) Bright field TEM microstructure and b) corresponding SAD pattern showing σ phase $\text{Co}_2(\text{Mo,Cr})_3$ (PDF code 00-029-0490) in 40HCP sample.
- Figure 4.2.20 Bright field TEM microstructure (a) and (b) corresponding SAD pattern from 40HCP sample showing ϵ -HCP plates embedded in FCC matrix with a $[2\bar{1}\bar{1}0]_{\epsilon} // [110]_{\alpha}, (0001)_{\epsilon} // (1\bar{1}1)_{\alpha}$ relationship.
- Figure 4.3.1 XRD spectra of (a) the FCC-PC sample and (b) comparasion between the FCC and FCC-PC samples.
- Figure 4.3.2 (a) Optical and (b) secondary electron micrographs showing plan-view surface morphology of the FCC-PC sample.
- Figure 4.3.3 (a) Optical and (b) SEM showing surface layer structure of the FCC-PC sample.
- Figure 4.3.4 GDS depth profiles of the FCC-PC sample: (a) all elements and (b) carbon.
- Figure 4.3.5 XRD spectra of (a) the HCP-PC sample and (b) comparasion between the HCP and HCP-PC samples (question mark for the unidentified peak).
- Figure 4.3.6 Optical microscope image showing the surface morphology of the HCP-PC sample.
- Figure 4.3.7 SEM image showing surface morphology of the HCP-PC sample.

- Figure 4.3.8 Optical microscope image showing the cross-sectional microstructure of the HCP-PC sample.
- Figure 4.3.9 SEM image showing the cross-sectional microstructure of the HCP-PC sample.
- Figure 4.3.10 GDS depth profiles of the HCP-PC sample: (a) all elements and (b) carbon.
- Figure 4.3.11 XRD spectra of (a) the HCP-PC sample and (b) comparison between the 40HCP and 40HCP-PC samples (question mark for the unidentified peak).
- Figure 4.3.12 Optical microstructure of surface morphology taken from 40HCP-PC sample. Bright contrast patches are ϵ -HCP grains; dark contrast patches are α -FCC grains.
- Figure 4.3.13 SEM image showing the cross-sectional microstructure of 40HCP-PC sample.
- Figure 4.3.14 GDS depth profiles of 40HCP-PC sample: (a) all elements and (b) carbon.
- Figure 4.3.15 (a) TEM microstructure and corresponding SAD patterns (b) from A area and (c) from B interface area, of the 40HCP-PC sample.
- Figure 4.3.16 (a) TEM microstructure of the 40HCP-PC sample and (b) corresponding SAD pattern and (c) the pattern indexes for the surface layer formed on HCP grain during PC treatment.
- Figure 4.3.17 TEM microstructure of the surface layer of the HCP-PC sample and irregular $M_{23}C_6$ particles.
- Figure 4.3.18 (a) Dark field TEM microstructure and (b) corresponding SAD pattern showing the $M_{23}C_6$ in the HCP-PC sample.
- Figure 4.4.1 Microhardness of AR and heat-treated materials (error bar showing the standard deviation).
- Figure 4.4.2 Surface hardness of plasma carburised materials (error bar showing the standard deviation).
- Figure 4.4.3 Depth hardness profiles of plasma carburised materials.

- Figure 4.4.4 Hardness and carbon concentration depth profiles of sample (a) FCC-PC, (b) 40HCP-PC and (c) HCP-PC.
- Figure 4.4.5 Load bearing capacity of plasma carburising samples under different loads.
- Figure 4.4.6 Back scattered electron images of indents on: (a) FCC-PC samples tested under 100g, (b) HCP-PC samples tested under 300g and (c and d) 40HCP-PC samples tested under 300g.
- Figure 4.4.7 Nanoindentation results of bulk α -FCC and ϵ -HCP Co-Cr materials before and post plasma carburising treatments: (a) H and E, (b) calculated H/E (error bar showing the standard deviation).
- Figure 4.4.8 (a) Phase map of 40HCP sample post nanoindentation tests (blue for ϵ -HCP Co, yellow for α -FCC Co, red for $M_{23}C_6$).
- Figure 4.4.8 (b) α -FCC Co phase normal direction grain map
- Figure 4.4.8 (c) nanoindentation results of different FCC grains (error bar showing the standard deviation).
- Figure 4.4.8 (d) ϵ -HCP Co phase normal direction grain map
- Figure 4.4.8 (e) nanoindentation results of different HCP grains (error bar showing the standard deviation).
- Figure 4.4.9 Cross-sectional observations before and post nanoindentation for the 40HCP-PC sample: (a) phase map showing cross-sectional phase distribution before nanoindentation, (b) secondary electron micrograph after nanoindentation and (c) phase map showing the positions of indents post nanoindentation.
- Figure 4.4.10 Depth profiles of nano-hardness of FCC and HCP originated grains after plasma carburising.
- Figure 4.5.1 Anodic polarisation curves of heat-treated samples.
- Figure 4.5.2 SEM observations on the (a-b) AR, (c-d) FCC, (e-f) HCP and (g-h) 40HCP samples before and after anodic polarisation tests.
- Figure 4.5.3 Anodic polarisation curves of plasma carburised samples.
- Figure 4.5.4 Anodic polarisation curves of materials before and after low-temperature

plasma carburising: (a) FCC and FCC-PC, (b) 40HCP and 40HCP-PC and (c) HCP and HCP-PC.

Figure 4.5.5 SEM observations on the FCC-PC samples (a) before and (b) after anodic polarisation tests.

Figure 4.5.6 SEM observation on the HCP-PC samples (a) before and (b) after anodic polarisation tests.

Figure 4.5.7 SEM observations on the 40HCP-PC samples (a) before and (b, c) after anodic polarisation tests.

Figure 4.6.1 Average friction coefficient of the AR and heat-treated samples (error bar showing the standard deviation).

Figure 4.6.2 Cross-section wear track profiles on the AR and heat-treated samples (load 30N).

Figure 4.6.3 Wear volume of the AR and heat-treated samples (error bar showing the standard deviation).

Figure 4.6.4 SEM observation of wear track on the AR sample: (a) low magnification SEM, (b) high magnification SEM and (c) EDX analysis.

Figure 4.6.5 (a) low and (b) high magnification SEM observations of wear tracks, (c) SEM observation of wear debris on the FCC sample and (d) EDX analysis.

Figure 4.6.6 (a) low and (b) high magnification SEM observations of wear tracks, (c) SEM observation of wear debris on the HCP sample

Figure 4.6.7 SEM observation of wear track on the 40HCP sample (a) low magnification and (b) high magnification SEM..

Figure 4.6.8 Average friction coefficient of samples before and after plasma carburising treatment (error bar showing the standard deviation).

Figure 4.6.9 Cross-section wear track profiles on the plasma carburised samples.

Figure 4.6.10 Wear volume of plasma carburised samples (error bar showing the standard deviation).

Figure 4.6.11 SEM observation of wear track on the FCC-PC sample: (a) low magnification SEM, (b) high magnification SEM and (c) EDX analysis.

- Figure 4.6.12 SEM observation of wear track on the HCP-PC sample: (a) low magnification SEM, (b) high magnification SEM and (c) EDX analysis.
- Figure 4.6.13 SEM observation of ball tested and wear track for 40HCP-PC: (a) low magnification and (b) high magnification SEM.
- Figure 4.6.14 Wear volume of the AR, heat-treated and plasma carburised samples (error bar showing the standard deviation).
- Figure 4.7.1 Potentiodynamic polarisation curves of the AR and heat-treated samples tested under rotation without load (corrosion) condition.
- Figure 4.7.2 Potentiodynamic polarisation curves of the AR and plasma carburised samples tested under rotation without load (corrosion) condition.
- Figure 4.7.3 Potentiodynamic polarisation curves of samples before plasma carburising treatments tested under rotation without load (corrosion) condition: (a) FCC and FCC-PC and (b) HCP and HCP-PC.
- Figure 4.7.4 Potentiodynamic polarisation curves of the AR and heat-treated samples tested under sliding (tribocorrosion) conditions.
- Figure 4.7.5 Coefficient of friction curves of the AR and heat-treated samples measured during potentiodynamic tests under sliding condition.
- Figure 4.7.6 Potentiodynamic polarisation curves of the AR and plasma carburised samples tested under sliding (tribocorrosion) condition.
- Figure 4.7.7 Coefficient of friction curves of the AR and plasma carburised samples measured during potentiodynamic tests under sliding.
- Figure 4.7.8 Potentiodynamic polarisation curves of samples before and after plasma carburising treatment tested under sliding (tribocorrosion) condition: (a) FCC and FCC-PC and (b) HCP and HCP-PC.
- Figure 4.7.9 Coefficient of friction curves of samples before and after plasma carburising treatment measured during potentiodynamic tests under sliding: (a) FCC and FCC-PC and (b) HCP and HCP-PC.
- Figure 4.7.10 Potentiodynamic polarisation curves tested under rotation without load (corrosion) and sliding (tribocorrosion) conditions: (a) AR, (b) FCC and FCC-PC and (c) HCP and HCP-PC.
- Figure 4.7.11 OCP of AR and heat-treated samples with time.

- Figure 4.7.12 The current of AR and heat-treated samples at different anodic potentials: (a) at -250mV (SCE), (b) 0mV (SCE) and (c) 400mV (SCE).
- Figure 4.7.13 OCP of AR and plasma carburised samples with time.
- Figure 4.7.14 The current of AR and plasma carburised samples at different anodic potentials: (a) at -250mV (SCE), (b) 0mV (SCE) and (c) 400mV (SCE).
- Figure 4.7.15 OCP of samples before and after plasma carburising treatment with time: (a) FCC and FCC-PC and (b) HCP and HCP-PC.
- Figure 4.7.16 The current of the FCC and FCC-PC samples at different anodic potentials: (a) at -250mV (SCE), (b) 0mV (SCE) and (c) 400mV (SCE).
- Figure 4.7.17 The current of the HCP and HCP-PC samples at different anodic potentials: (a) at -250mV (SCE), (b) 0mV (SCE) and (c) 400mV (SCE).
- Figure 4.7.18 Typical cross-section profiles of wear tracks of AR (a) at OCP and (b) at -250, 0 and 400 mV (SCE).
- Figure 4.7.19 Typical cross-section profiles of wear tracks of FCC and FCC-PC (a) at OCP and (b) 0mV (SCE).
- Figure 4.7.20 Typical cross-section profiles of wear tracks of HCP and HCP-PC (a) at OCP and (b) 400 mV(SCE).
- Figure 4.7.21 Total wear volume of all samples as a function of potentials (error bar showing the standard deviation).
- Figure 4.7.22 Coefficient of friction of the AR and heat-treated samples as a function of applied potential (error bar showing the standard deviation).
- Figure 4.7.23 Secondary electron images of wear tracks generated (a) at OCP and (b) at 400mV (SCE) for AR. Optical microscopic images of balls tested (c) at OCP and (d) at 400mV (SCE) for AR.
- Figure 4.7.24 Secondary electron images of wear tracks generated (a) at OCP and (b) at 0mV (SCE) for FCC. Optical microscopic images of balls tested (c) at OCP and (d) at 0mV (SCE) for FCC.
- Figure 4.7.25 Secondary electron images of wear tracks generated (a) at OCP and (b) at 400mV (SCE) for HCP. Optical microscopic images of balls tested (c) at OCP and (d) at 400mV (SCE) for HCP.

- Figure 4.7.26 Coefficient of friction of the AR and plasma carburised samples as a function of applied potential (error bar showing the standard deviation).
- Figure 4.7.27 Secondary electron images of wear tracks generated (a) at OCP and (b) at 0mV (SCE) for near FCC-PC. Optical microscopic images of balls tested (c) at OCP and (d) at 0mV (SCE) for FCC-PC.
- Figure 4.7.28 Secondary electron images of wear tracks generated (a) at OCP and (b) at 400mV (SCE) for HCP-PC. Optical microscopic images of balls tested (c) at OCP and (d) at 400mV (SCE) for HCP-PC.
- Figure 4.7.29 Coefficient of friction of samples before and after plasma carburising treatment as a function of applied potential: (a) FCC and FCC-PC and (b) HCP and HCP-PC (error bar showing the standard deviation).
- Figure 5.2.1 Co-C phase diagram. [149]
- Figure 5.2.2 Ellingham diagram for (a) the first-transition-series carbides including Cr_{23}C_6 , Cr_7C_3 , Cr_3C_2 and Co_2C and (b) the second- and third-transition series carbides including Mo_2C . [152]
- Figure 5.2.3 Qualitative phase diagram of a Co-C system on the (G, X) coordinates. [153]
- Figure 5.5.1 (a) Results of V_{chem} and V_{mech} and (b) the ratio of V_{chem} -to- V_{mech} for the AR sample.
- Figure 5.5.2 (a) Results of V_{chem} and V_{mech} and (b) the ratio of V_{chem} -to- V_{mech} for the FCC and FCC-PC samples.
- Figure 5.5.3 (a) Results of V_{chem} and V_{mech} and (b) the ratio of V_{chem} -to- V_{mech} for the HCP and HCP-PC samples.

Table 1.1.1 Typical mechanical properties of implant metals. [1]

Material	ASTM designation	Condition	Young's modulus (GPa)	Yield strength (MPa)	Tensile strength (MPa)	Fatigue endurance limit (at 10^7 cycles, $R = -1^c$) (MPa)
Stainless steel	F745	Annealed	190	221	483	221–280
	F55, F56, F138, F139	Annealed	190	331	586	241–276
		30% Cold worked	190	792	930	310–448
		Cold forged	190	1213	1351	820
Co–Cr alloys	F75	As-cast/annealed	210	448–517	655–889	207–310
		P/M HIP ^b	253	841	1277	725–950
	F799	Hot forged	210	896–1200	1399–1586	600–896
	F90	Annealed	210	448–648	951–1220	Not available
		44% Cold worked	210	1606	1896	586
	F562	Hot forged	232	965–1000	1206	500
		Cold worked, aged	232	1500	1795	689–793
Ti alloys	F67	30% Cold-worked Grade 4	110	485	760	300
	F136	Forged annealed	116	896	965	620
		Forged, heat treated	116	1034	1103	620–689

^bP/M HIP; Powder metallurgy product, hot-isostatically pressed.

^cR is defined as $\sigma_{\min}/\sigma_{\max}$.

Table 1.1.2 Metal ion concentrations of patients. [8, 9]

Head diameter (mm)	Number of joint	Follow-up (years)	materials combination	Cobalt (mg/L)		Chromium (mg/L)	
				preoperative concentration	final concentration	preoperative concentration	final concentration
28 mm	22	2	metal-on-metal articulation (wrought Co-28Cr-6Mo-0.23C alloy)	0.14 (0.09-0.17) in the blood	1.10 (0.66-2.43) in the blood	1.09 (0.67-1.96) in the blood	2.50 (1.18-3.13) in the blood
				0.42 (0.30-0.61) in the urine	14.73 (5.29-28.78) in the urine	0.26 (0.21-0.45) in the urine	4.53 (2.80-9.22) in the urine
	18	2	metal-on-UHMWPE articulation (Ti-6Al-4V alloy)	0.11 (0.09-0.15) in the blood	0.17 (0.12-0.23) in the blood	0.58 (0.38-1.02) in the blood	1.30 (1.00-1.83) in the blood
				0.39 (0.22-0.53) in the urine	0.29 (0.20-0.37) in the urine	0.23 (0.17-0.32) in the urine	0.30 (0.21-0.44) in the urine
28 mm	50	2	metal-on-metal articulation (wrought Co-28Cr-6Mo alloy)	0.15 (0.15-0.15) in the serum	0.75 (0.75-0.75) in the serum		
				0.15 (0.15-0.15) in the serum	0.70 (0.70-0.70) in the serum		
	50	2	ceramic-on-UHMWPE articulation (Al2O3)	0.15 (0.15-0.15) in the serum	0.15 (0.15-0.15) in the serum		
				0.15 (0.15-0.15) in the serum	0.15 (0.15-0.15) in the serum		

Table 1.1.3 Revision rates by prosthesis type at one, three and five years for primary hip replacement procedures, undertaken between 1st April 2003 and 31st December 2009, which were linked to a HES/PEDWepisode. [10]

Prosthesis type	Number of patients	Revision rates (95% CI)		
		One year	Three years	Five years
Cemented	99,359	0.6% (0.6% to 0.7%)	1.4% (1.3% to 1.5%)	2.0% (1.8% to 2.1%)
Cementless	62,937	1.3% (1.2% to 1.4%)	2.5% (2.4% to 2.7%)	3.4% (3.2% to 3.7%)
Hybrid	31,662	0.9% (0.8% to 1.0%)	1.8% (1.6% to 1.9%)	2.7% (2.4% to 3.0%)
Resurfacing	13,853	2.1% (1.9% to 2.3%)	4.3% (4.0% to 4.8%)	6.3% (5.7% to 7.0%)
LHMoM THR	8,882	1.3% (1.1% to 1.6%)	4.7% (4.2% to 5.4%)	7.8% (6.6% to 9.3%)
All	216,693	1.0% (0.9% to 1.0%)	2.1% (2.0% to 2.1%)	2.9% (2.8% to 3.0%)

Table 2.1.1 Chemical composition of biomedical grade Co-Cr alloys.

Alloy	Co	Ni	N	Cr	Ti	Mo	Al	Fe	Mn	W	C	Si
ASTM F75	bal	<2.0		27.0-30.0		4.5-7.0		<1.5	<1.0		<0.35	<1.0
ASTM F90	bal	9.0-11.0		19.0-20.0				<3.0	<2.5	14.0-16.0	<0.15	<1.0
ASTM F562	bal	33.0-37.0		19.0-21.0	<1.0	9.0-11.0		<1.0	<0.15			<0.15
ASTM F1537	bal	<1.0	<0.25	26.0-30.0		5.0-7.0	0.3-1.0	<0.75	<1.0		<0.35	<1.0

Table 2.2.1 Mechanical properties of cobalt-based biomedical grade alloys. [1]

Alloy	Condition	Young's modulus (GPa)	Yield strength (MPa)	Tensile strength (MPa)	Fatigue endurance limit (at 10 ⁷ cycles, R=-1e) (MPa)
ASTM F75	As-case/annealed	210	448-517	655-889	207-310
	P/M HIP ^b	253	841	1277	725-950
ASTM F799	Hot forged	210	896-1200	1399-1586	600-896
ASTM F90	Annealed	210	448-648	951-1220	Not available
	44% Cold worked	210	1606	1896	586
	Hot forged	232	965-1000	1206	500
ASTM F562	Cold worked, aged	232	1500	1795	689-793 (axial tension R=0.05, 30Hz)

Table 3.1.1 Chemical compositions of as-received materials.

Element	C	Mn	Si	Cr	Mo	N	Co
wt%	0.25	0.76	0.72	28.35	6.9	0.15	bal.

Table 3.2.1 Sample code and corresponding treatment conditions.

Sample Code	Sample Treatment
AR (as-received)	None
FCC	Solution treatment at 1250 °C for 1.5 hours (air cooling)
FCC-PC	FCC followed by LTTPC at 450 °C for 10 hours
40HCP	FCC followed by aging at 850 °C for 4 hours (water quenching)
40HCP-PC	40HCP followed by LTTPC at 450 °C for 10 hours
HCP	FCC followed by aging at 850 °C for 15 hours (water quenching)
HCP-PC	HCP followed by LTTPC at 450 °C for 10 hours

Table 4.2.1 Area fractions of ϵ -HCP of different heat-treated samples based on EBSD analysis.

	FCC	40HCP	HCP
HCP area fraction %	0.10	49.70	94.40
Standard deviation	0.01	1.08	0.55
Unresolved area	0.52	1.10	0.72

Table 4.5.1 Corrosion potentials of heat-treated samples based on anodic polarisation curves.

Sample code	E_{corr} (mV vs. Ag/AgCl)
AR	-138.3
FCC	-177.4
40HCP	-224.1
HCP	-228.9

Table 4.5.2 Corrosion potentials of all plasma carburised sample surface based on anodic polarisation curves.

Sample code	E_{corr} (mV vs. Ag/AgCl)
AR	-138.3
FCC-PC	-102.4
40HCP-PC	-185.3
HCP-PC	-181.4

Table 4.7.1 Summary of tribocorrosion results.

Potential, mV/SCE	Average current, mA				Average COF										
	AR	FCC	FCC-PC	HCP	HCP-PC	AR	AR standard deviation	FCC	FCC standard deviation	FCC-PC	FCC-PC standard deviation	HCP	HCP standard deviation	HCP-PC	HCP-PC standard deviation
-800	-0.0180	-0.0299	-0.1133	-0.0409	-0.1106	0.3181	0.0165	0.3330	0.0151	0.3309	0.0161	0.3105	0.017	0.3102	0.0176
-526.00 (OCP, HCP)	-	-	-	0.0019 (Icorr)	-	-	-	-	-	-	-	0.3754	0.0122	-	-
-523.38 (OCP, FCC)	-	0.0024 (Icorr)	-	-	-	-	-	0.3898	0.0142	-	-	-	-	-	-
-517.66 (OCP, AR)	0.0027 (Icorr)	-	-	-	-	0.4154	0.0298	-	-	-	-	-	-	-	-
-433.71 (OCP, FCC-PC)	-	-	0.0048 (Icorr)	-	-	-	-	-	-	0.3908	0.0142	-	-	-	-
-388.01 (OCP, HCP-PC)	-	-	-	-	0.0031 (Icorr)	-	-	-	-	-	-	-	-	0.3565	0.0294
-250	0.0540	0.0772	0.0222	0.0543	0.0130	0.3227	0.0164	0.3234	0.0153	0.3531	0.0151	0.2805	0.0037	0.2531	0.0157
0	0.1291	0.1120	0.0500	0.1443	0.0475	0.3351	0.0165	0.3283	0.0151	0.3874	0.0193	0.3299	0.0136	0.2781	0.0275
400	0.1354	0.1755	0.0656	0.1672	0.0932	0.3169	0.0132	0.3339	0.0098	0.3883	0.0162	0.3317	0.012	0.3739	0.0308

Table 4.7.1 Summary of tribocorrosion results.

Potential, mV/SCE	Total wear, mm ³									
	AR		near FCC		near FCC-PC		near HCP		near HCP-PC	
	AR	standard deviation	near FCC	standard deviation	near FCC-PC	standard deviation	near HCP	standard deviation	near HCP-PC	standard deviation
-800	0.0006	0.00003	0.0014	0.00014	0.0005	0.00014	0.0007	0.00007	0.0003	0.00002
-526.00(OCP, near HCP)	-	-	-	-	-	-	0.0010	0.0004	-	-
-523.38 (OCP, near FCC)	-	-	0.0036	0.0002	-	-	-	-	-	-
-517.66 (OCP, AR)	0.0012	0.0005	-	-	-	-	-	-	-	-
-433.71 (OCP, near FCC-PC)	-	-	-	-	0.0040	0.0002	-	-	-	-
-388.01 (OCP, near HCP-PC)	-	-	-	-	-	-	-	-	0.0021	0.0001
-250	0.0240	0.0010	0.0240	0.0011	0.0091	0.0004	0.0202	0.0009	0.0024	0.0001
0	0.0345	0.0015	0.0311	0.0016	0.0126	0.0008	0.0364	0.0017	0.0101	0.0004
400	0.0403	0.0019	0.0370	0.0017	0.0154	0.0006	0.0467	0.0022	0.0177	0.0008
Potential, mV/SCE	V _{mech} , mm ³					V _{chem} , mm ³				
	AR		FCC-PC		HCP-PC	AR	FCC	FCC-PC	HCP	HCP-PC
	AR	FCC	FCC-PC	HCP	HCP-PC	AR	FCC	FCC-PC	HCP	HCP-PC
-800	0.0006	0.0014	0.0005	0.0007	0.0003	0.0000	0.0000	0.0000	0.0000	0.0000
-526.00(OCP, near HCP)	-	-	-	0.0008	-	-	-	-	0.0002	-
-523.38 (OCP, near FCC)	-	0.0034	-	-	-	-	0.0002	-	-	-
-517.66 (OCP, AR)	0.0009	-	-	-	-	0.0003	-	-	-	-
-433.71 (OCP, near FCC-PC)	-	-	0.0035	-	-	-	-	0.0005	-	-
-388.01 (OCP, near HCP-PC)	-	-	-	-	0.0018	-	-	-	-	0.0003
-250	0.0183	0.0158	0.0068	0.0145	0.0011	0.0057	0.0081	0.0023	0.0057	0.0014
0	0.0209	0.0193	0.0074	0.0212	0.0051	0.0136	0.0118	0.0053	0.0152	0.0050
400	0.0260	0.0186	0.0085	0.0291	0.0079	0.0142	0.0184	0.0069	0.0176	0.0098

Table 5.5.1 Total wear factor of all samples.

potential (mV/SCE)	total wear factor (mm ³ /N/s)				
	AR	FCC	FCC-PC	HCP	HCP-PC
-800	7.77E-09	1.95E-08	6.84E-09	3.63E-09	7.54E-09
-526.00(OCP, HCP)	-	-	-	1.32E-08	-
-523.38 (OCP, FCC)	-	5.00E-08	-	-	-
-517.66 (OCP, AR)	1.60E-08	-	-	-	-
-433.71 (OCP, FCC-PC)	-	-	5.56E-08	-	-
-388.01 (OCP, HCP-PC)	-	-	-	-	2.88E-08
-250	3.33E-07	3.33E-07	1.27E-07	2.80E-07	3.38E-08
0	4.79E-07	4.32E-07	1.75E-07	5.05E-07	1.40E-07
400	5.59E-07	5.15E-07	2.13E-07	6.48E-07	2.46E-07

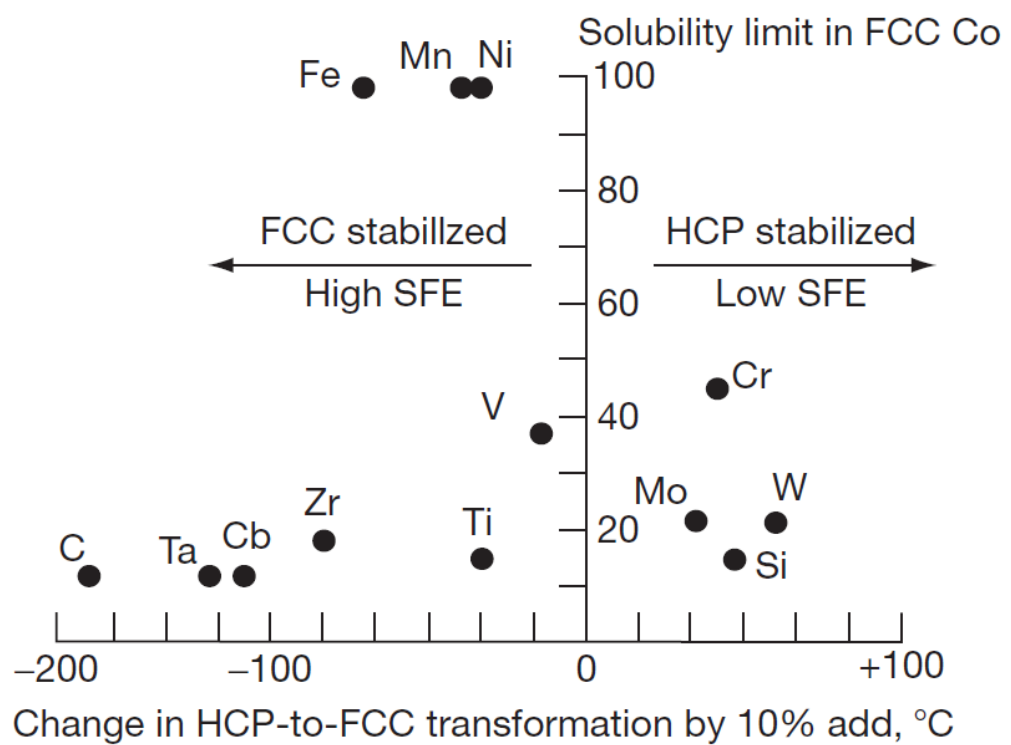


Figure 2.2.1 Effect of alloying additions on the HCP to FCC transformation in cobalt as a function of solubility in FCC cobalt, showing relating solubility with the effect of an element on the transformation temperature. [30]

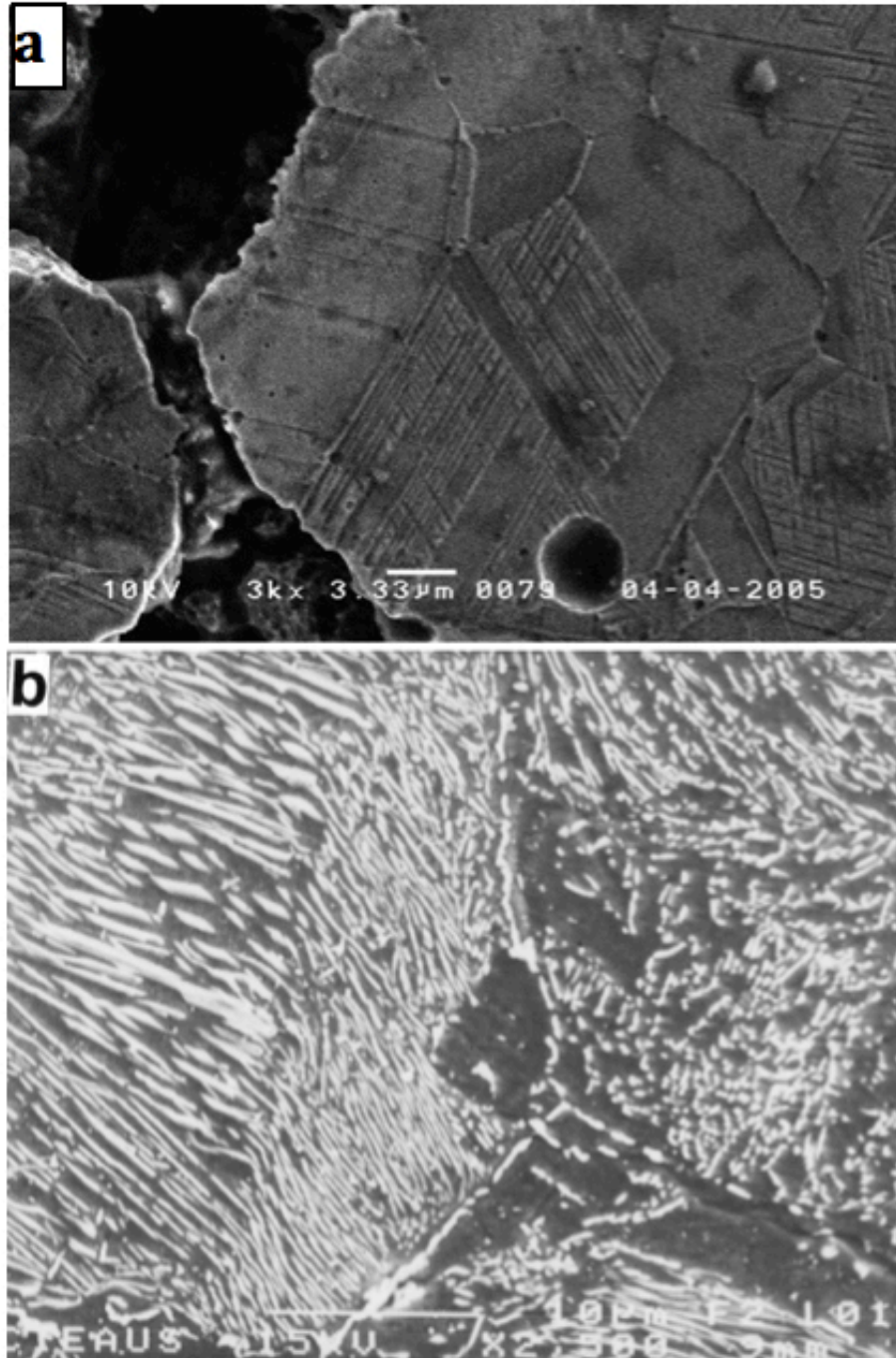


Figure 2.2.2 SEM microtaphs showing the morphology of (a) athermal martensite (striations) in a powder structure Co-Cr alloy [32] and (b) isothermal mattensite (discontinuous lamellae) in a wrought low carbon Co-Cr alloy [36].

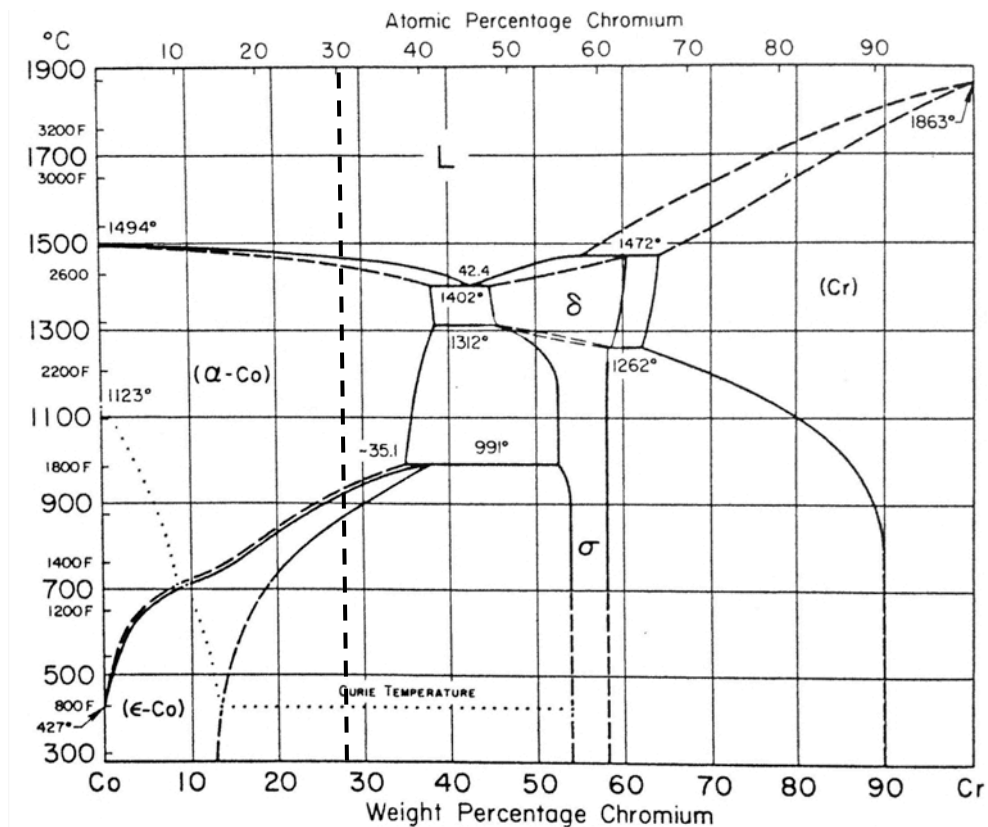


Figure 2.2.3 The Co-Cr phase diagram with the vertical dotted line corresponding to the 28 % Cr-containing Co-based alloy which is the composition of Cr in ASTM F1537 Co-Cr-Mo alloy. [38]

5	6	7	8	9	10	11	3
V <i>bcc</i> 1.34 Mn Fe Co Ni Re	Cr <i>bcc</i> 1.30 Mn Fe Co Tc Ru Re Os	Mn 1.35 (1.30) V Cr Mo Tc Re	Fe <i>fcc</i> 1.26 V Cr Mo Tc Re	Co <i>hcp</i> 1.25 V Cr Mo	Ni <i>fcc</i> 1.24 V		Al <i>fcc</i> 1.43 Nb Ta
Nb <i>bcc</i> 1.46 Rh Re Os Ir Pt	Mo <i>bcc</i> 1.39 Al Mn Fe Co Tc Ru Re Os Ir	Tc <i>hcp</i> 1.36 Cr Mn Fe Mo W	Ru <i>hcp</i> 1.34 Cr Mo W	Rh <i>fcc</i> 1.34 Nb Ta	Pd <i>fcc</i> 1.37 Ta		
Ta <i>bcc</i> 1.49 Al Rh Pd Re Os Ir Pt Au	W <i>bcc</i> 1.41 Tc Ru Re Os Ir	Re <i>hcp</i> 1.37 V Cr Mn Fe Nb Mo Ta W	Os <i>hcp</i> 1.35 Cr Nb Mo Ta W	Ir <i>fcc</i> 1.36 Nb Mo Ta W	Pt <i>fcc</i> 1.39 Nb Ta	Au <i>fcc</i> 1.46 Ta	

Figure 2.2.4 Periodic table showing the element pairs for the formation of σ phase. The crystal structure and atomic radius of pure Cr, Co and Mo and the possible element pairs of σ phase are highlighted. [40]

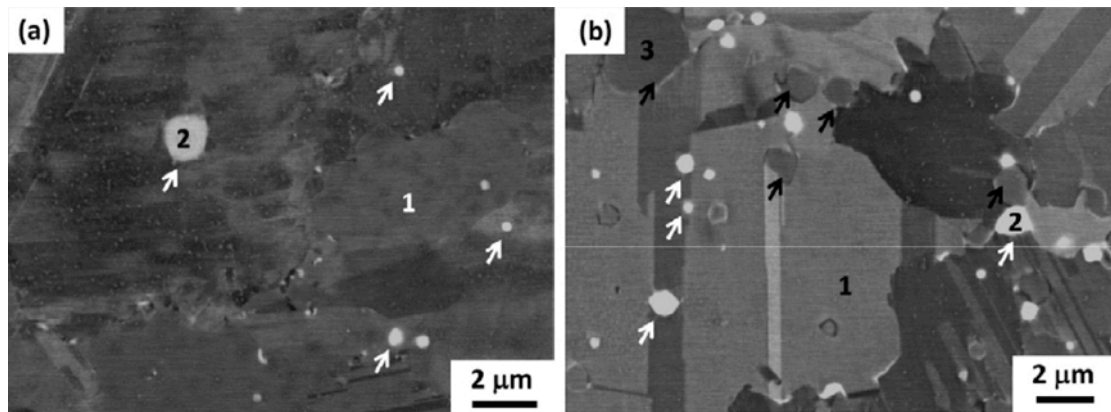


Figure 2.2.5 Compositional images showing the σ phases denoted by white arrows, respectively, for (a) low carbon and (b) high carbon alloys. [44]

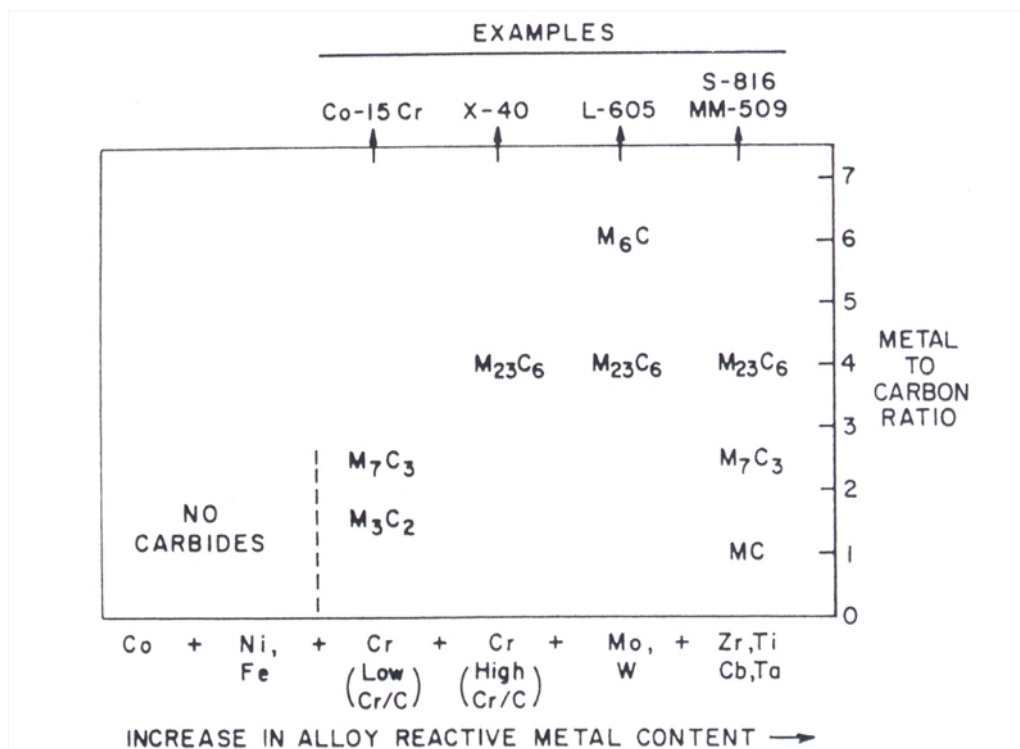


Figure 2.2.6 Effect of adding elements of varying electronegativity on type of carbides formed in Co-based alloys, carbon assumed 0.1-0.6 %. [46]

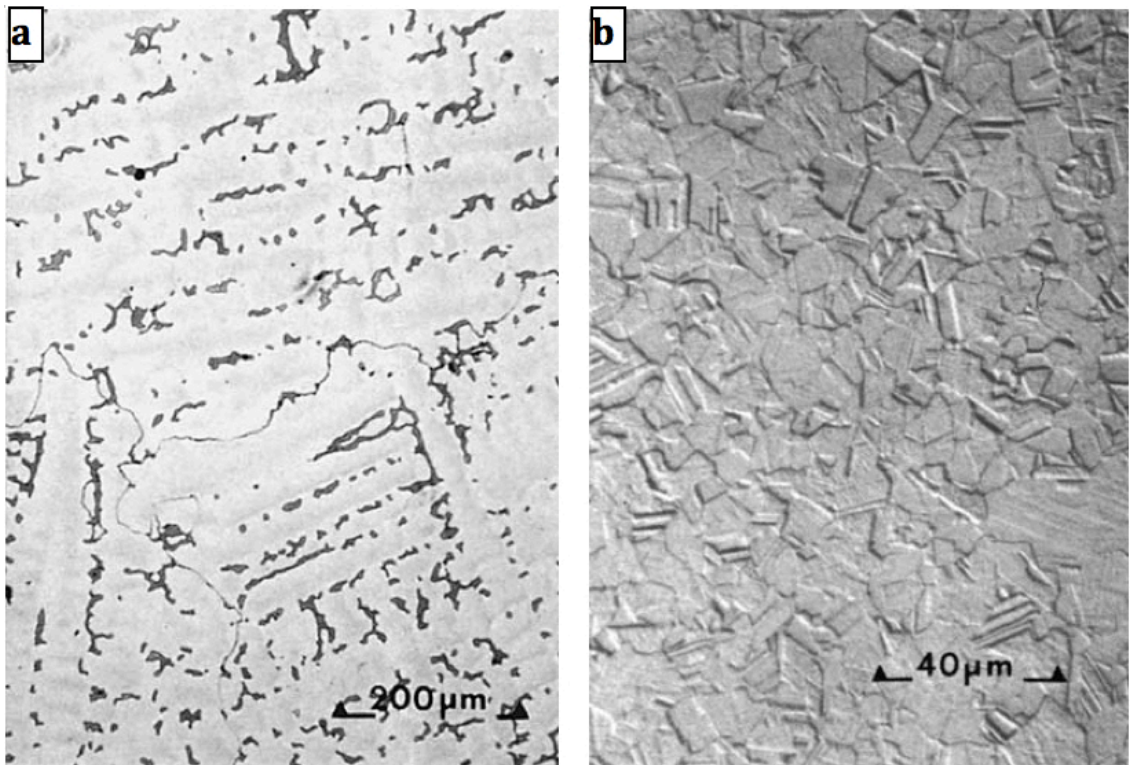


Figure 2.2.7 Effect of processing on the microstructure of Co-Cr-Mo surgical implant alloys. (a) Investment-cast alloy. (b) Forged alloy. [54]

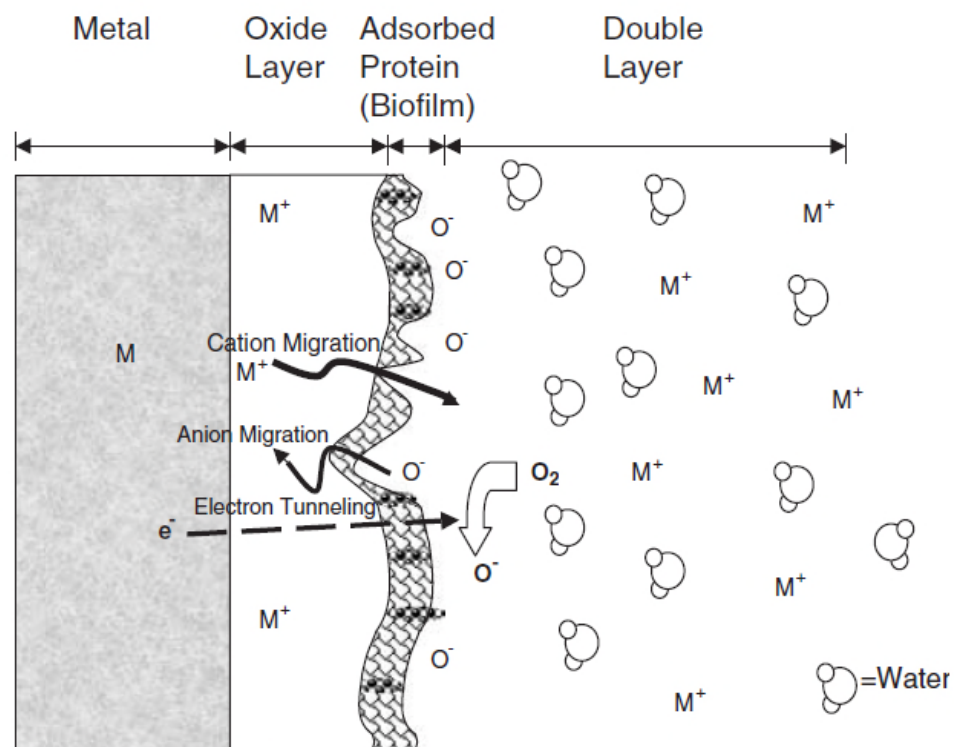


Figure 2.3.1 Schematic of the interface of a passivated metal surface in a biological solution. [1]

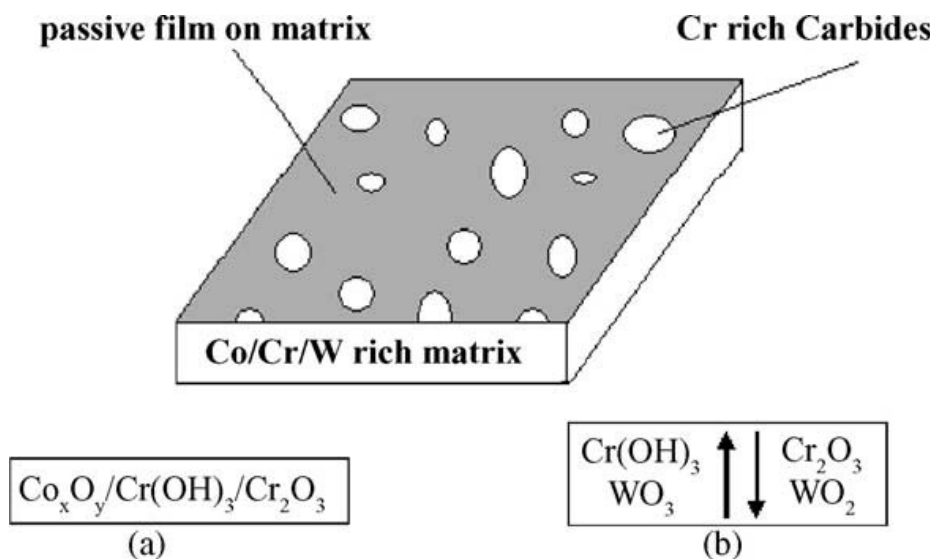


Figure 2.3.2 Key components of (a) the air-formed passive film and (b) corroded surface. [56]

Stellite6 / WC-Co

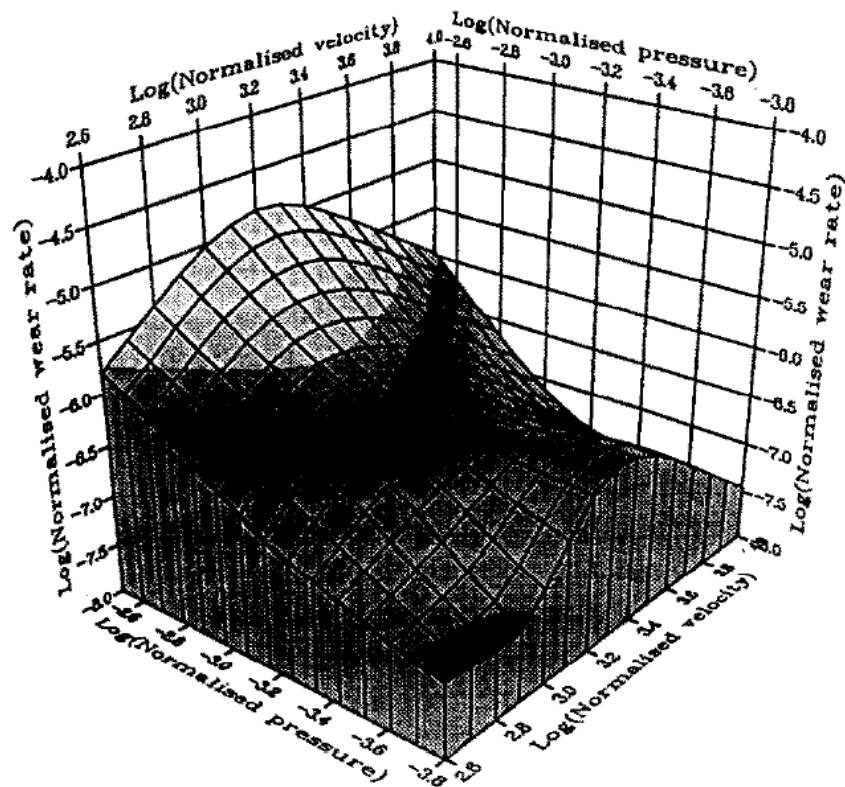


Figure 2.4.1 Dry sliding wear map for Stellite 6 against a WC-Co 90/10 disc. [72]

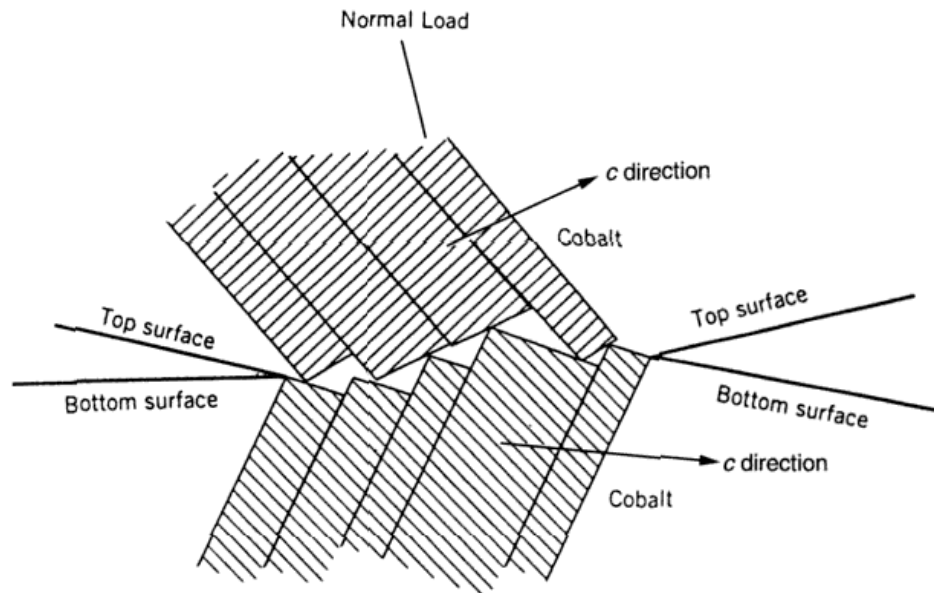


Figure 2.4.2 Schematic of plastic flow for hexagonal metals. Because of the limited number of slip planes, the two metals do not conform after slippage which reduces the degree of metal-metal contact. [74]

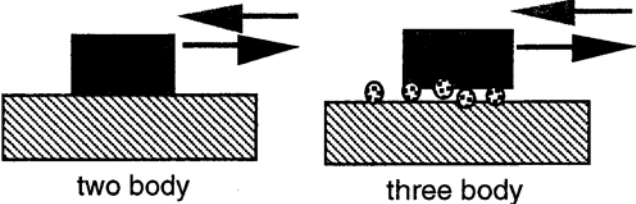
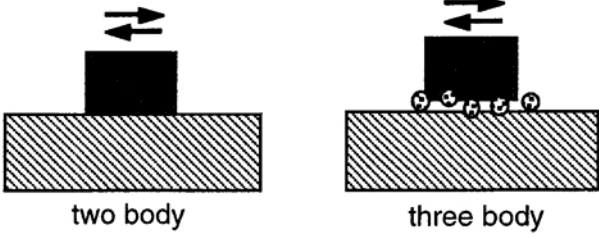
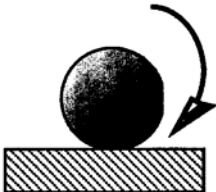
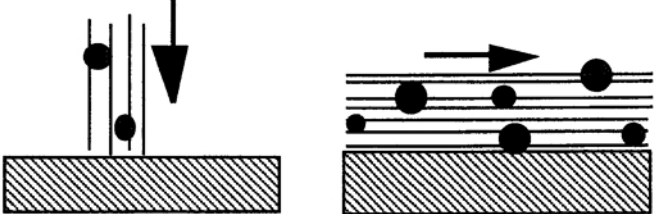
CONTACT MODE (names)	SCHEMATIC
Sliding <ul style="list-style-type: none"> - unidirectional - reciprocating <i>corrosive wear</i> <i>wear accelerated corrosion</i> <i>chemo-mechanical polishing</i>	 <p>two body three body</p>
Fretting	 <p>two body three body</p>
Rolling	
Impingement	

Figure 2.5.1 Different contact modes involving tribocorrosion. [81]

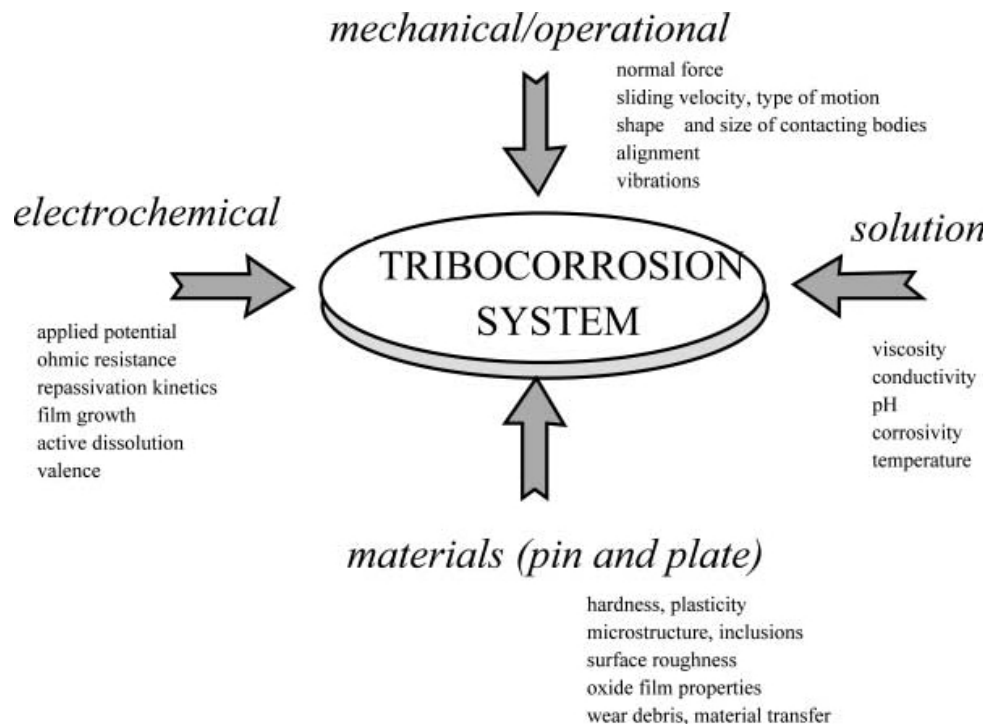


Figure 2.5.2 Schematic of four types of factors affecting the tribocorrosion system under electrochemical condition. [81]

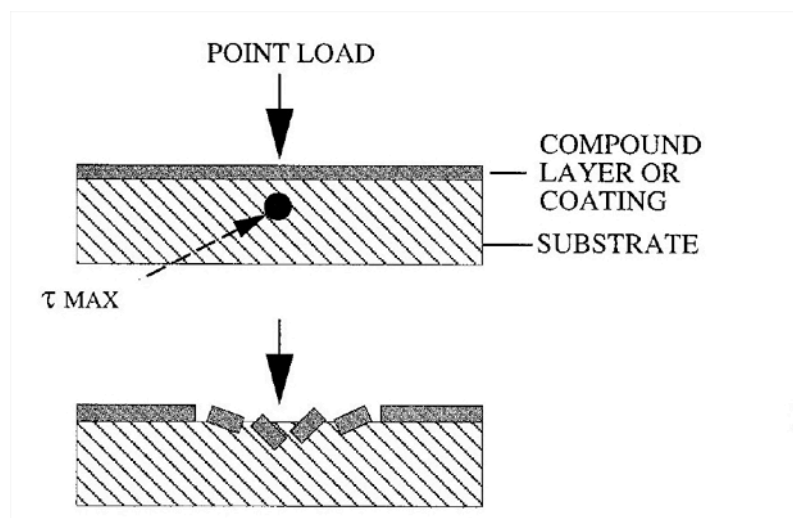


Figure 2.6.1 Schematic depiction of coating collapse caused by excessive point contact loading – the ‘thin-ice effect’. [92]

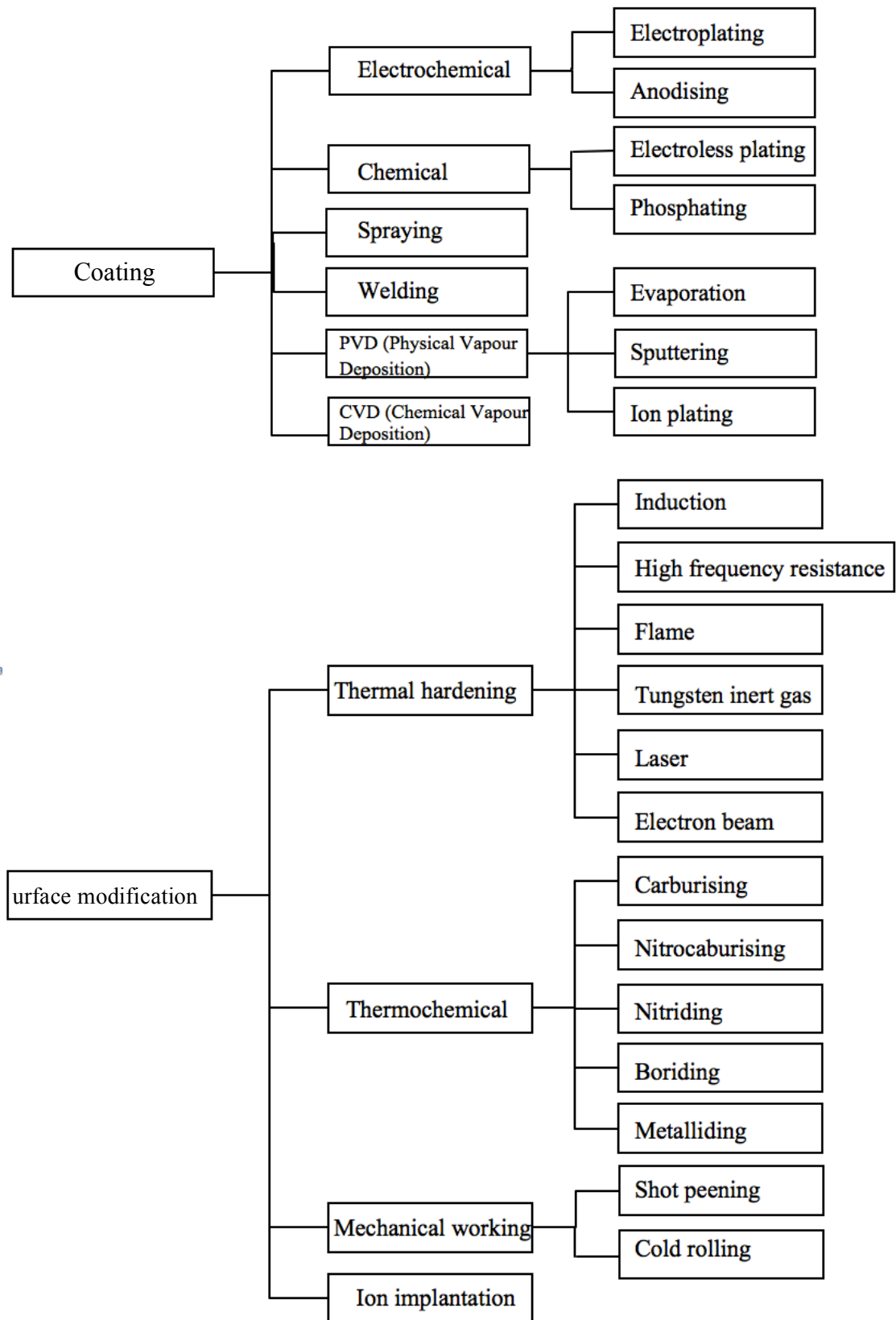


Figure 2.6.2 Classification of surface engineering technologies. [101]

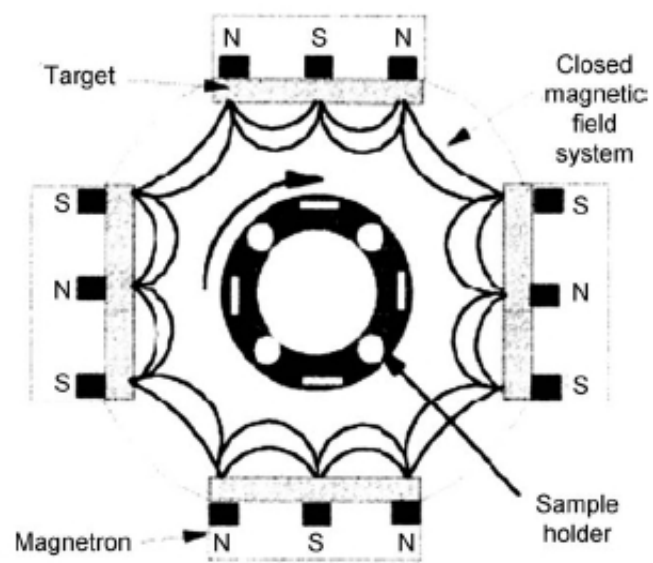


Figure 2.6.3 The closed field unbalanced magnetron sputter ion plating system (plan view). [121]

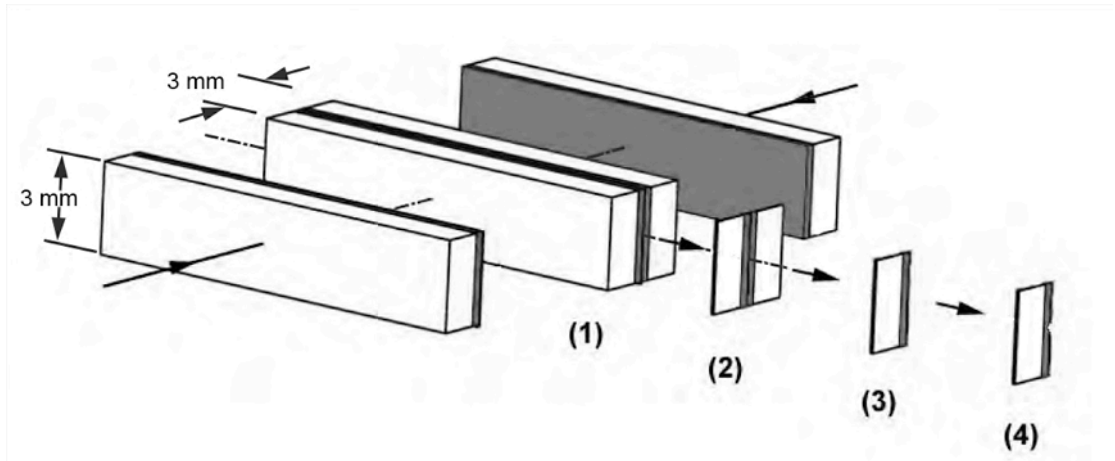


Figure 3.3.1 Schematic of the steps of a cross-sectional TEM sample preparation. [142]

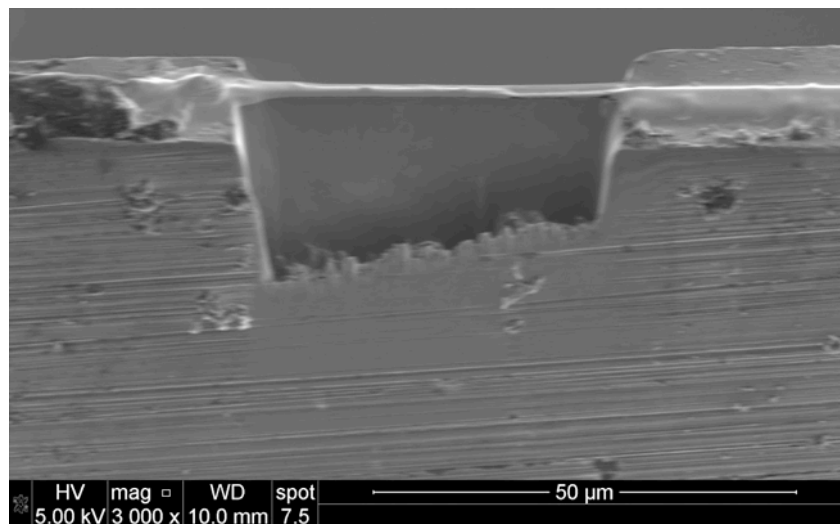


Figure 3.3.2 Secondary electron image of cross-sectional TEM sample thinned using a Quanta 3D FEG FIB miller

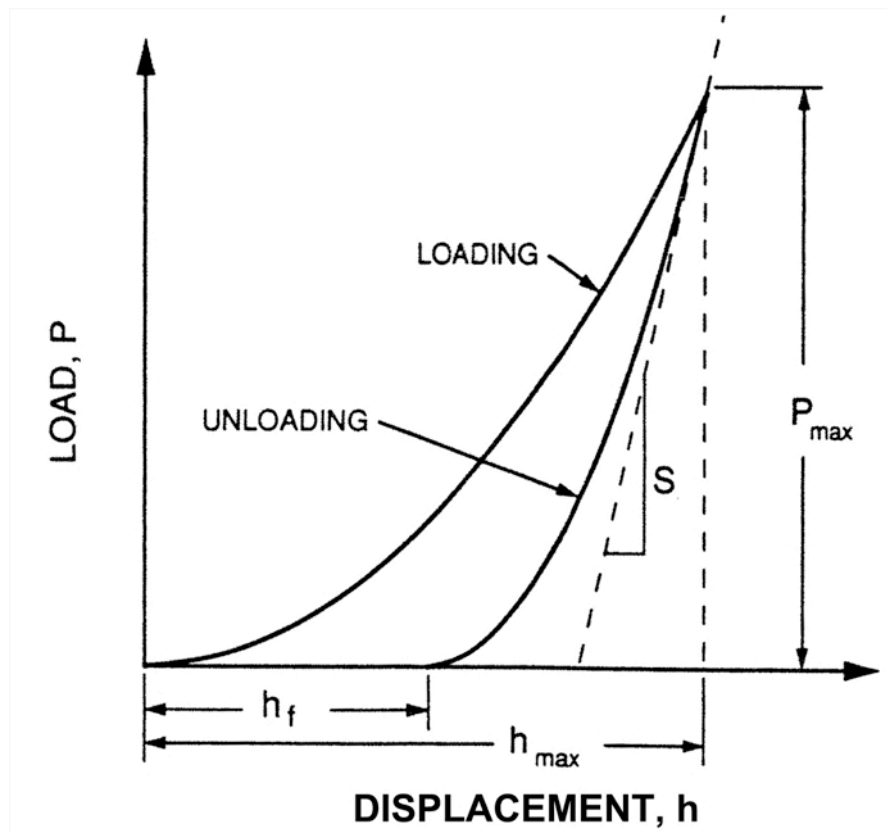


Figure 3.3.3 typical load-displacement curve measured using nanoindentation device. [143]

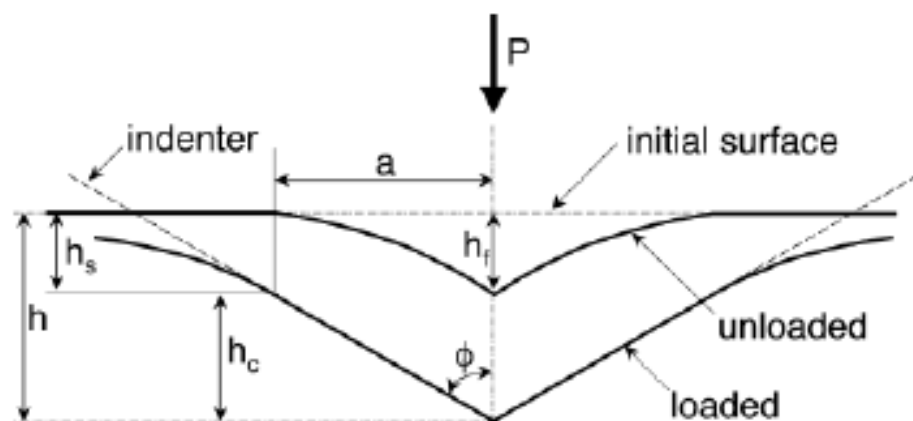


Figure 3.3.4 Schematic representation of cross-sectional view of an indent showing the parameters used for calculating hardness (H) and reduced elastic modulus (E_r). [143]

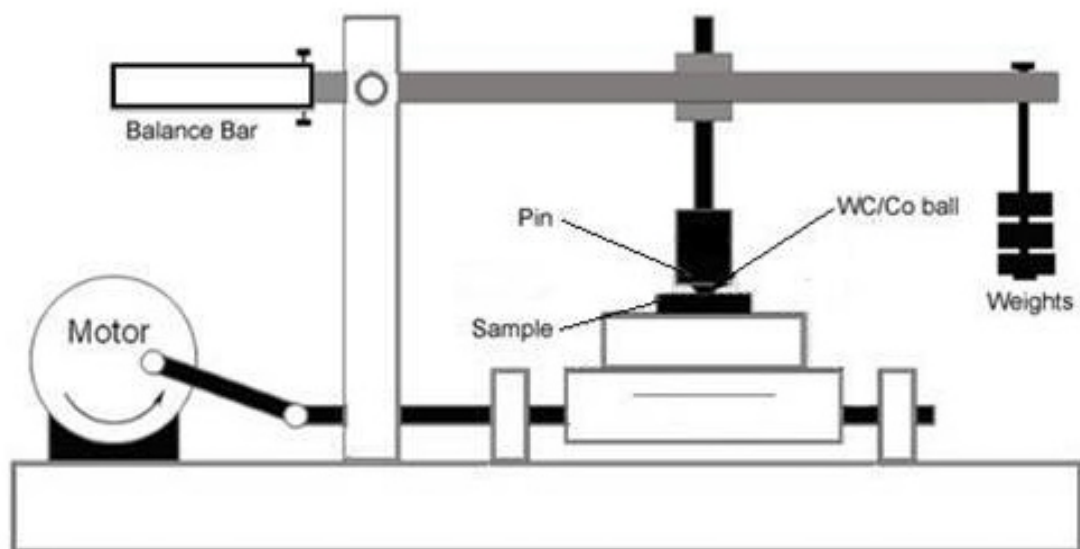


Figure 3.3.5 Schematic diagram of the reciprocating tribometer.

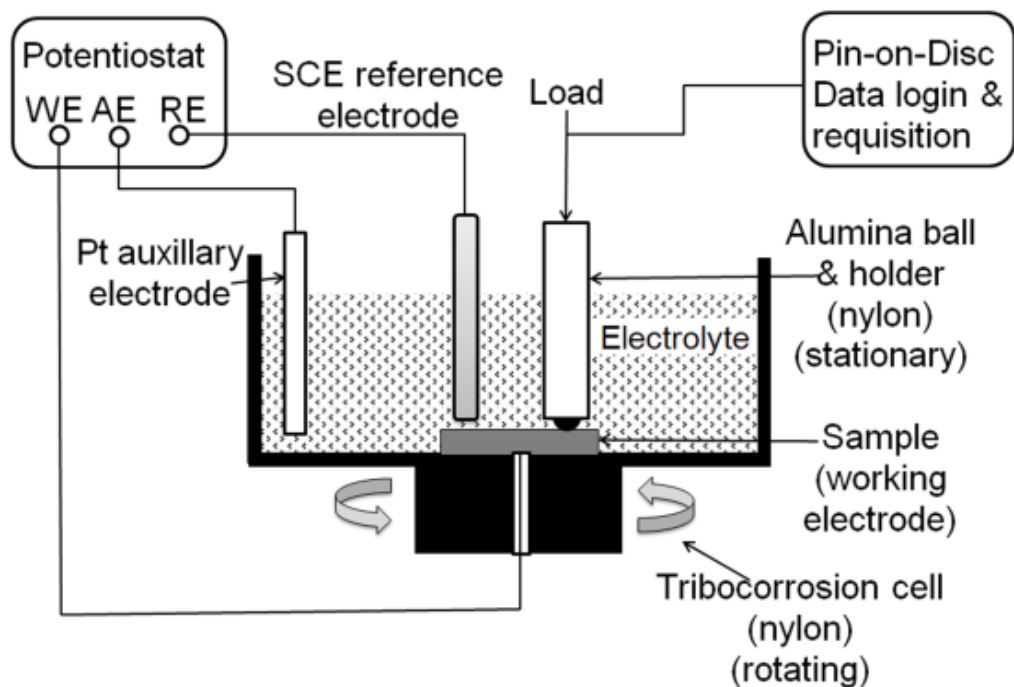


Fig. 3.3.6 Schematic diagram of the tribo-electrochemical cell. [84]

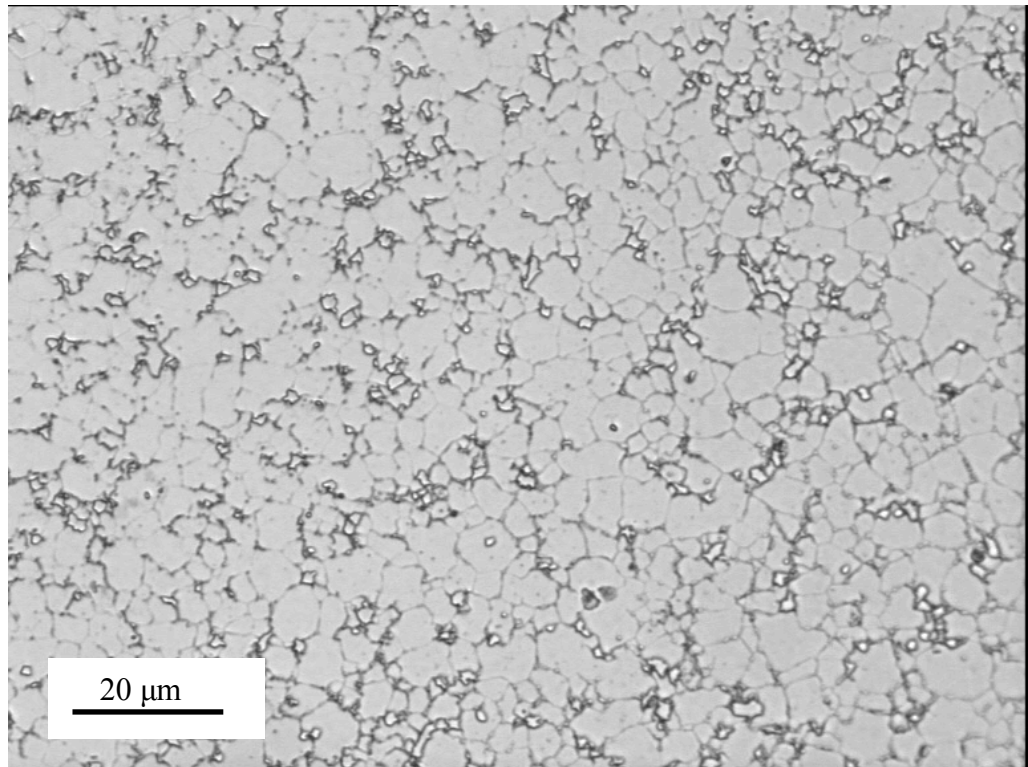


Figure 4.1.1 Optical micrographs showing the microstructure of the AR sample.

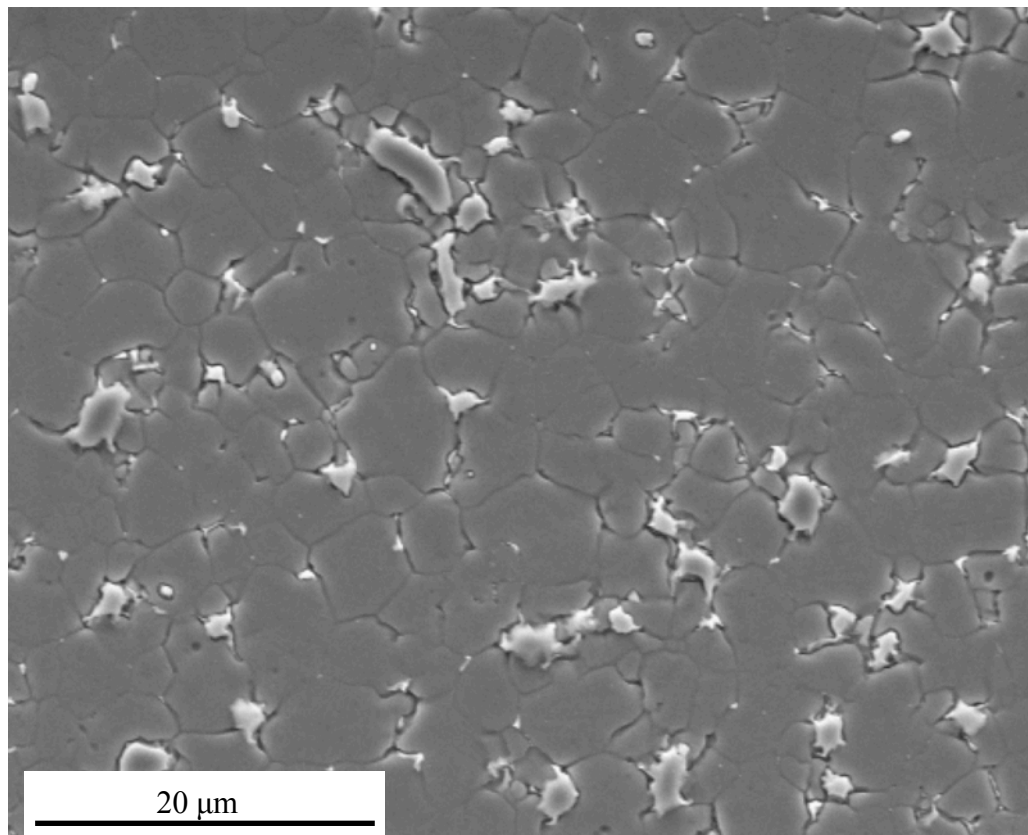


Figure 4.1.2 SEM observation showing the microstructure of the AR sample.

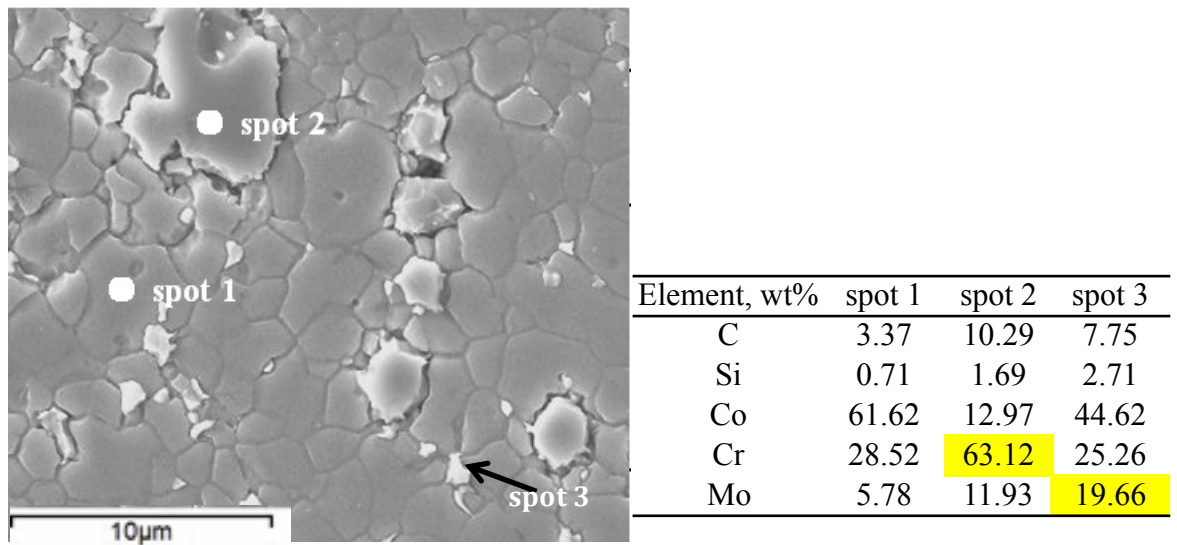


Figure 4.1.3 Secondary electron micrographs showing the microstructure of the AR sample and EDX analysis of the AR sample (high content of Cr or Mo is highlighted).

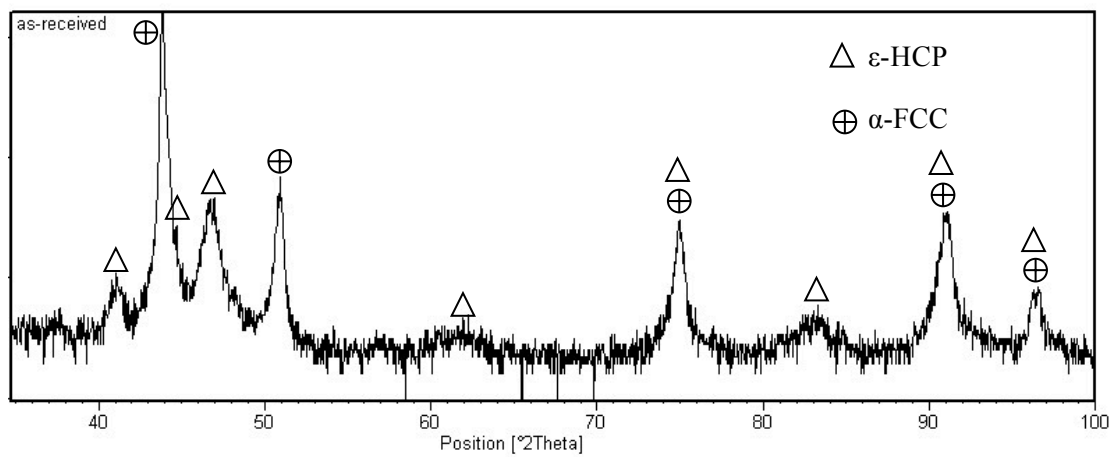
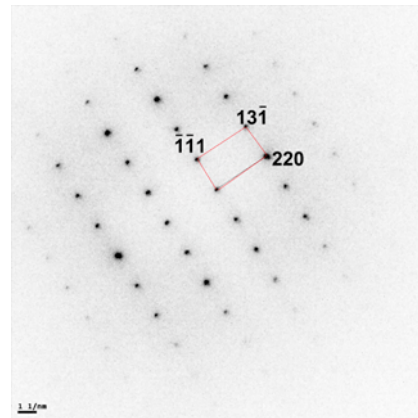
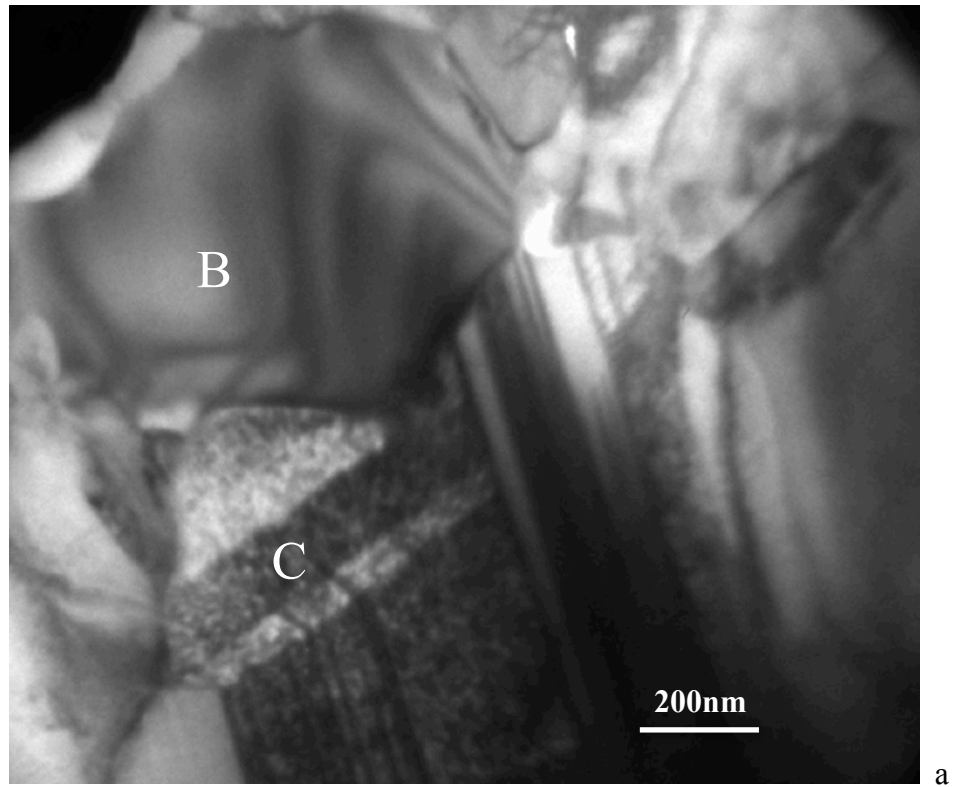
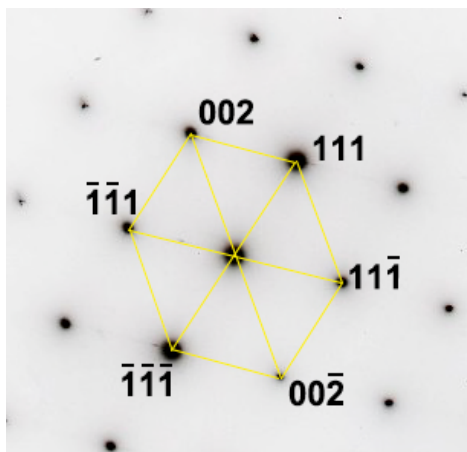


Figure 4.1.4 XRD spectra for the AR sample.

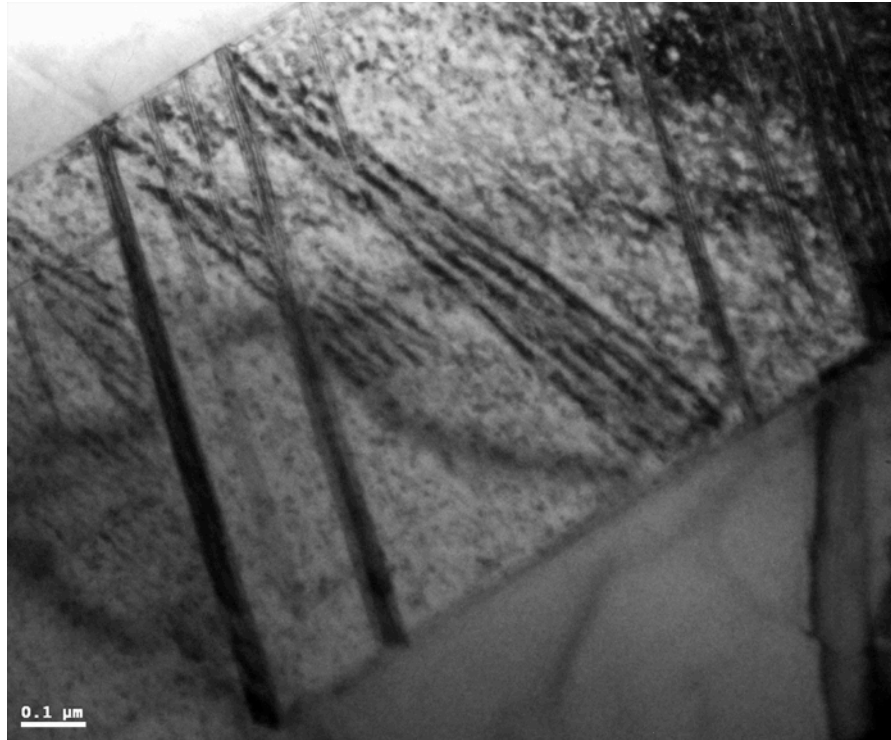


b $M_{23}C_6$ [$\bar{1}12$]

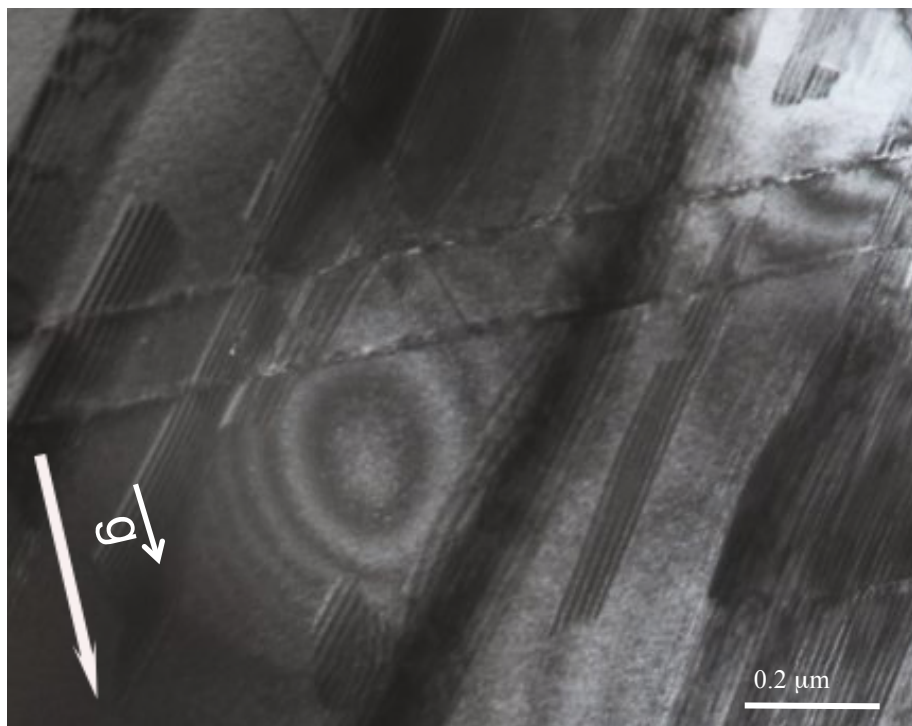


c FCC [110]

Figure 4.1.5 (a) TEM microstructure of AR sample and corresponding SAD patterns of (b) $M_{23}C_6$ carbide ($B=[\bar{1}12]$) from B area and (c) α -FCC phase ($B=[1\bar{1}0]$) from C area.

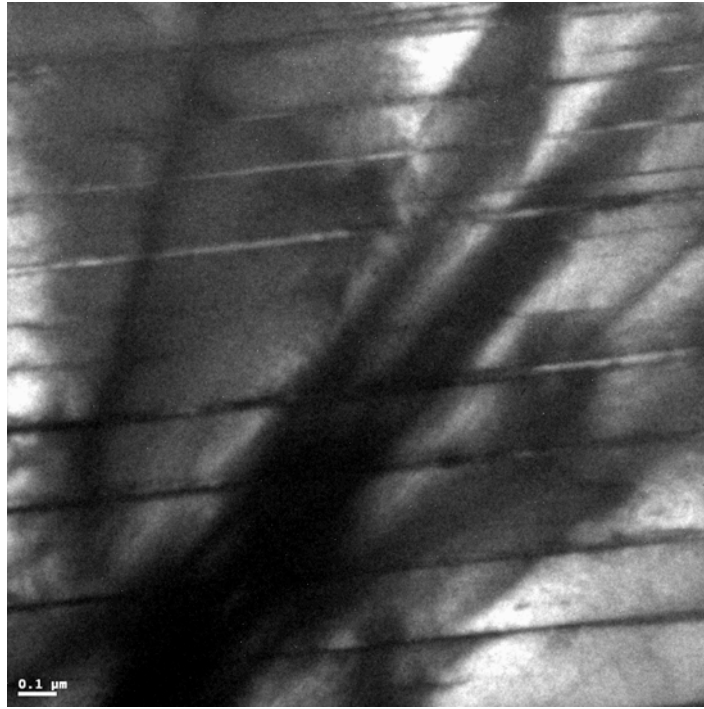


a

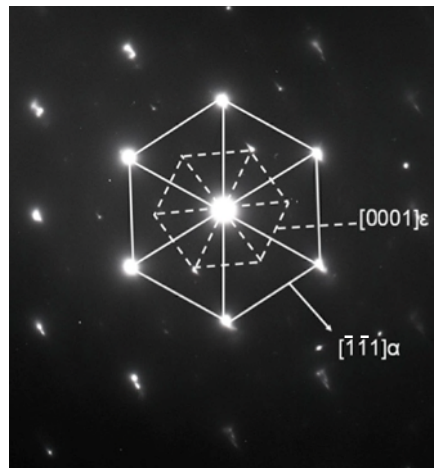


b

Figure 4.1.6 TEM microstructure of defects observed in the AR sample: a) Micro twins and b) stacking faults ($\vec{g} = [220]$).



a



b

Figure 4.1.7 (a) TEM micrograph and (b) corresponding SAD pattern from α -FCC and ϵ -HCP phases in the AR sample.

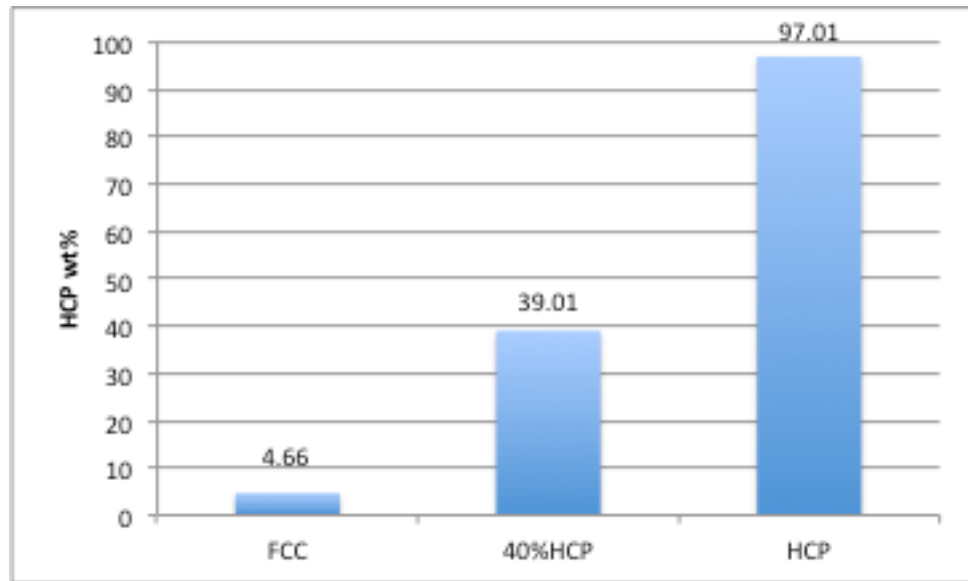


Figure 4.2.1 Amount of HCP phase after designed heat treatments based on XRD.

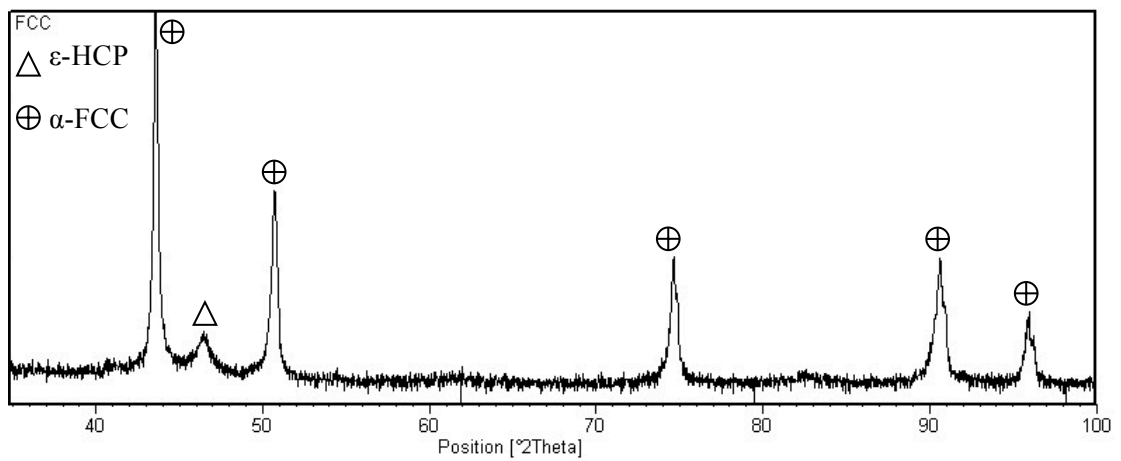
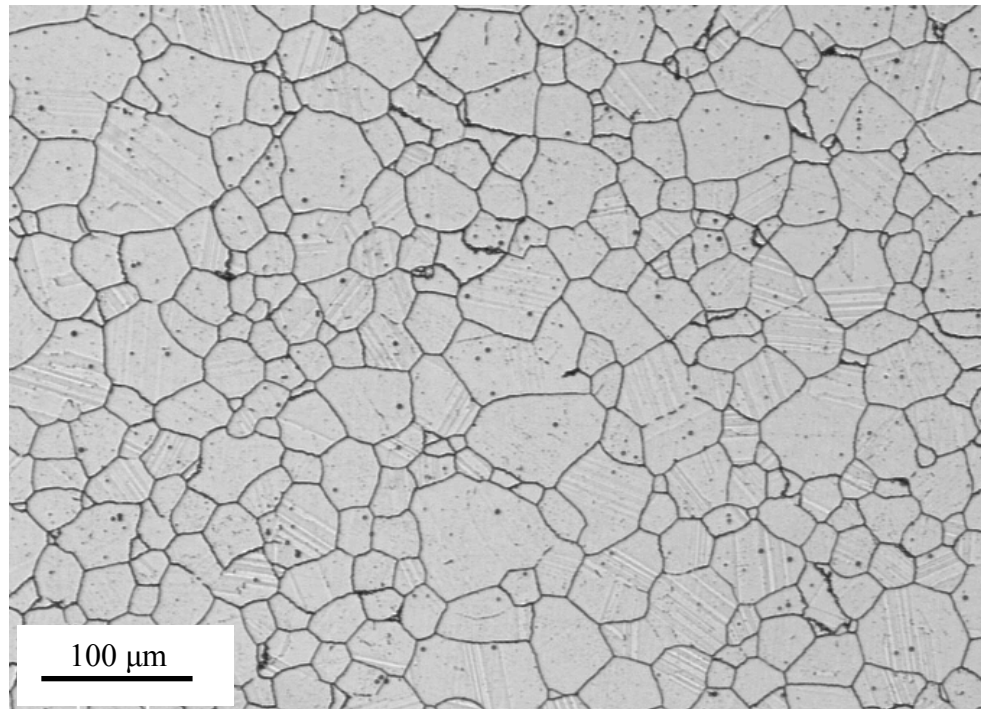
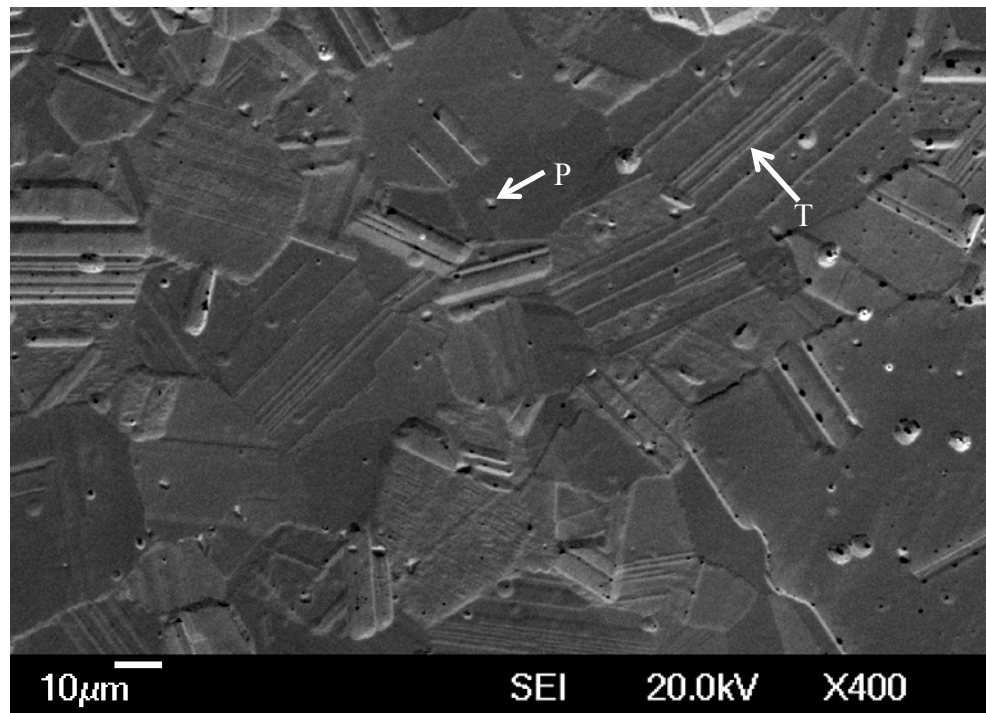


Figure 4.2.2 XRD spectra for the FCC sample



a



b

Figure 4.2.3 (a) Optical and (b) SEM microstructure of the FCC sample.

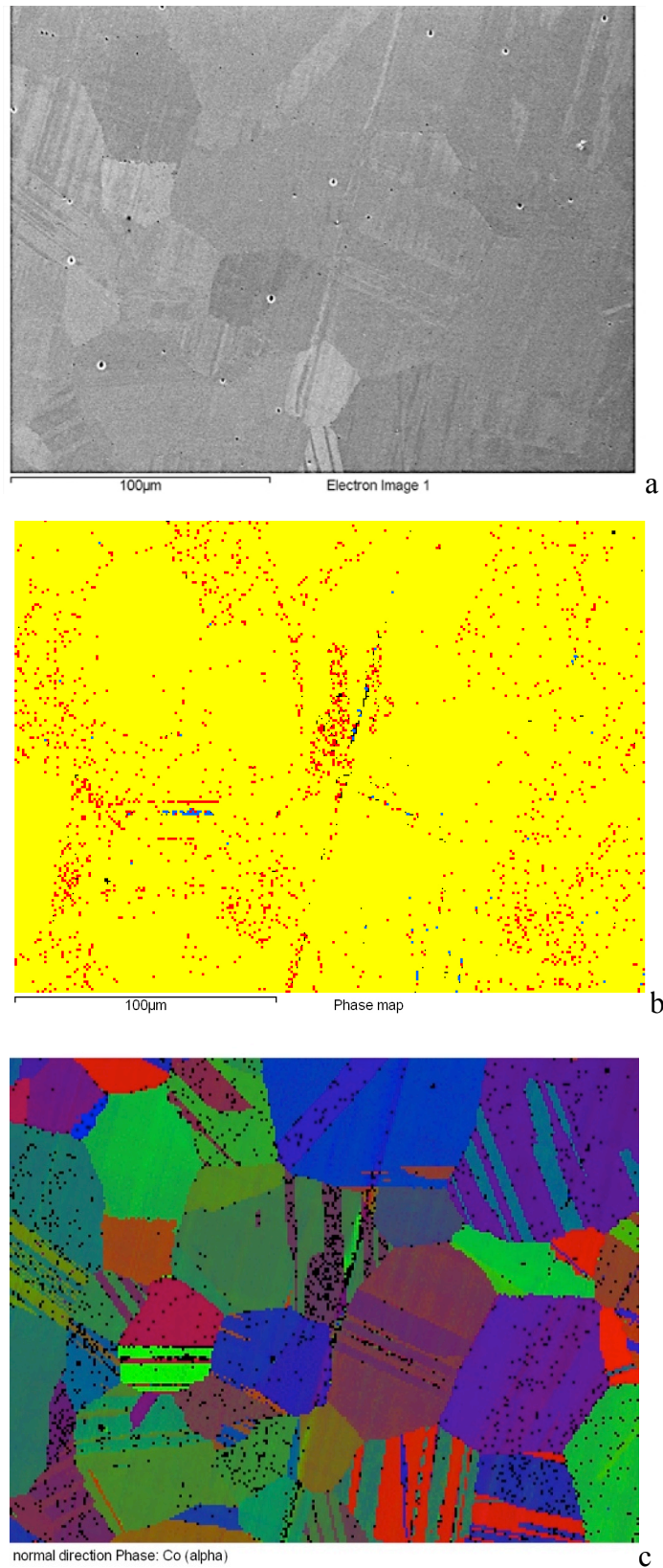


Figure 4.2.4 (a) SEM of as-polished (b) phase map showing the phase distribution with yellow for α -FCC, blue for ϵ -HCP and red for $M_{23}C_6$ ($M=Cr_{0.77}Co_{0.15}Mo_{0.08}$) and (c) crystal orientation map of the FCC sample,

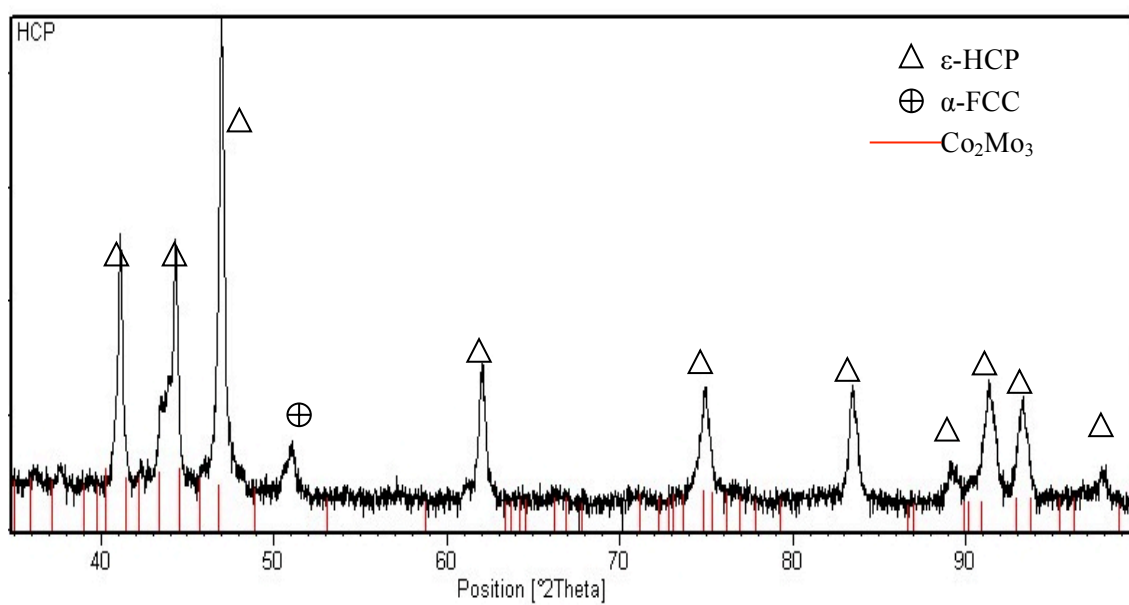
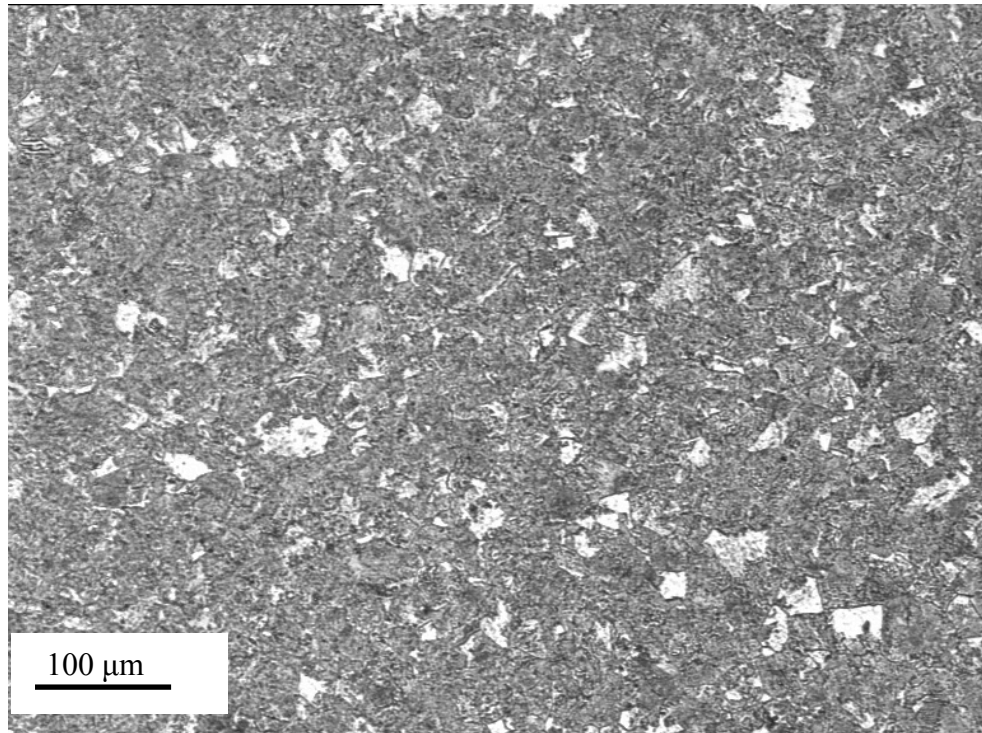
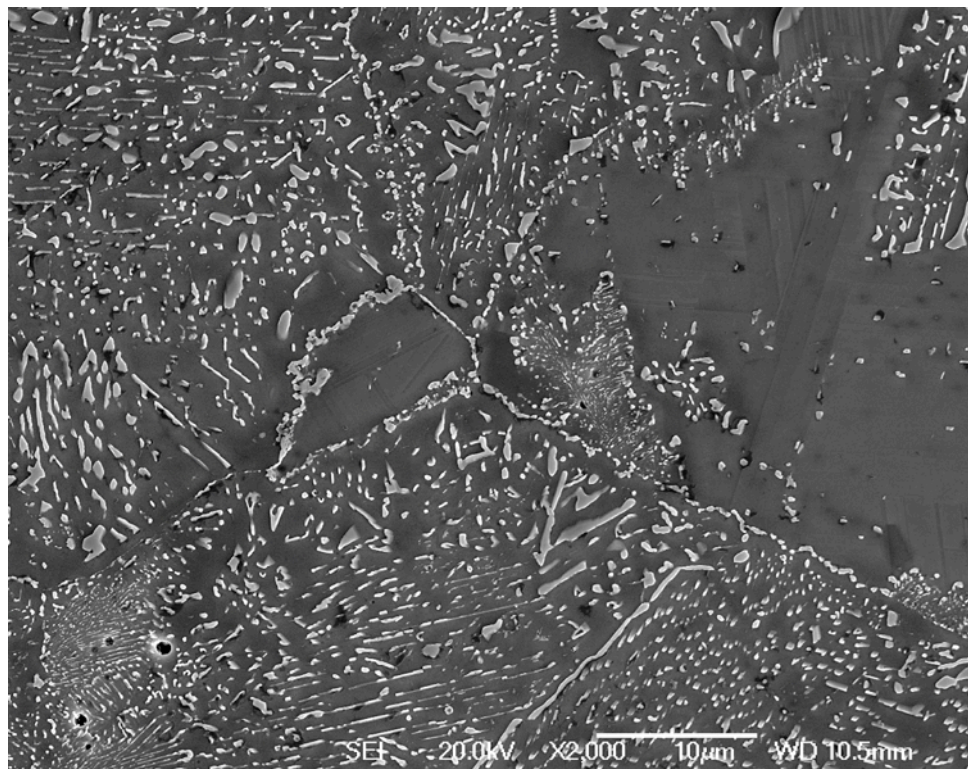


Figure 4.2.5 XRD spectra for the HCP sample.



a



b

Figure 4.2.6 Optical and SEM micrograph showing the microstructure of HCP sample.

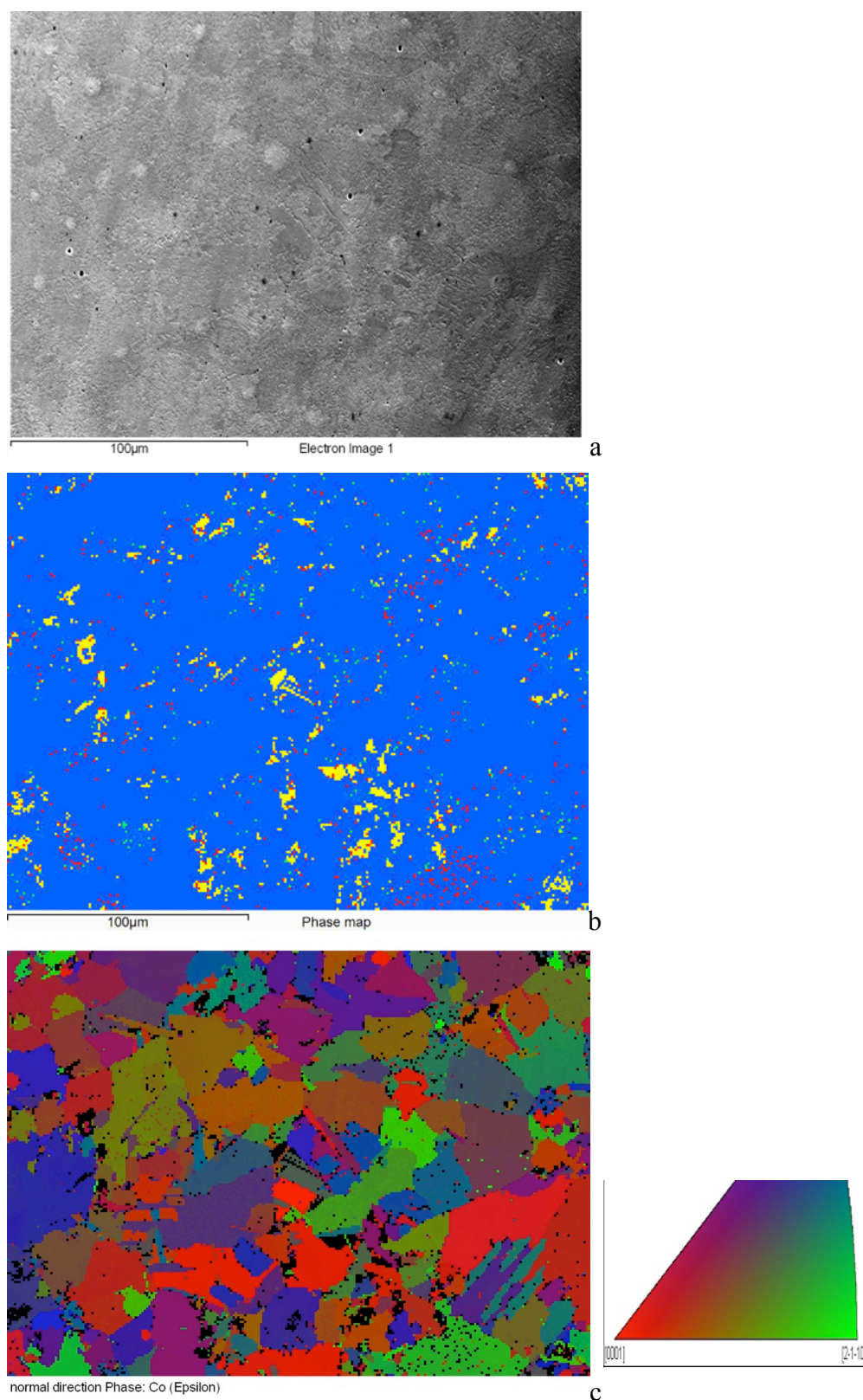


Figure 4.2.7 (a) SEM, (b) phase map (yellow for α -FCC, blue for ϵ -HCP, red for $M_{23}C_6$ ($M=Cr_{0.77}Co_{0.15}Mo_{0.08}$)) and light green for sigma phase (c) crystal orientation map of ϵ -HCP coloured according to the crystal direction parallel to the normal direction of HCP sample.

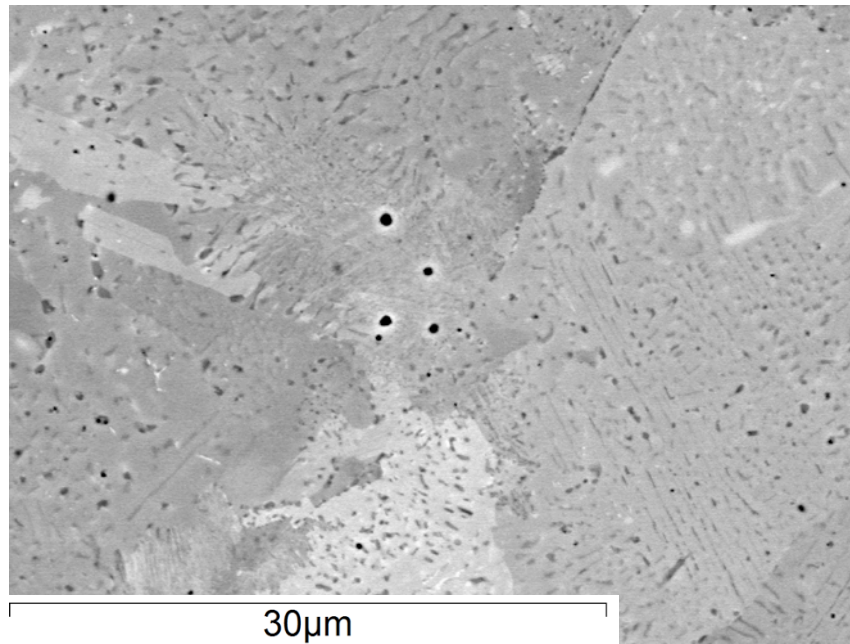


Figure 4.2.8 Back-scattered electron microscope image showing the microstructure of the HCP sample.

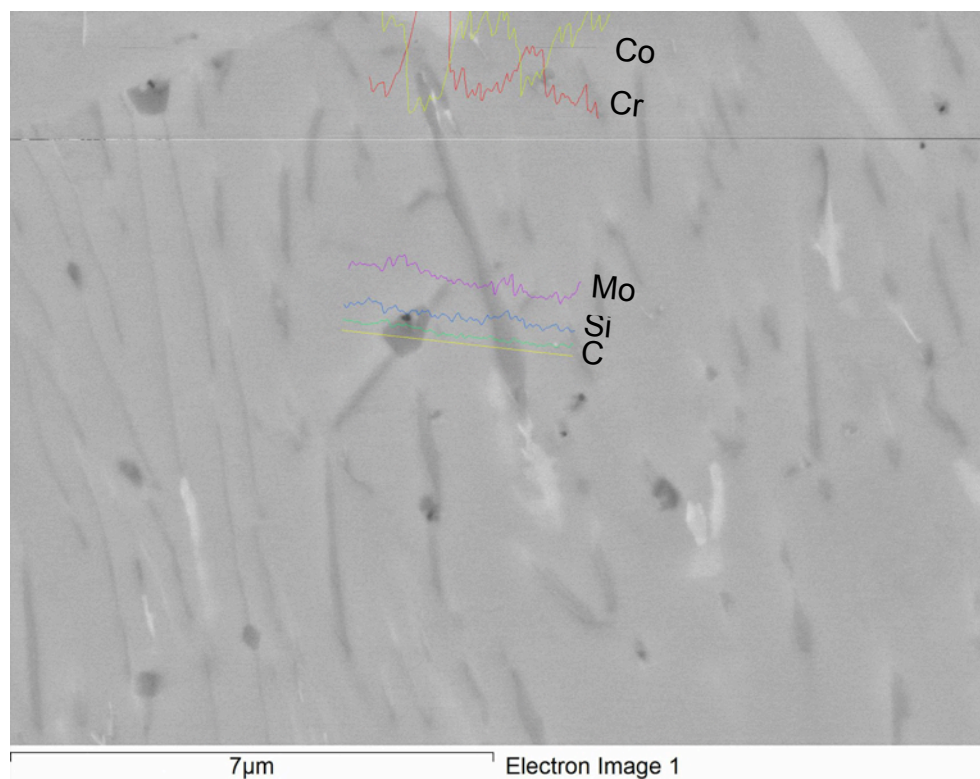
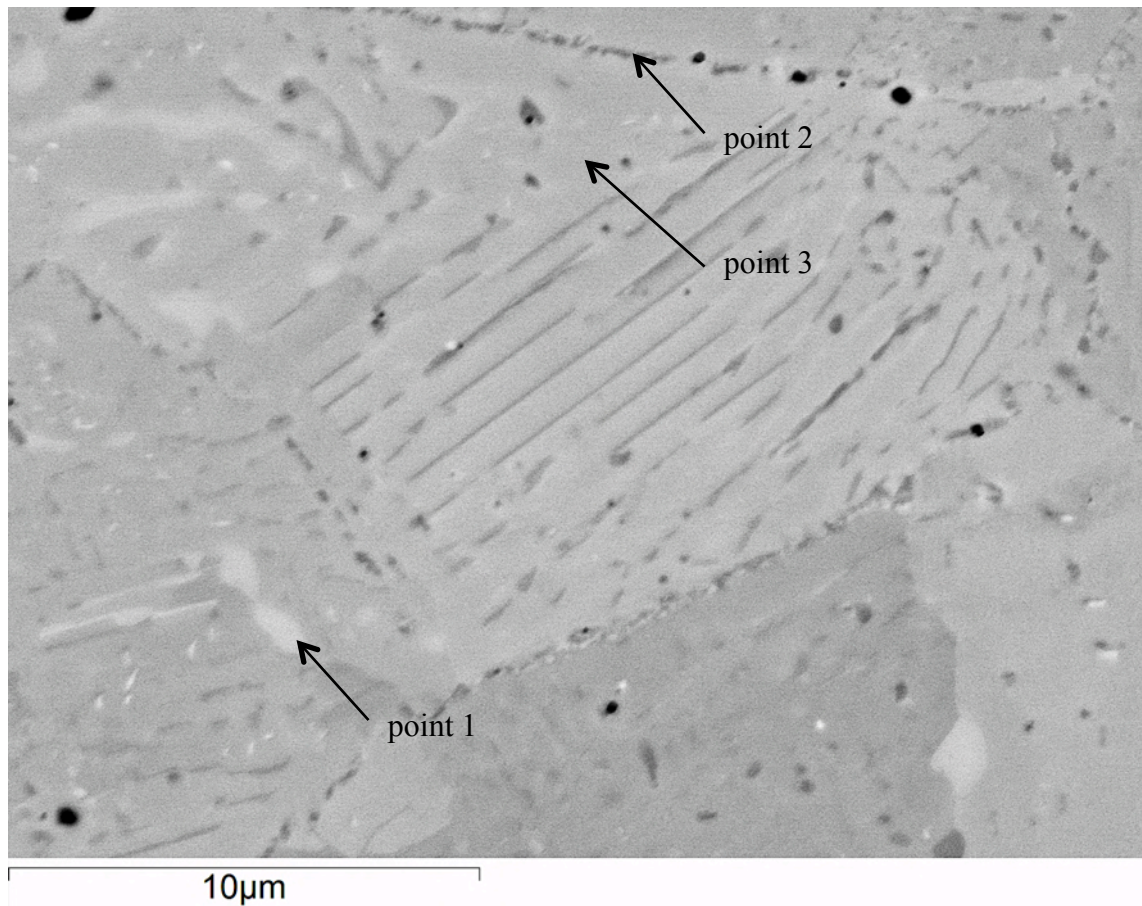


Figure 4.2.9 EDX line scan across the dark contrasted thin plate and irregular shape microstructures



wt %	C	Si	Cr	Mn	Co	Mo	Possible phase
point 1	4.05	0.92	34.57	0.84	49.84	9.77	$\text{Co}_2(\text{Cr},\text{Mo})_3$ σ
point 2	5.94	0.67	29.17	0.73	58.12	5.36	M_{23}C_6
point 3	3.97	0.45	27.32	0.89	62.58	4.79	HCP Co

Figure 4.2.10 EDX analysis on white and dark contrasted particles.

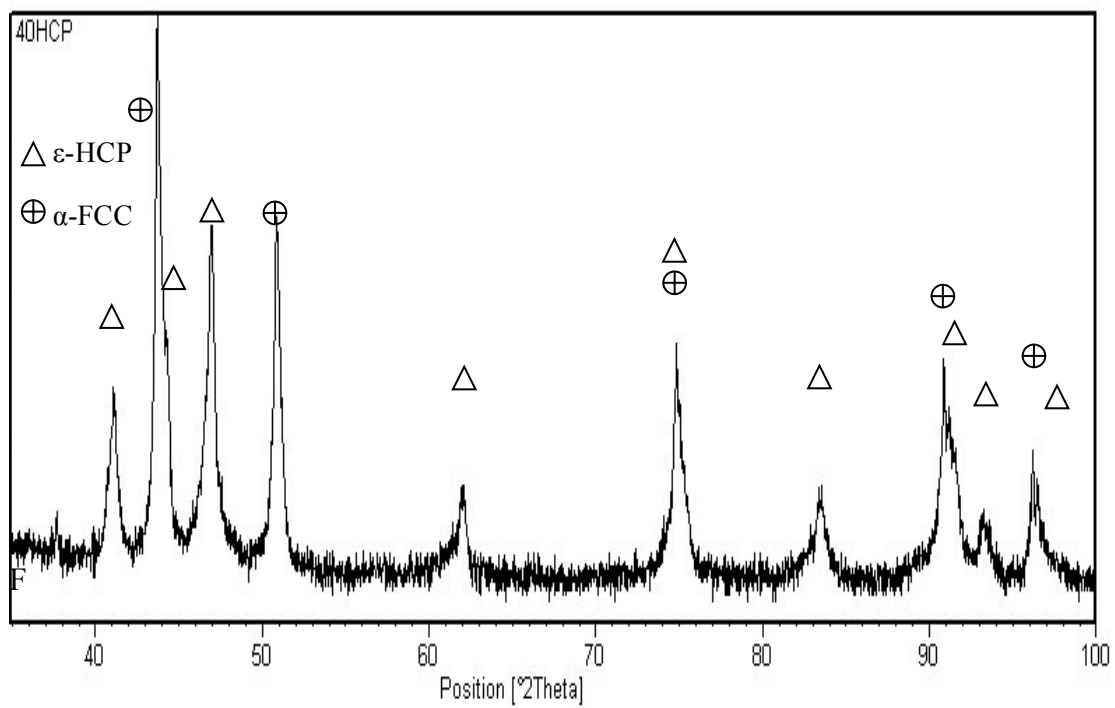


Figure 4.2.11 XRD spectra for 40HCP sample.

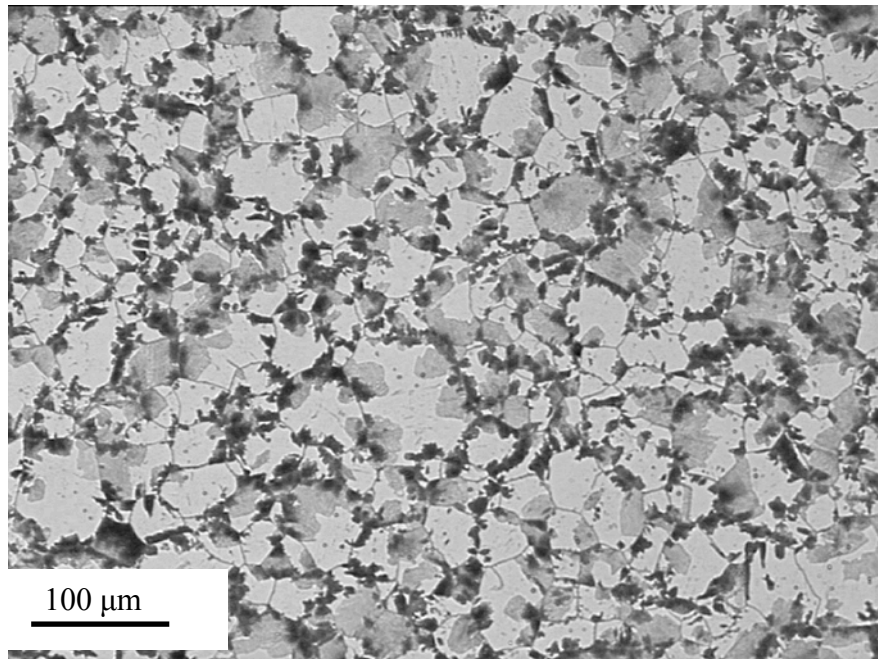


Figure 4.2.12 optical micrograph showing the microstructure of 40HCP sample.

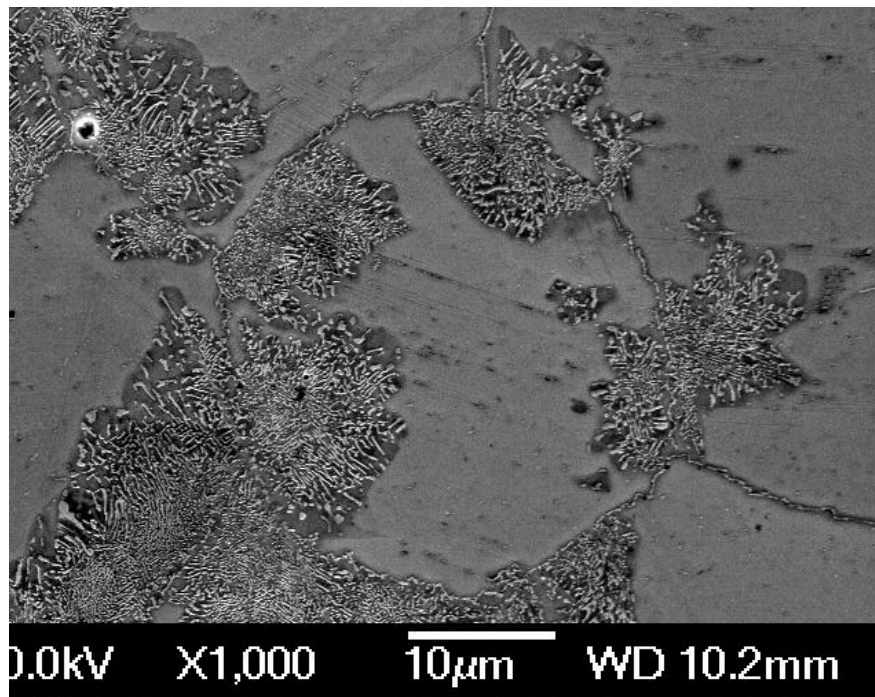


Figure 4.2.13 SEM micrograph showing the microstructure of 40HCP sample.

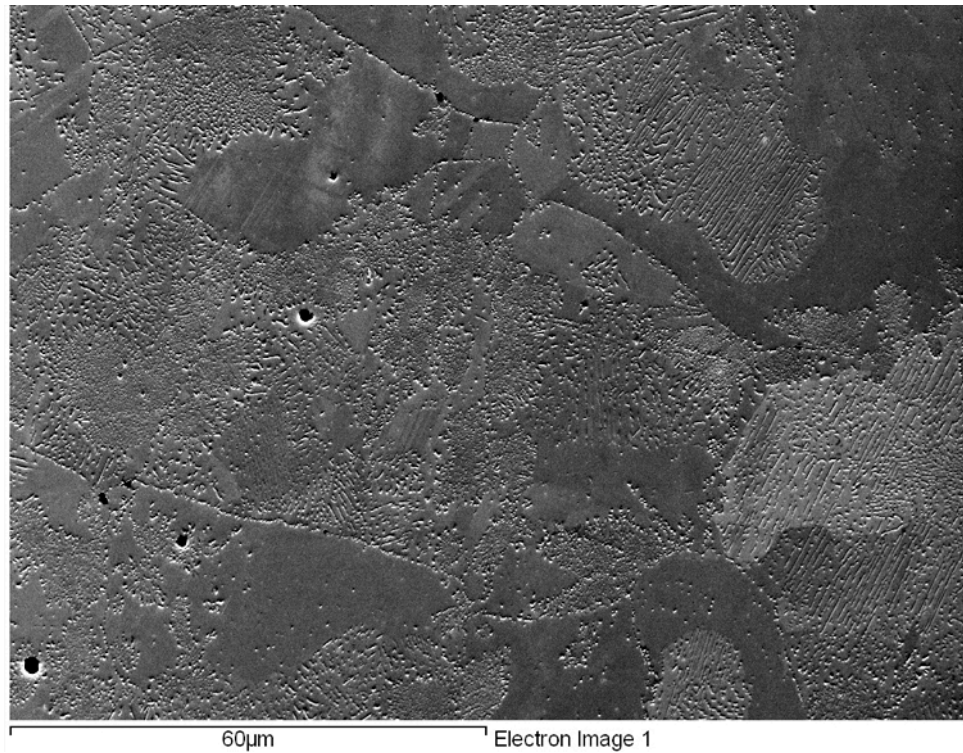


Figure 4.2.14 (a) secondary electron micrograph of as-polished 40HCP sample.

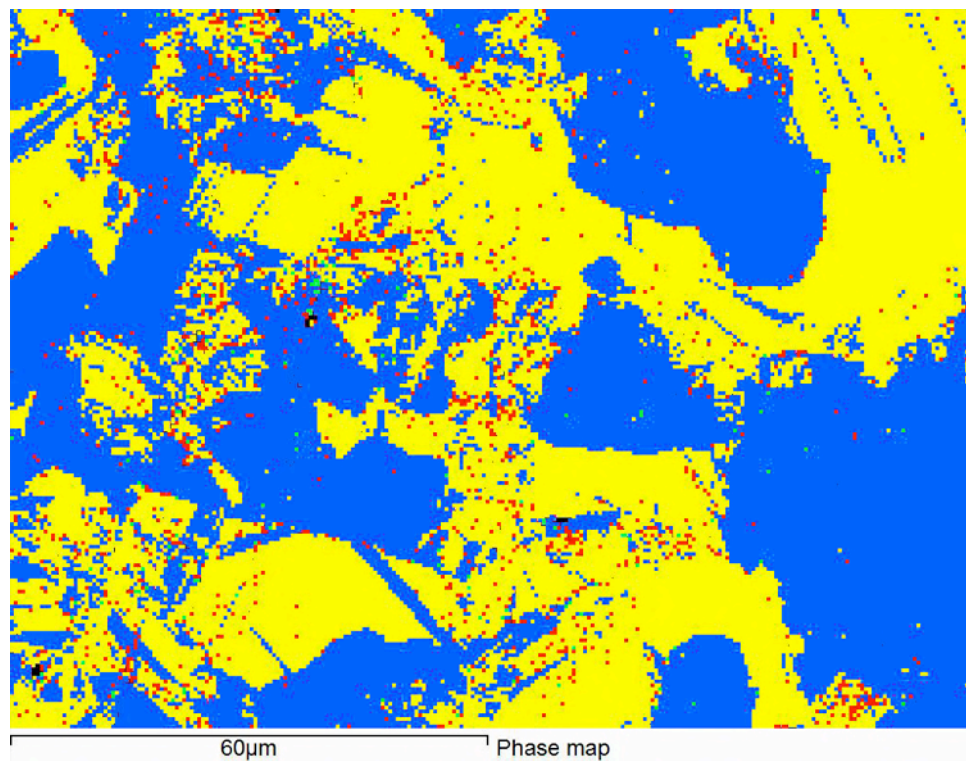


Figure 4.2.14 (b) phase map showing the phase distribution with yellow for α -FCC, blue for ϵ -HCP, red for $M_{23}C_6$ ($M=Cr_{0.77}Co_{0.15}Mo_{0.08}$) and light green for sigma phase.

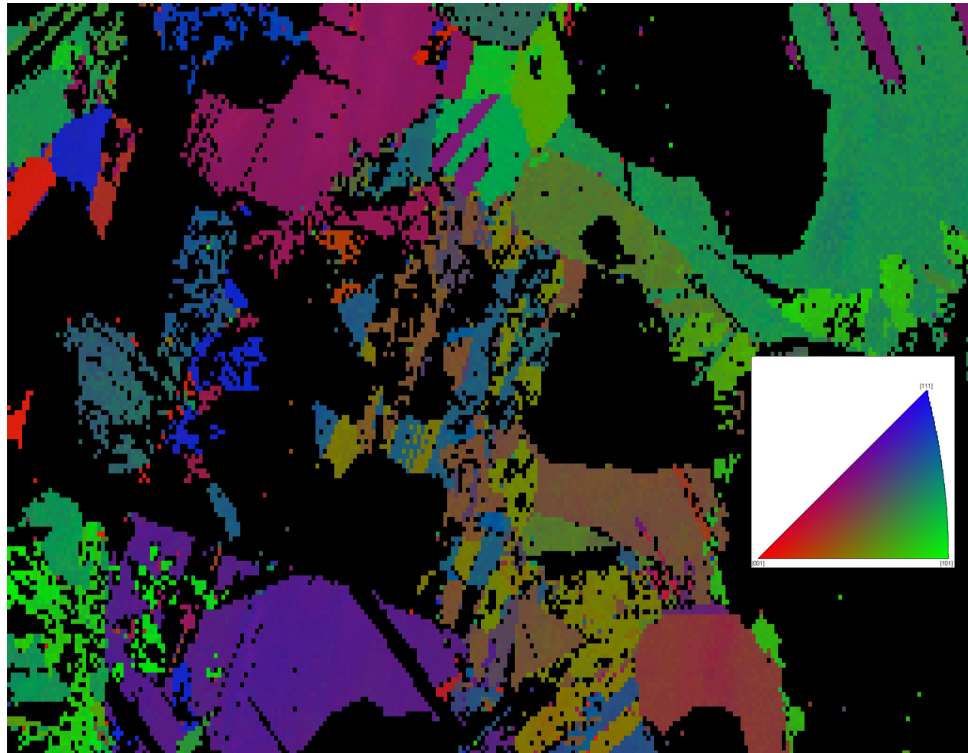


Figure 4.2.14 (c) crystal orientation map of α -FCC coloured according to the crystal direction parallel to the normal direction of 40HCP sample.

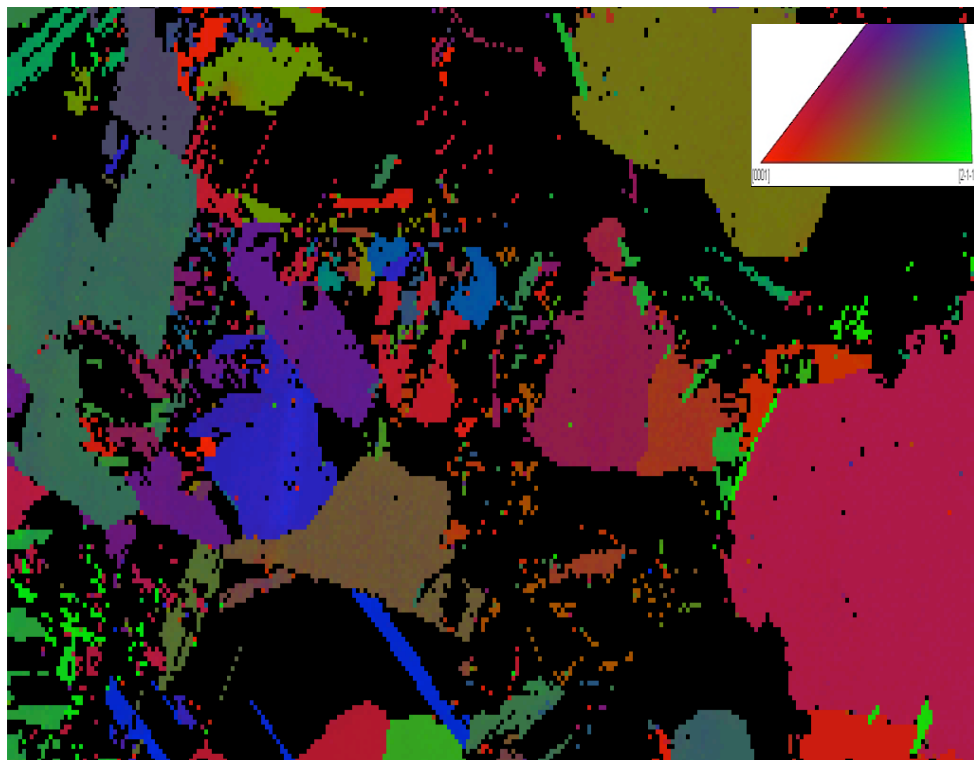
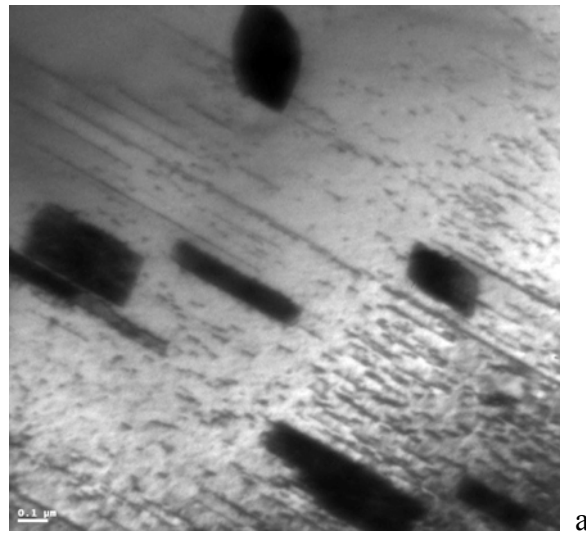
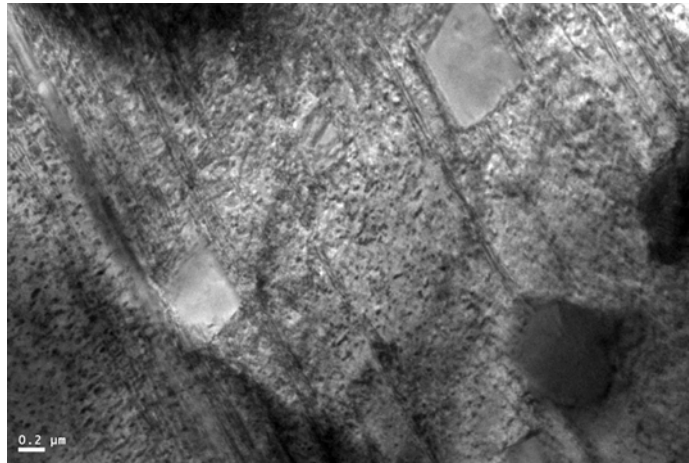


Figure 4.2.14 (d) crystal orientation map of ϵ -HCP coloured according to the crystal direction parallel to the normal direction of 40HCP sample.

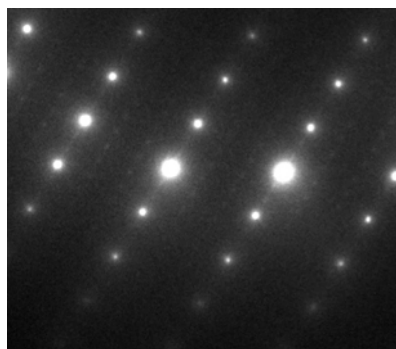


a

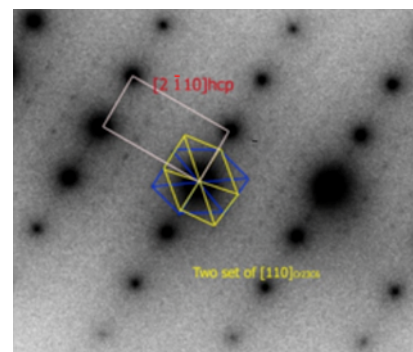


b

Figure 4.2.15 Bright field TEM microstructure of thin rectangle blocks from 40HCP sample (a) longitudinal view and (b) transverse view.

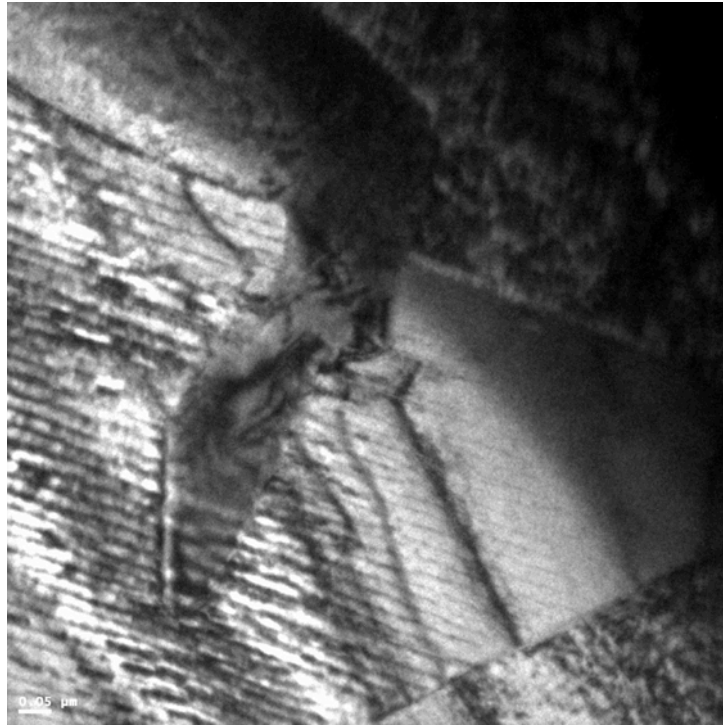


a

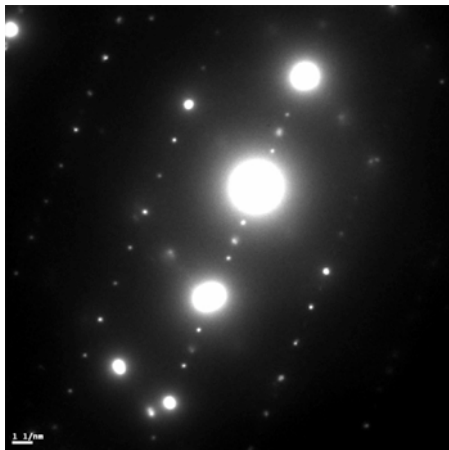


b

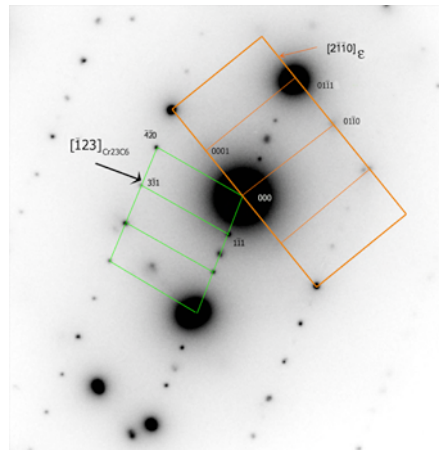
Figure 4.2.16 (a) SAD pattern taken from the precipitates shown in Figure 4.2.15. (b) Indexing of the patterns: $[2\bar{1}10]_{\text{HCP}} // [110]_{\text{M}_{23}\text{C}_6}$



a

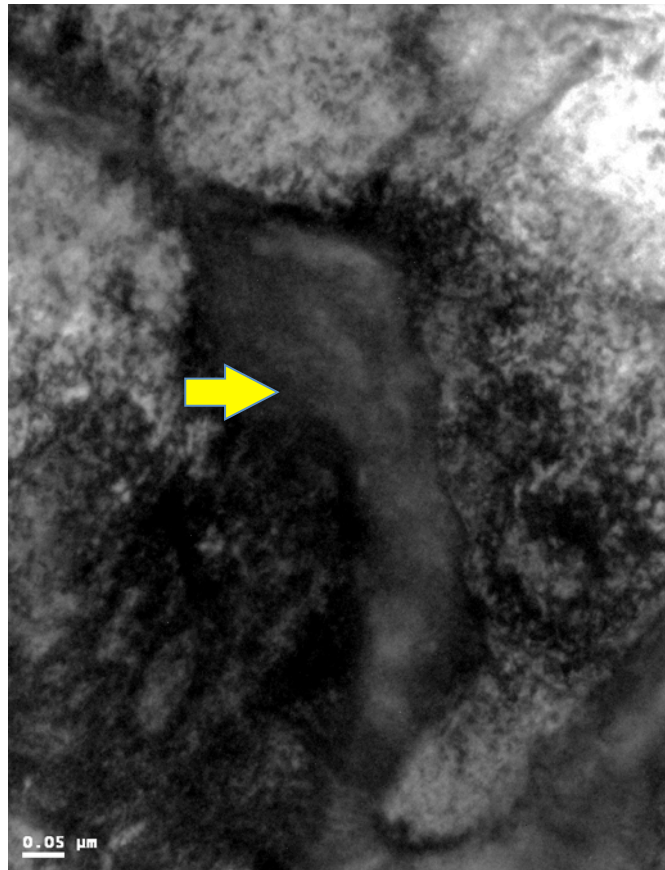


b

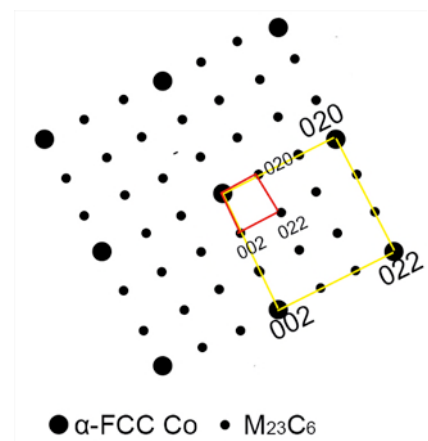


$[2\bar{1}\bar{1}0]_{\epsilon}/[\bar{1}23]_{M_{23}C_6}$, $(01\bar{1}1)_{\epsilon}/(1\bar{1}1)_{M_{23}C_6}$

Figure 4.2.17 (a) Bright field TEM microstructure and b) corresponding SAD pattern showing ϵ -HCP matrix and irregular shaped $M_{23}C_6$ particle in 40HCP sample.

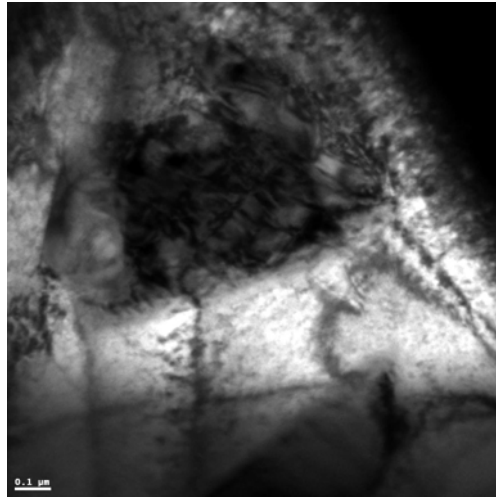


a



b $[100]_{\alpha} // [100]_{M_{23}C_6}$, $(002)_{\alpha} // (002)_{M_{23}C_6}$

Figure 4.2.18 (a) Bright field TEM microstructure and b) corresponding SAD pattern, showing irregular shaped $M_{23}C_6$ particles along FCC matrix grains in 40HCP sample.



a

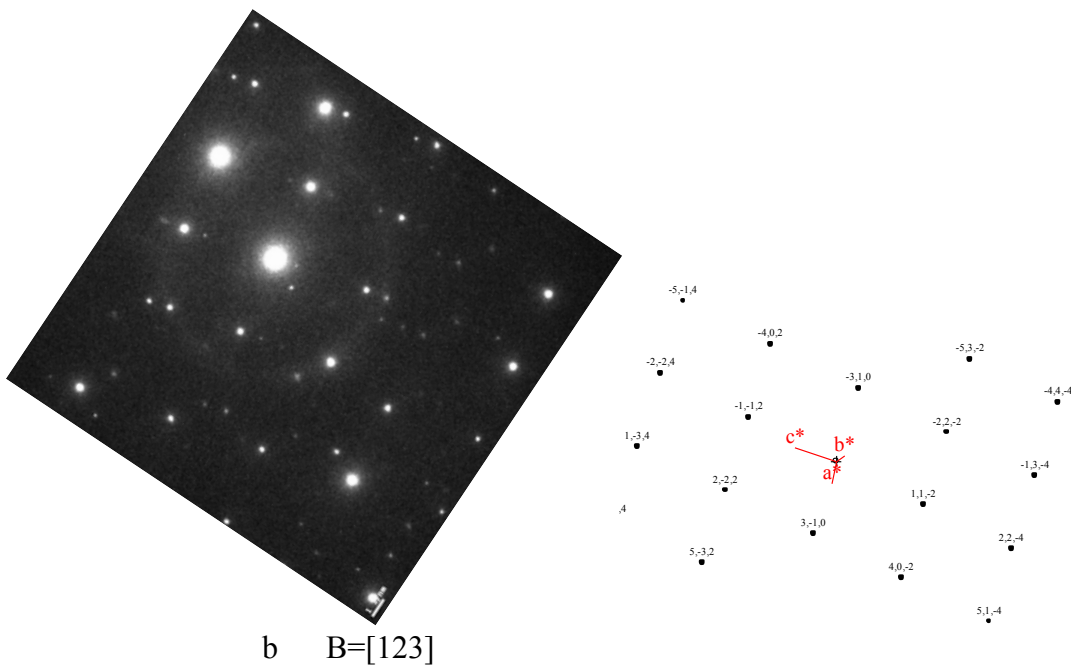
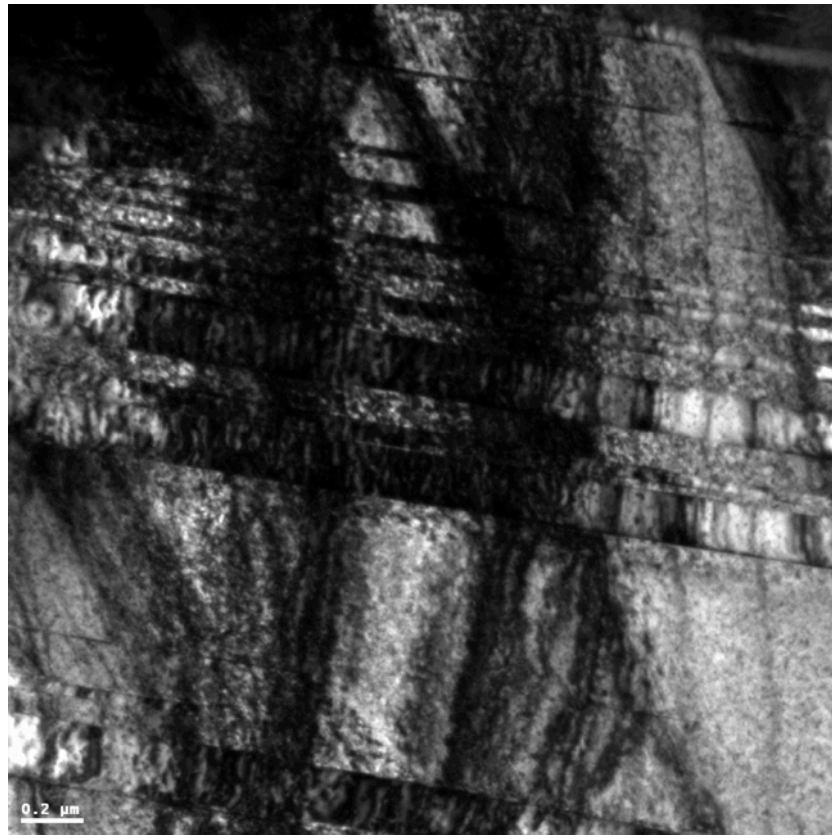
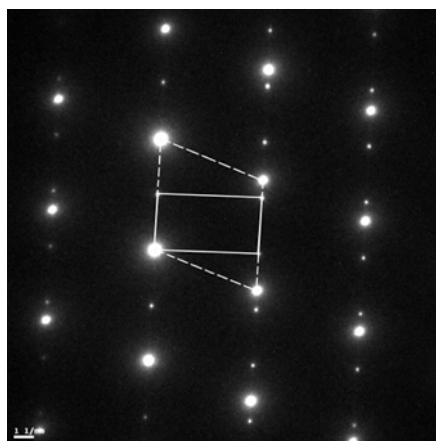


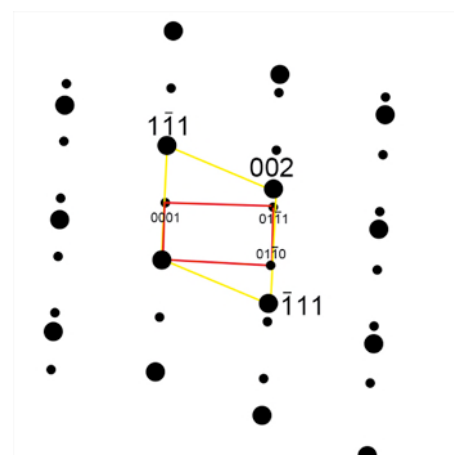
Figure 4.2.19 (a) Bright field TEM microstructure and b) corresponding SAD pattern showing σ phase $\text{Co}_2(\text{Mo,Cr})_3$ (PDF code 00-029-0490) in 40HCP sample.



a

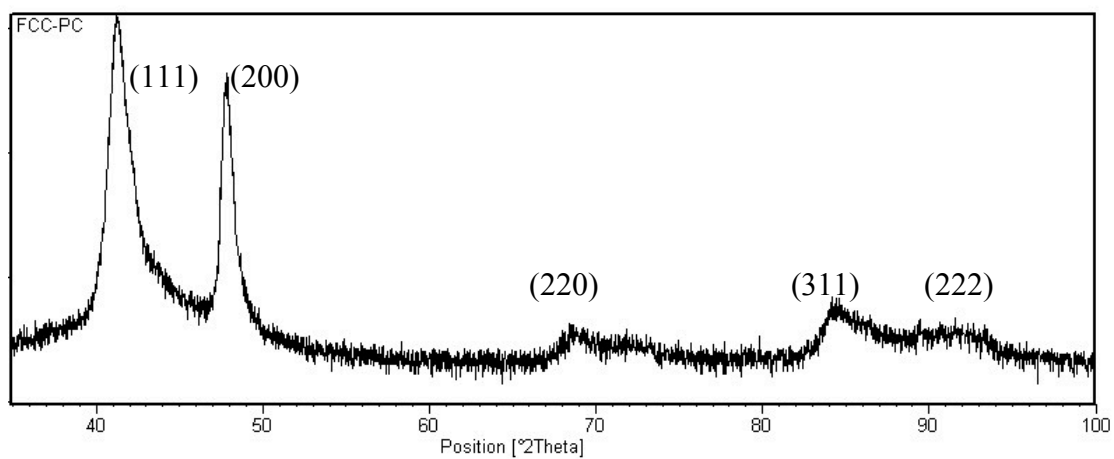


b

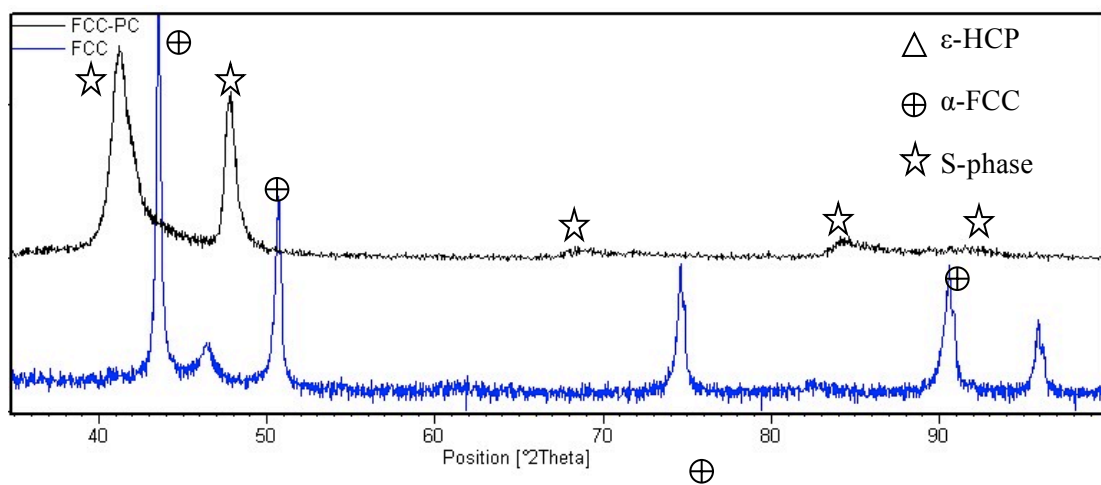


$[2\bar{1}\bar{1}0]_{\epsilon} // [110]_{\alpha}, (0001)_{\epsilon} // (1\bar{1}1)_{\alpha}$

Figure 4.2.20 Bright field TEM microstructure (a) and (b) corresponding SAD pattern from 40HCP sample showing ϵ -HCP plates embedded in FCC matrix with a $[2\bar{1}\bar{1}0]_{\epsilon} // [110]_{\alpha}, (0001)_{\epsilon} // (1\bar{1}1)_{\alpha}$ relationship.

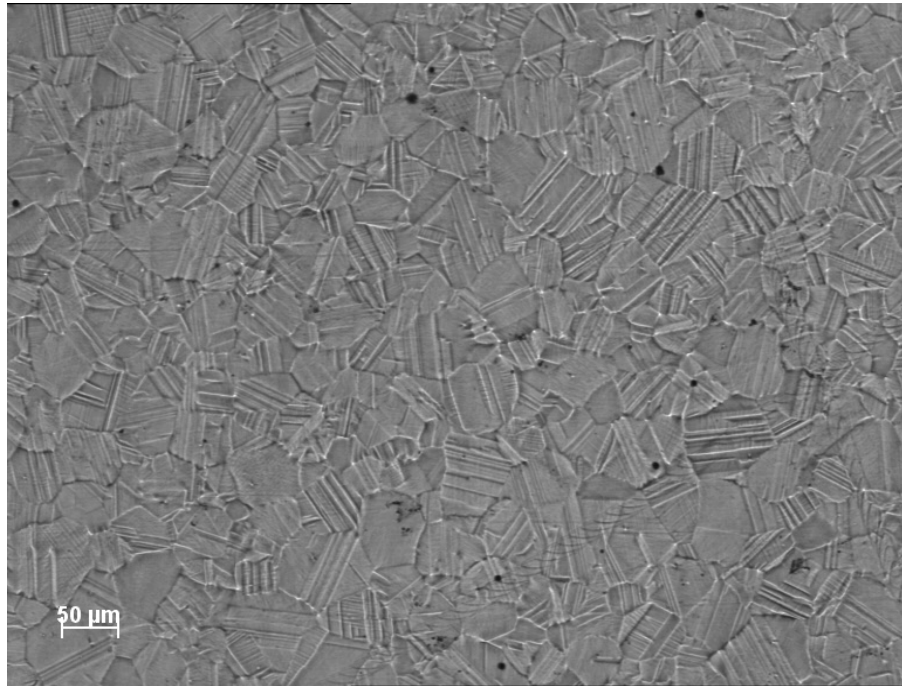


a



b

Figure 4.3.1 XRD spectra of (a) the FCC-PC sample and (b) comparison between the FCC and FCC-PC samples.

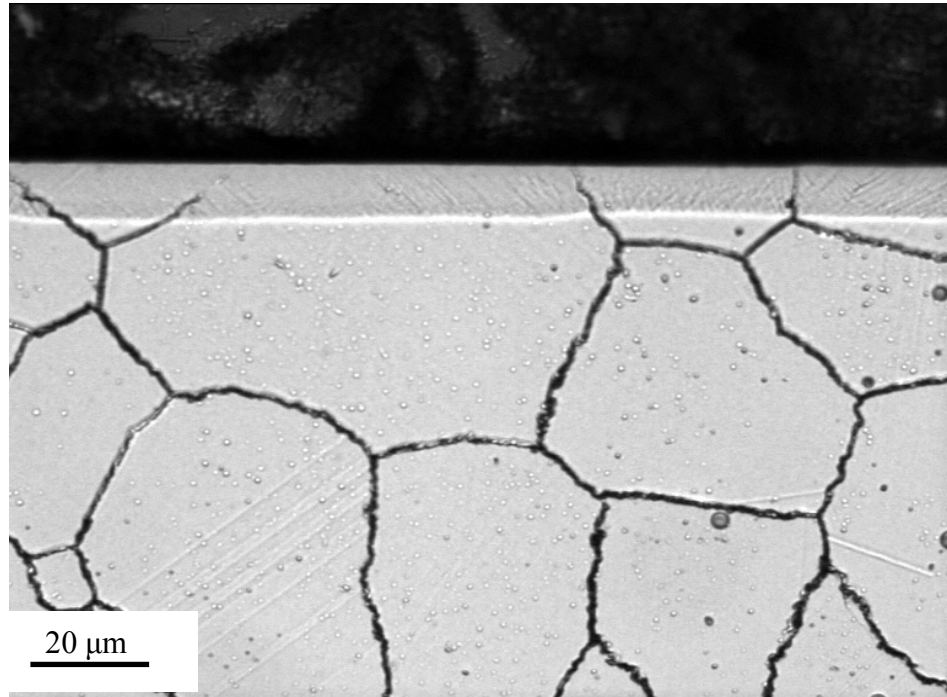


a

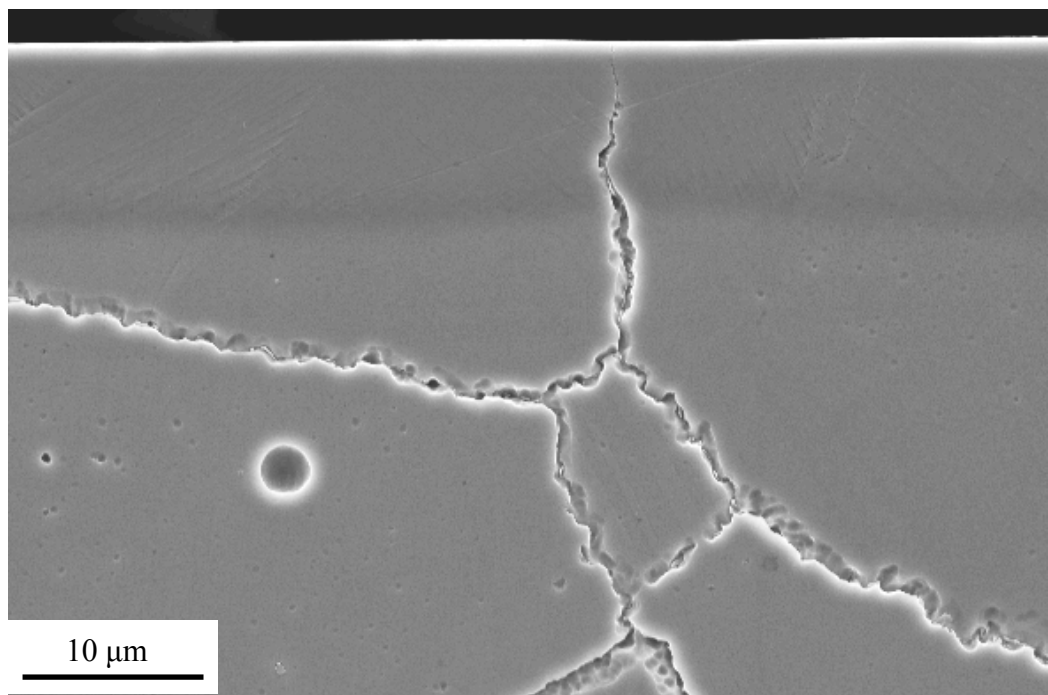


b

Figure 4.3.2 (a) Optical and (b) secondary electron micrographs showing plan-view surface morphology of the FCC-PC sample.

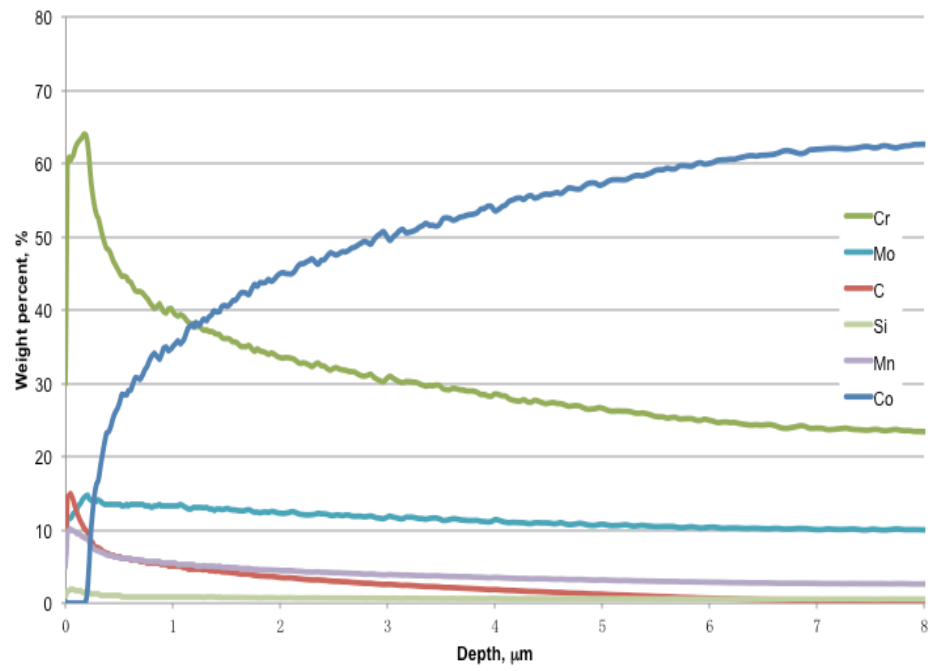


a

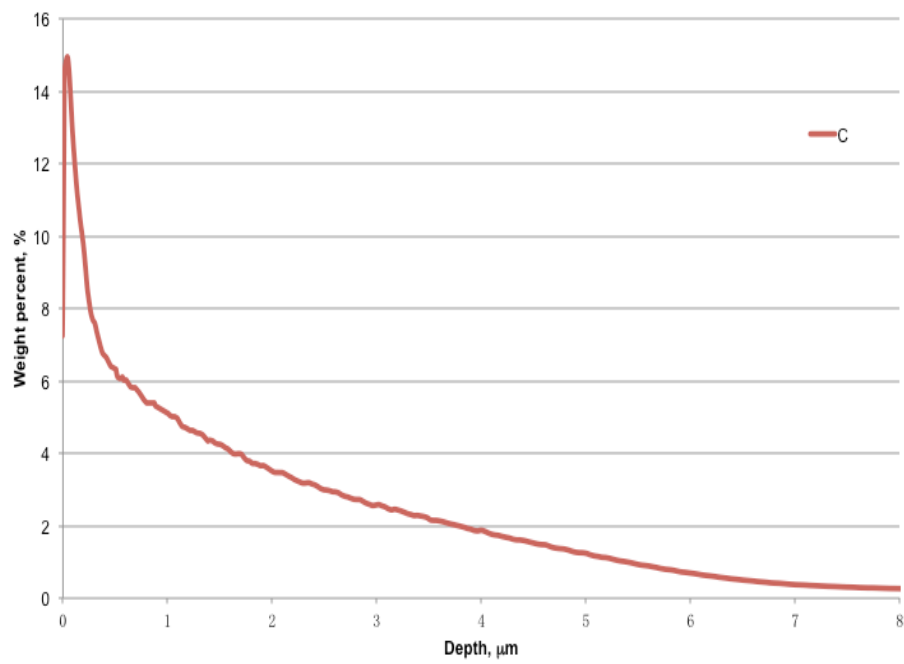


b

Figure 4.3.3 (a) Optical and (b) SEM showing surface layer structure of the FCC-PC sample.

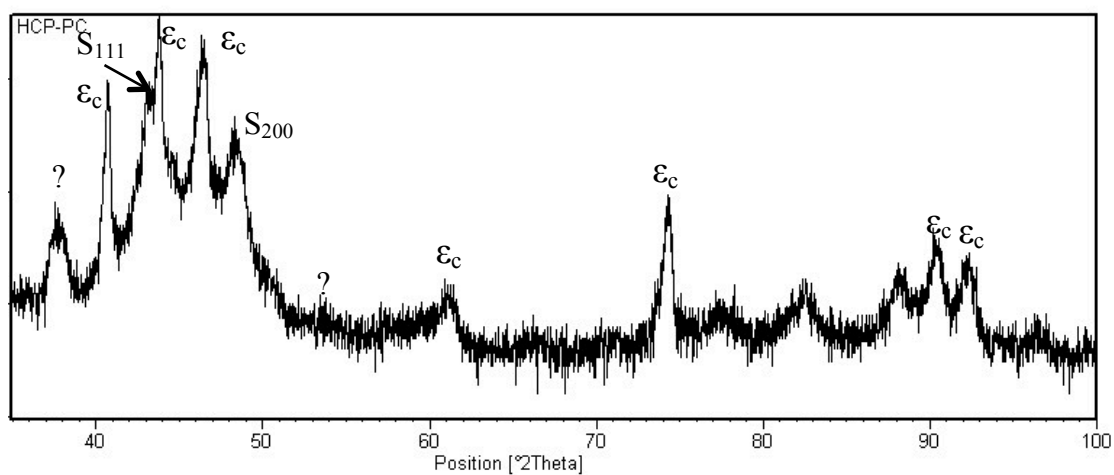


a

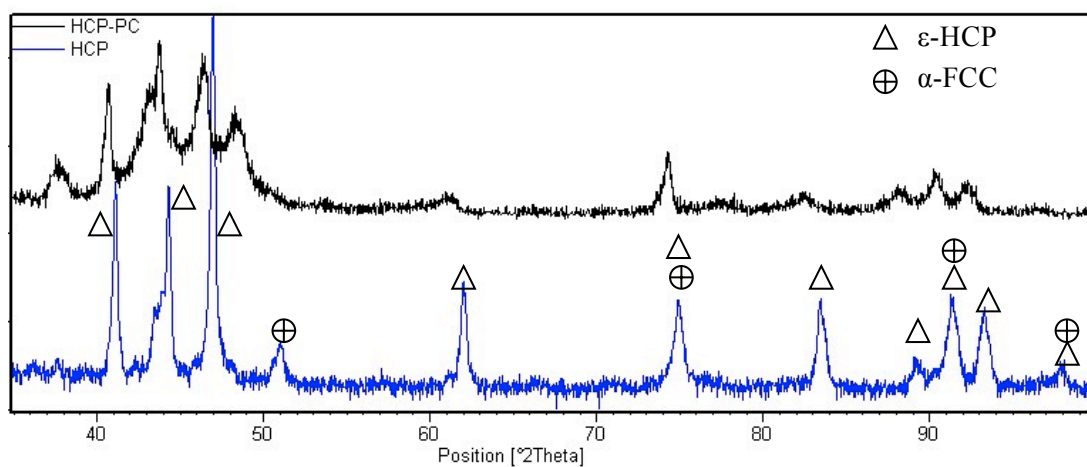


b

Figure 4.3.4 GDS depth profiles of the FCC-PC sample: (a) all elements and (b) carbon.



a



b

Figure 4.3.5 XRD spectra of (a) the HCP-PC sample and (b) comparison between the HCP and HCP-PC samples (question marks for the unidentified peaks).

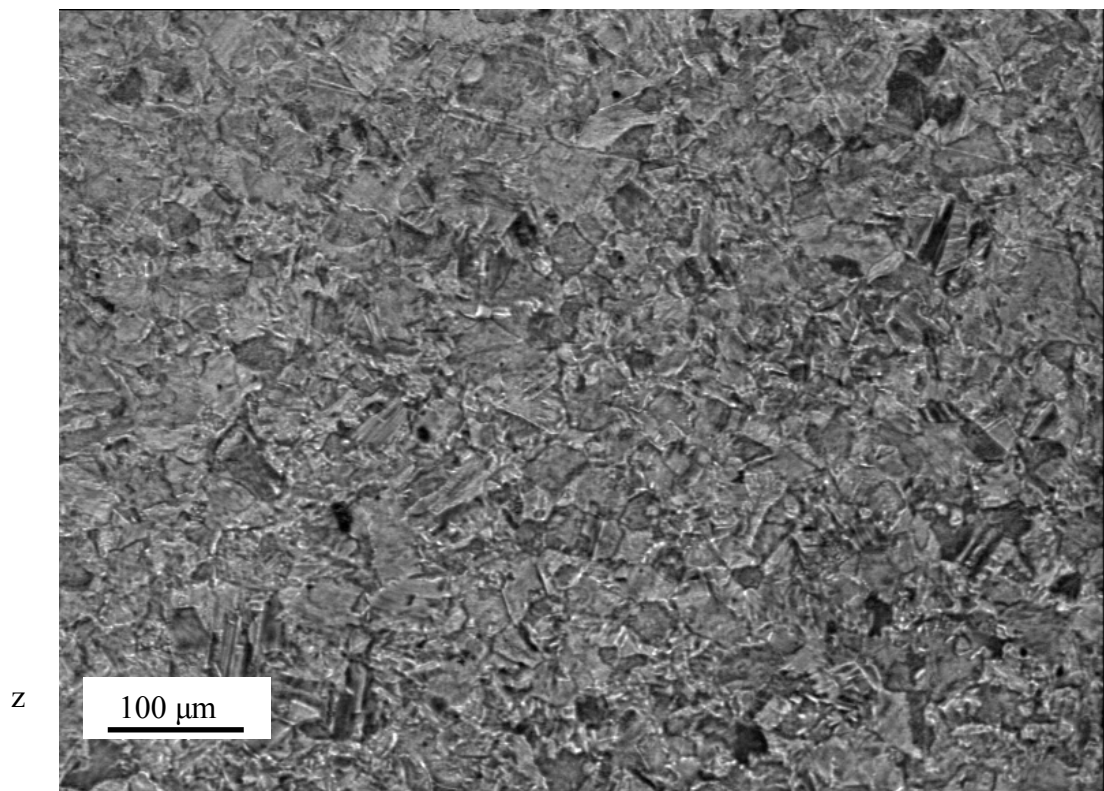


Figure 4.3.6 Optical microscope image showing the surface morphology of the HCP-PC sample.

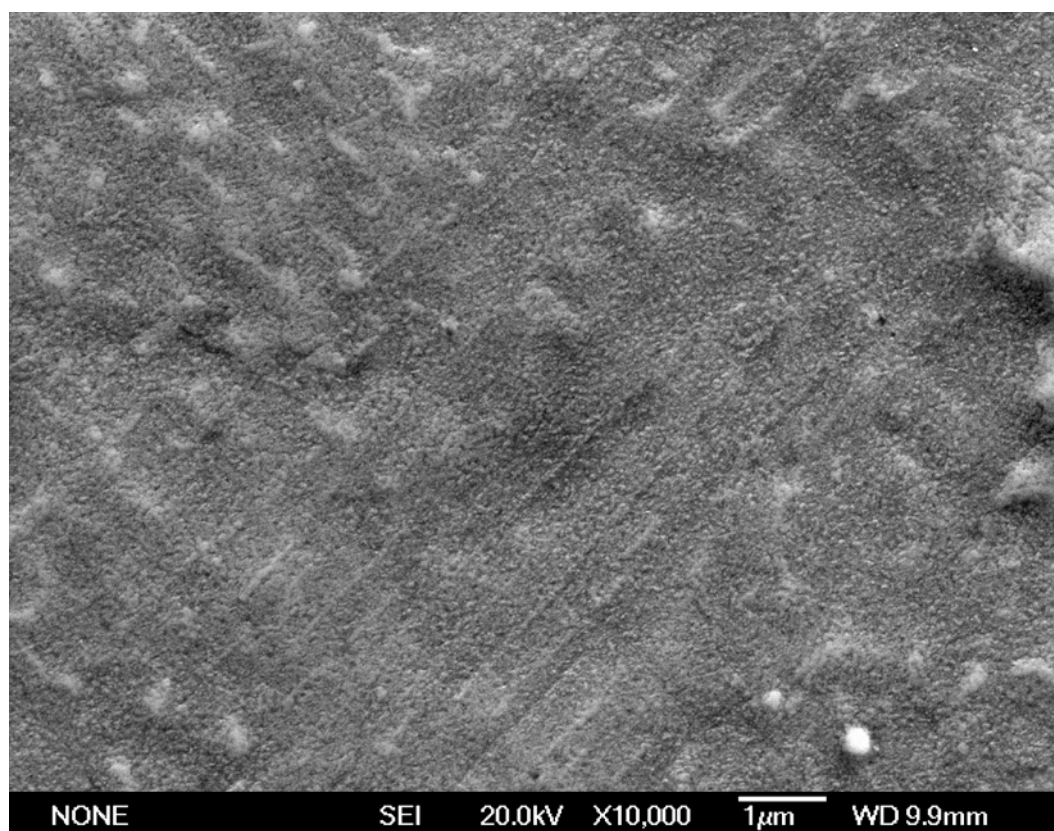


Figure 4.3.7 SEM image showing surface morphology of the HCP-PC sample.

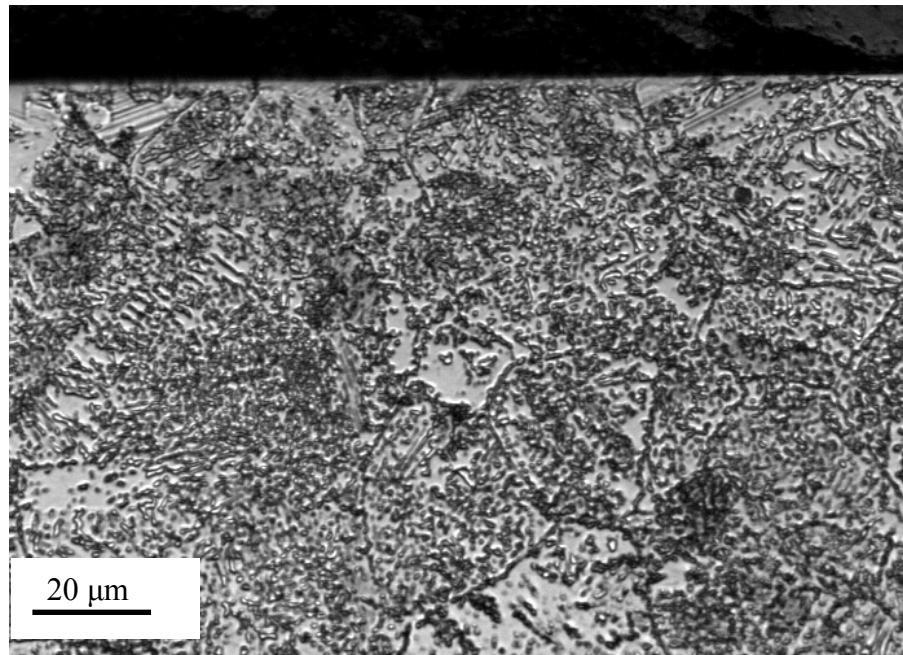


Figure 4.3.8 Optical microscope image showing the cross-sectional microstructure of the HCP-PC sample.

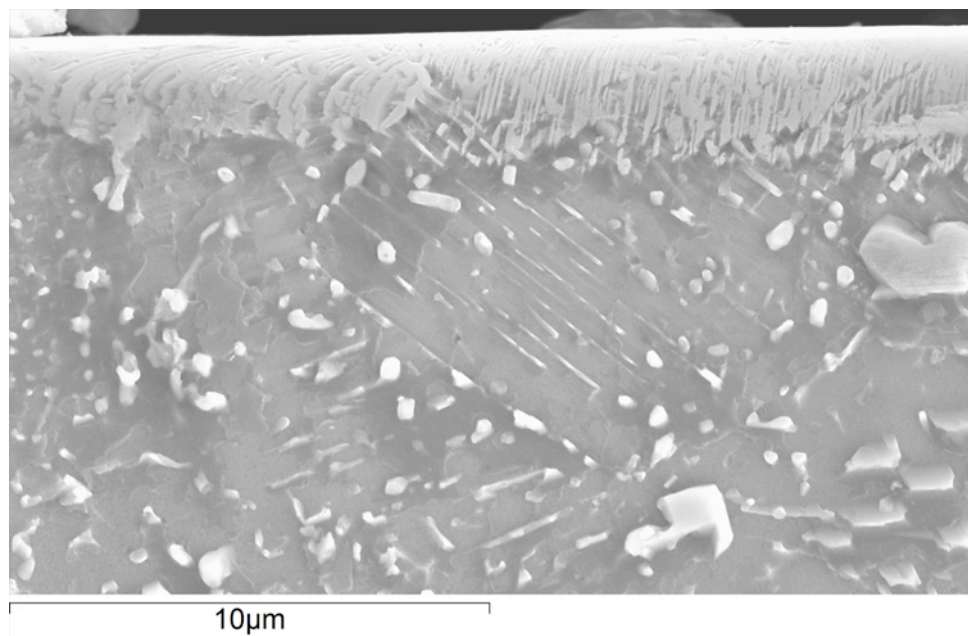
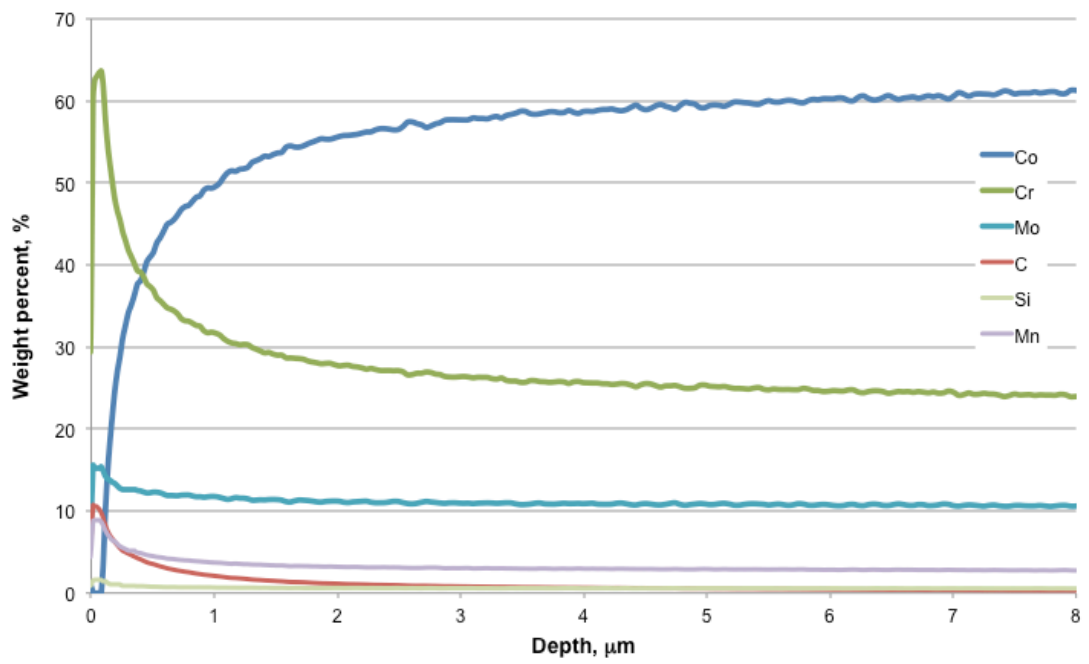
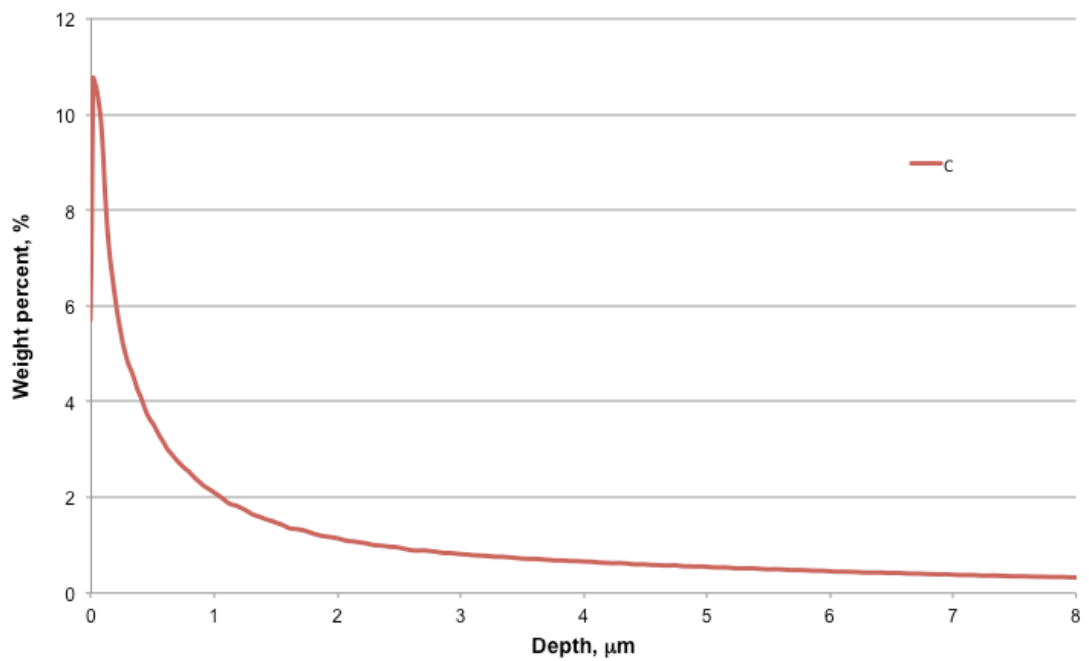


Figure 4.3.9 SEM image showing the cross-sectional microstructure of the HCP-PC sample.

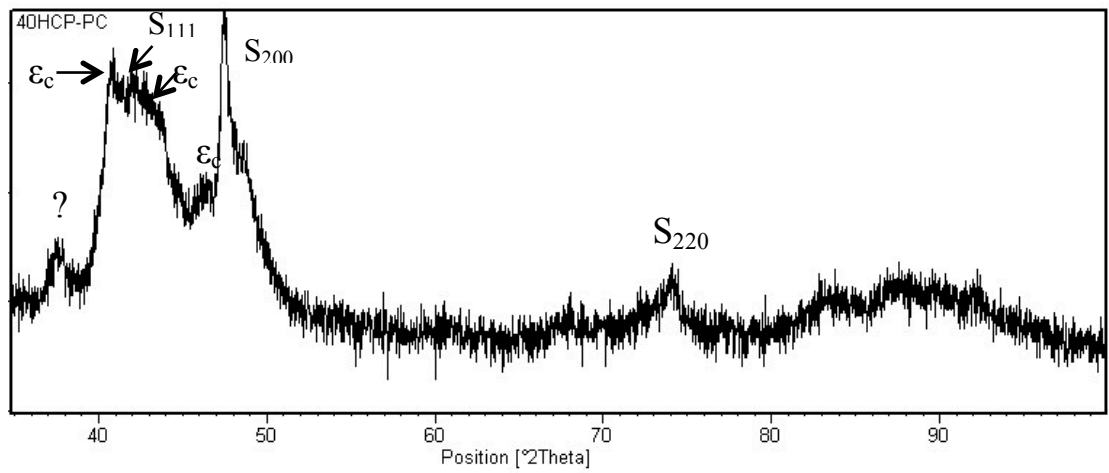


a

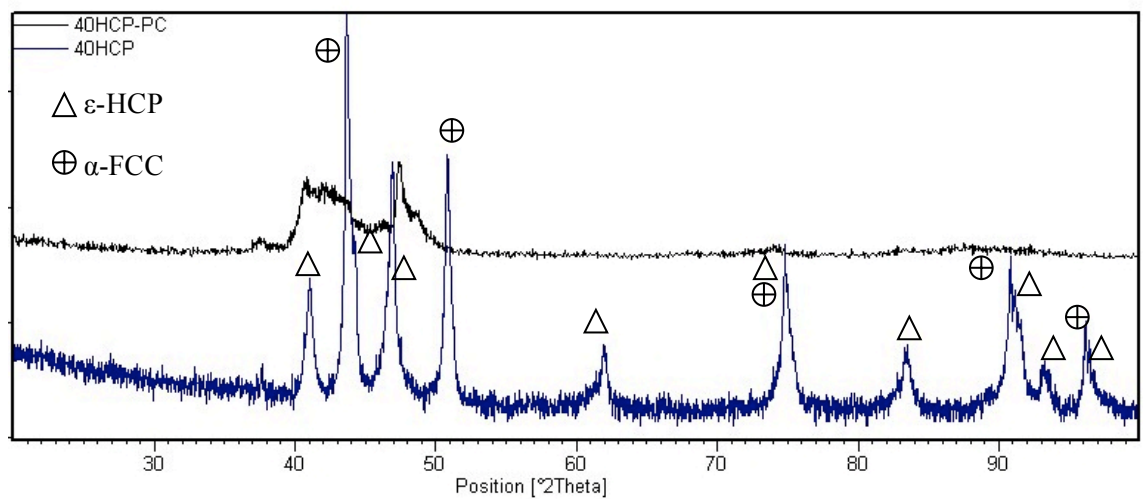


b

Figure 4.3.10 GDS depth profiles of the HCP-PC sample: (a) all elements and (b) carbon.



a



b

Figure 4.3.11 XRD spectra of (a) the HCP-PC sample and (b) comparison between the 40HCP and 40HCP-PC samples (question mark for the unidentified peak).

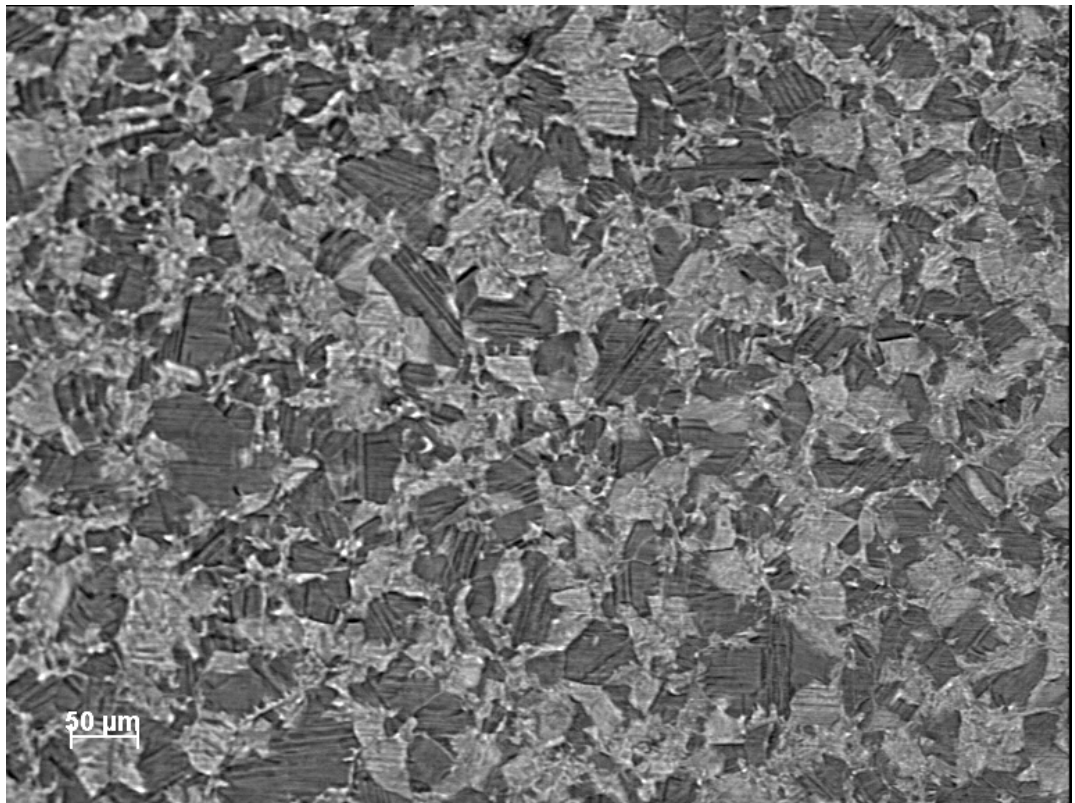


Figure 4.3.12 Optical microstructure of surface morphology taken from 40HCP-PC sample. Bright contrast patches are ϵ -HCP grains; dark contrast patches are α -FCC grains.

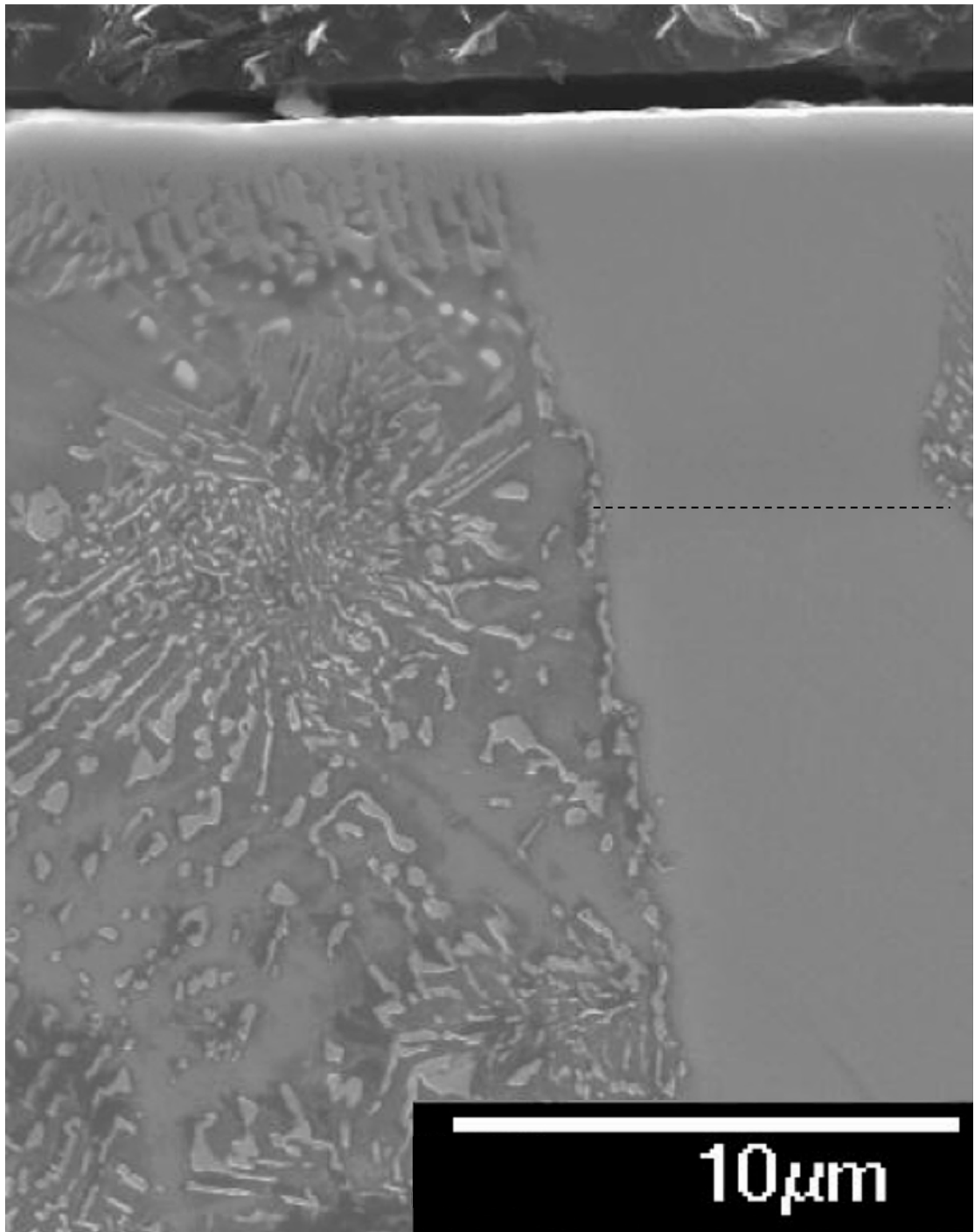
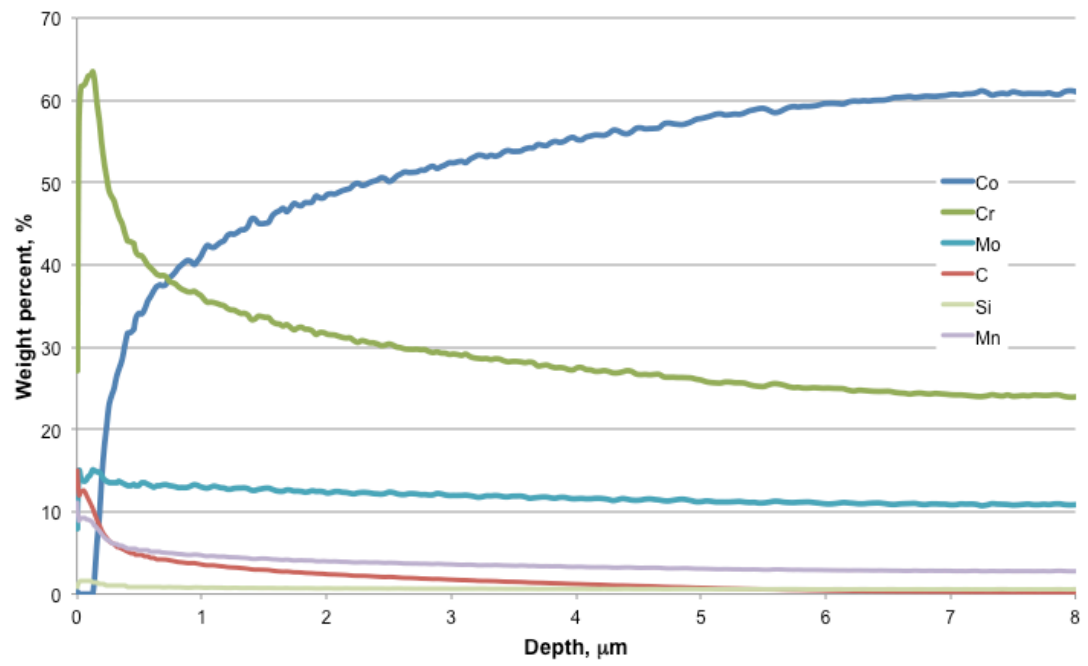
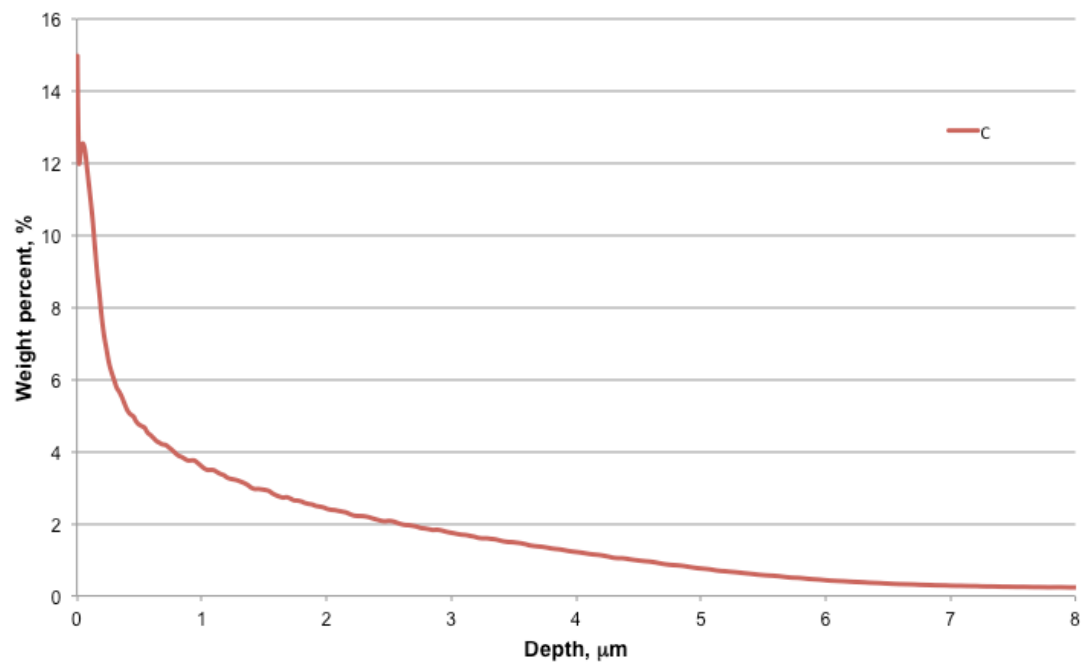


Figure 4.3.13 SEM image showing the cross-sectional microstructure of 40HCP-PC sample.

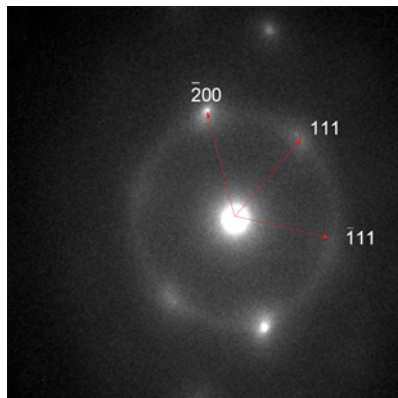
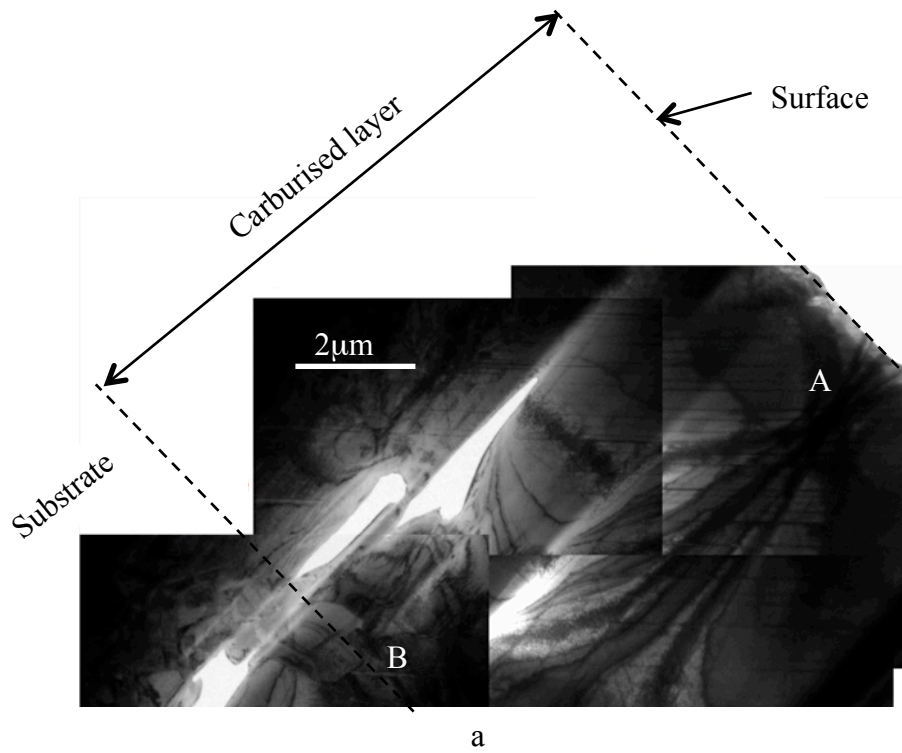


a

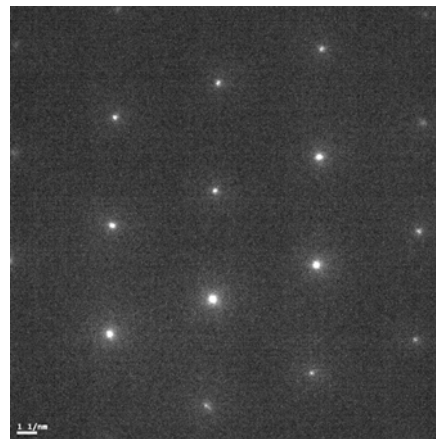


b

Figure 4.3.14 GDS depth profiles of 40HCP-PC sample: (a) all elements and (b) carbon.



b



c

Figure 4.3.15 (a) TEM microstructure and corresponding SAD patterns (b) from A area and (c) from B interface area, of the 40HCP-PC sample.

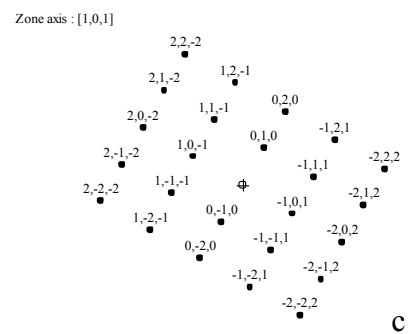
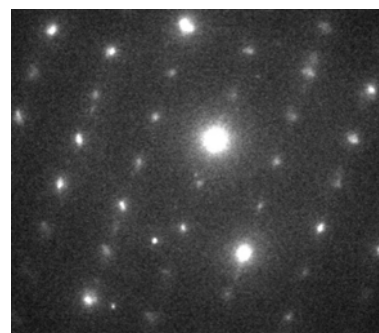
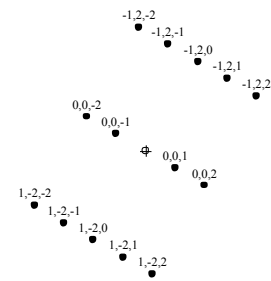
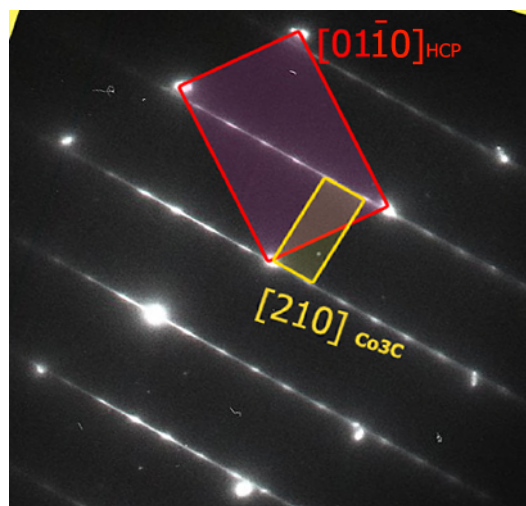
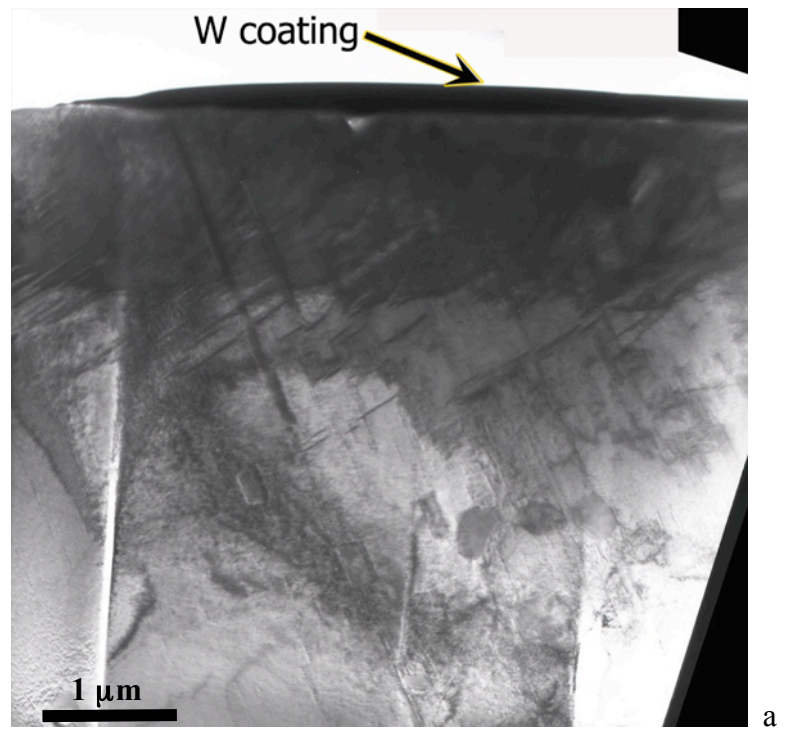


Figure 4.3.16 (a) TEM microstructure of the 40HCP-PC sample and (b and c) corresponding SAD patterns for the surface layer formed on HCP grain during PC treatment.

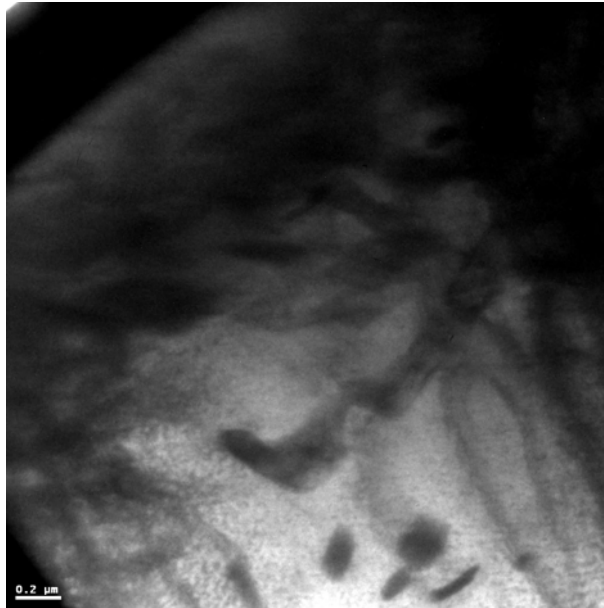


Figure 4.3.17 TEM microstructure of the surface layer of the HCP-PC sample and irregular $M_{23}C_6$ particles.

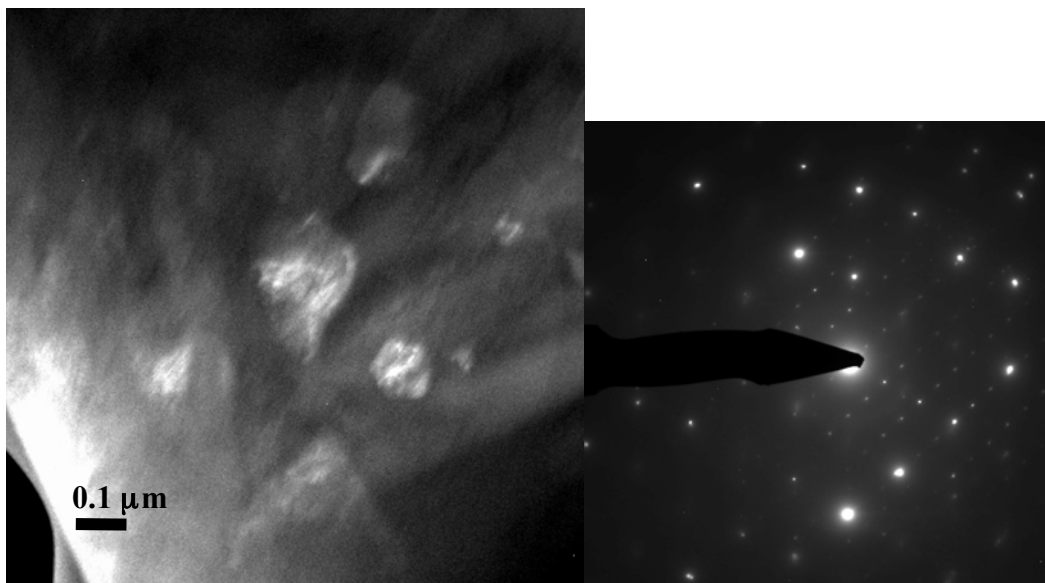


Figure 4.3.18 (a) Dark field TEM microstructure and (b) corresponding SAD pattern showing the $M_{23}C_6$ in the HCP-PC sample.

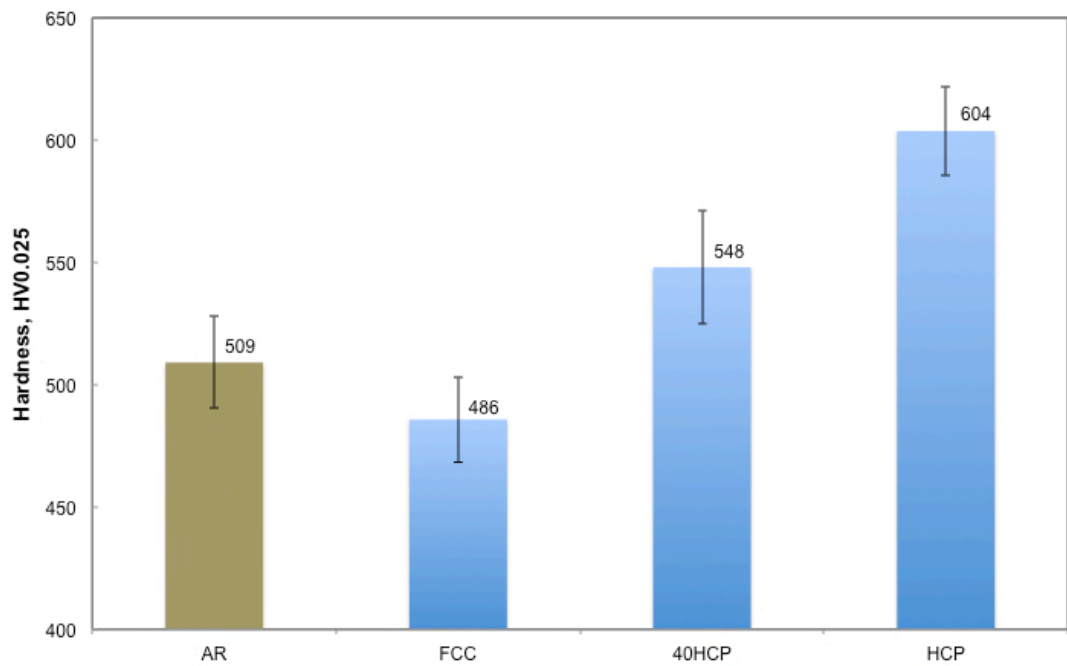


Figure 4.4.1 Microhardness of AR and heat-treated materials (error bar showing the standard deviation).

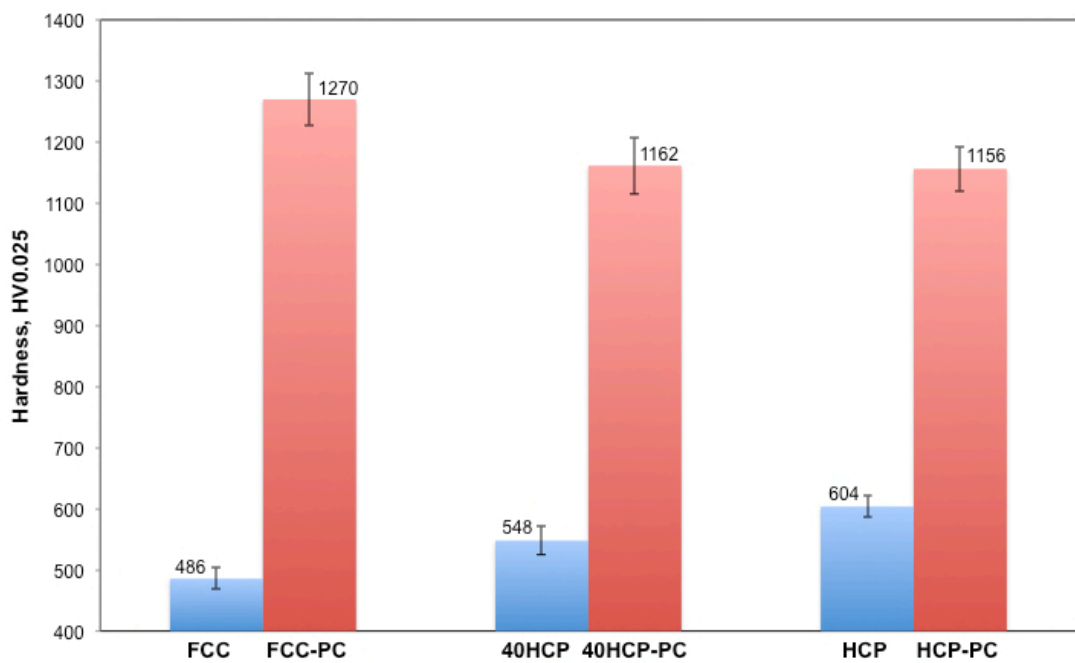


Figure 4.4.2 Surface hardness of plasma carburised materials (error bar showing the standard deviation).

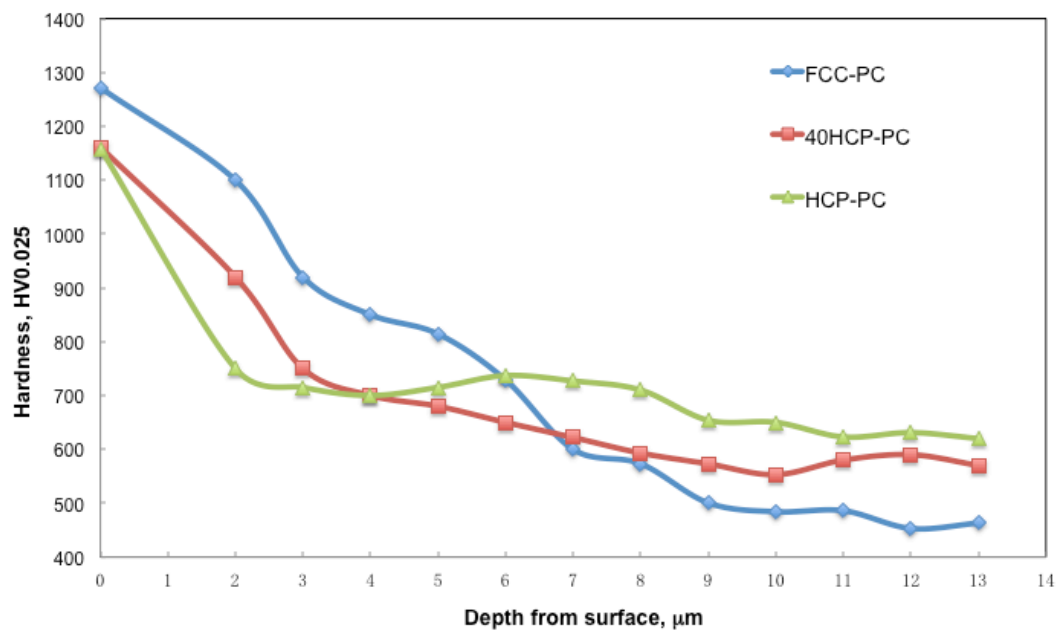


Figure 4.4.3 Depth hardness profiles of plasma carburised materials.

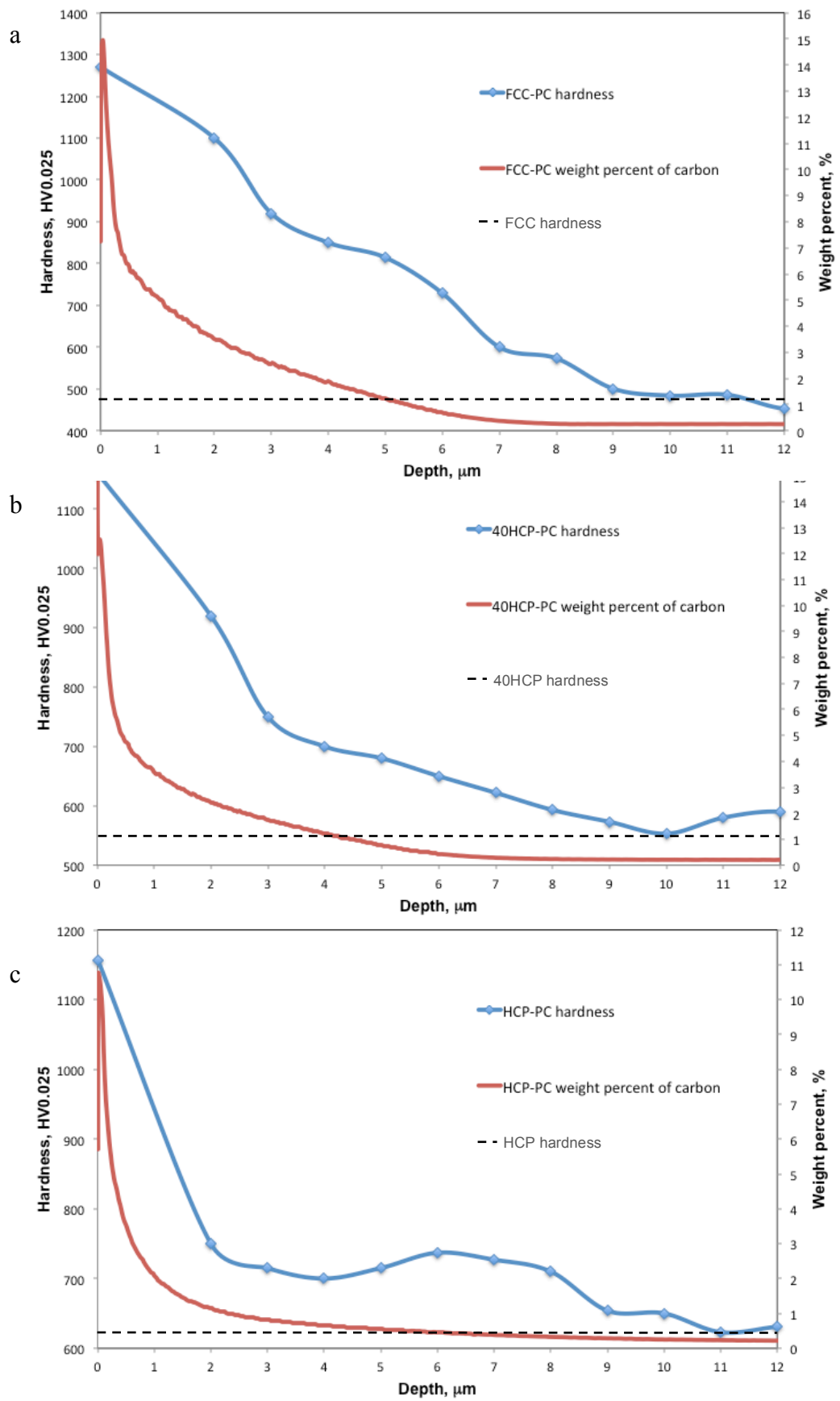


Figure 4.4.4 Hardness and carbon concentration depth profiles of sample (a) FCC-PC, (b) 40HCP-PC and (c) HCP-PC.

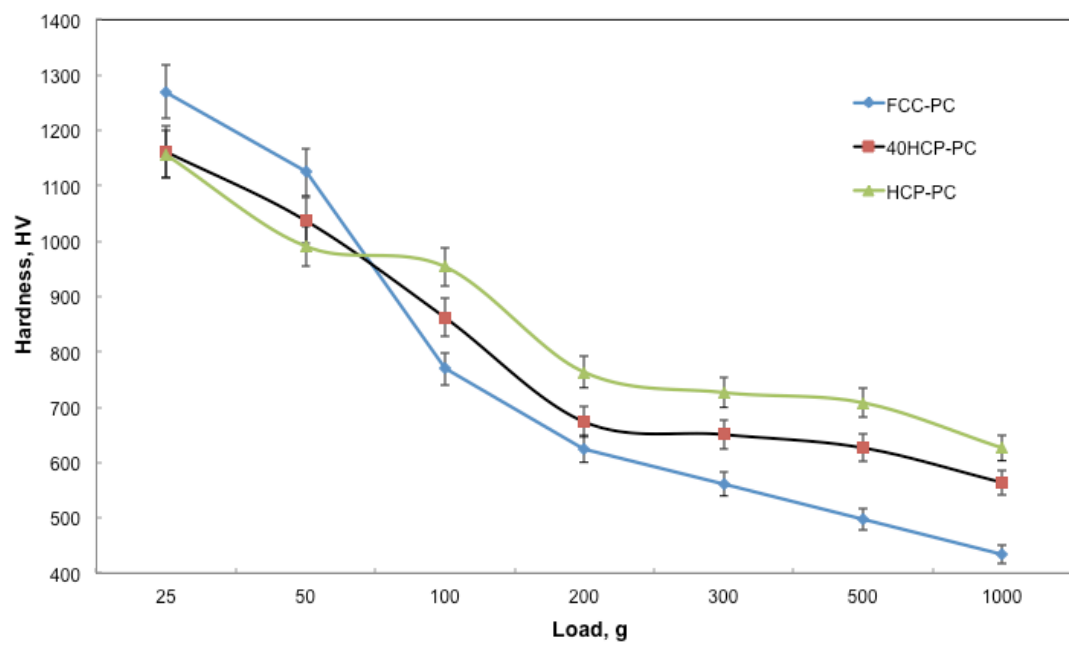


Figure 4.4.5 Load bearing capacity of plasma carburising samples under different loads (error bar showing the standard deviation).

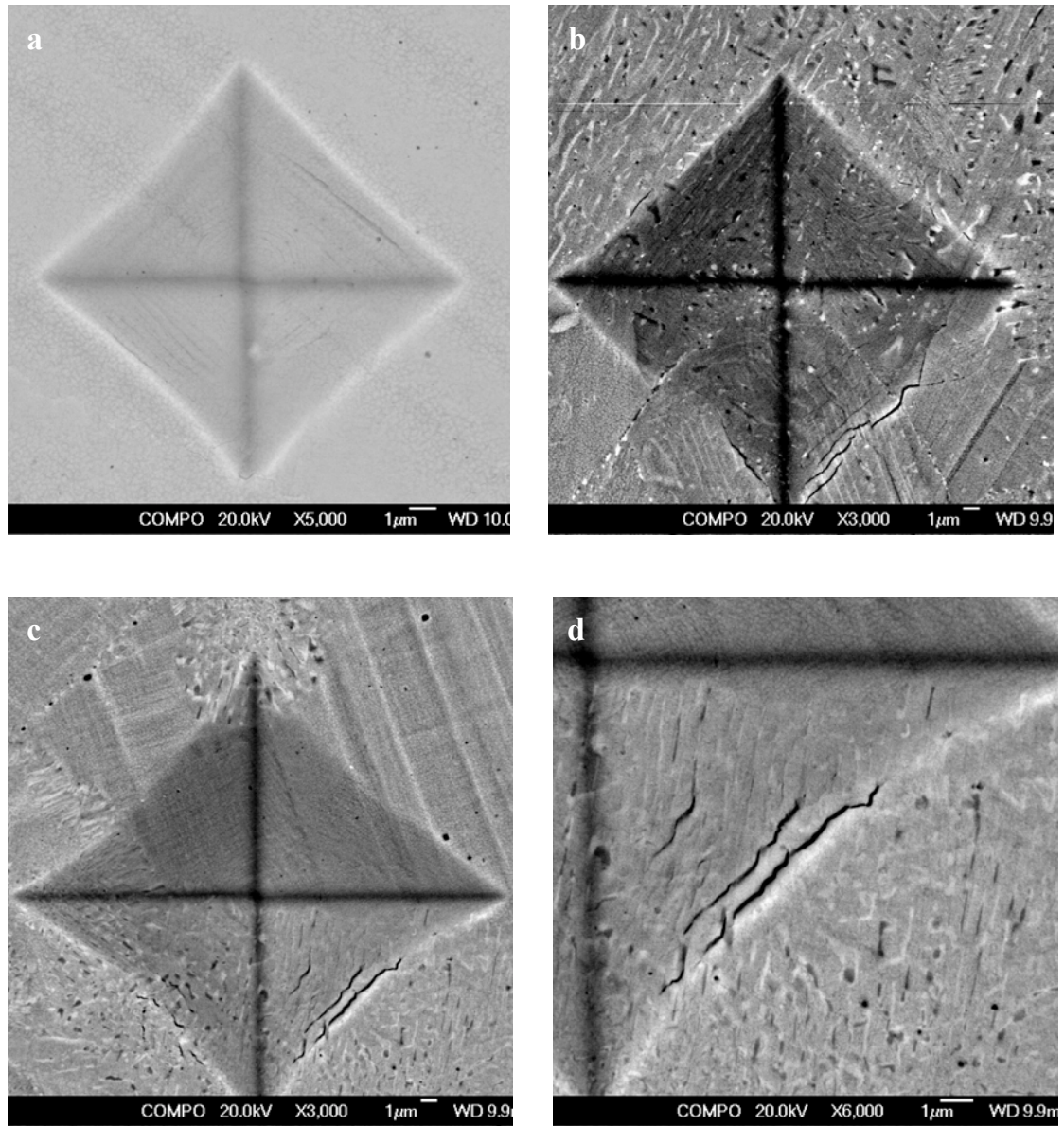


Figure 4.4.6 Back scattered electron images of indents on: (a) FCC-PC samples tested under 100g, (b) HCP-PC samples tested under 300g and (c and d) 40HCP-PC samples tested under 300g.

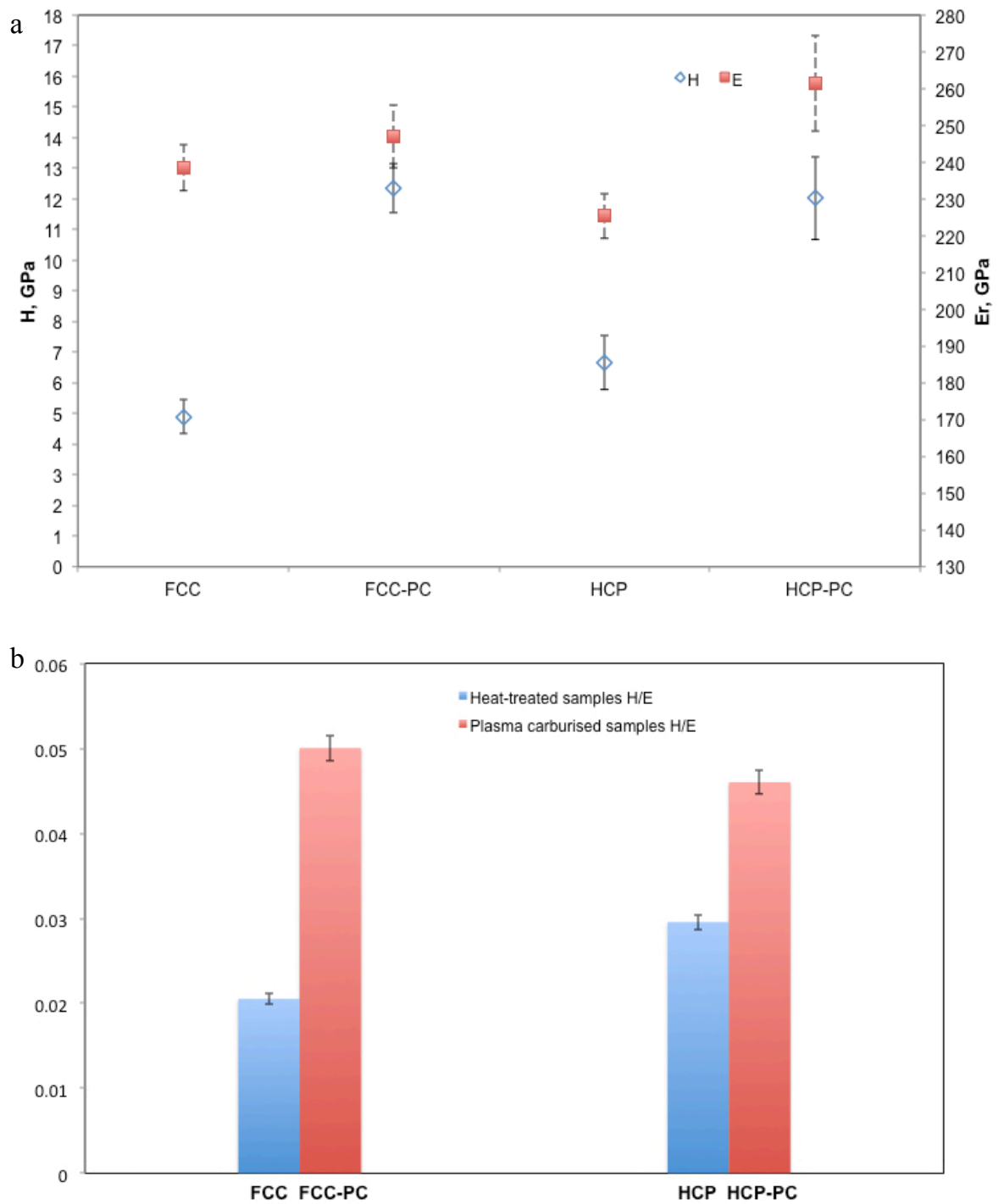
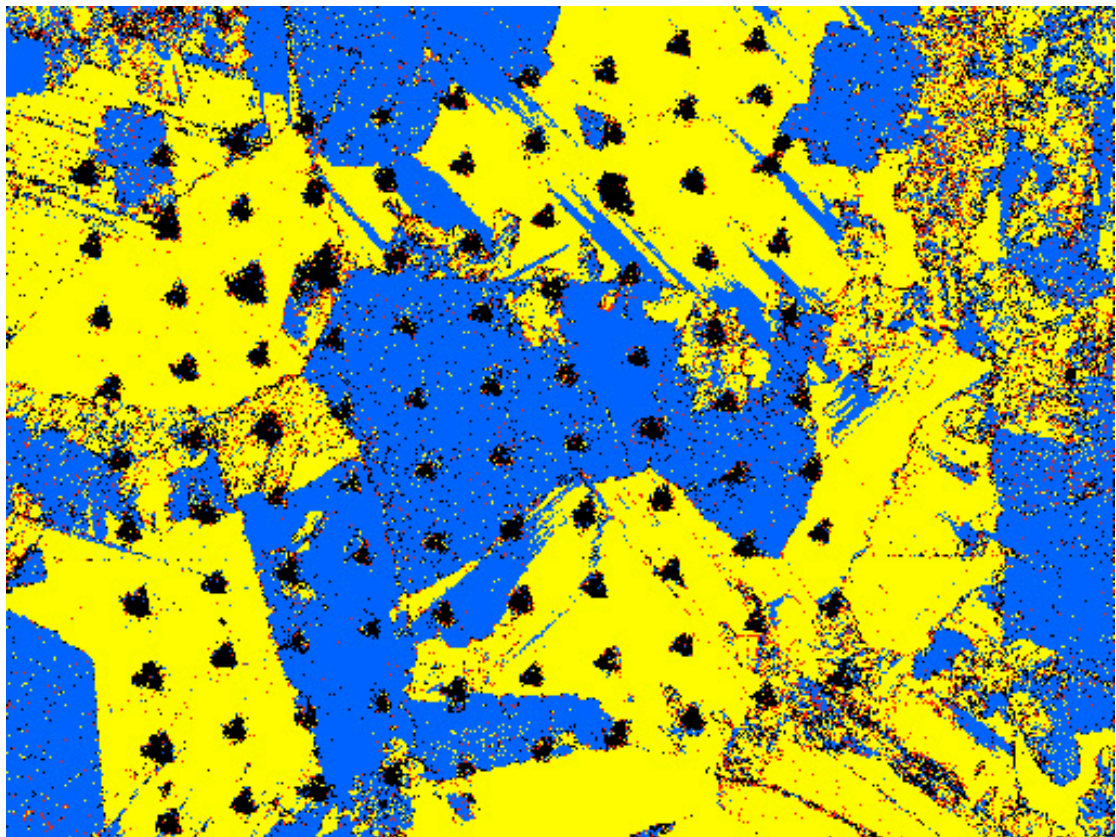


Figure 4.4.7 Nanoindentation results of bulk α -FCC and ϵ -HCP Co-Cr materials before and post plasma carburising treatments: (a) H and E and (b) calculated H/E (error bar showing the standard deviation).



60 μm

Figure 4.4.8 (a) Phase map of 40HCP sample post nanoindentation tests (blue for ϵ -HCP Co, yellow for α -FCC Co, red for $M_{23}C_6$).

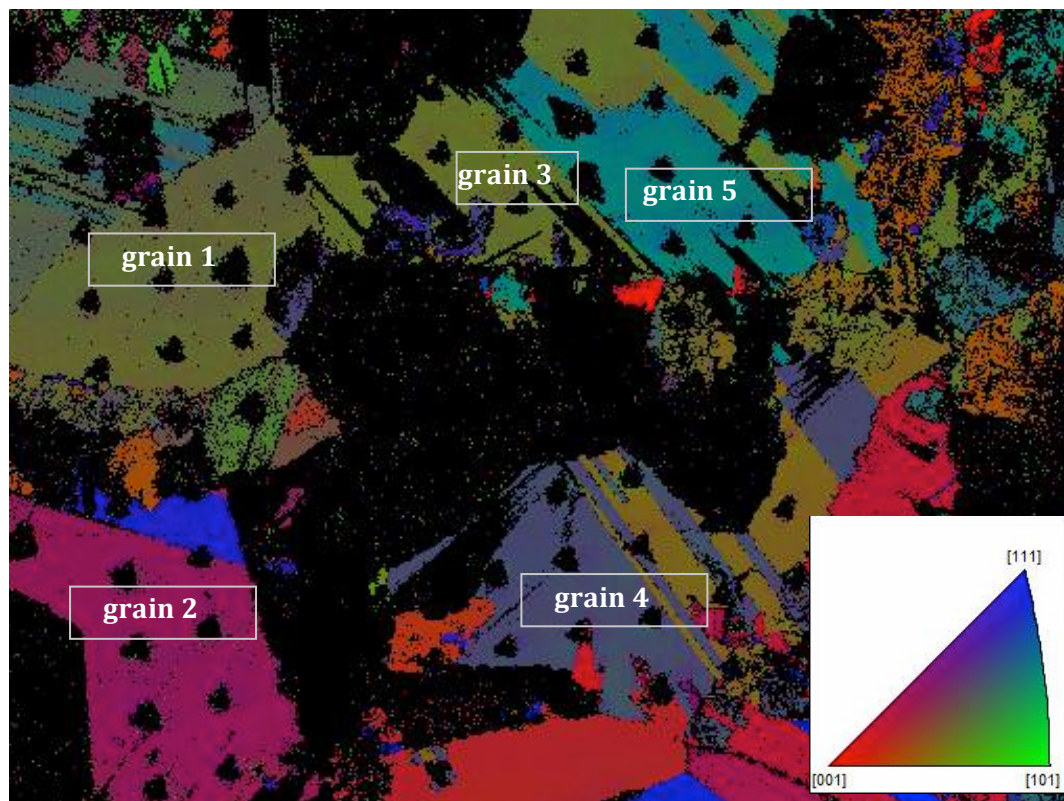


Figure 4.4.8 (b) α -FCC Co phase normal direction grain map.

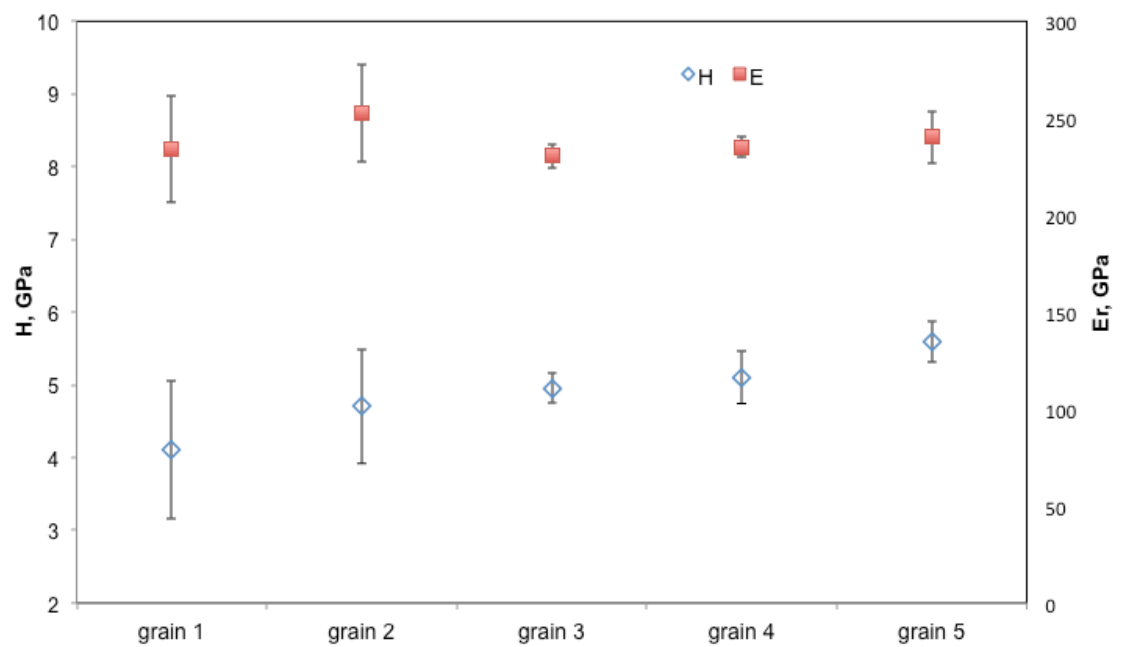


Figure 4.4.8 (c) nanoindentation results of different FCC grains (error bar showing the standard deviation).

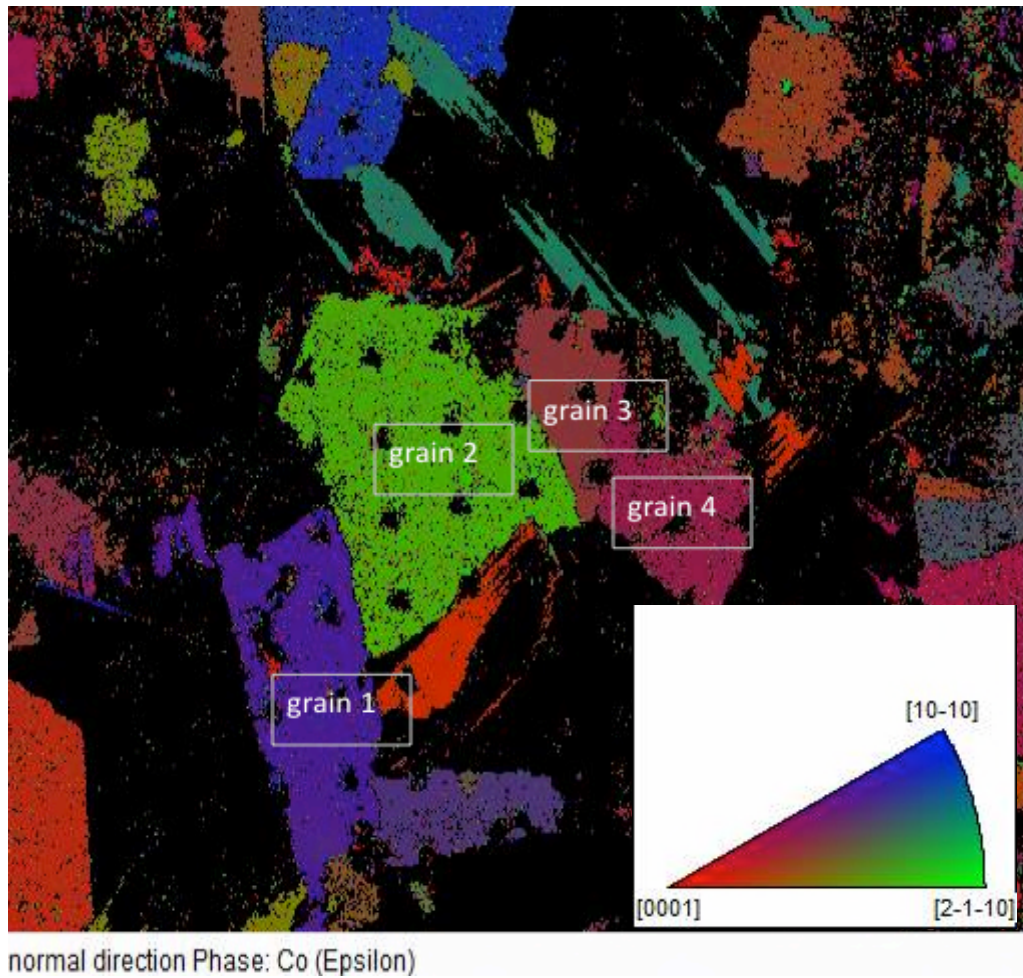


Figure 4.4.8 (d) ϵ -HCP Co phase normal direction grain map.

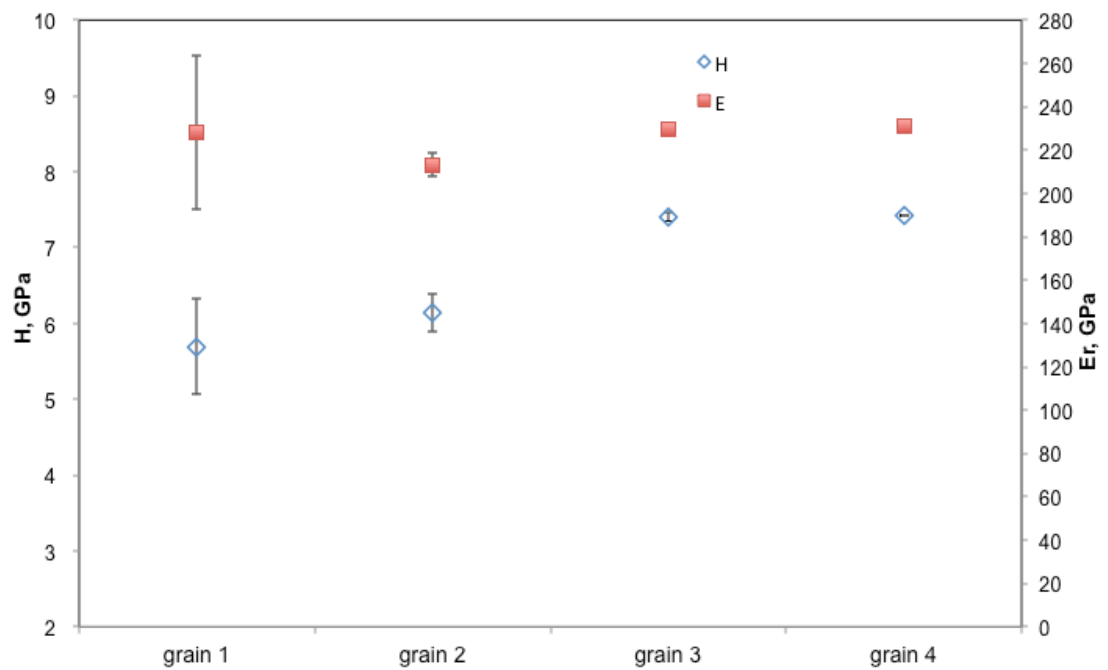


Figure 4.4.8 (e) nanoindentation results of different HCP grains (error bar showing the standard deviation).

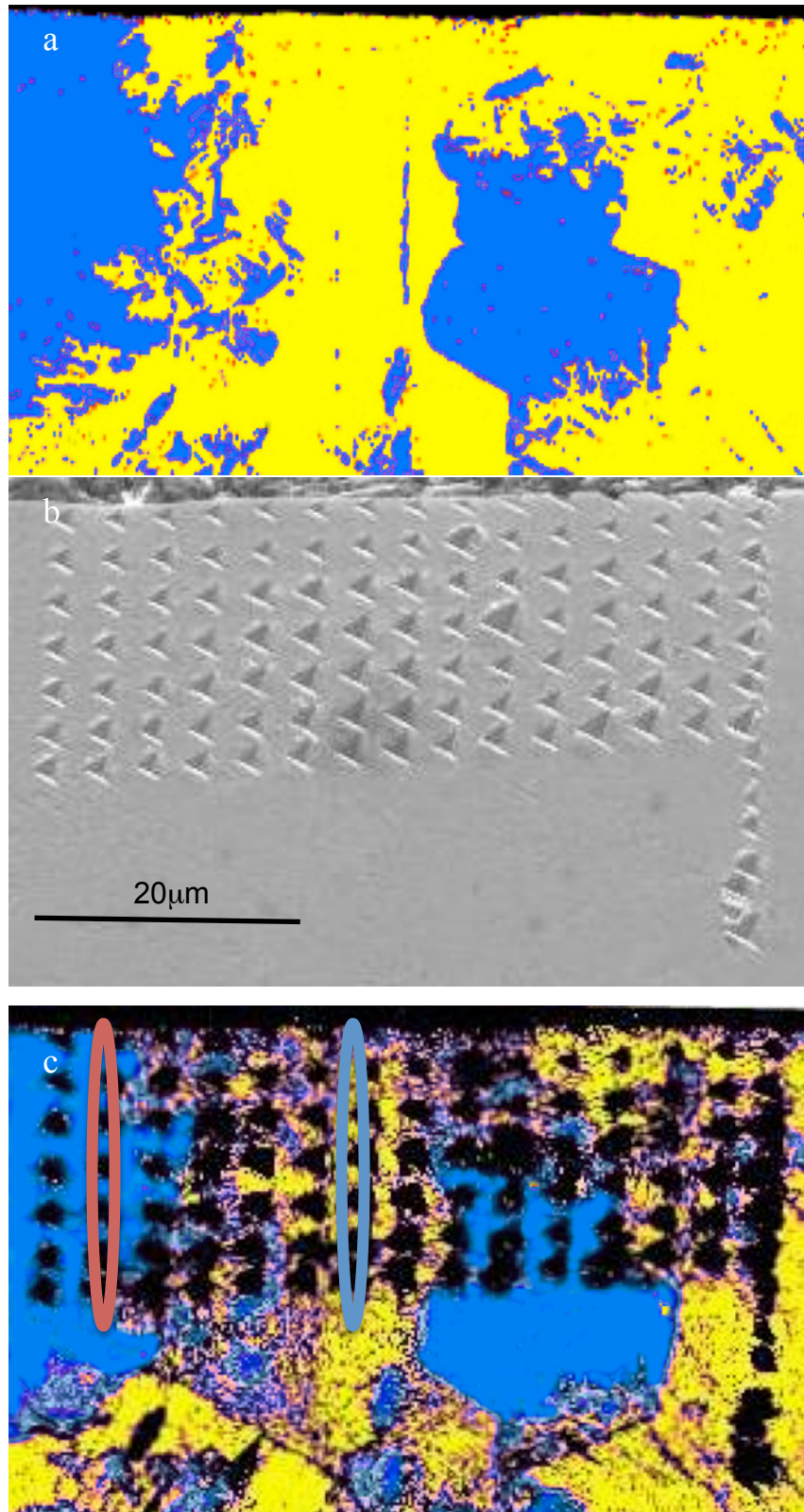


Figure 4.4.9 Cross-sectional observations before and post nanoindentation for the 40HCP-PC sample: (a) phase map showing cross-sectional phase distribution before nanoindentation, (b) secondary electron micrograph after nanoindentation and (c) phase map showing the positions of indents post nanoindentation.

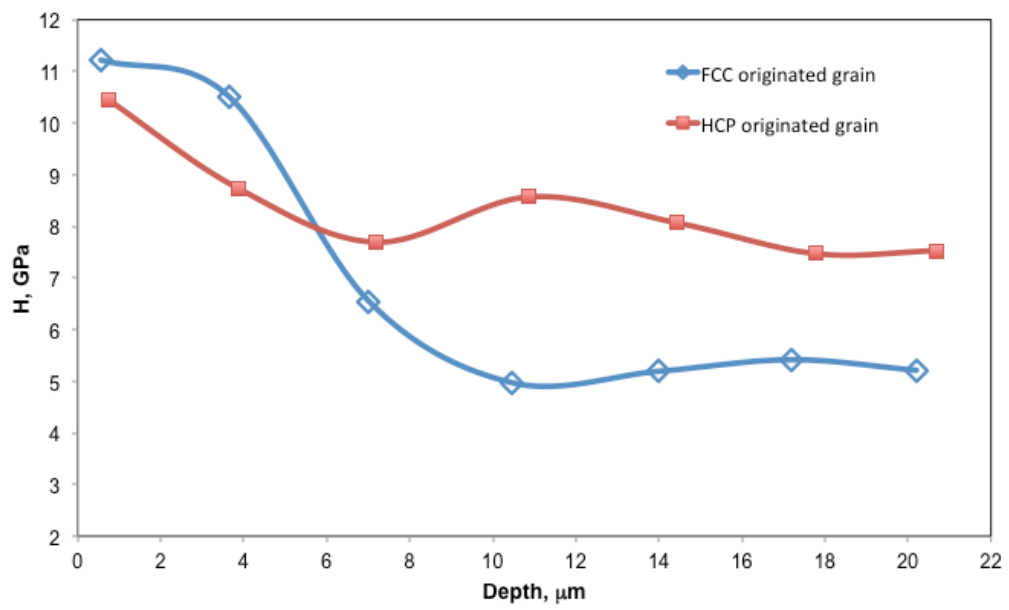


Figure 4.4.10 Depth profiles of nano-hardness of FCC and HCP originated grains after plasma carburising.

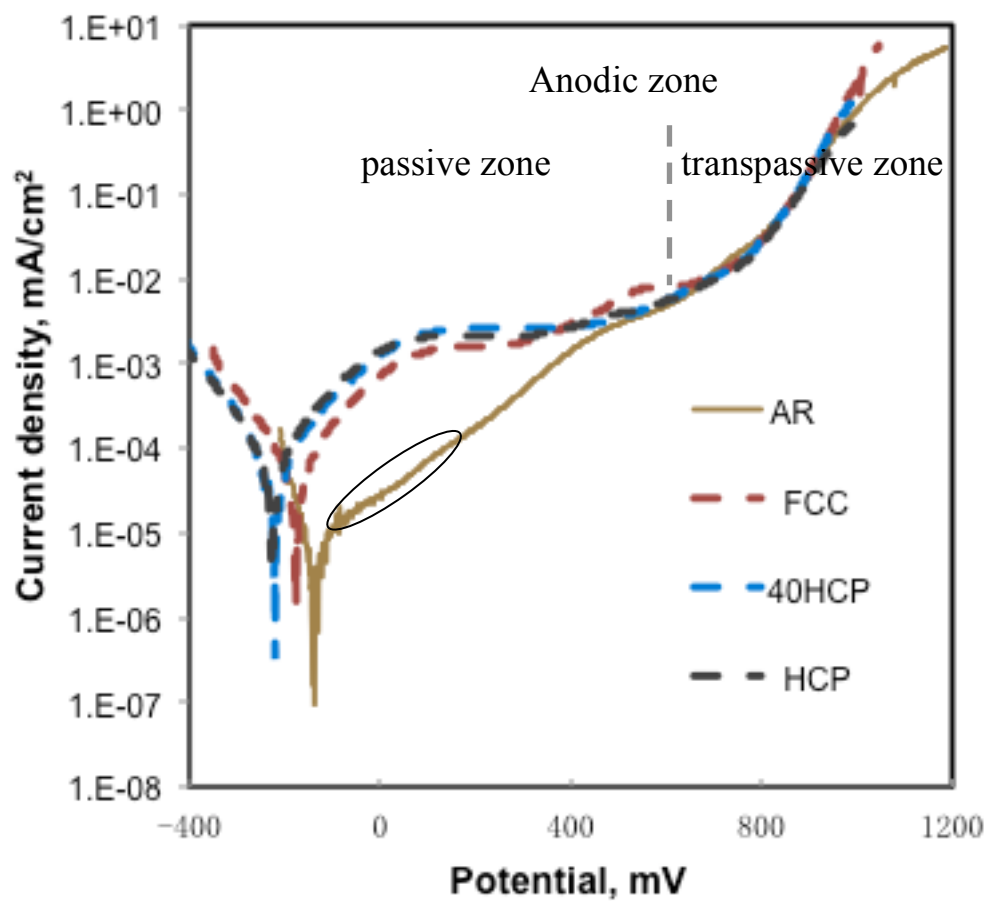


Figure 4.5.1 Anodic polarisation curves of heat-treated samples.

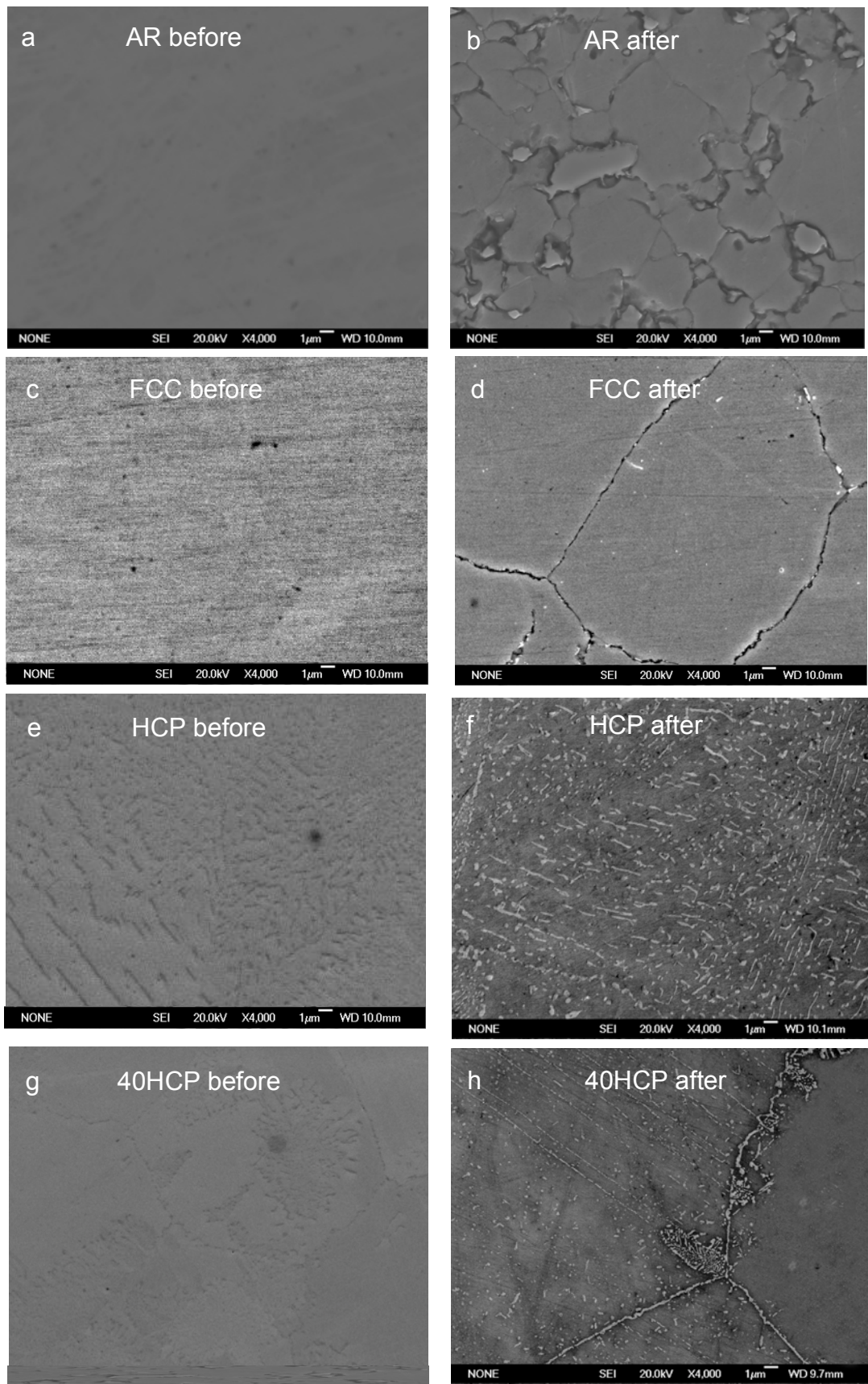


Figure 4.5.2 SEM observations on the (a-b) AR, (c-d) FCC, (e-f) HCP and (g-h) 40HCP samples before and after anodic polarisation tests.

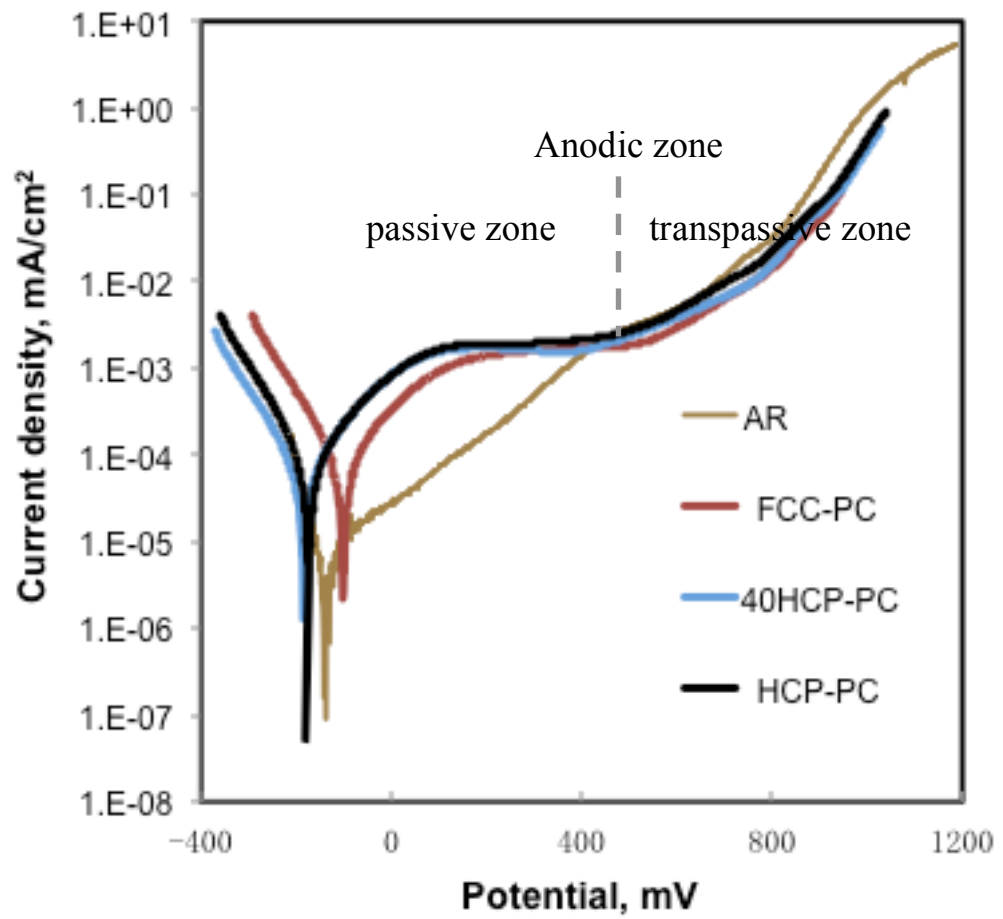


Figure 4.5.3 Anodic polarisation curves of (a) plasma carburised samples.

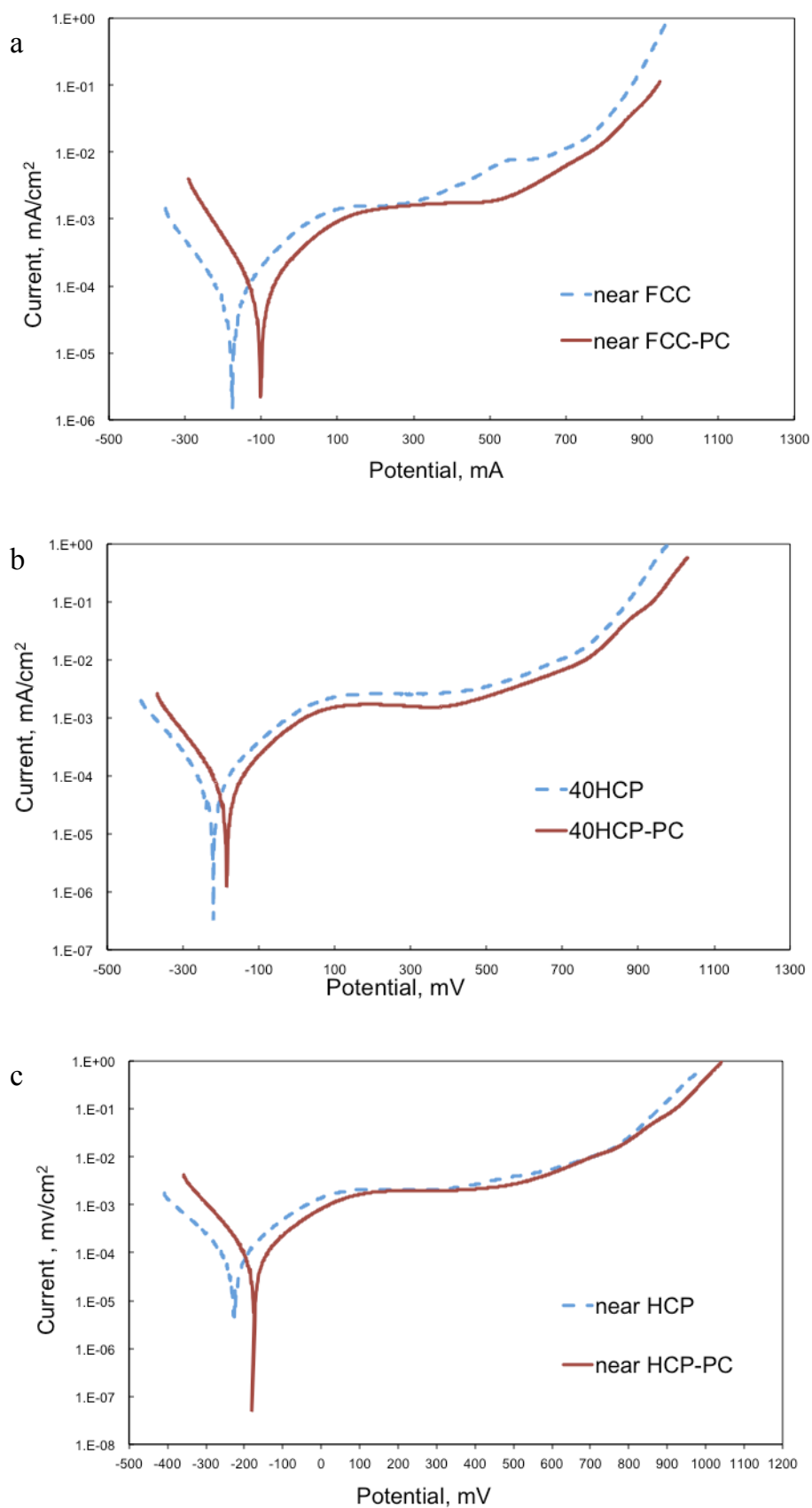


Figure 4.5.4 Anodic polarisation curves of materials before and after low-temperature plasma carburising: (a) FCC and FCC-PC, (b) 40HCP and 40HCP-PC and (c) HCP and HCP-PC.

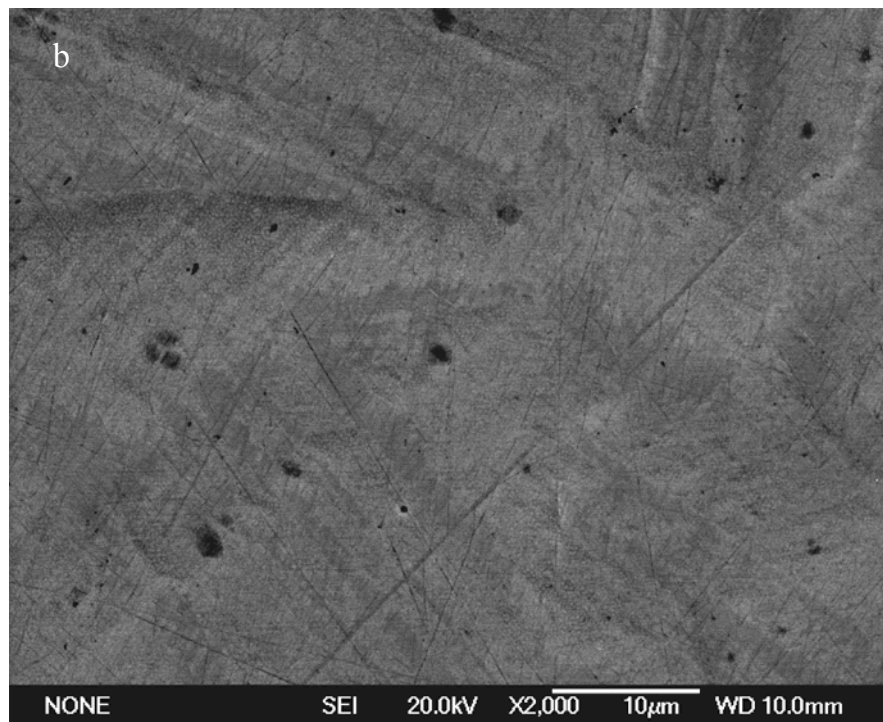


Figure 4.5.5 SEM observations on the FCC-PC samples (a) before and (b) after anodic polarisation tests.

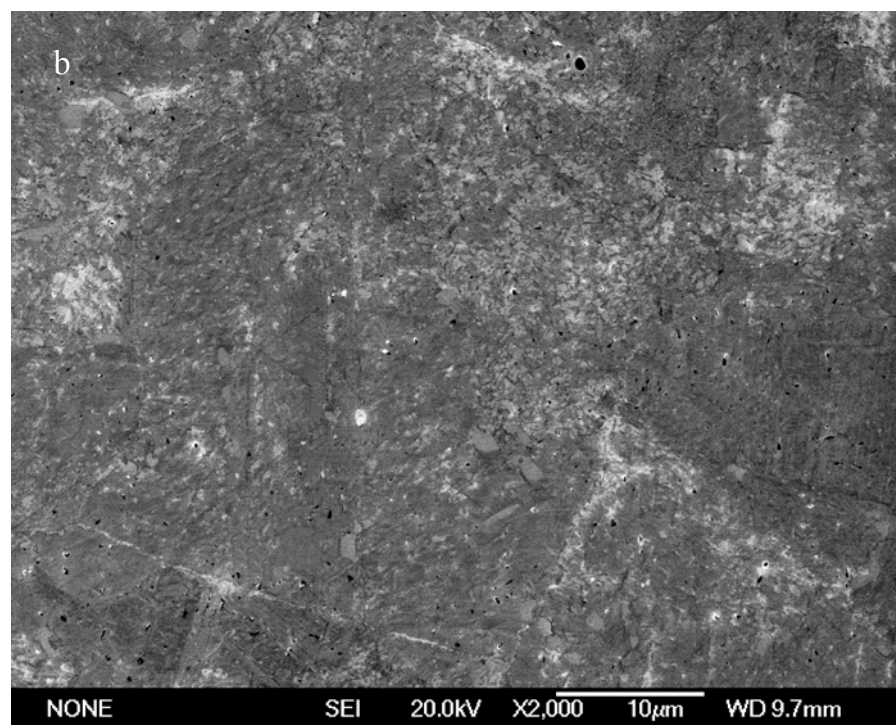
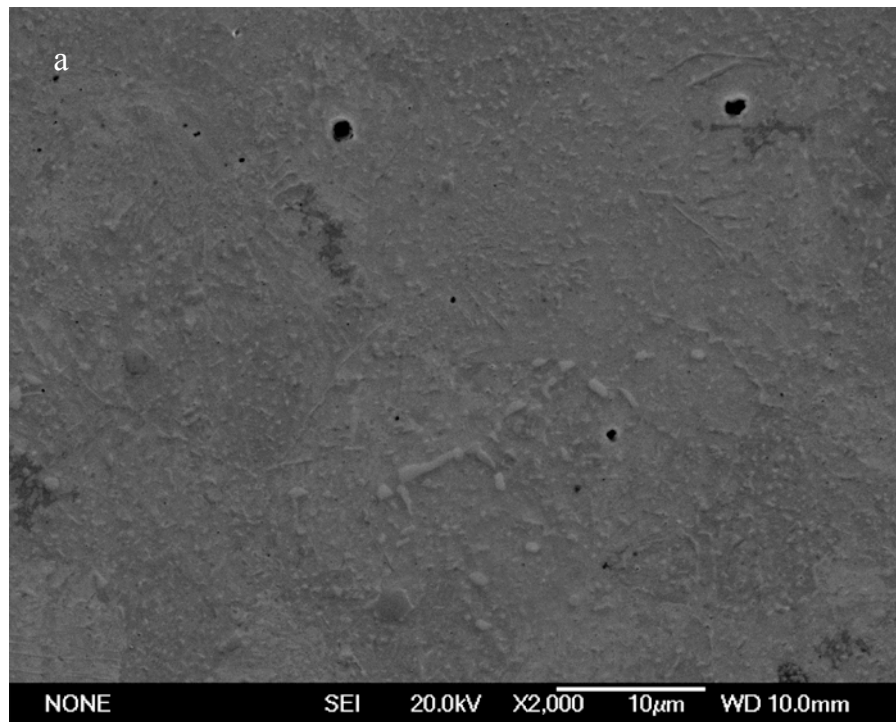


Figure 4.5.6 SEM observation on the HCP-PC samples (a) before and (b) after anodic polarisation tests.

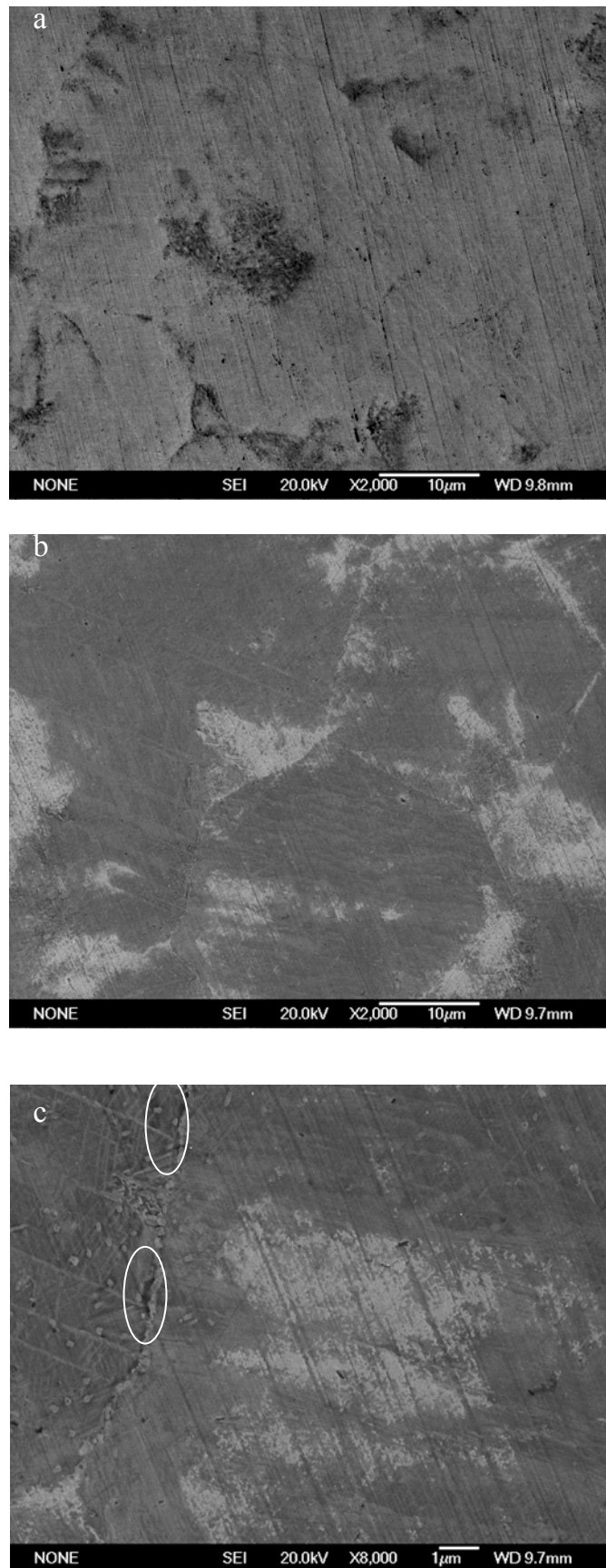


Figure 4.5.7 SEM observations on the 40HCP-PC samples (a) before and (b, c) after anodic polarisation tests.

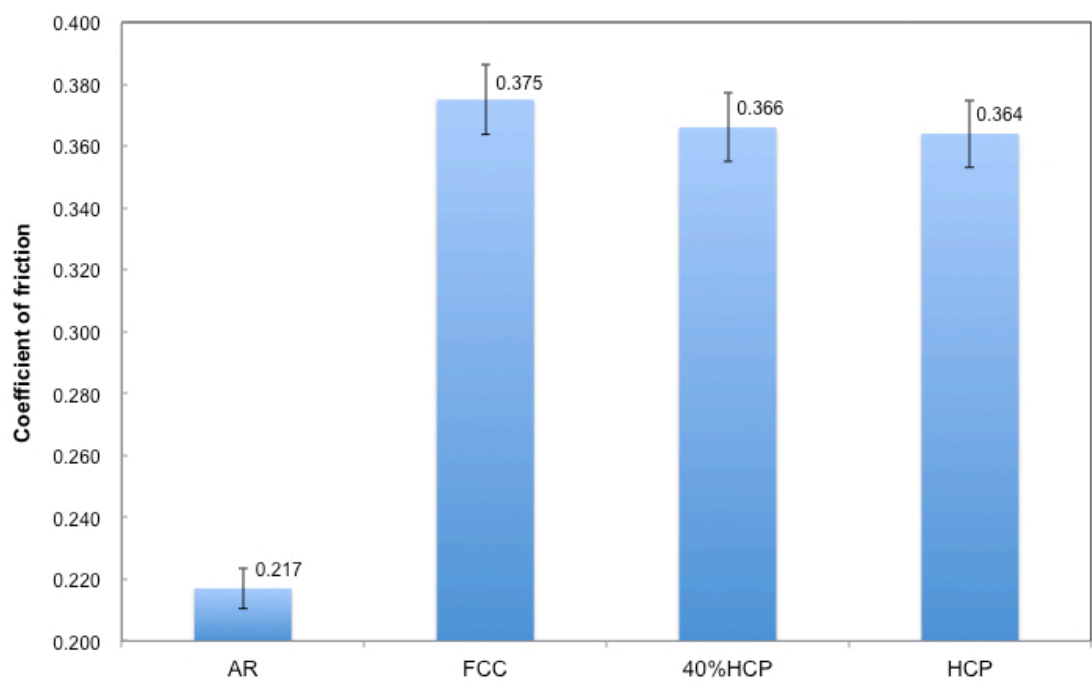


Figure 4.6.1 Average friction coefficient of the AR and heat-treated samples (error bar showing the standard deviation).

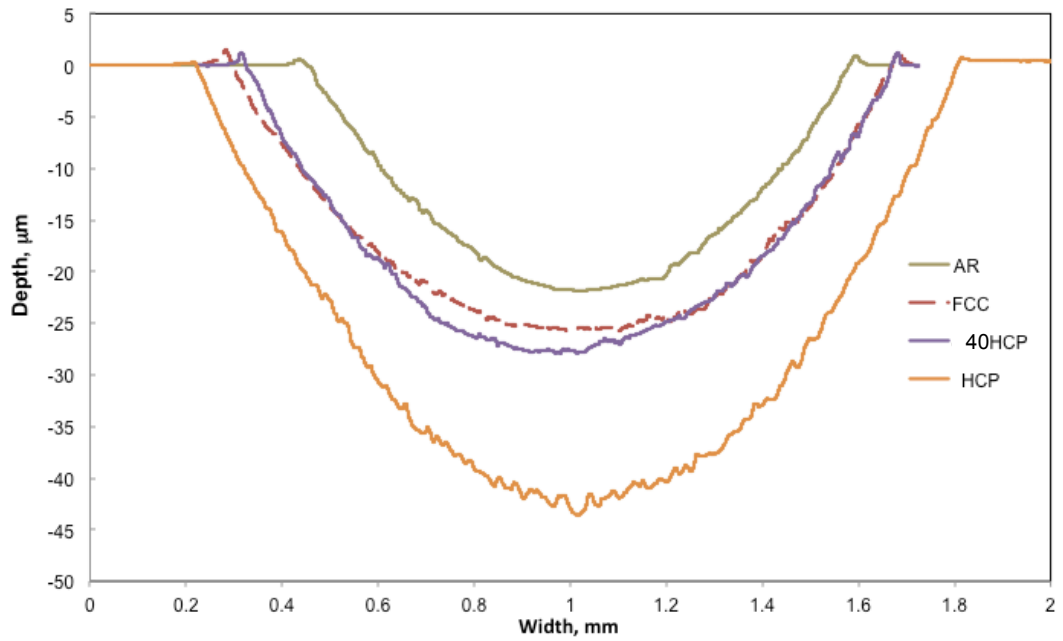


Figure 4.6.2 Cross-section wear track profiles on the AR and heat-treated samples (load 30N).

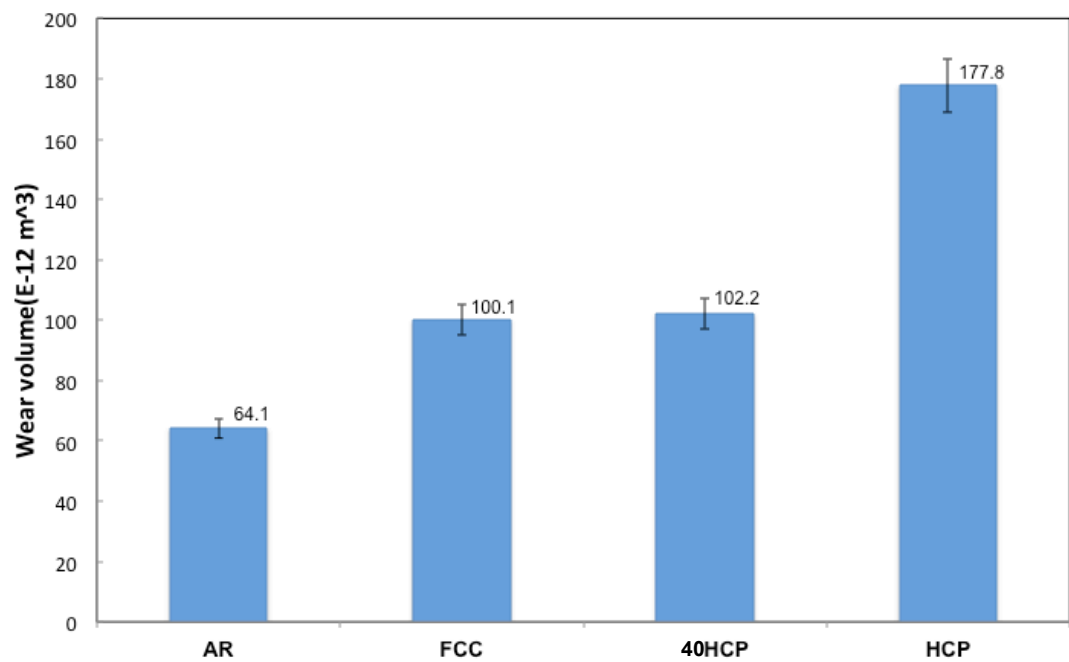


Figure 4.6.3 Wear volume of the AR and heat-treated samples (error bar showing the standard deviation).

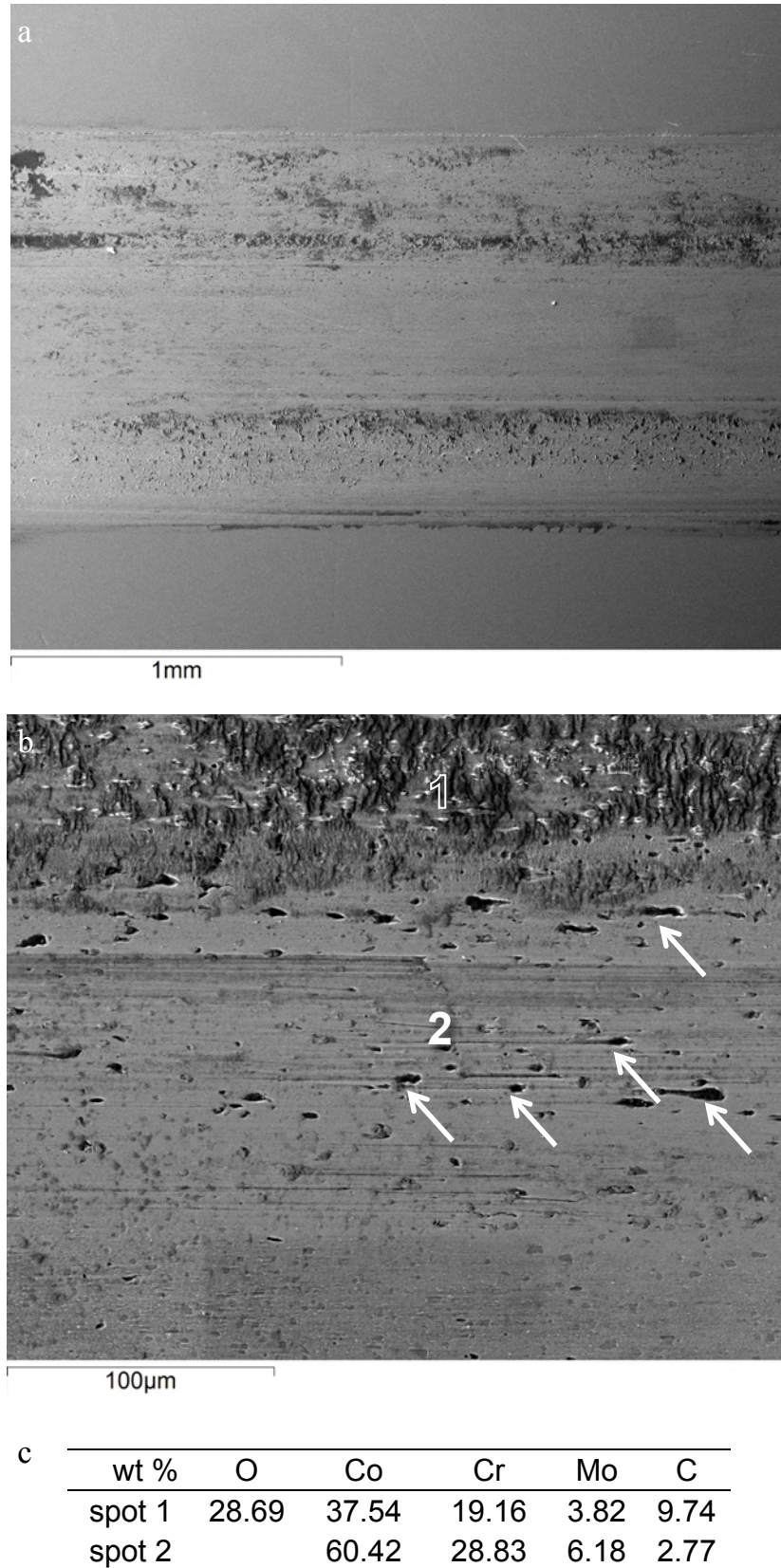
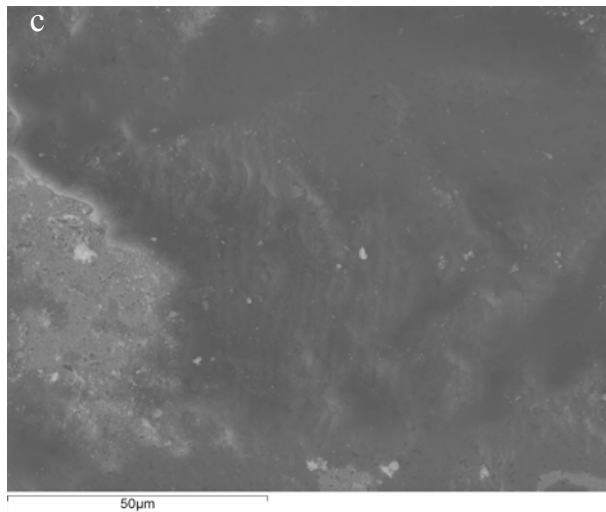
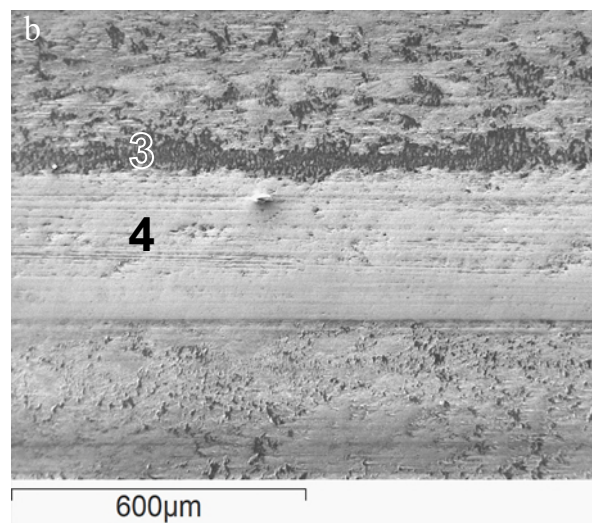
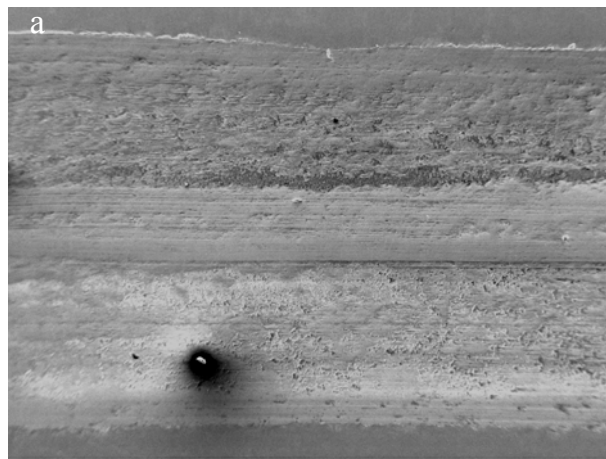


Figure 4.6.4 SEM observation of wear track on the AR sample: (a) low magnification SEM, (b) high magnification SEM and (c) EDX analysis.



d

wt %	O	Co	Cr	Mo	C
spot 3	33.25	6.76	19.07	4.61	5.08
spot 4		59.03	28.76	6.59	3.9

Figure 4.6.5 (a) low and (b) high magnification SEM observations of wear tracks, (c) SEM observation of wear debris on the FCC sample and (d) EDX analysis.

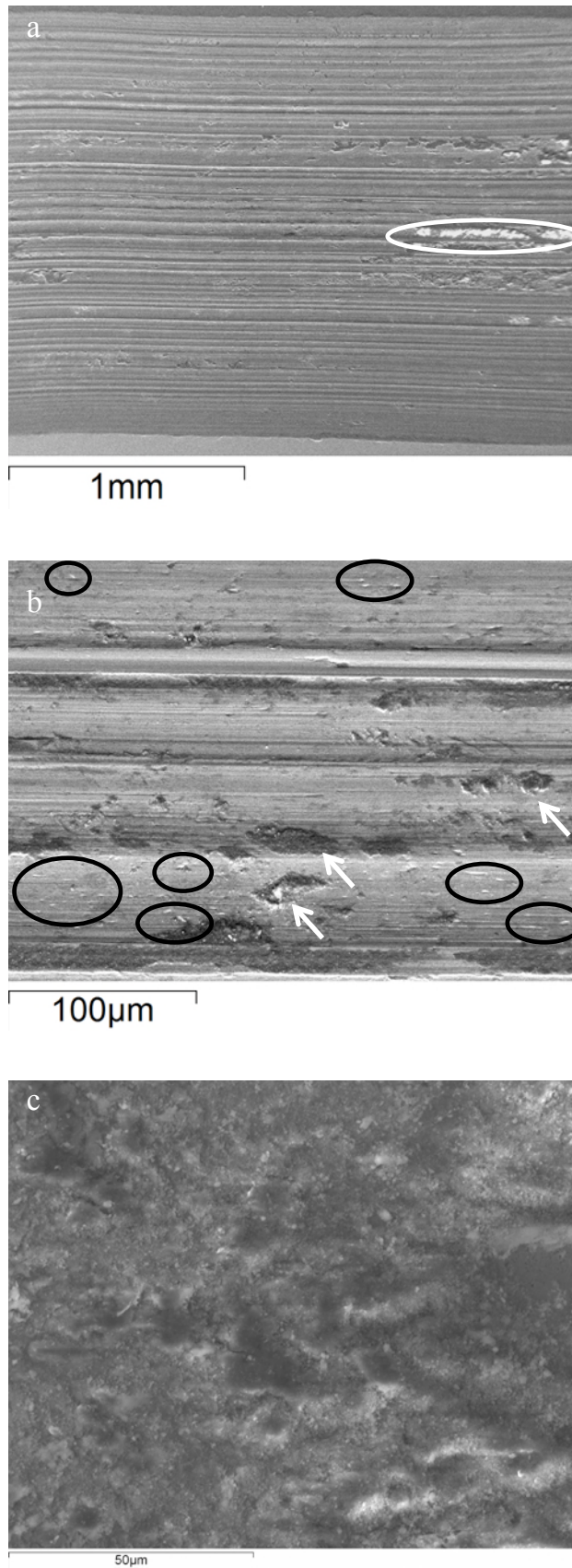


Figure 4.6.6 (a) low and (b) high magnification SEM observations of wear tracks, (c) SEM observation of wear debris on the HCP sample

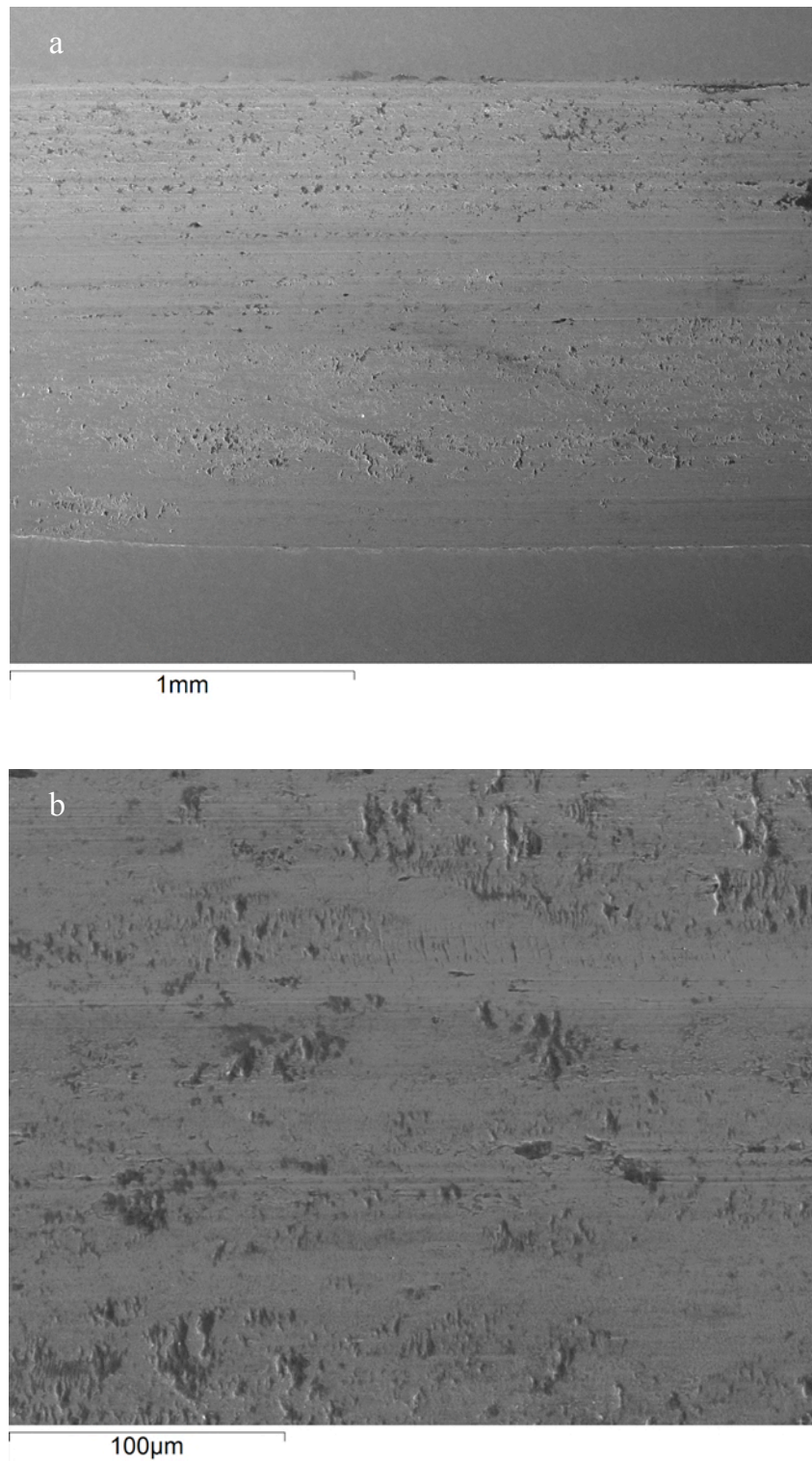


Figure 4.6.7 SEM observation of wear track on the 40HCP sample (a) low magnification and (b) high magnification SEM.

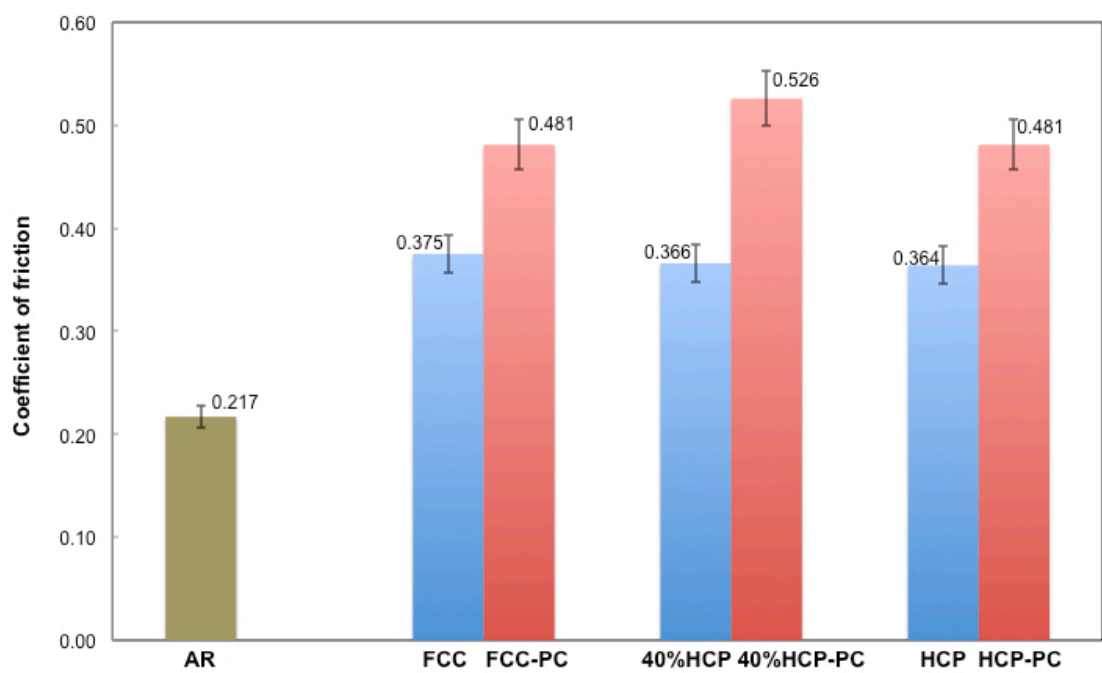


Figure 4.6.8 Average friction coefficient of samples before and after plasma carburising treatment (error bar showing the standard deviation).

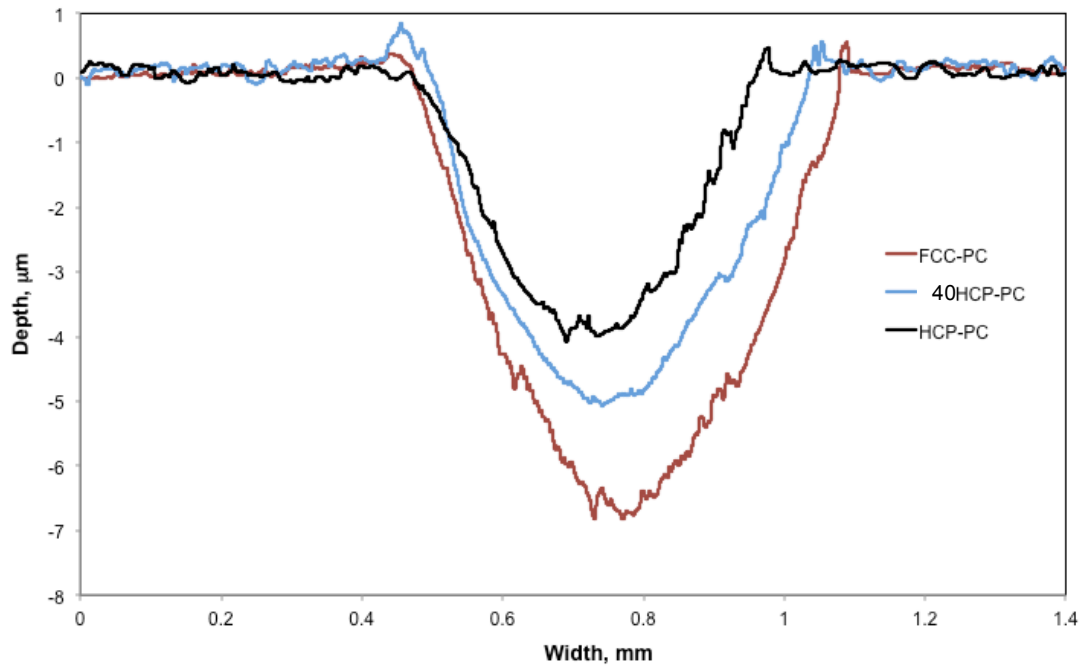


Figure 4.6.9 Cross-section wear track profiles on the plasma carburised samples.

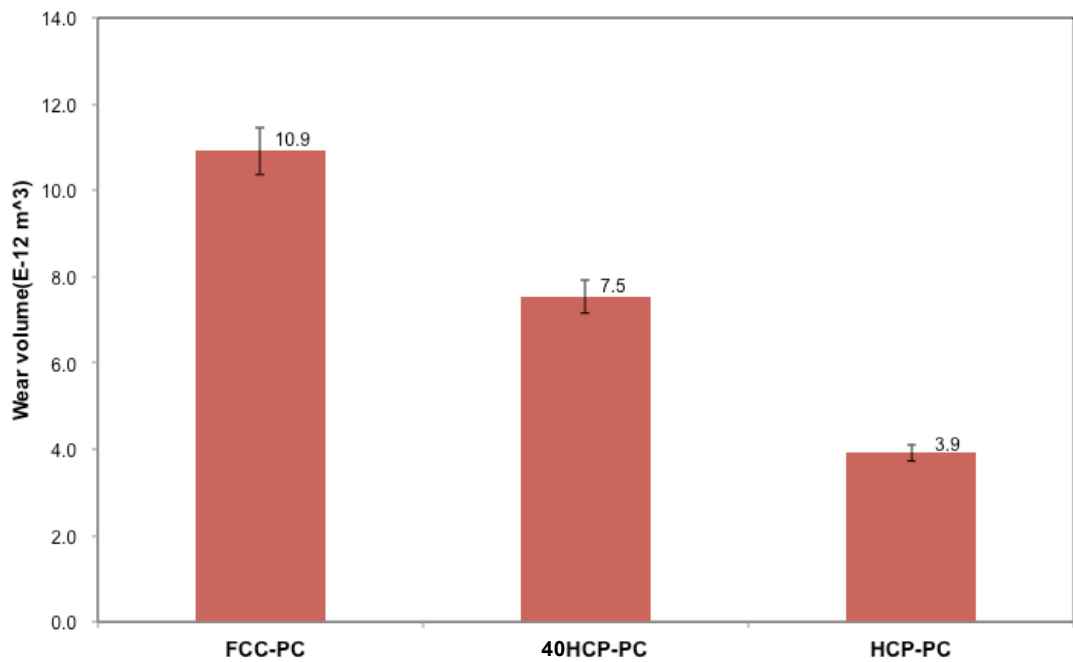
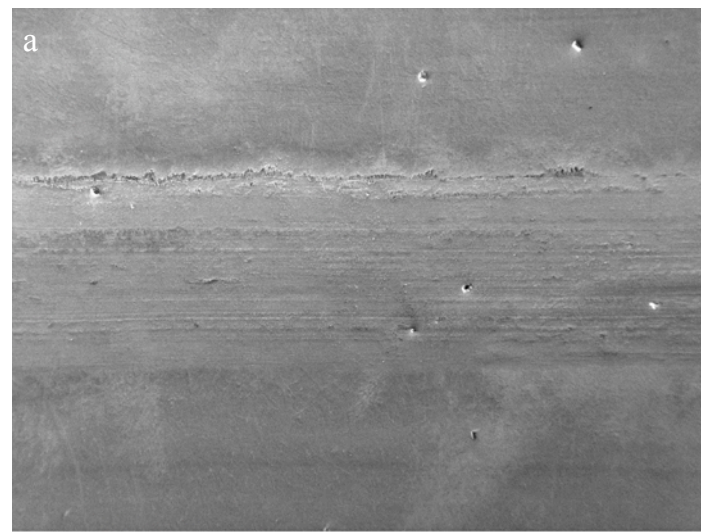
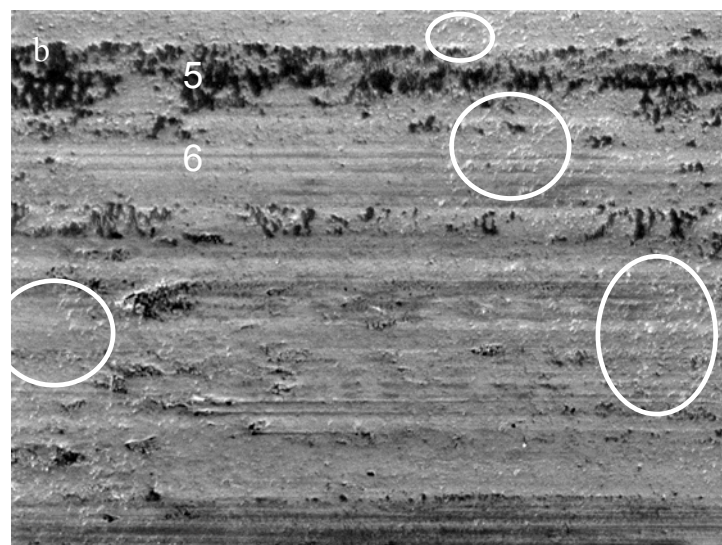


Figure 4.6.10 Wear volume of different samples: (a) plasma carburised samples, (b) samples before and after plasma carburising treatments (error bar showing the standard deviation).



1mm



100μm

c	wt %	O	Co	Cr	Mo	C
spot 5	29.12	40.94	20.20	4.67	4.13	
spot 6		56.23	28.15	7.09	7.02	

Figure 4.6.11 SEM observation of wear track on the FCC-PC sample: (a) low magnification SEM, (b) high magnification SEM and (c) EDX analysis.

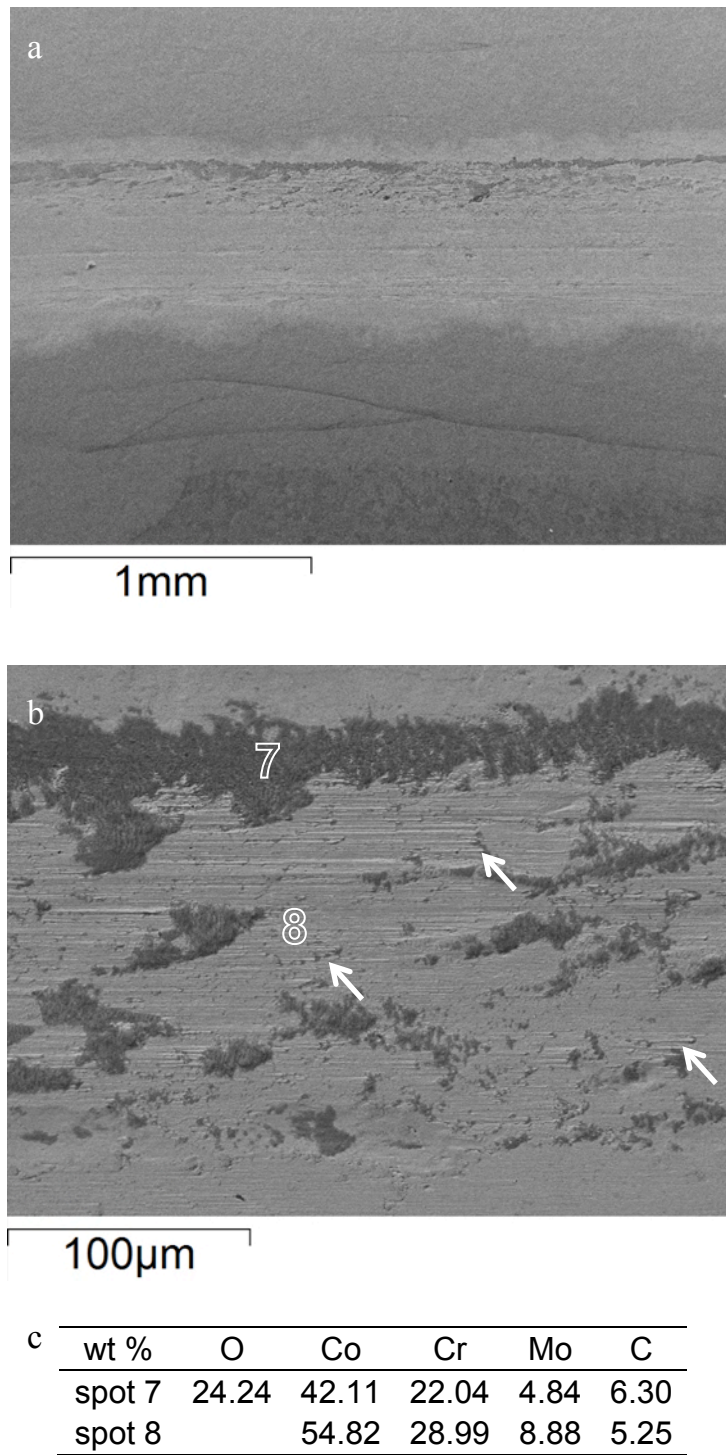


Figure 4.6.12 SEM observation of wear track on the HCP-PC sample: (a) low magnification SEM, (b) high magnification SEM and (c) EDX analysis.

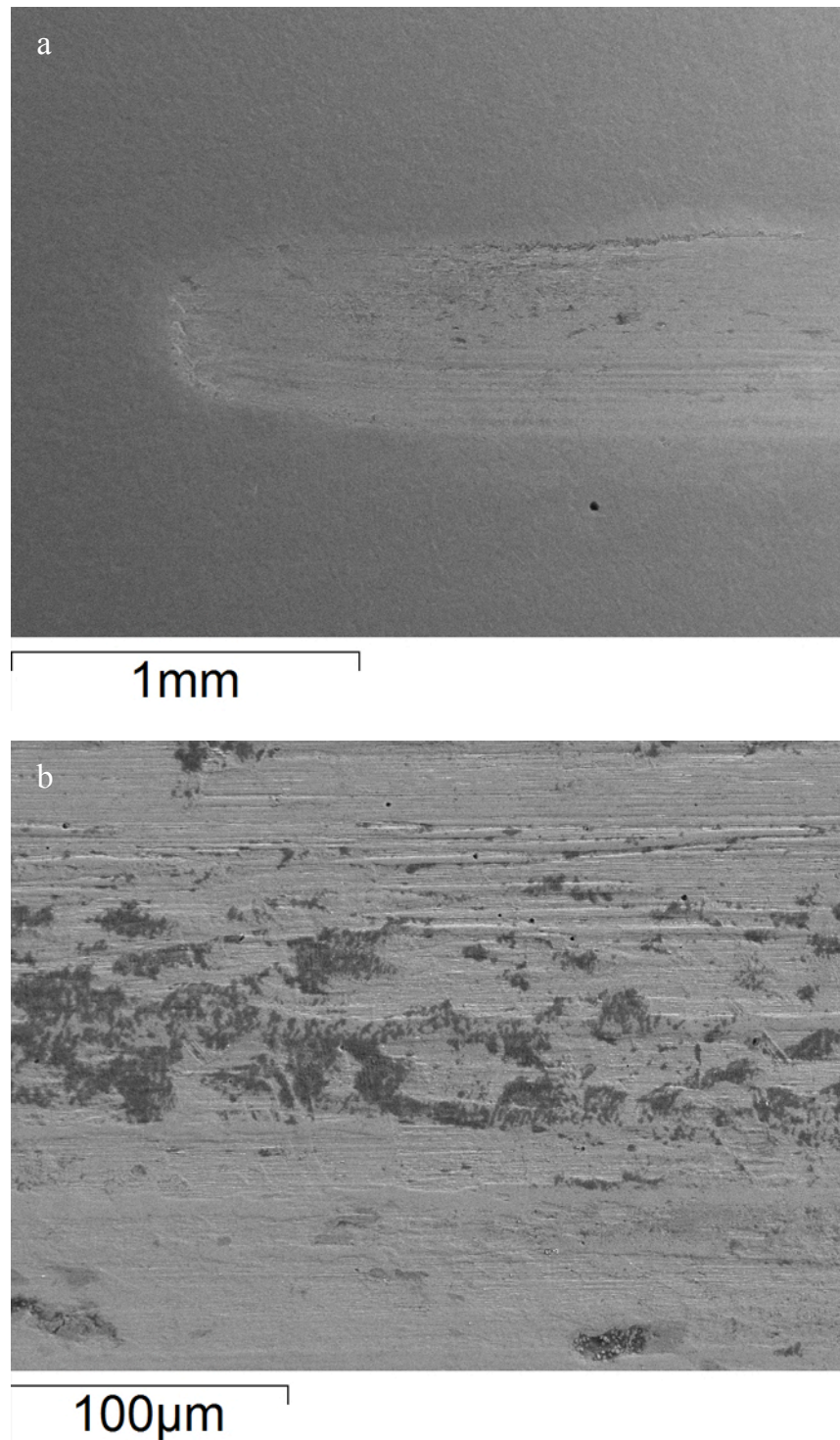


Figure 4.6.13 SEM observation of ball tested and wear track for 40HCP-PC: (a) low magnification and (b) high magnification SEM.

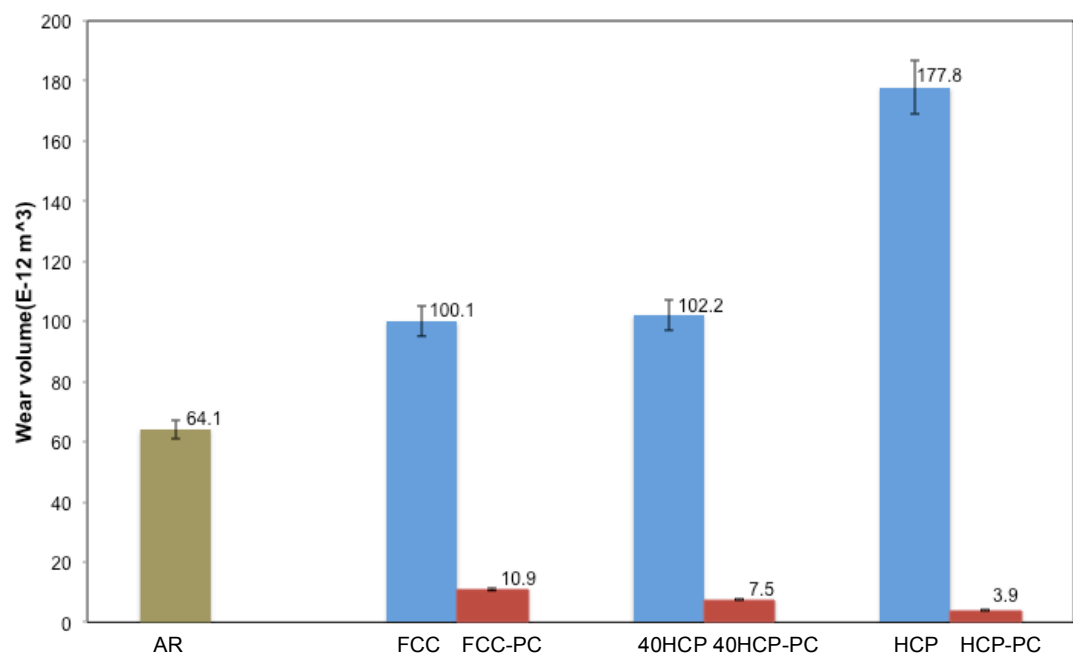


Figure 4.6.14 Wear volume of the AR, heat-treated and plasma carburised samples (error bar showing the standard deviation).

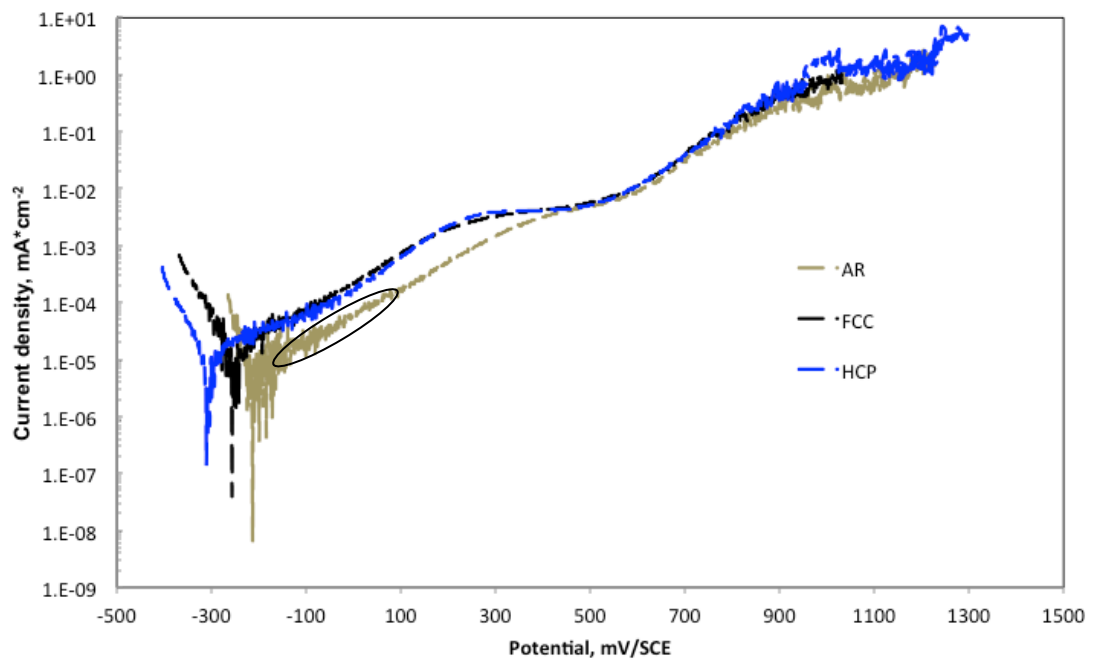


Figure 4.7.1 Potentiodynamic polarisation curves of the AR and heat-treated samples tested under rotation without load (corrosion) condition.

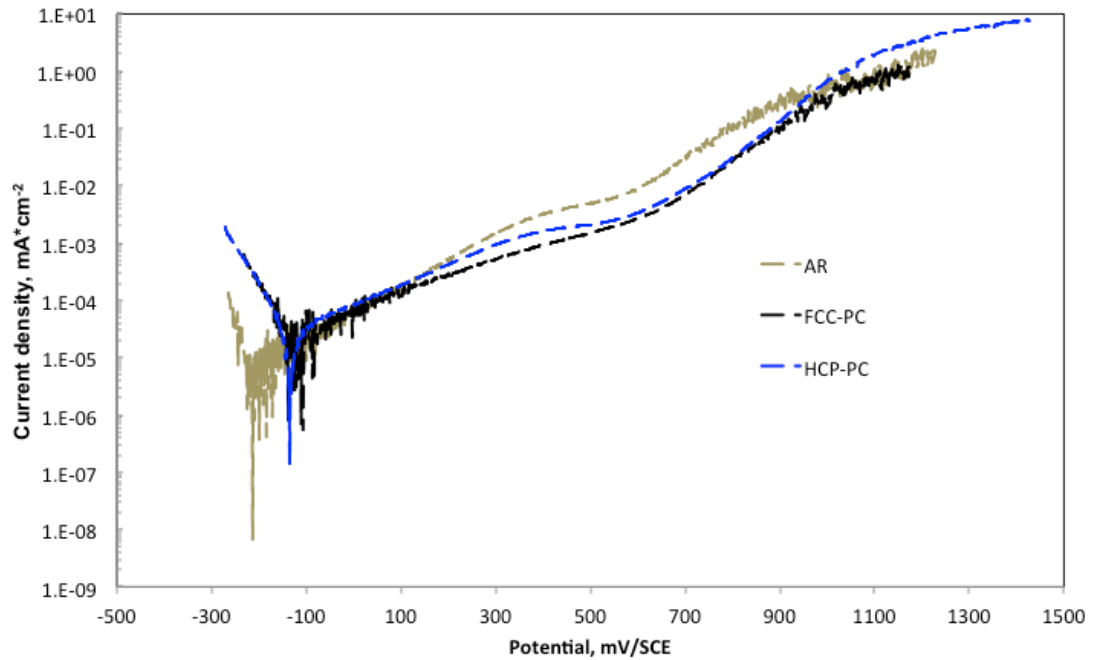


Figure 4.7.2 Potentiodynamic polarisation curves of the AR and plasma carburised samples tested under rotation without load (corrosion) condition.

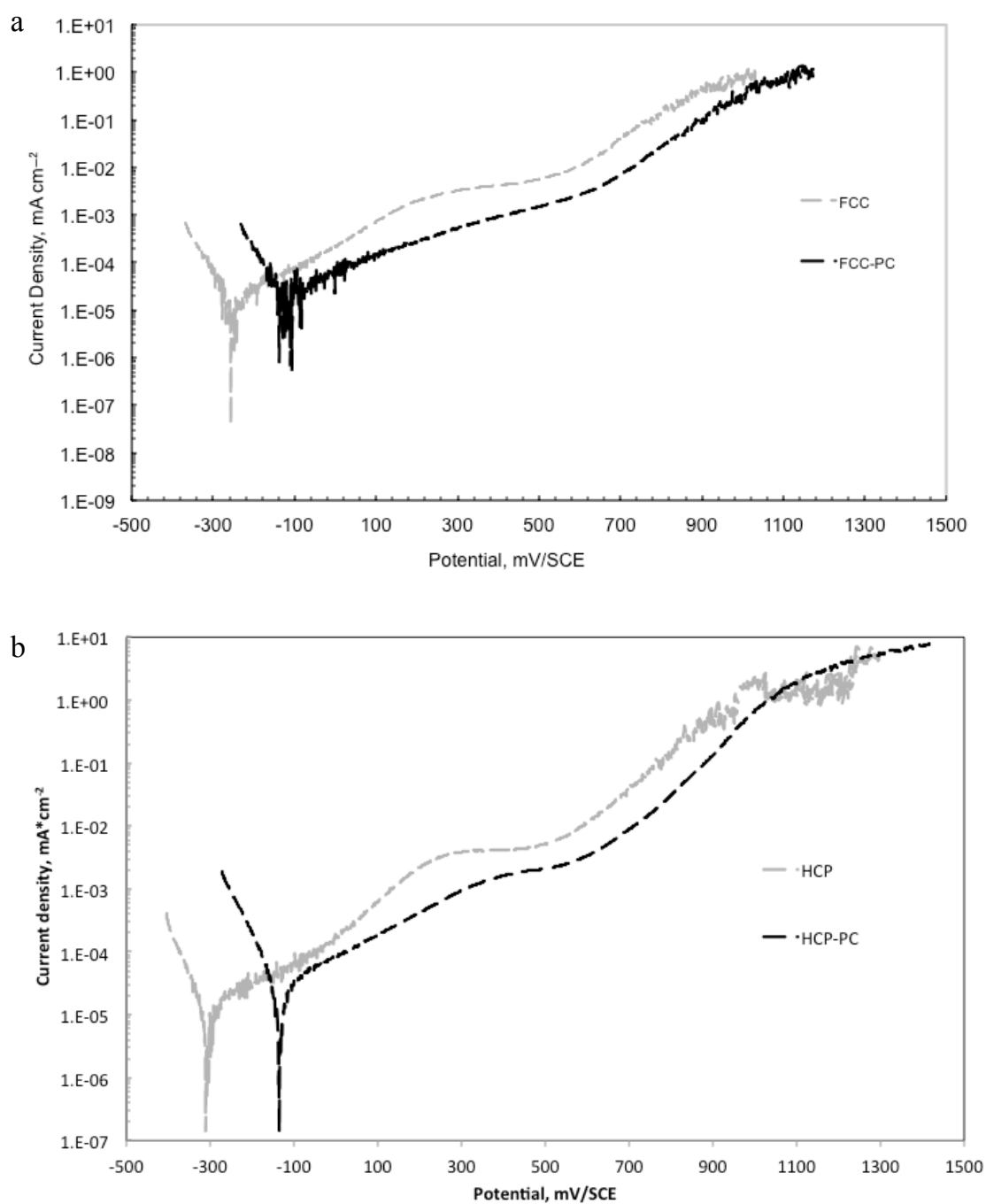


Figure 4.7.3 Potentiodynamic polarisation curves of samples before plasma carburising treatments tested under rotation without load (corrosion) condition: (a) FCC and FCC-PC and (b) HCP and HCP-PC.

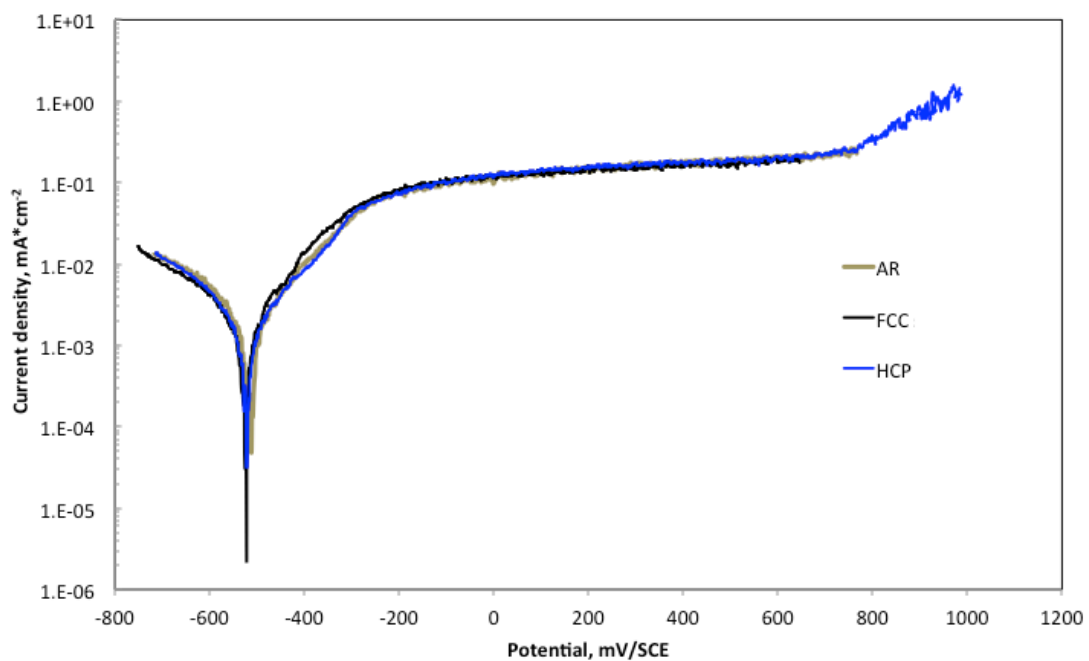


Figure 4.7.4 Potentiodynamic polarisation curves of the AR and heat-treated samples tested under sliding (tribocorrosion) conditions.

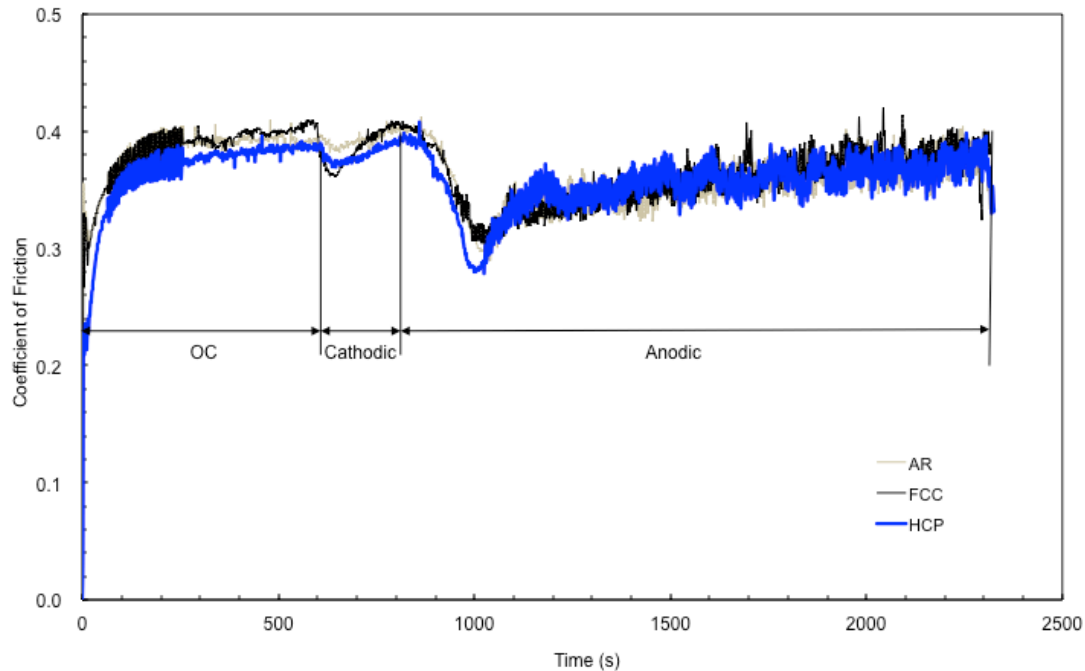


Figure 4.7.5 Coefficient of friction curves of the AR and heat-treated samples measured during potentiodynamic tests under sliding condition.

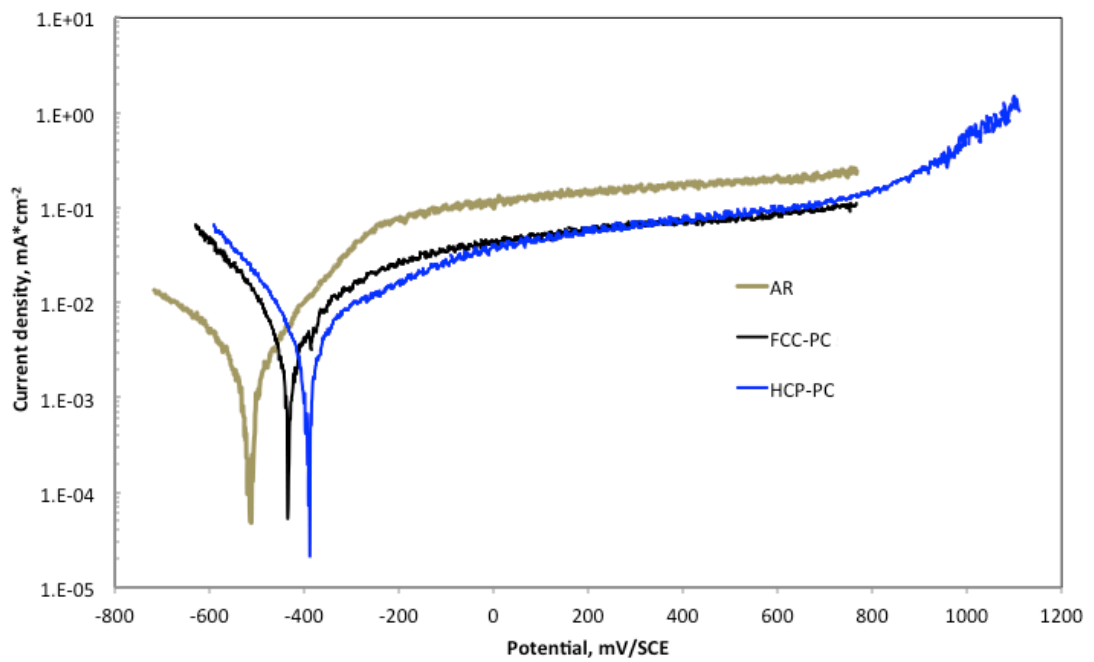


Figure 4.7.6 Potentiodynamic polarisation curves of the AR and plasma carburised samples tested under sliding (tribocorrosion) condition.

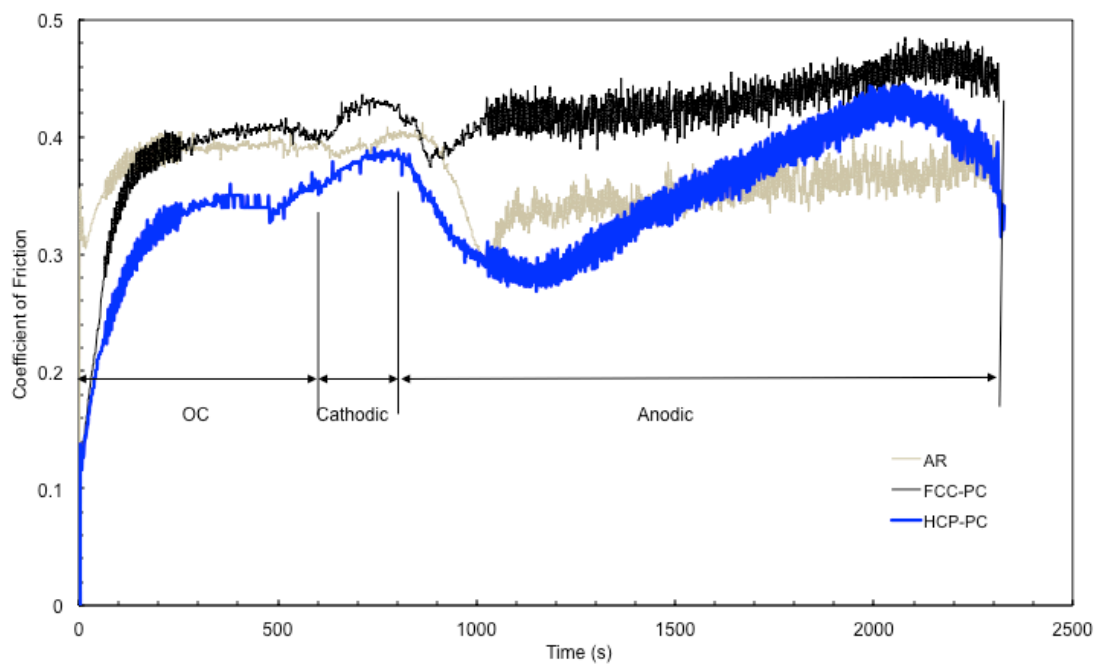


Figure 4.7.7 Coefficient of friction curves of the AR and plasma carburised samples measured during potentiodynamic tests under sliding.

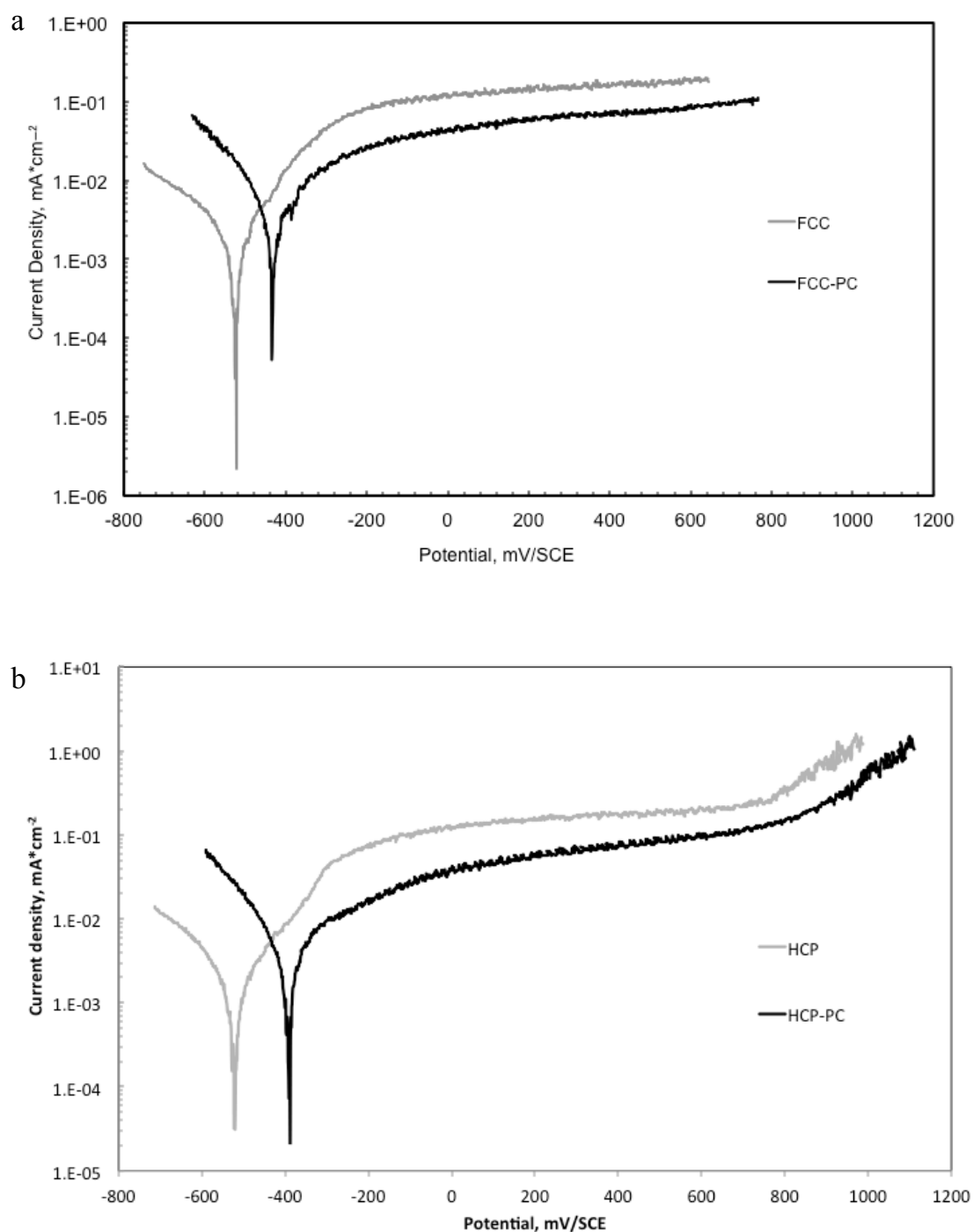


Figure 4.7.8 Potentiodynamic polarisation curves of samples before and after plasma carburising treatment tested under sliding (tribocorrosion) condition: (a) FCC and FCC-PC and (b) HCP and HCP-PC.

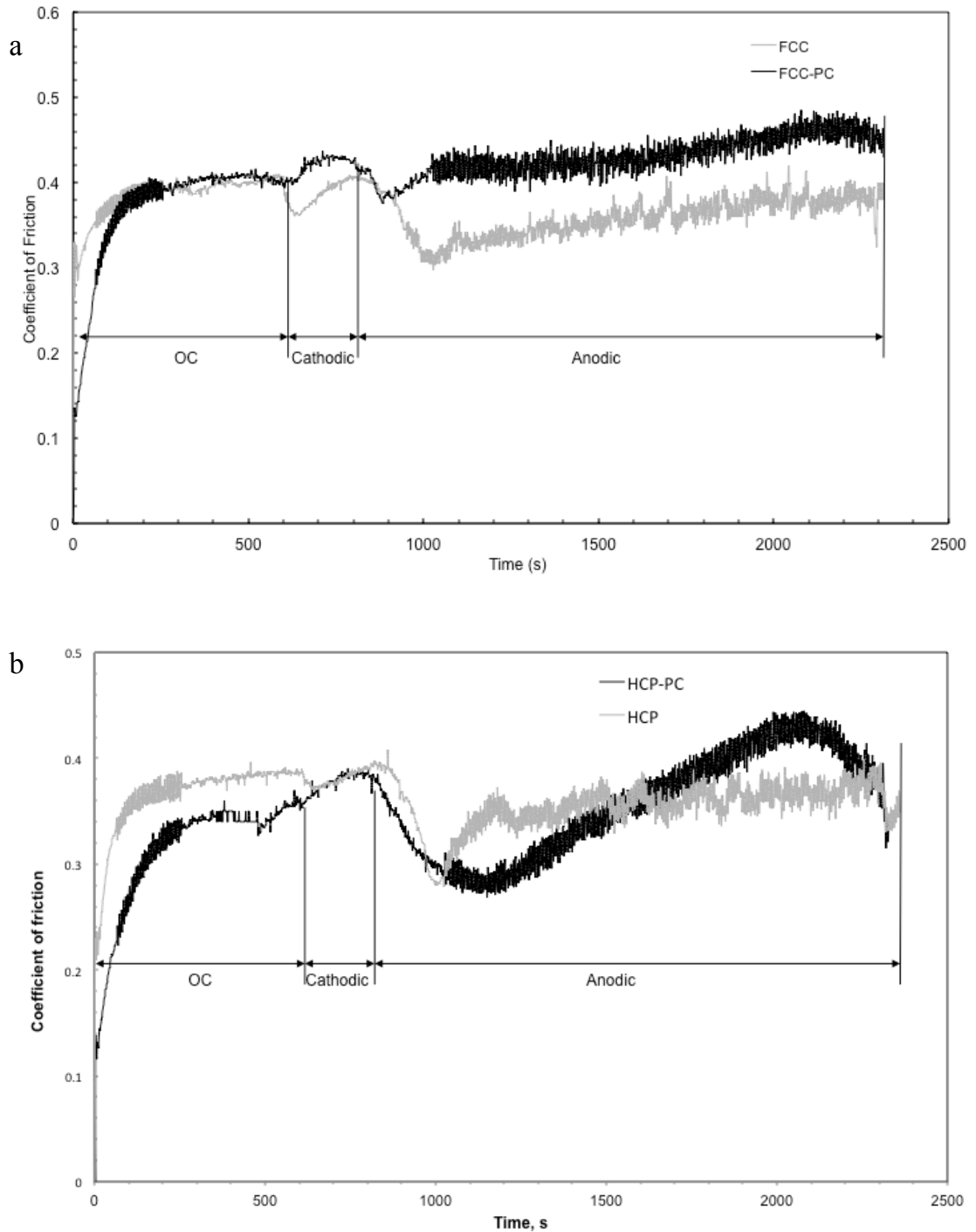


Figure 4.7.9 Coefficient of friction curves of samples before and after plasma carburising treatment measured during potentiodynamic tests under sliding: (a) FCC and FCC-PC and (b) HCP and HCP-PC.

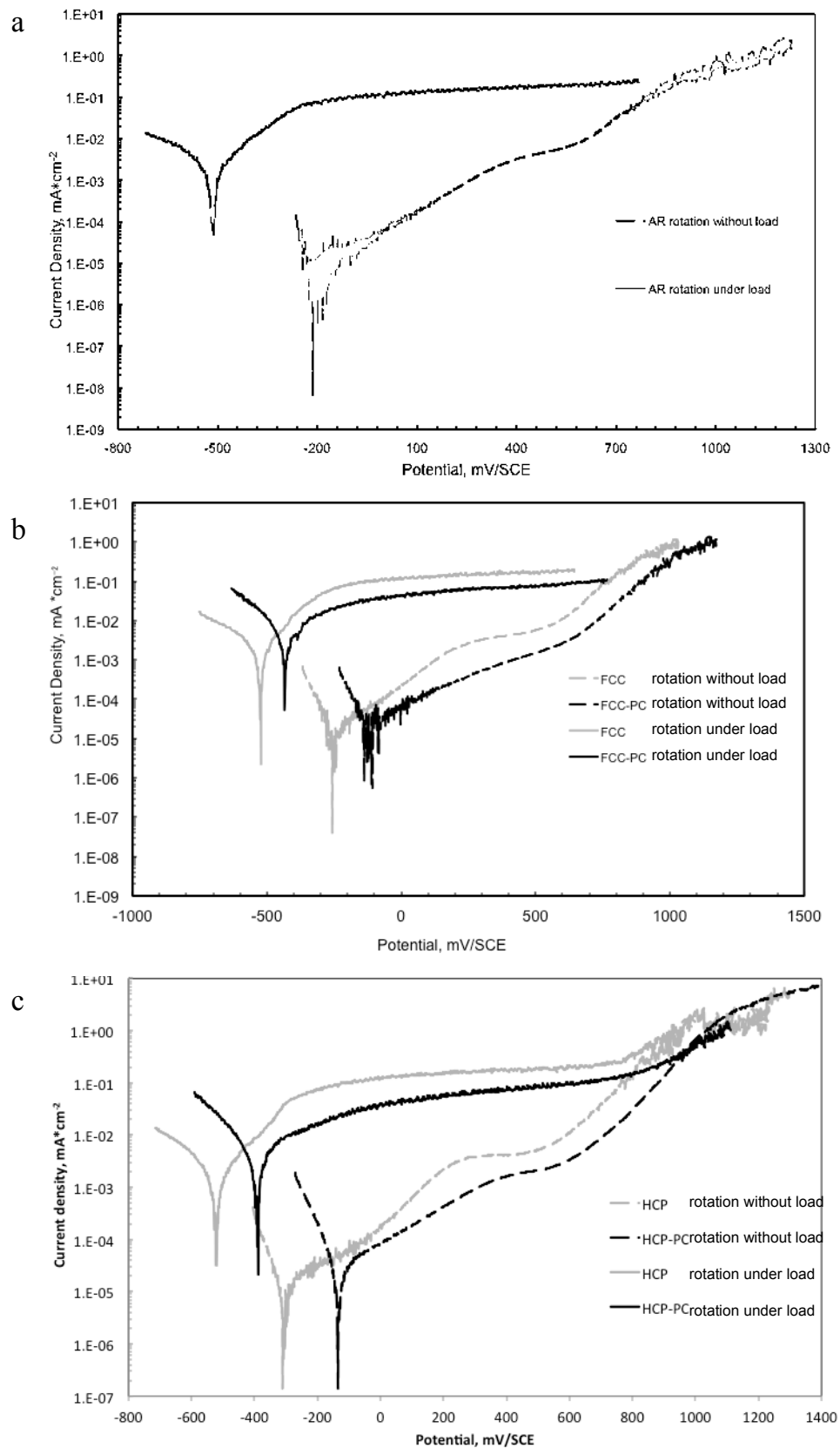


Figure 4.7.10 Potentiodynamic polarisation curves tested under rotation without load (corrosion) and sliding (tribocorrosion) conditions: (a) AR, (b) FCC and FCC-PC and (c) HCP and HCP-PC.

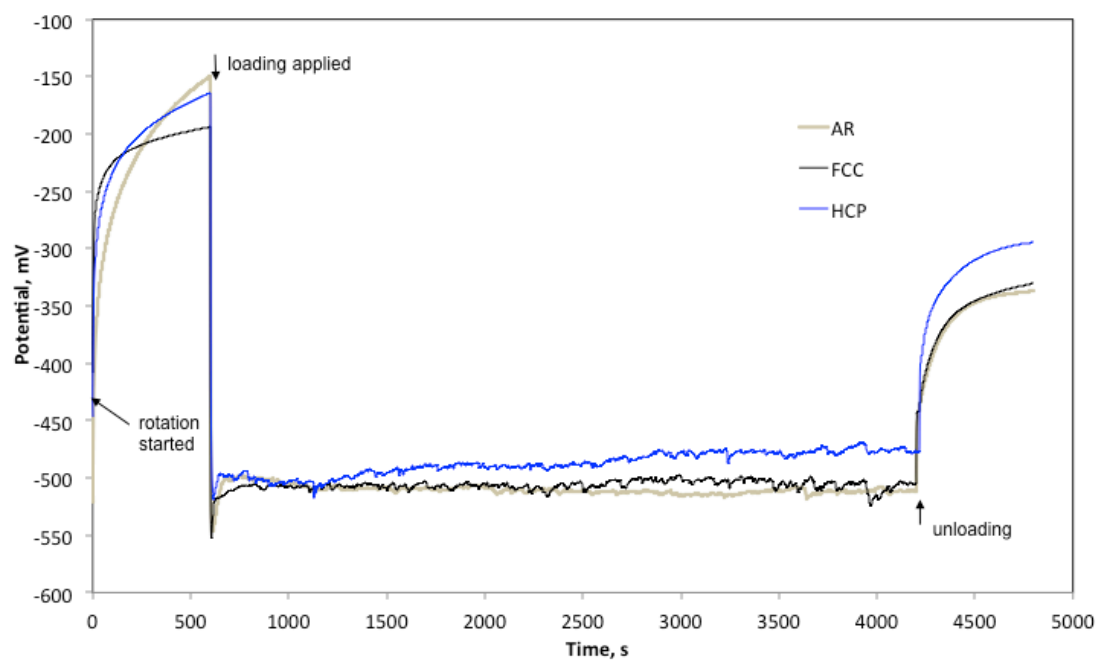


Figure 4.7.11 OCP of AR and heat-treated samples with time.

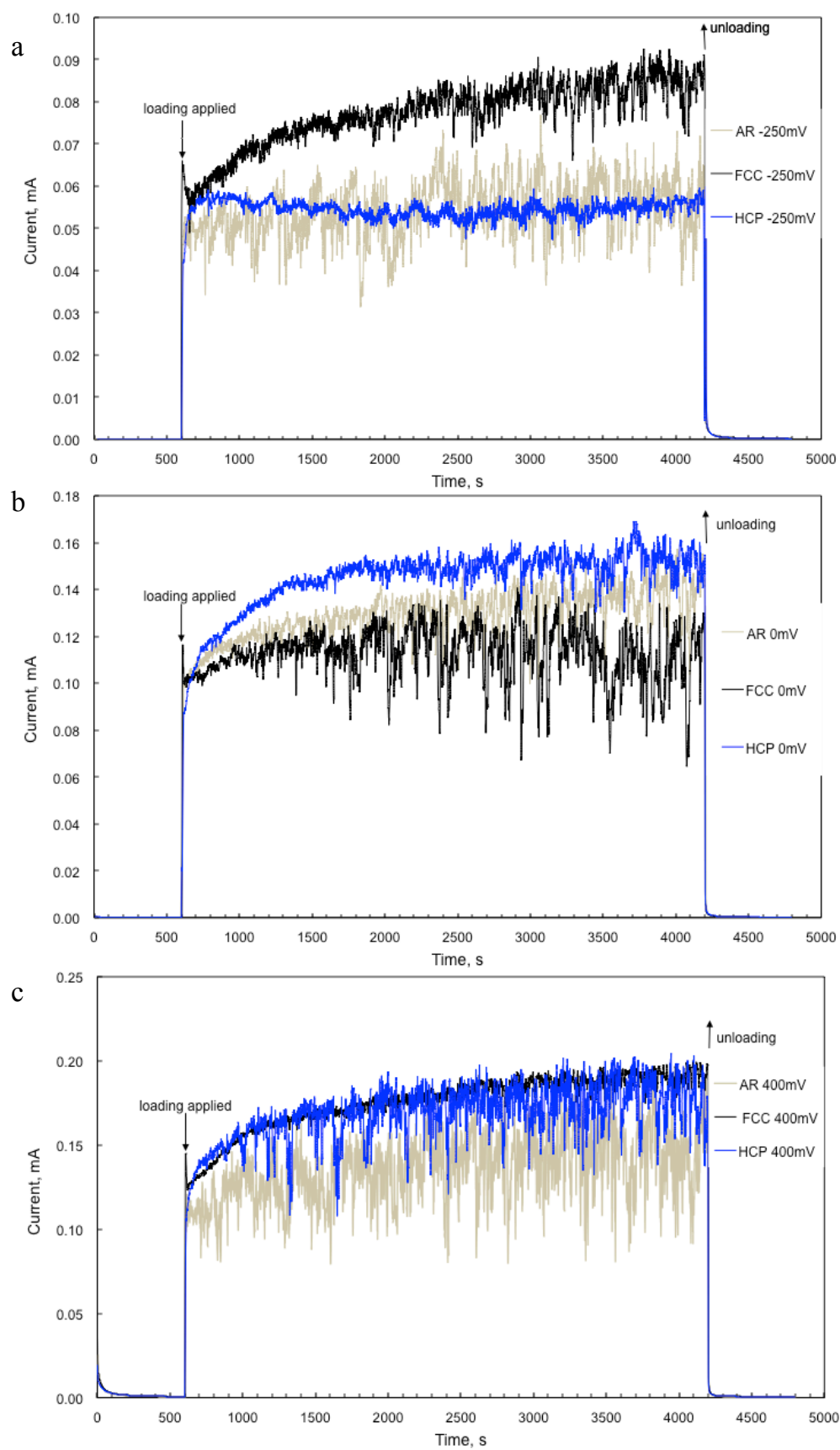


Figure 4.7.12 The current of AR and heat-treated samples at different anodic potentials: (a) at -250mV (SCE), (b) 0mV (SCE) and (c) 400mV (SCE).

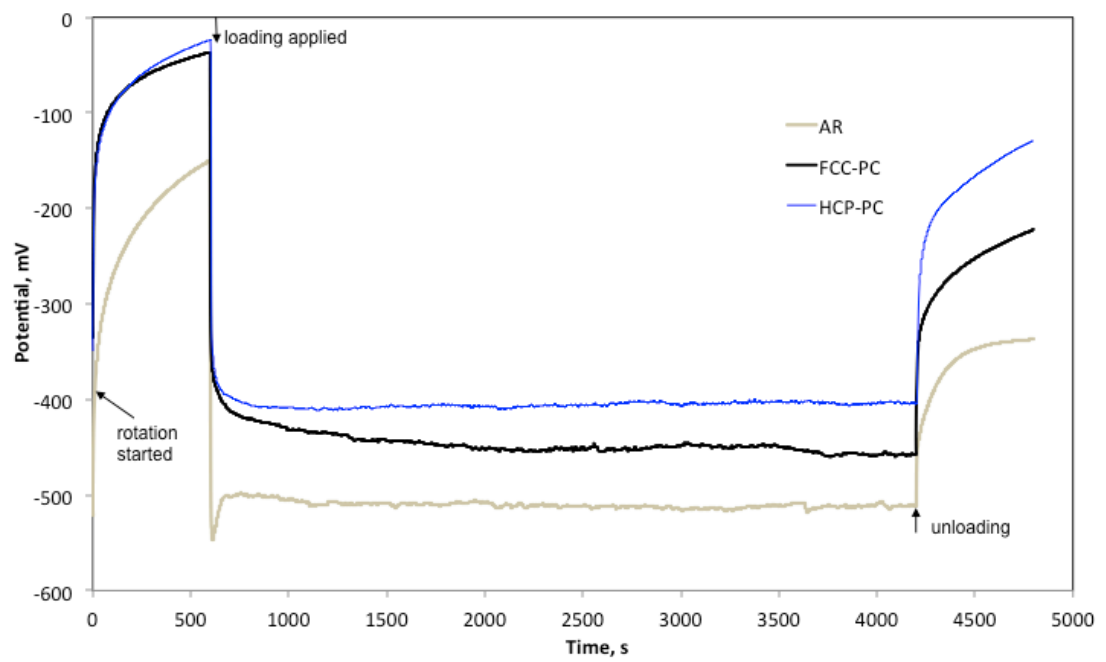


Figure 4.7.13 OCP of AR and plasma carburised samples with time.

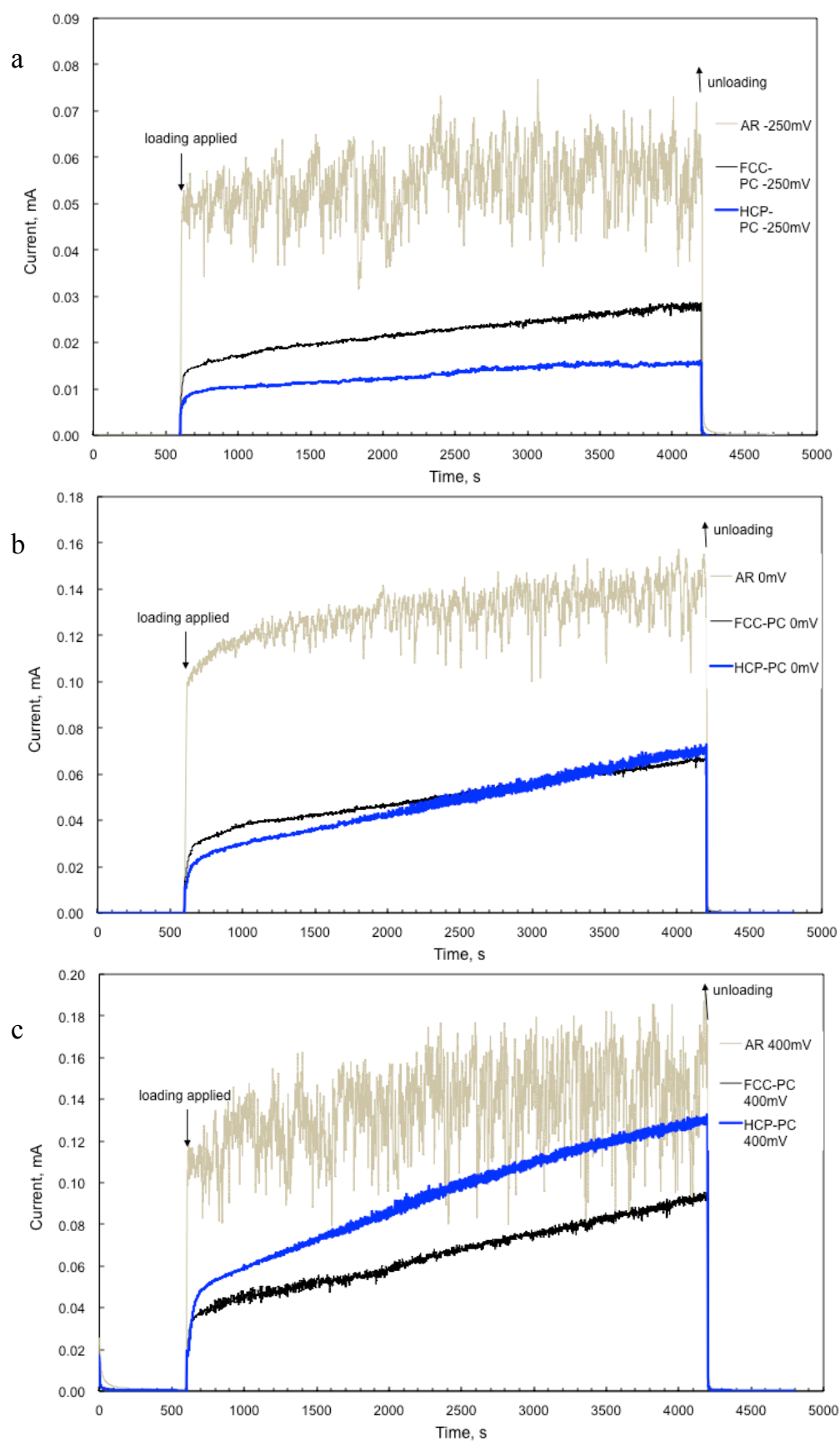


Figure 4.7.14 The current of AR and plasma carburised samples at different anodic potentials: (a) at -250mV (SCE), (b) 0mV (SCE) and (c) 400mV (SCE).

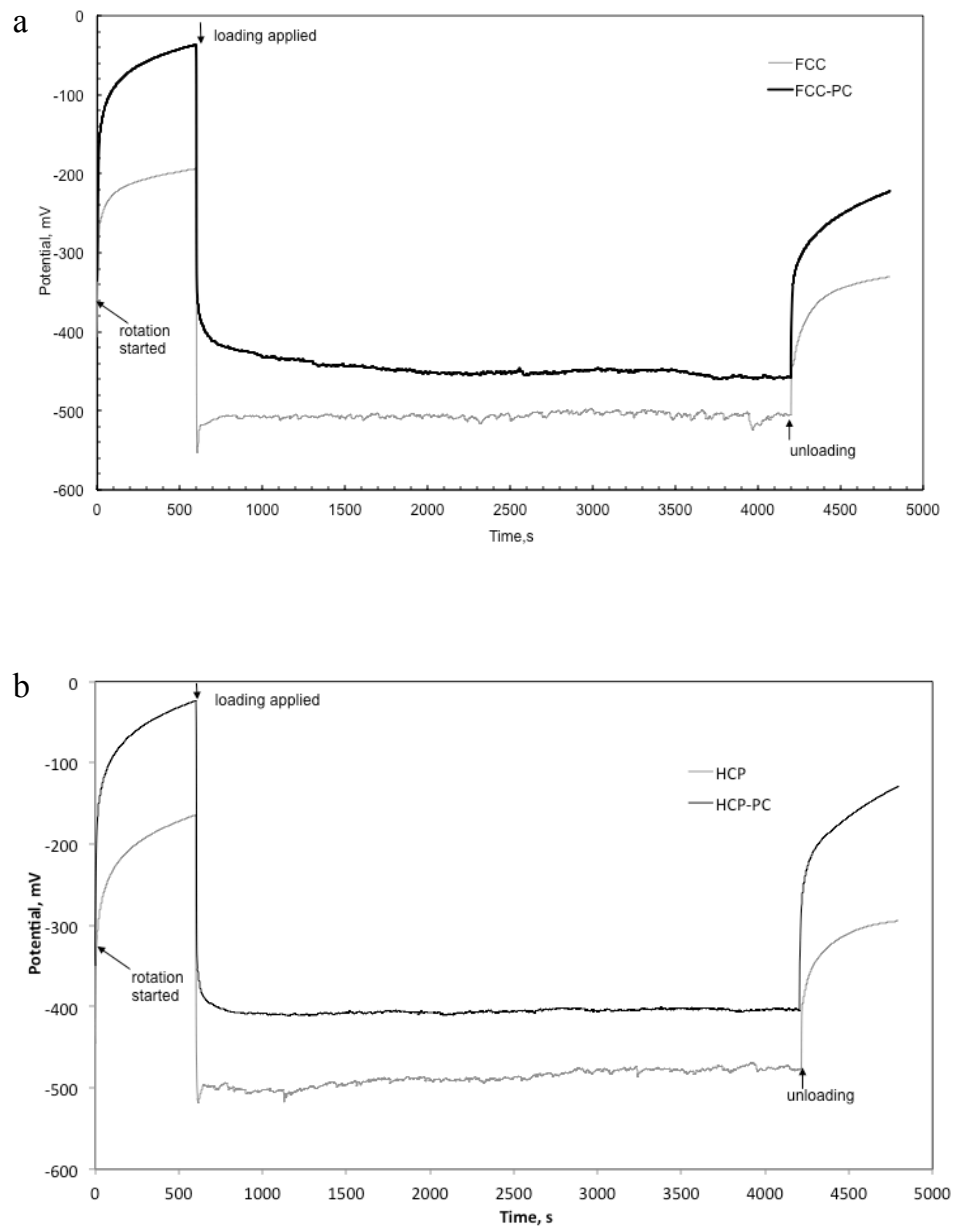


Figure 4.7.15 OCP of samples before and after plasma carburising treatment with time: (a) FCC and FCC-PC and (b) HCP and HCP-PC.

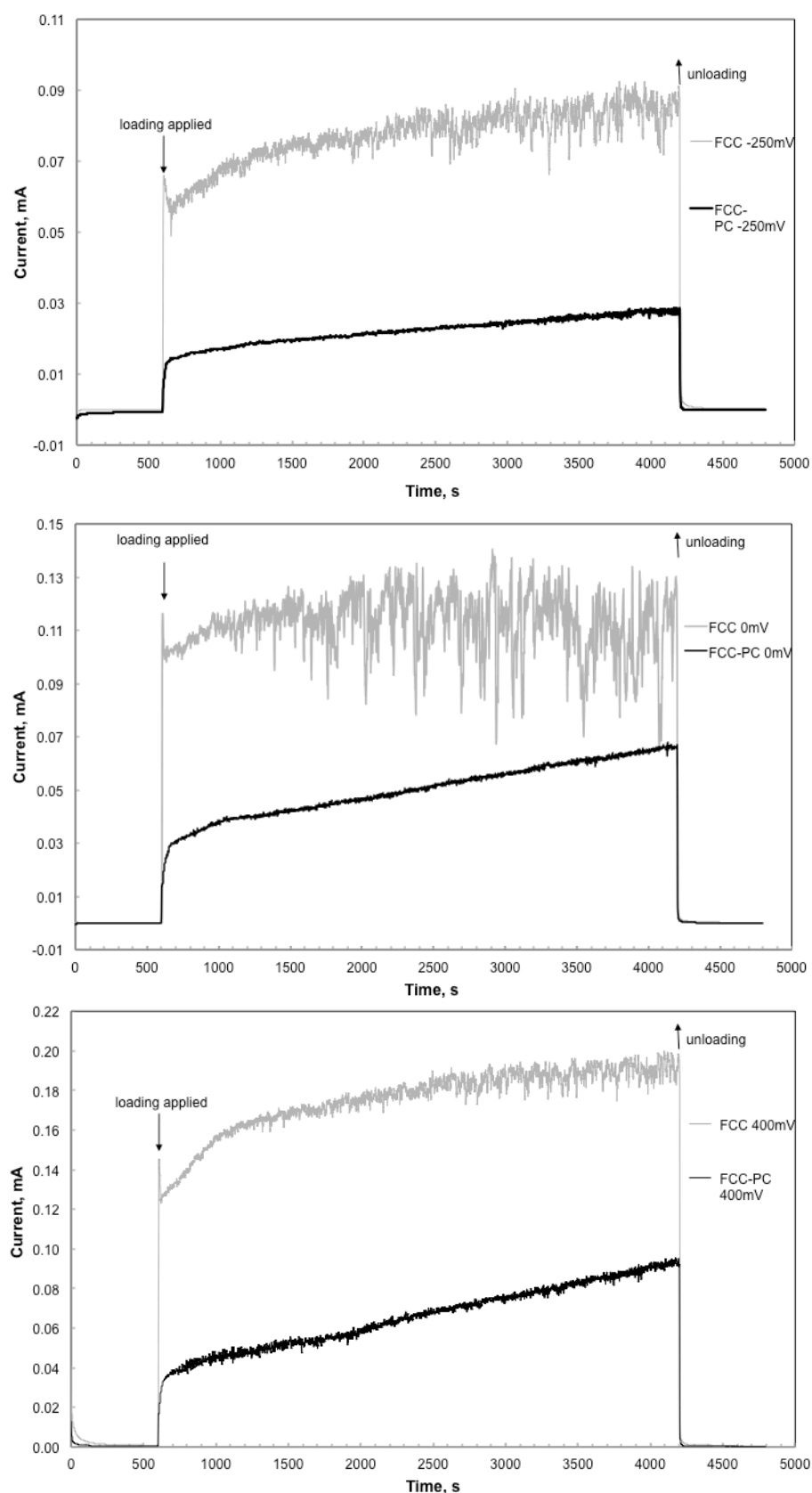


Figure 4.7.16 The current of the FCC and FCC-PC samples at different anodic potentials: (a) at -250mV (SCE), (b) 0mV (SCE) and (c) 400mV (SCE).

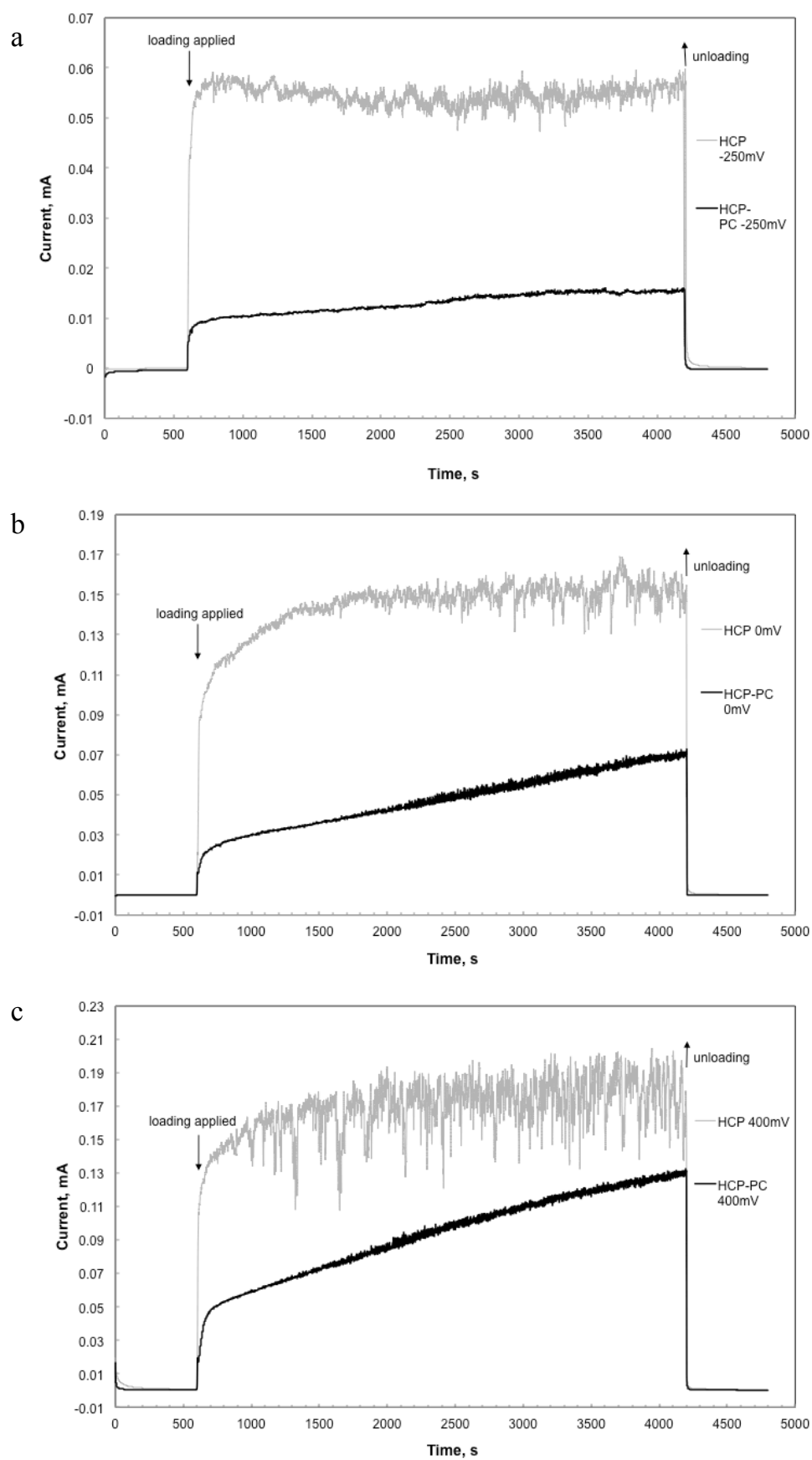


Figure 4.7.17 The current of the HCP and HCP-PC samples at different anodic potentials: (a) at -250mV (SCE), (b) 0mV (SCE) and (c) 400mV (SCE).

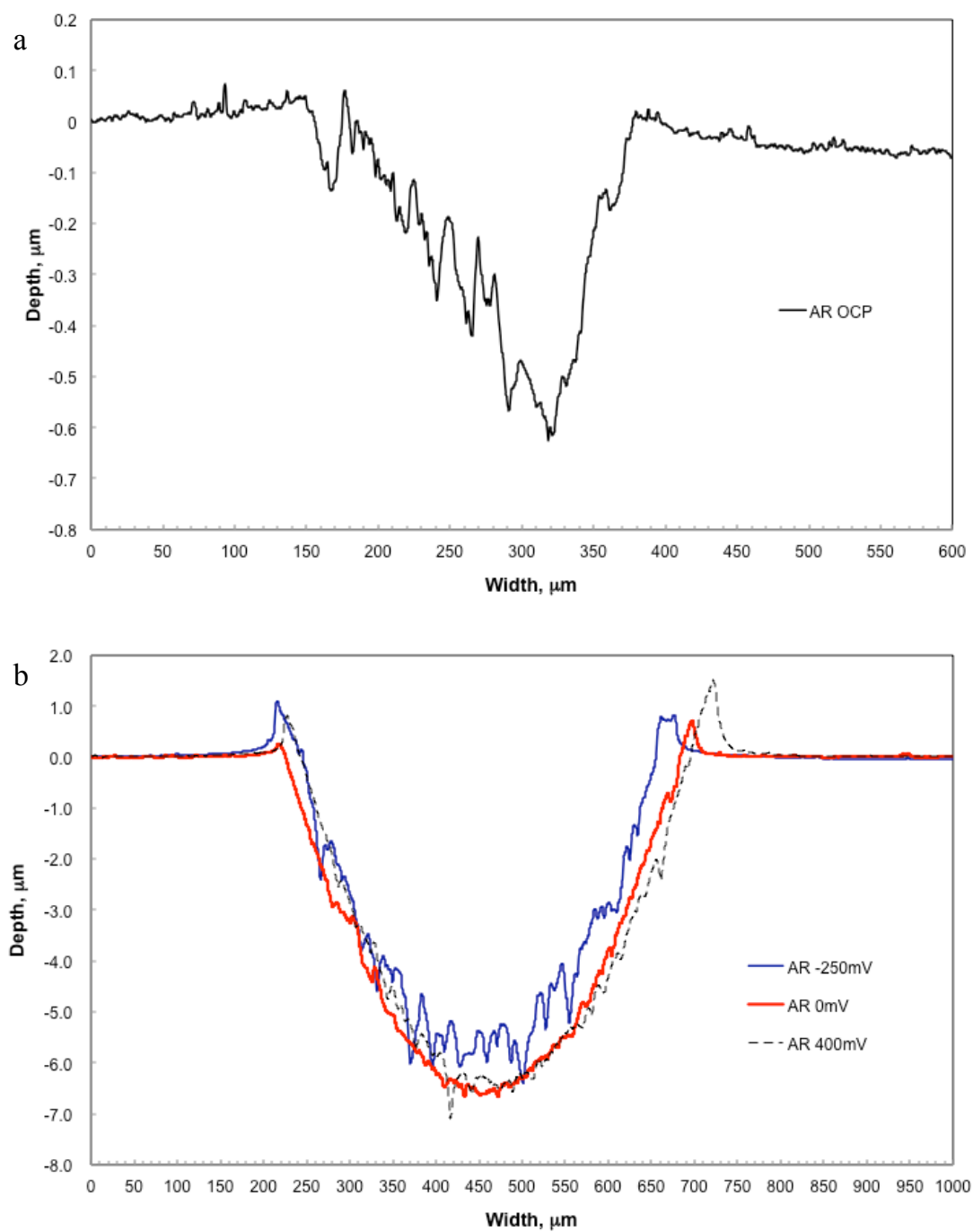


Figure 4.7.18 Typical cross-section profiles of wear tracks of AR (a) at OCP and (b) at -250, 0 and 400 mV (SCE).

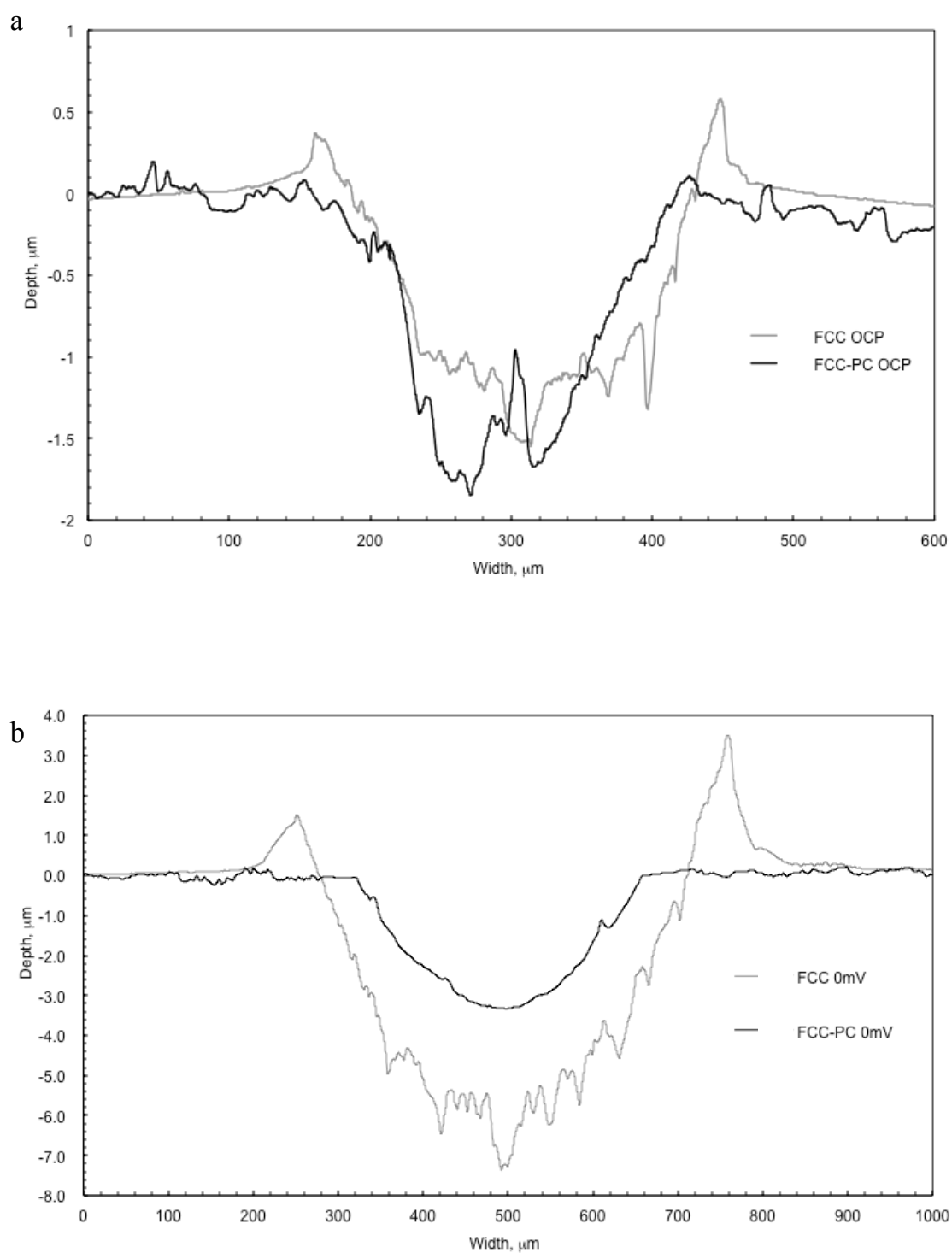


Figure 4.7.19 Typical cross-section profiles of wear tracks of FCC and FCC-PC (a) at OCP and (b) 0mV (SCE).

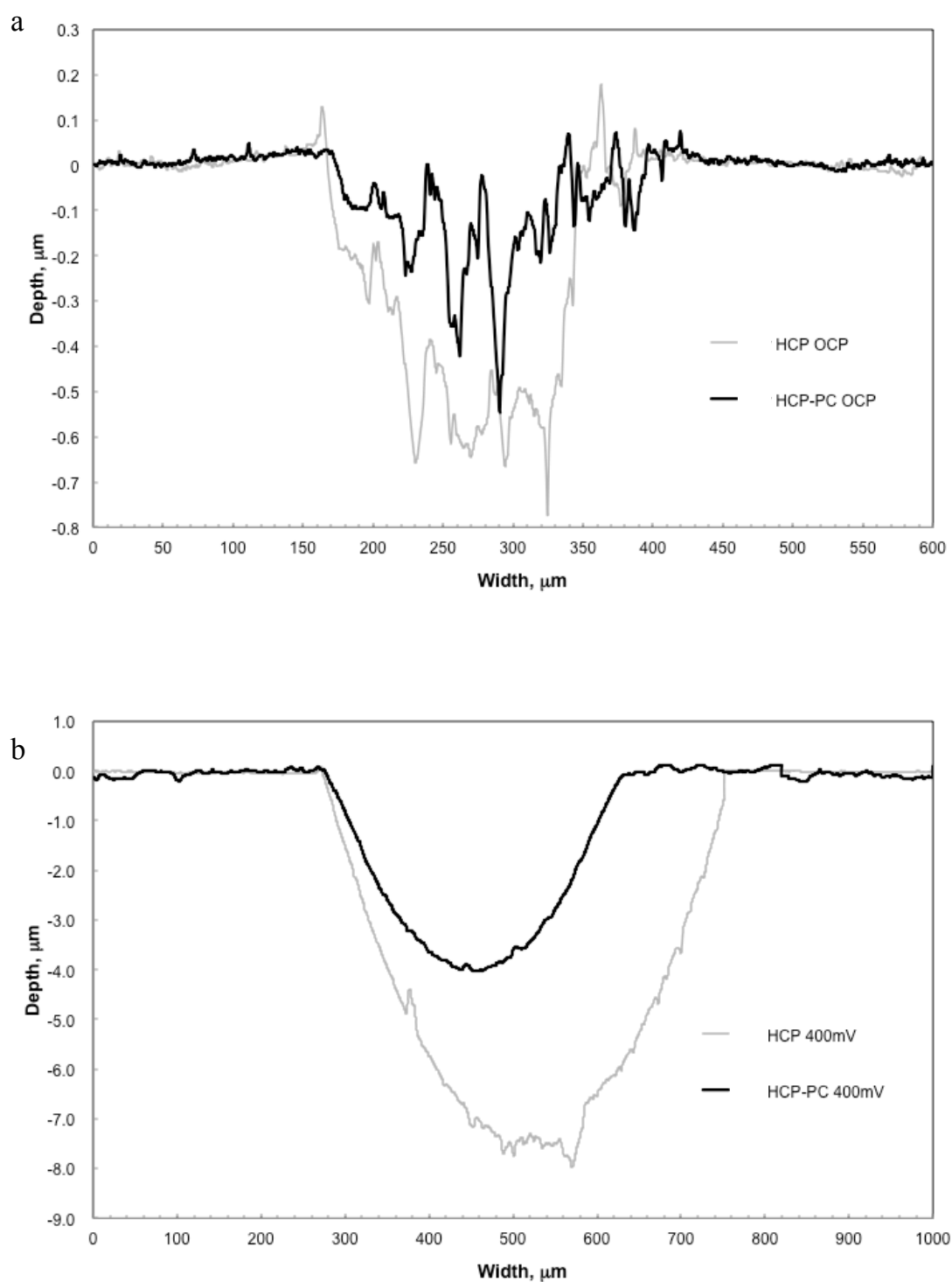


Figure 4.7.20 Typical cross-section profiles of wear tracks of HCP and HCP-PC (a) at OCP and (b) 400 mV(SCE).

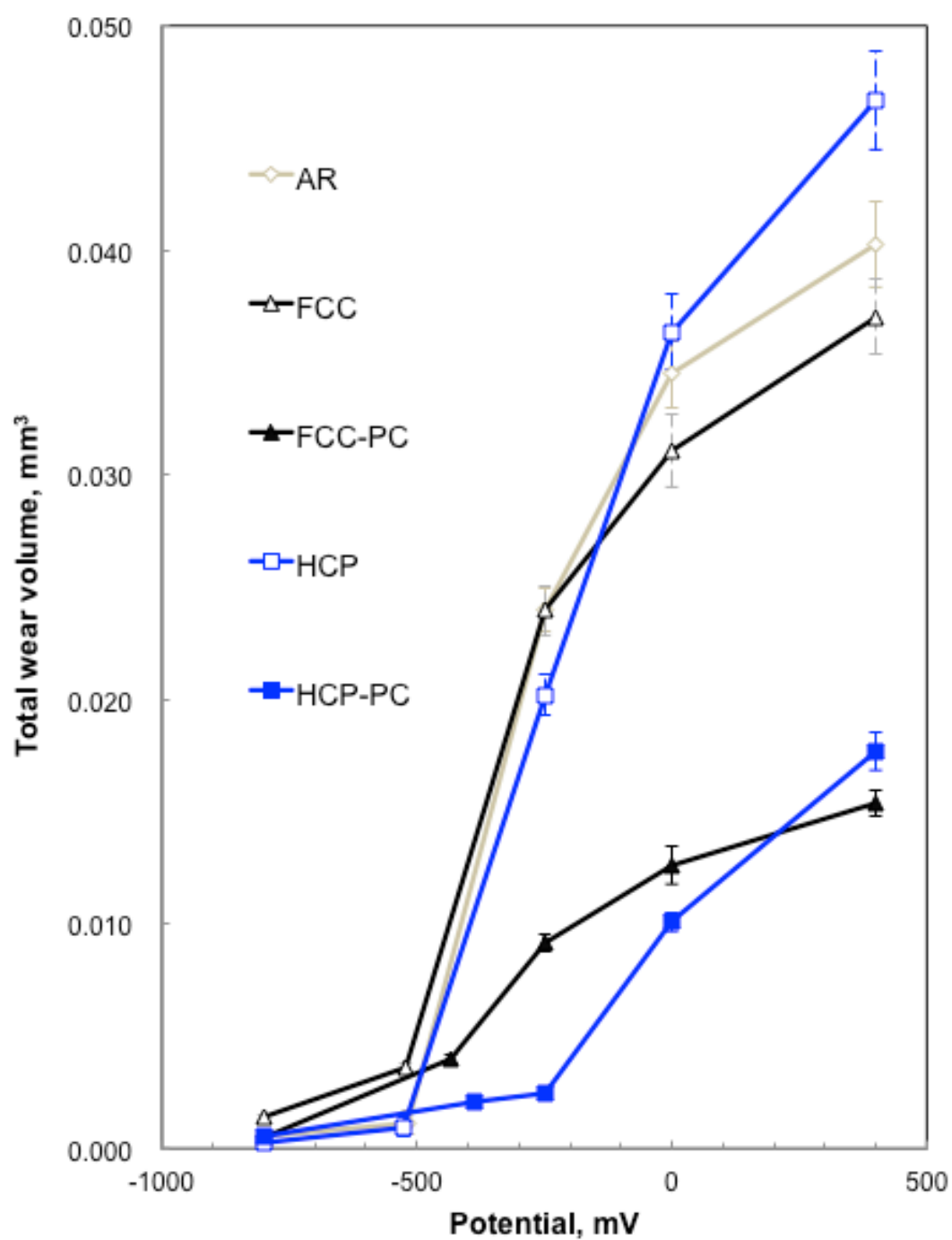


Figure 4.7.21 Total wear volume of all samples as a function of potentials (error bar showing the standard deviation).

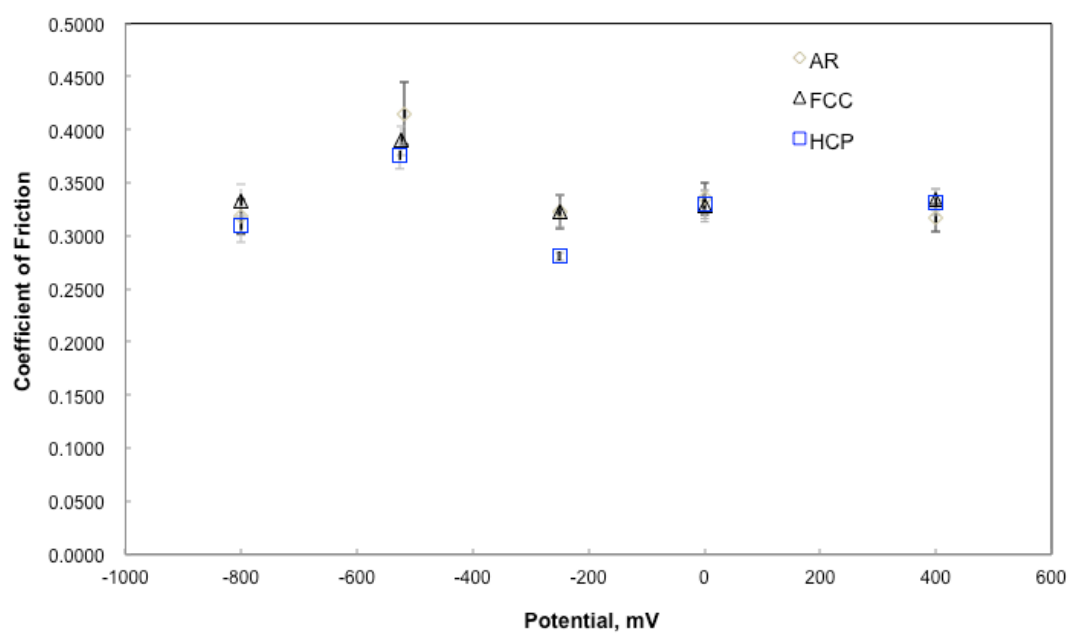


Figure 4.7.22 Coefficient of friction of the AR and heat-treated samples as a function of applied potential (error bar showing the standard deviation).

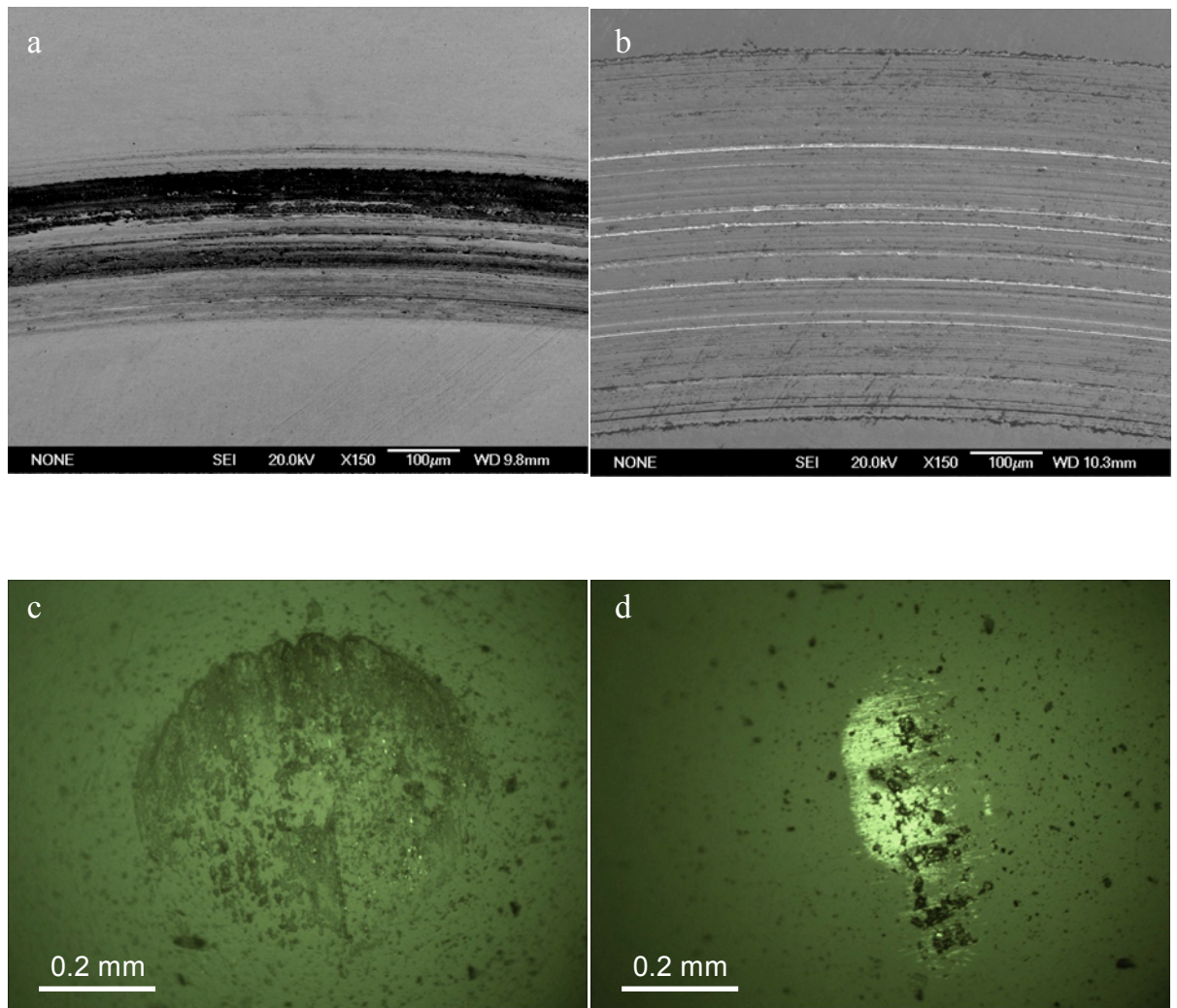


Figure 4.7.23 Secondary electron images of wear tracks generated (a) at OCP and (b) at 400mV (SCE) for AR. Optical microscopic images of balls tested (c) at OCP and (d) at 400mV (SCE) for AR.

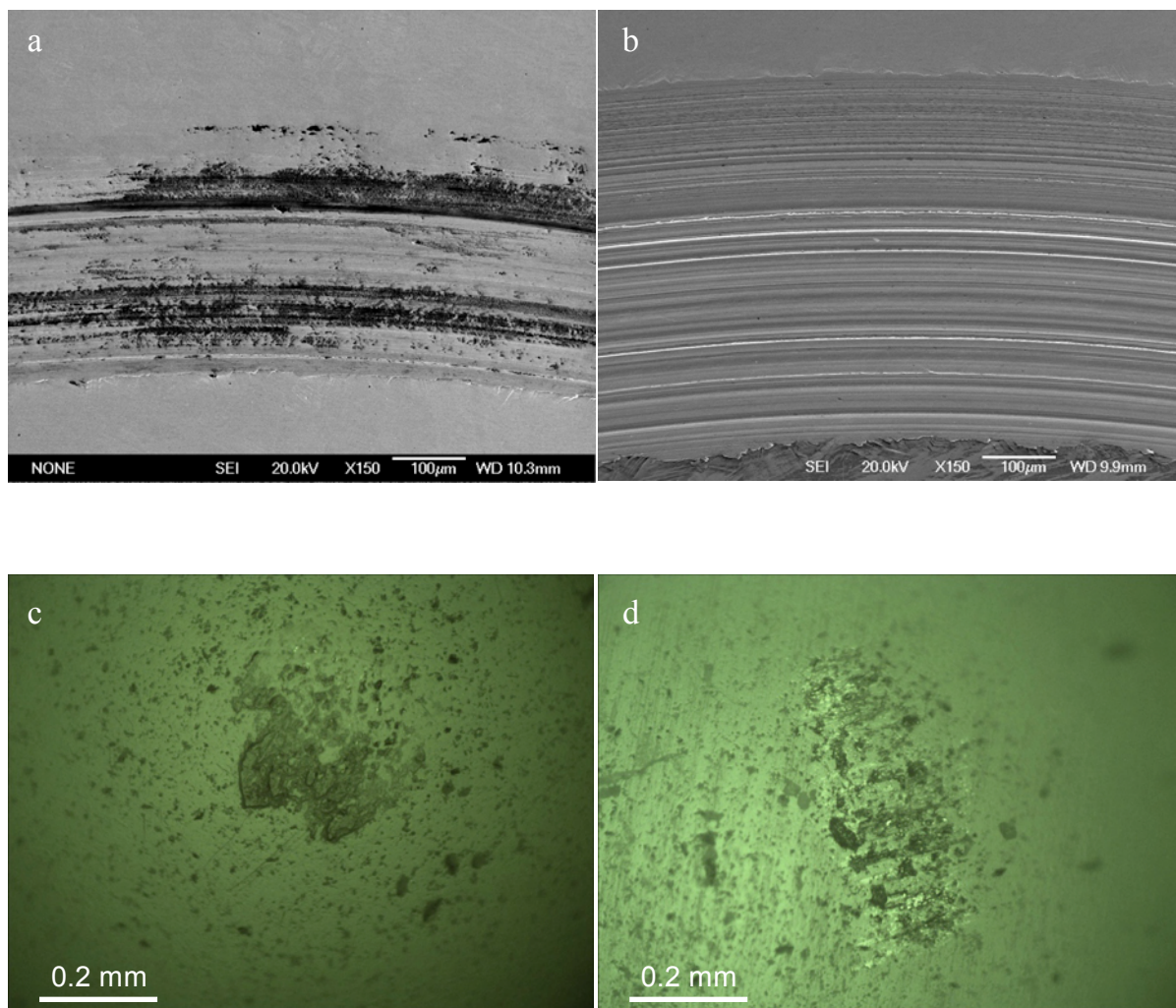


Figure 4.7.24 Secondary electron images of wear tracks generated (a) at OCP and (b) at 0mV (SCE) for FCC. Optical microscopic images of balls tested (c) at OCP and (d) at 0mV (SCE) for FCC.

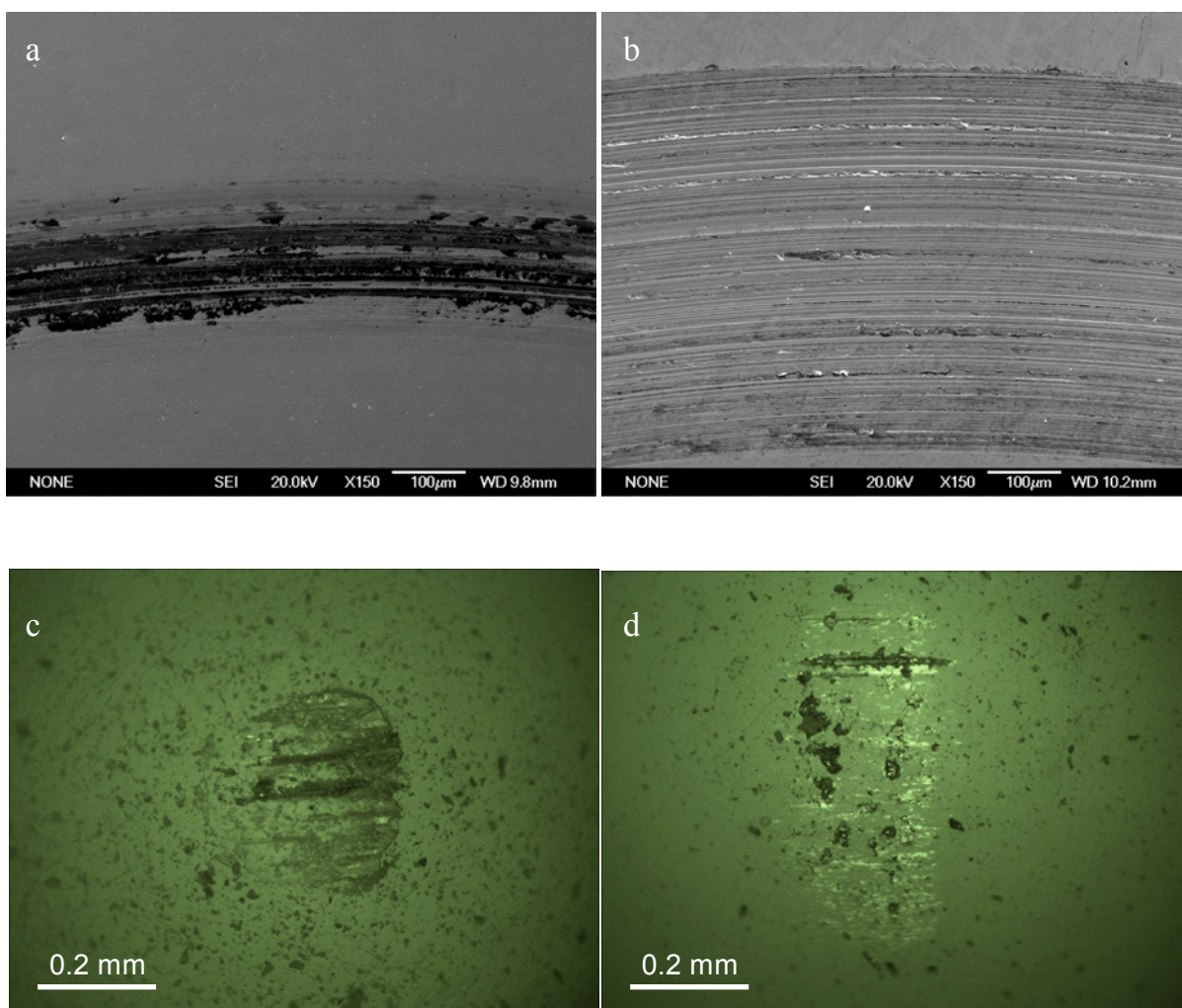


Figure 4.7.25 Secondary electron images of wear tracks generated (a) at OCP and (b) at 400mV (SCE) for HCP. Optical microscopic images of balls tested (c) at OCP and (d) at 400mV (SCE) for HCP.

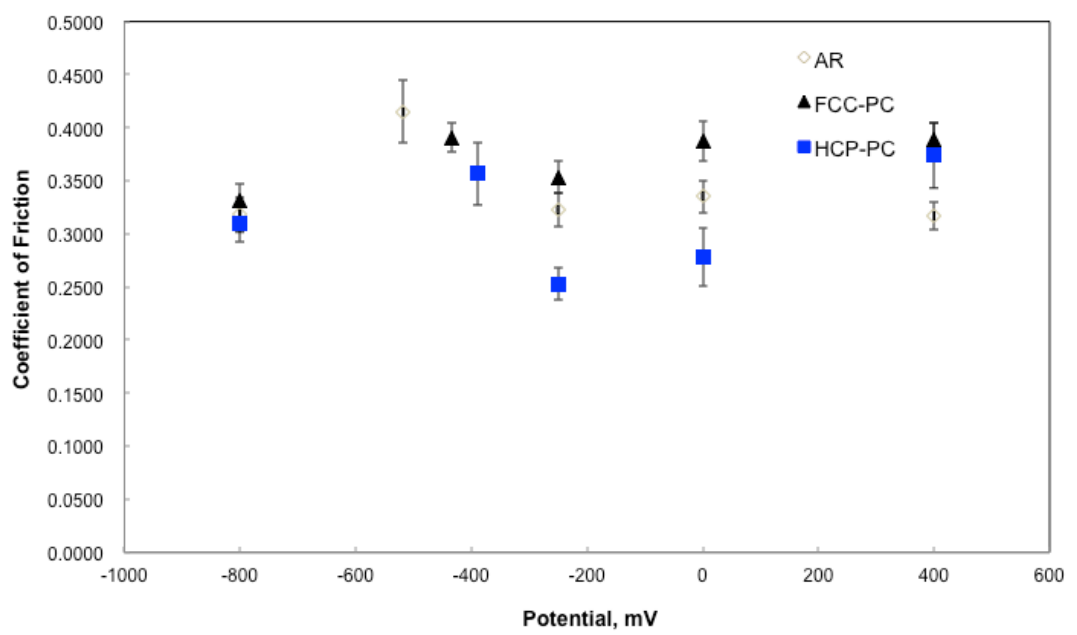


Figure 4.7.26 Coefficient of friction of the AR and plasma carburised samples as a function of applied potential (error bar showing the standard deviation).

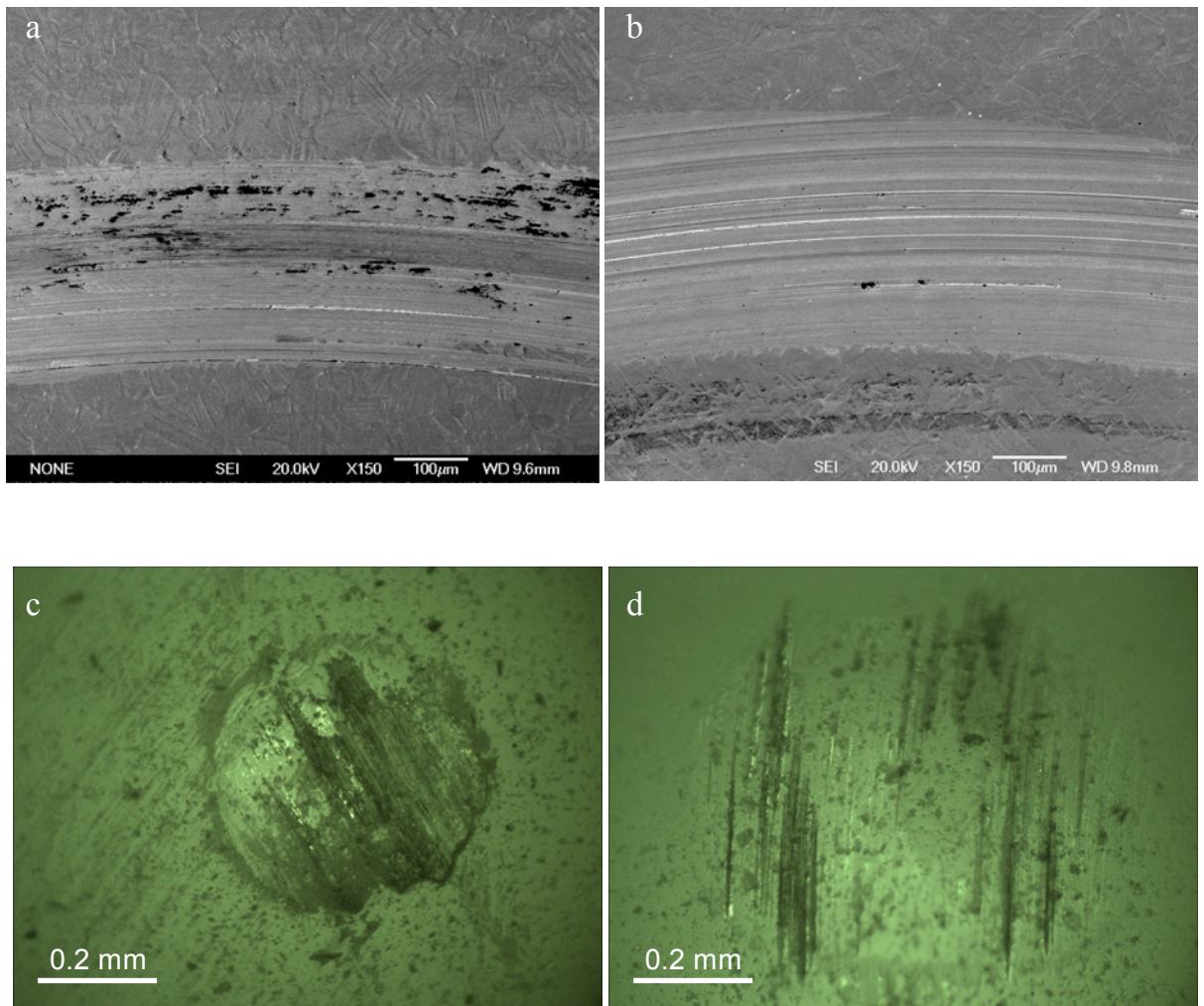


Figure 4.7.27 Secondary electron images of wear tracks generated (a) at OCP and (b) at 0mV (SCE) for near FCC-PC. Optical microscopic images of balls tested (c) at OCP and (d) at 0mV (SCE) for FCC-PC.

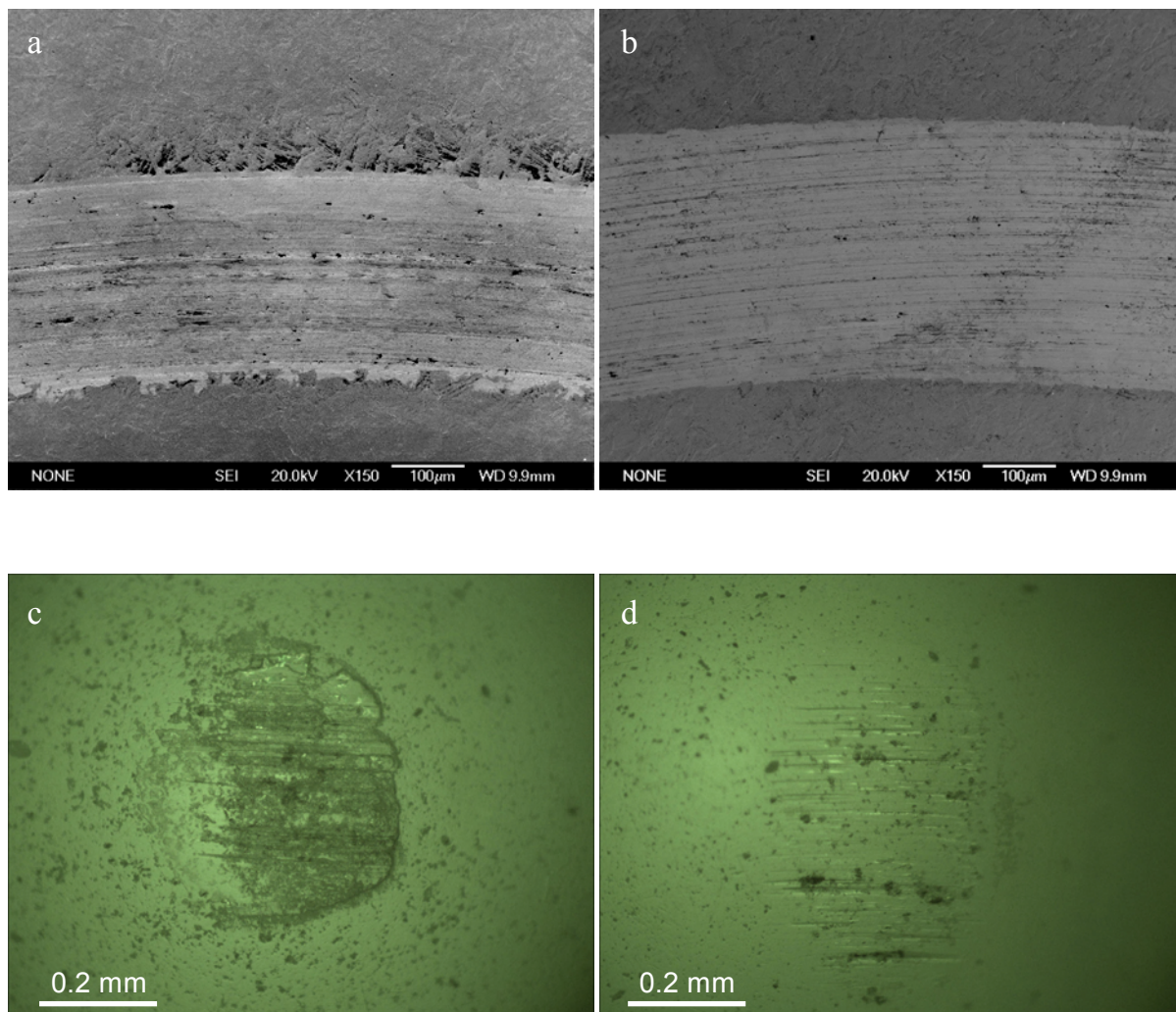


Figure 4.7.28 Secondary electron images of wear tracks generated (a) at OCP and (b) at 400mV (SCE) for HCP-PC. Optical microscopic images of balls tested (c) at OCP and (d) at 400mV (SCE) for HCP-PC.

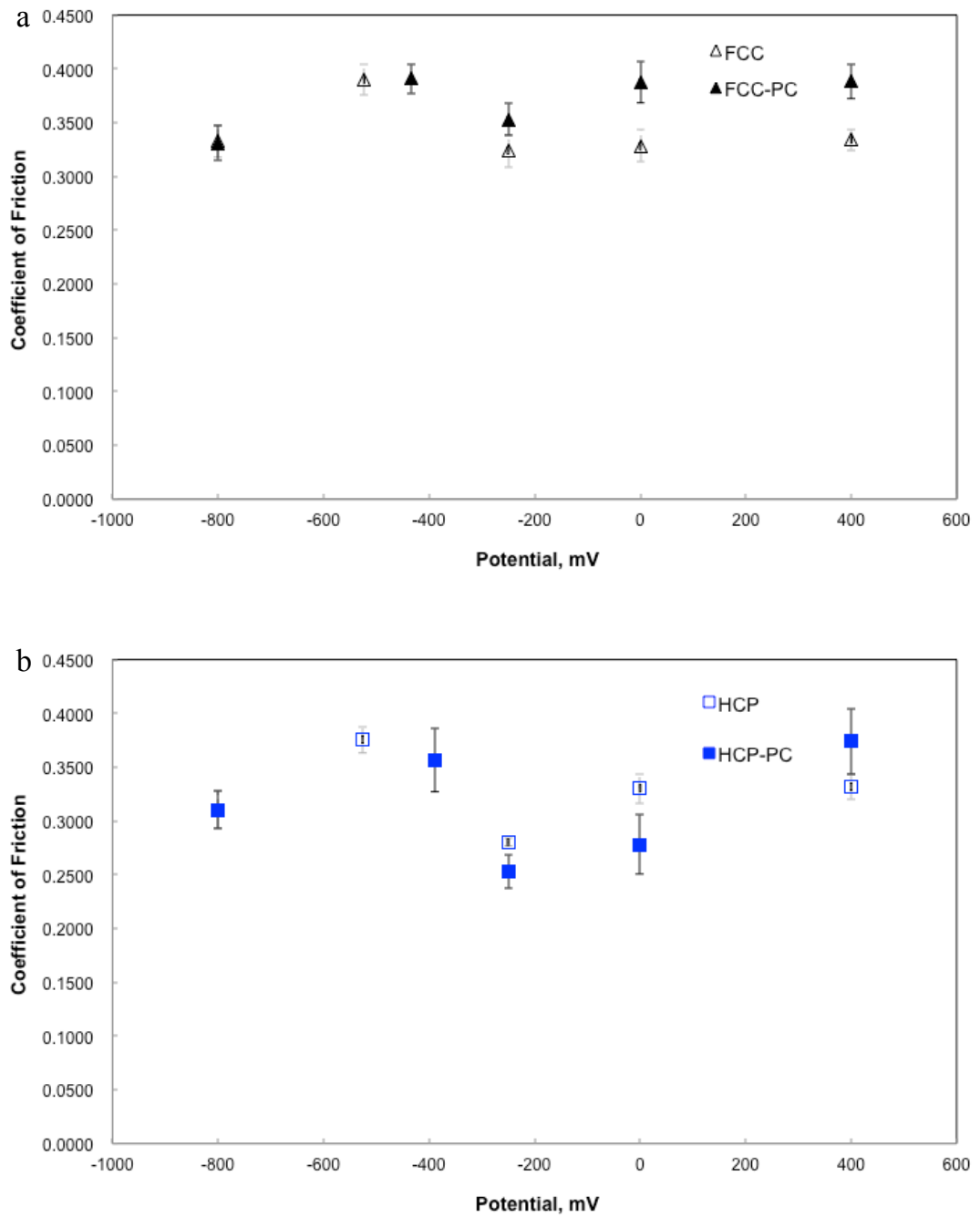


Figure 4.7.29 Coefficient of friction of samples before and after plasma carburising treatment as a function of applied potential: (a) FCC and FCC-PC and (b) HCP and HCP-PC (error bar showing the standard deviation).

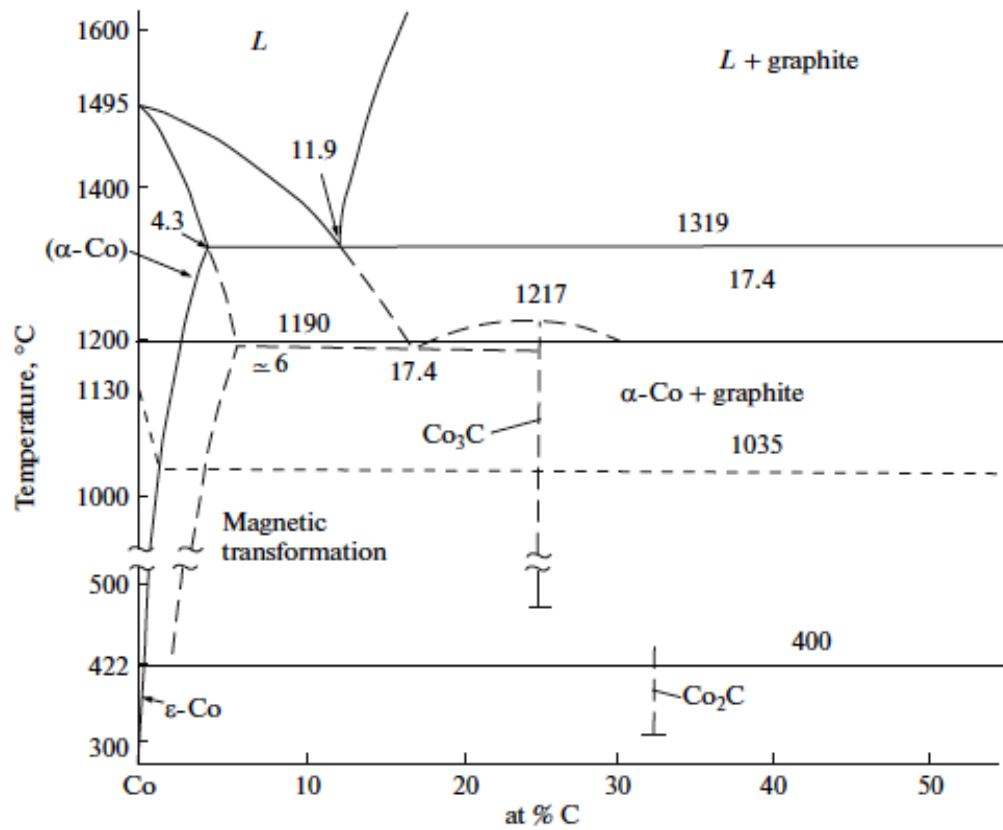


Figure 5.2.1 Co-C phase diagram. [149]

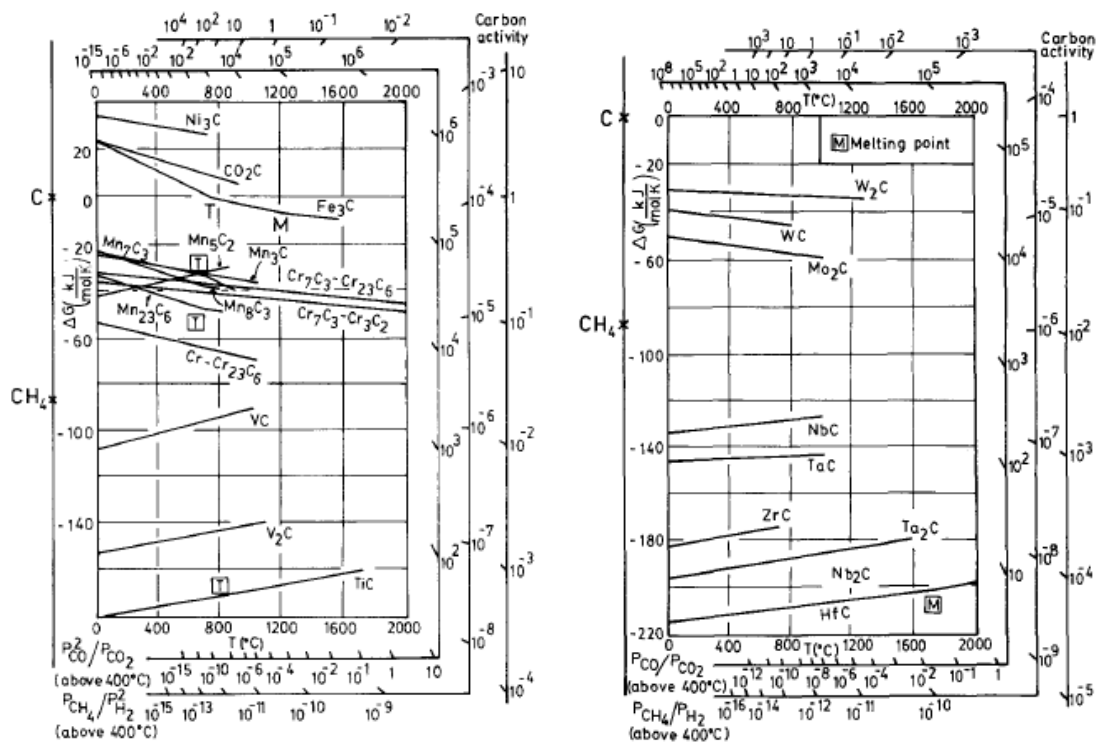


Figure 5.2.2. Ellingham diagram for (a) the first-transition-series carbides including Cr_{23}C_6 , Cr_7C_3 , Cr_3C_2 and Co_2C and (b) the second- and third-transition series carbides including Mo_2C . [152]

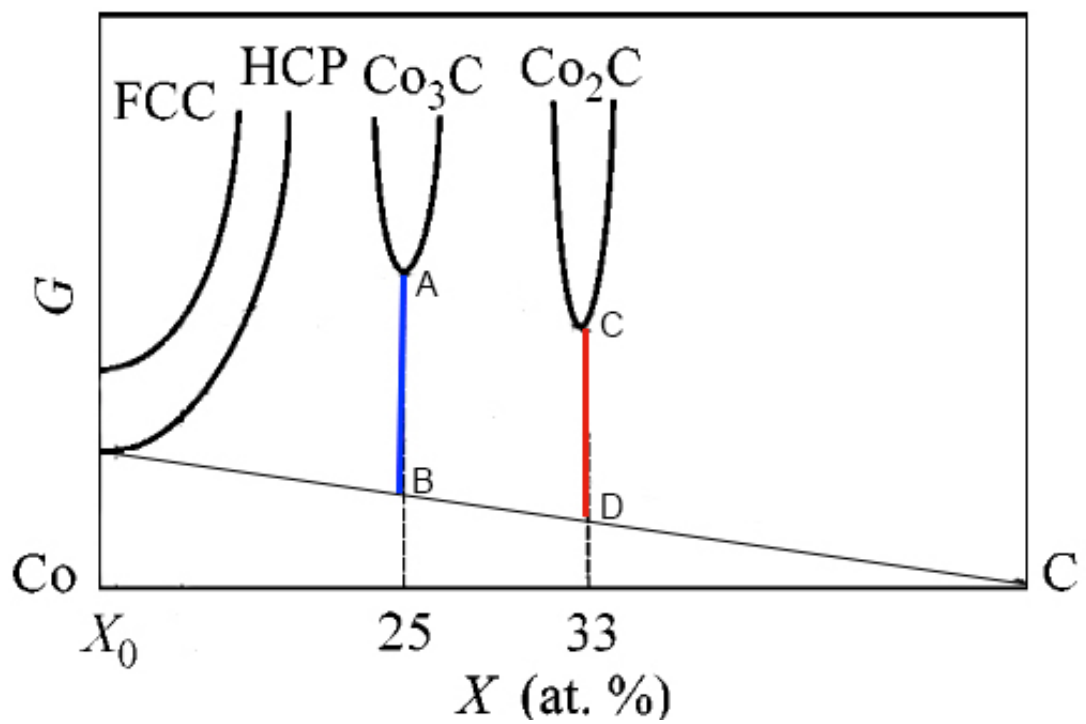


Figure 5.2.3 Qualitative phase diagram of a Co-C system on the (G, X) coordinates. [153]

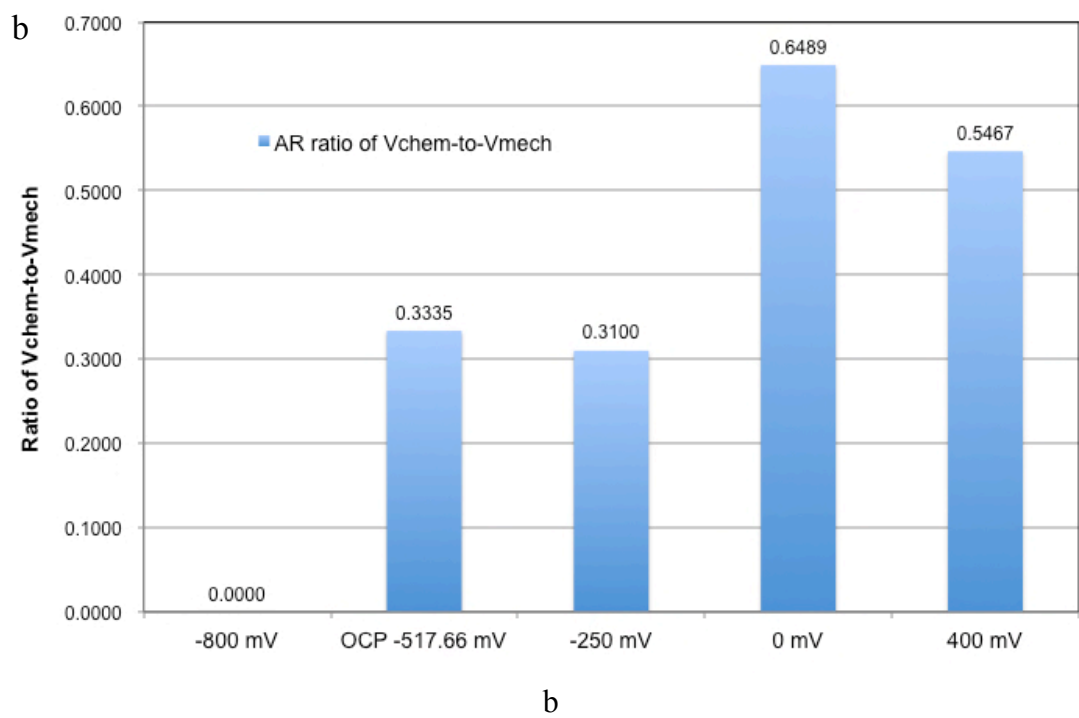
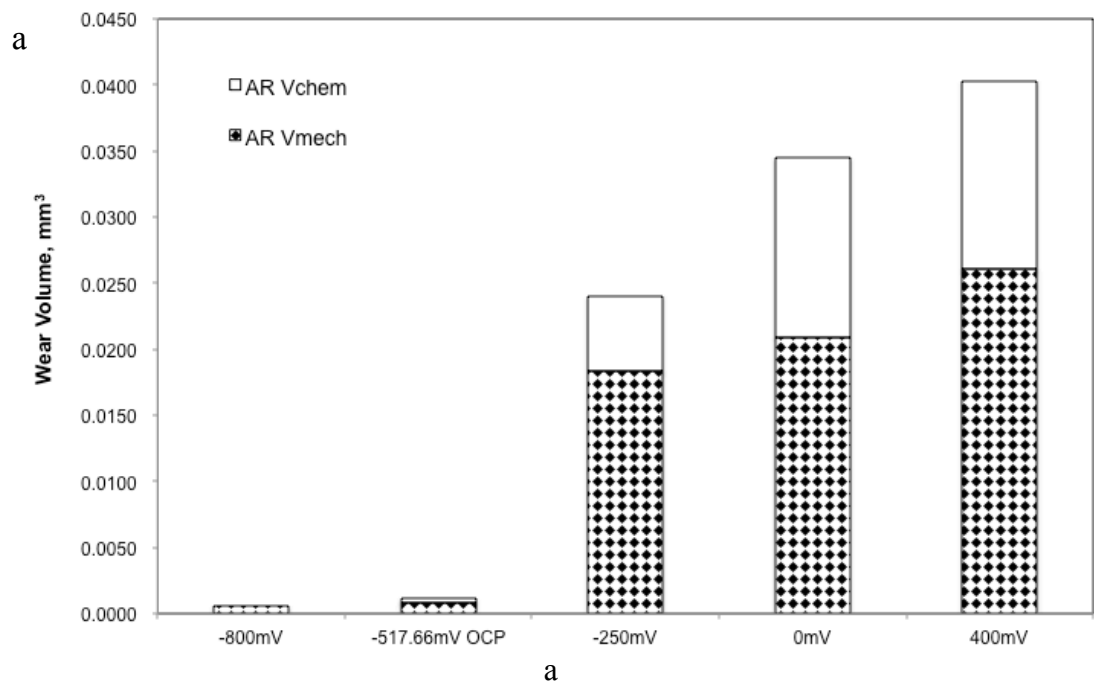


Figure 5.5.1 (a) Results of V_{chem} and V_{mech} and (b) the ratio of V_{chem} -to- V_{mech} for the AR sample.

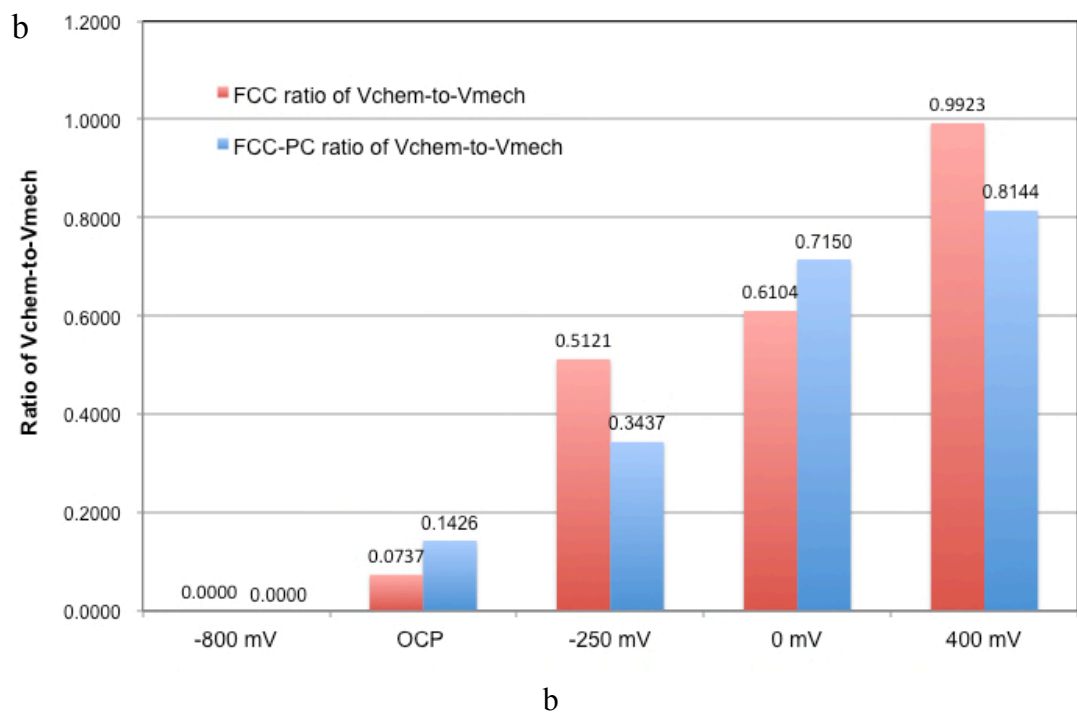
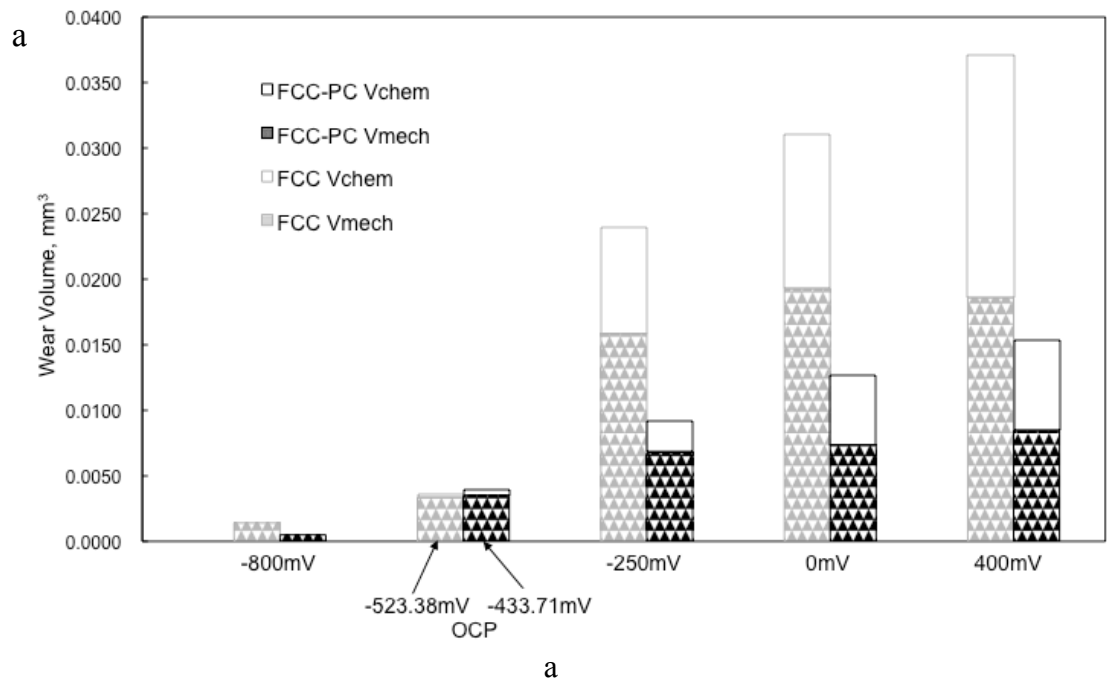


Figure 5.5.2 (a) Results of V_{chem} and V_{mech} and (b) the ratio of V_{chem} -to- V_{mech} for the FCC and FCC-PC samples.

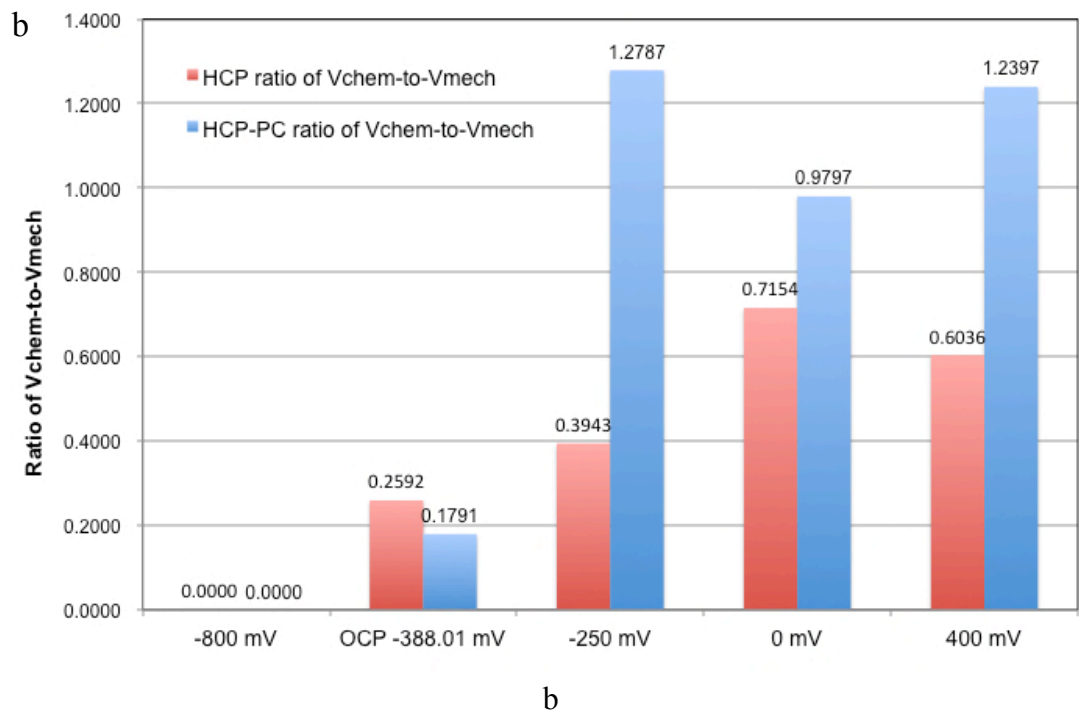
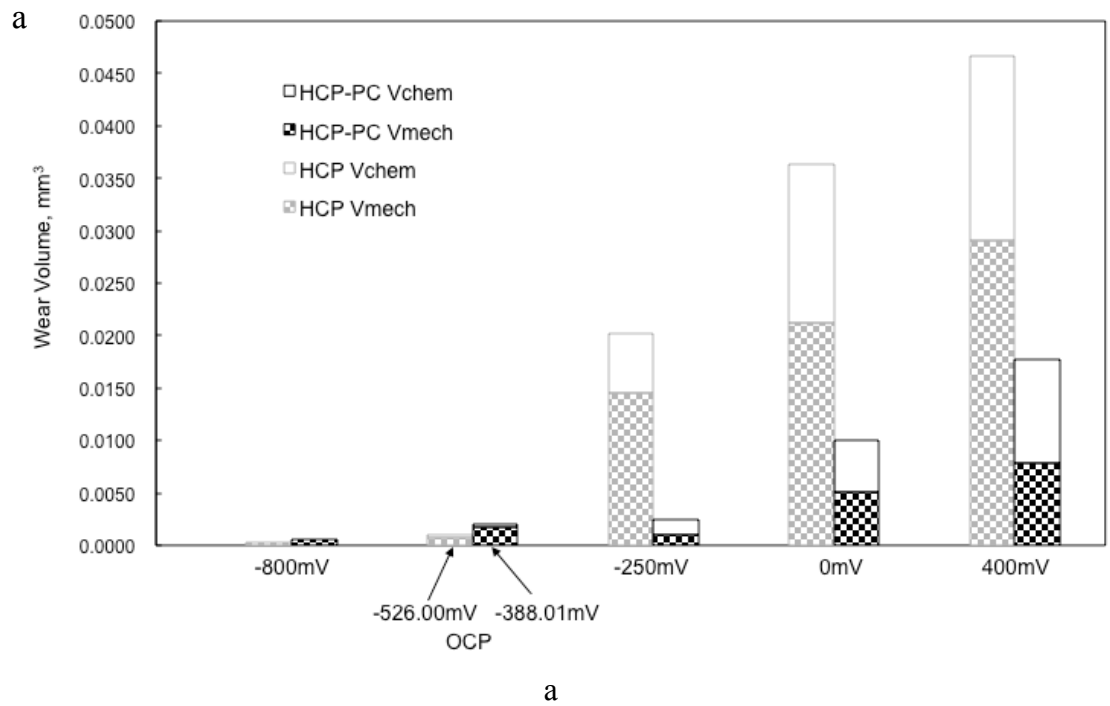


Figure 5.5.3 (a) Results of V_{chem} and V_{mech} and (b) the ratio of V_{chem} -to- V_{mech} for the HCP and HCP-PC samples.